

UCLA

UCLA Electronic Theses and Dissertations

Title

Forging Experimental Pathways to Planetary Core Convection

Permalink

<https://escholarship.org/uc/item/9dg5s239>

Author

Xu, Yufan

Publication Date

2023

Peer reviewed|Thesis/dissertation

UNIVERSITY OF CALIFORNIA

Los Angeles

Forging Experimental Pathways to Planetary Core Convection

A dissertation submitted in partial satisfaction
of the requirements for the degree
Doctor of Philosophy in Geophysics and Space Physics

by

Yufan Xu

2023

© Copyright by

Yufan Xu

2023

ABSTRACT OF THE DISSERTATION

Forging Experimental Pathways to Planetary Core Convection

by

Yufan Xu

Doctor of Philosophy in Geophysics and Space Physics

University of California, Los Angeles, 2023

Professor Jonathan M. Aurnou, Chair

Many planetary bodies can generate and sustain large-scale magnetic fields. The kinetic energy of electrically conducting fluids inside the bodies converts into magnetic energy through so-called “dynamo” processes. Turbulent thermo-chemical convective flows in a planet’s electrically conducting fluid core often generate a planetary-scale, dipole-dominated magnetic field. The magnetic field generated by dynamo processes acts back on the convective flow via Lorentz forces, creating a complex turbulent magnetohydrodynamic (MHD) system. Investigating the planetary dynamos will elucidate the fundamental dynamics of planetary interiors, providing essential information on the formation and evolution of the host planet. Moreover, strong planetary-scale magnetic fields can shield the planets from high-energy cosmic radiation and charged particles from the stars, making dynamo study crucial for habitability and searching for life on candidate bodies in the solar system and other exoplanetary systems.

In this thesis, I present a series of laboratory experiments to investigate the essential force balance and turbulence dynamics of planetary-core-style convection, in which magnetic field, rotation, and thermal buoyancy are applied to a liquid metal (gallium) fluid body on the

ROMAG device. These experimental investigations help bridge dynamics at planetary core boundaries and the interior of the fluid core, providing valuable insights into the fundamental physics of dynamo processes. They also provided an experimental pathway to connect small-scale dynamics that can be studied in the laboratory and large-scale dynamics within the planetary cores. This pathway is essential as current numerical simulations and experiments cannot capture large-scale dynamics directly.

I investigate the MHD effects at the planetary boundaries using a simplified end-member system of core-style convection: non-rotating magnetoconvection (MC). I have characterized a self-sustaining thermoelectric effect in liquid metal turbulent MC with electrically conducting boundaries. The thermoelectric currents at the boundaries generate a large-scale precession of the turbulent convective flow. To explain this phenomenon, I have developed a solid-liquid analytical model that predicts precession frequencies agreeing with the lab data. This model also produces a set of new dimensionless parameters to describe under what conditions the thermoelectric effect could become prominent near the Earth's core-mantle boundary (CMB).

Furthermore, I study liquid metal MC's heat transfer and behavior regimes from onset to highly supercritical. I have compared the effects of magnetic constraints in MC with the rotational constraints. With a better understanding of the MC system as a building block, I have carried out a set of rotating convection (RC) and rotating magnetoconvection (RMC) experiments to probe the internal flow dynamics of planetary cores. Our preliminary results hint that the turbulent liquid metal RC can form large-scale, barotropic vortices through an inverse cascade in kinetic energy. This stairway of energy cascade could potentially connect laboratory scale dynamics to planetary scale flows and provide insights into the dynamical origin of the observed large-scale magnetic structures.

The dissertation of Yufan Xu is approved.

Susanne Horn

James C. McWilliams

Lars Stixrude

Carolina Lithgow-Bertelloni

Jonathan M. Aurnou, Committee Chair

University of California, Los Angeles

2023

To my parents and my wife ...

TABLE OF CONTENTS

1	Introduction	1
1.1	Earth’s and planetary magnetic fields	1
1.2	Investigating the geodynamo through geomagnetic field observation	4
1.2.1	The induction equation	4
1.2.2	Geomagnetic field model	6
1.2.3	South Atlantic Anomaly: CMB heterogeneity or deeper core origin?	10
1.3	Forward modeling of core dynamics	13
1.3.1	Governing equations	14
1.3.2	Nondimensional parameters	16
1.3.3	Boundary heterogeneity	18
1.3.4	Interior core dynamics	19
1.3.5	Inverse cascade as a possible pathway	22
1.4	Research questions	26
2	Laboratory Analog of Planetary Cores	27
2.1	Laboratory simulation of the planetary cores	28
2.2	The RoMag Device	30
2.2.1	The cylinder tanks	31
2.2.2	Cooling system	33
2.2.3	Power system: heat pad and Argantix power supply	35
2.2.4	Power system: magnet power supply	35
2.2.5	The solenoid	36

2.2.6	Rotating System	41
2.2.7	Data acquisition system	43
2.2.8	Control systems	55
2.3	Other auxiliary systems	58
2.3.1	Holiday emergency heating system (HEHS)	58
2.3.2	Remote access	59
2.3.3	Current protection	60
2.3.4	Thermal Insulation	61
2.3.5	Mini-jacks	62
2.4	Calibration	63
2.4.1	Thermal conduction profile and heat loss	63
2.4.2	Material properties	67
2.4.3	Thermometry calibration	70
2.4.4	Doppler velocimetry calibration	70
2.4.5	Magnetometry calibration	70
2.4.6	Rotation rate calibration	71
2.5	A catalog of RoMag’s Standard Operating Procedures (SOPs) and manuals .	72
2.6	Open issues and future upgrades	74
2.6.1	Open issues	74
2.6.2	Future upgrades	75
3	The Transition from Wall Mode to Multimodal Magnetoconvection in Liquid Gallium	78
3.1	Introduction	79

3.2	Control parameters and linear prediction	80
3.3	Methods	84
3.4	Results	90
3.4.1	Comparing onset predictions	90
3.4.2	Transition to multimodality	93
3.5	Discussion	97
3.5.1	Wall modes stability and the cellular flow regime	97
3.5.2	The Nu vs. Ra MC party	98
3.5.3	Comparison between magnetoconvection and rotating convection in liquid metal	100
3.5.4	Summary	103
3.6	Appendix: Tables	105
3.7	Appendix: RBC heat transfer in the 40-cm tank	114
4	Thermoelectric Magnetoconvection at Planetary Boundaries	115
4.1	Introduction	116
4.2	Background	118
4.2.1	Thermoelectric Effects	118
4.2.2	Governing Equations and Nondimensional Parameters	121
4.2.3	Previous Studies of Turbulent Magnetoconvection	127
4.3	Experimental Set-up and Methods	129
4.4	Magnetoconvection with Electrically Insulating Boundaries	134
4.5	Thermoelectric Magnetoconvection with Conducting Boundaries	140
4.6	Fixed Rayleigh Number TEMC Survey	146

4.7	Thermoelectric Precession Model	151
4.7.1	Angular Momentum of the LSC Flywheel	152
4.7.2	Thermoelectric Currents at the Electrically Conducting Boundaries	153
4.7.3	Thermoelectric Forces and Torques	155
4.7.4	Thermoelectrically-driven LSC Precession	158
4.7.5	Experimental Verification	160
4.8	Discussion	165
4.9	TEMC at Earth’s core-mantle boundary	168
4.10	Weakly rotating Magneto-Coriolis Waves	172
4.11	LSC torsional/sloshing modes in liquid gallium	174
4.11.1	Torsional and sloshing modes in liquid metal convection	174
4.11.2	No Sloshing or Torsional Modes in <i>Long Conducting RBC</i>	182
4.11.3	No Sloshing or Torsional Modes in <i>Insulating MC-</i>	187
4.11.4	Weak Sloshing and Strong Torsional Modes in <i>Long Conducting MC</i>	191
5	Large Scale Structures in Turbulent RC and RMC	196
5.1	Large-scale flows in core convection	197
5.2	Experimental methods	201
5.3	Large-scale vortices in liquid metal rotating convection turbulence?	202
5.3.1	The bulk mode onset	202
5.3.2	Experimental results	204
5.4	Comparison with other cases	209
5.4.1	RC 2kW	209
5.4.2	RMC cases	210

5.5	Discussion and future works	212
5.5.1	Wave propagations in RMC	212
5.5.2	Characterizing the turbulence	214
5.5.3	The wall modes	215
5.5.4	Transport efficiency and scaling law	218
6	Conclusion	219
6.1	Thesis work	219
6.2	Collaborations	221

LIST OF FIGURES

1.1	Radial magnetic field at CMB.	9
1.2	South Atlantic Anomaly.	11
1.3	Rotating Magnetoconvection (RMC) and its reduced systems.	13
1.4	Three-dimensional Rotating Convection DNS generates Large-scale vortices (LSVs).	23
2.1	Laboratory simulation of the planetary core—the ROMAG device.	28
2.2	Photos of the ROMAG device.	31
2.3	Schematics of the ROMAG’s major systems.	32
2.4	40-cm tank design.	33
2.5	Argantix XDS 300-17 power supply.	35
2.6	Solenoid drawing.	36
2.7	ROMAG’s magnetic field characterization.	38
2.8	Horizontal magnetic field flux density contour of 20.2 A at 40 cm from the top.	39
2.9	Measured B-field, D mT, as a function of output current from the Magna power supply.	40
2.10	ROMAG’s Lab Frame Rail.	41
2.11	ROMAG’s current rotary union.	42
2.12	ROMAG’s DAQ system.	43
2.13	SCXI boxes.	45
2.14	The upgraded 66-ports Channel terminal.	46
2.15	Four-layer circuit board design for the upgraded 66-port BNC channel terminal.	47
2.16	Amphenol thermistors.	48

2.17	ROMAG’s thermometry.	49
2.18	Schematics (not to scale) of Ultrasonic Doppler Velocimetry.	50
2.19	Ultrasonic Doppler Velocimetry operating range.	51
2.20	Ultrasonic Doppler Velocimetry setup on a 40-cm tank.	52
2.21	3MH3A Magnetic Field Digital Teslameter.	54
2.22	Schematics of the control system.	55
2.23	Power vs. Delta T.	56
2.24	Magna Power Supply.	57
2.25	Holiday Emergency Heating System (HEHS).	59
2.26	Thermal insulation blanket.	61
2.27	ROMAG’s mini-jacks.	62
2.28	Material profile of ROMAG’s tanks with different end-block boundaries.	63
2.29	One-Dimensional thermal conduction profile.	65
2.30	Estimating thermal diffusivity using the spectral method in a conduction case.	69
2.31	Rotation rate vs. magnet power supply output current.	72
2.32	80-cm tank design.	77
3.1	Different prediction of critical Rayleigh number (Ra_{crit}) as a function of the Chandrasekhar number.	85
3.2	a) Thermometry schematic for the $\Gamma = 2R/H = 2.0$ tank ($R = 98.6$ mm)	87
3.3	$Nu - Ra$ survey with various Ch from current study and one set of $Ch = 10^6$ data by King & Aurnou (2015).	89
3.4	Temperature and velocity fields from $\Gamma = 2.0$ laboratory experiments at $Ch = 4.0 \times 10^4$	92

3.5	Azimuthal mode number m as a function of Ra	93
3.6	Collection of Nu - Ra data from this study and previous MC laboratory experiments in liquid metal.	99
3.7	Normalised Nusselt number (Nu/Nu_0) versus magnetic Rossby number (Ro_m).	101
3.8	Nu vs. Ra Rayleigh-Bénard convection of liquid gallium in $\Gamma = 0.5$ and 1.0 tank.	114
4.1	A thermoelectric current loop.	120
4.2	Schematic of the laboratory apparatus.	132
4.3	Temperature time series for the $Ra = 1.61 \times 10^6$, $Nu = 5.8$ electrically-insulated (Teflon) boundary conditions experiment.	135
4.4	Electrically-insulating boundary study.	137
4.5	Temperature data of the <i>Insulating RBC</i> case shifted azimuthally into the best fit LSC frame.	139
4.6	Temperature time series for the $Ra \simeq 1.82 \times 10^6$, $Nu \simeq 5.86$ electrically-conducting boundary conditions experiment.	141
4.7	Identical to figure 4.4, but showing the $Ra \approx 1.8 \times 10^6$, $Nu \approx 5.8$ <i>Conducting MC⁺</i> , <i>Conducting RBC</i> , <i>Conducting MC⁻</i> subcases experiment.	143
4.8	Temperature anomaly \tilde{T}_{ij}^k as defined eq. (4.38).	144
4.9	Spectrogram.	147
4.10	Time series of the horizontal temperature difference at different heights.	150
4.11	Cross-section view of the precessional flywheel model (pink) in the LSC plane (yellow).	153
4.12	Cross-sectional schematics of the experimental MC system with electrically conducting boundaries.	154
4.13	Free-body diagram of thermoelectric LSC precession.	156

4.14	Time series of LSC precessional rate for the <i>Conducting MC⁻</i> case.	162
4.15	Normalized precessional frequency, $\tilde{f} = f/f_{\kappa}$, versus convective interaction parameter, $N_{\mathcal{C}}$	164
4.16	Convective and thermoelectric interaction parameters.	166
4.17	Schematic adapted from Garnero <i>et al.</i> (2016) and Deschamps <i>et al.</i> (2018) showing thermoelectric currents \mathbf{J}_{TE} and forces \mathbf{F}_{TE} in the vicinity of the core-mantle boundary (CMB).	169
4.18	The Seebeck number Se as a function of the net Seebeck coefficient \tilde{S}	171
4.19	Hovmöller diagrams of the sidewall midplane temperature fluctuation.	176
4.20	A three-dimensional diagram showing the LSC that undergoes sloshing oscillation.	178
4.21	The torsional oscillations at different heights and phases in the mean LSC frame.	180
4.22	A top-view schematic diagram of the LSC.	181
4.23	Timeseries of the azimuthal angles of the temperature extrema.	182
4.24	Timeseries of the $\delta\phi_j^{mid}/\pi - 1$ for the <i>Long Conducting RBC</i> case for 5 thermal diffusion time.	183
4.25	FFT of $\delta\phi_j^{mid}$ with Hanning window for the <i>Long Conducting RBC</i> case.	184
4.26	Timeseries of $\Delta\phi_{max}/\pi$ and $\Delta\phi_{min}/\pi$ for the <i>Long Conducting RBC</i> case.	185
4.27	Hanning window FFT of $\Delta\phi_{max}$ and $\Delta\phi_{min}$	186
4.28	Timeseries of the $\delta\phi_j^{mid}/\pi - 1$ for the <i>Insulating MC⁻</i> case.	187
4.29	FFT of $\delta\phi_j^{mid}$ with Hanning window for the <i>Insulating MC⁻</i> case.	188
4.30	Timeseries of $\Delta\phi_{max}/\pi$ and $\Delta\phi_{min}/\pi$ for the <i>Insulating MC⁻</i> case.	189
4.31	Hanning window FFT of $\Delta\phi_{max}$ and $\Delta\phi_{min}$	190
4.32	Timeseries of the $\delta\phi_j^{mid}/\pi - 1$ for the <i>Long Conducting MC⁻</i> case for 5 thermal diffusion time.	191

4.33	FFT of $\delta\phi_j^{mid}$ with Hanning window for the <i>Long Conducting MC⁻</i> case. . . .	192
4.34	Timeseries of $\Delta\phi_{max}/\pi$ and $\Delta\phi_{min}/\pi$ for the <i>Long Conducting MC⁻</i> case. . . .	193
4.35	Hanning window FFT of $\Delta\phi_{max}$ and $\Delta\phi_{min}$	194
5.1	Critical <i>Ra</i> of steady modes in RC, MC, and RMC.	197
5.2	Experimental cases of RC and RMC.	200
5.3	Experimental setup on ROMAG with 40-cm tank.	201
5.4	Top-lid sensors.	202
5.5	Azimuthal velocity on a horizontal plane of RC onset oscillatory bulk mode at $Ek = 8 \times 10^{-7}$, $Pr = 0.027$, and $\Gamma = 0.5$	203
5.6	Hovmöller diagrams of UDVs for the RC 60W case.	206
5.7	Synthetic UDV Hovmöller diagrams for $m = 2$ LSV – D6.	207
5.8	Synthetic UDV Hovmöller diagrams for $m = 2$ LSV – D7.	208
5.9	Hovmöller diagrams of UDVs for the RC 60W case.	209
5.10	Hovmöller diagrams of UDVs for the RMC 60W and 2kW cases.	211
5.11	Frequency-wavenumber (f-k) spectra of the vertical velocity data from the RMC 60W case.	213
5.12	Sidewall midplane thermometry Hovmöller diagram of 60W cases in both RMC and RC.	217
6.1	Dinosaur.	222

LIST OF TABLES

1.1	Nondimensional parameters in rotating magnetoconvection.	25
2.1	Measured current load on ROMAG’s electronic deck.	60
3.1	Values of different predicted critical Ra	84
3.2	Current study. Liquid gallium. $Pr = 0.027, \Gamma = 2$	106
3.3	Current study. DNS. $Pr = 0.025, \Gamma = 2$	107
3.4	Current study. Liquid gallium. $Pr = 0.027, \Gamma = 1$	107
3.5	Current study. Liquid gallium. $Pr = 0.027, \Gamma = 1$. Continued.	108
3.6	Cioni <i>et al.</i> (2000 <i>a</i>). Liquid mercury. $Pr = 0.025, \Gamma = 1$	109
3.7	Cioni <i>et al.</i> (2000 <i>a</i>). Liquid mercury. $Pr = 0.025, \Gamma = 1$. Continued	110
3.8	Aurnou & Olson (2001). Liquid gallium. $Pr = 0.023, \Gamma = 6$	111
3.9	Burr & Müller (2001). Liquid Na-K alloy. $0.017 < Pr < 0.021$, rectangular box 20 : 10 : 1.	112
3.10	King & Aurnou (2015). Liquid gallium. $Pr = 0.025, \Gamma = 1$	112
3.11	Zürner <i>et al.</i> (2020). Liquid GaInSn. $Pr = 0.029, \Gamma = 1$	113
4.1	Nondimensional parameters and parameter groups in thermoelectric magneto- convection (TEMC).	125
4.2	Experimental parameter values from the <i>Conducting MC⁻</i> subcase.	159
4.3	Parameters used to estimate Seebeck numbers (4.62) across Earth’s core-mantle boundary (CMB).	171
5.1	Experimental parameters for liquid gallium RC and RMC cases in the 40-cm tank.	199

ACKNOWLEDGMENTS

I would like to extend my heartfelt appreciation to my advisor, Jon Aurnou, whose ideas, wisdom, and infectious enthusiasm have been a constant source of inspiration. His insightful comments during our countless hours of intellectually stimulating discussions have shaped me into a better scientist and person. His genuine care and scientific rigor have motivated me, and I'm always ready to join him on a "restaurant crawl" for both food and scientific enlightenment.

I want to express my gratitude to Susanne Horn, whose numerical simulations have played a vital role in various aspects of my thesis work. Her keen understanding of fluid dynamics has led to many fruitful discussions. I also want to thank my current and past committee members, Carolina Lithgow-Bertelloni, Lars Stixrude, Paul Davis, and James McWilliams, for their thoughtful feedback and guidance on my thesis work and other collaborations.

To my amazing lab mates in Spinlab, I couldn't be more grateful for your support throughout my entire Ph.D. A special shout-out to my former colleague, Ashna Aggarwal, whose athletic mindset and "second lunch" routine always brought energy and joy to the lab. Your funny socks day never failed to make me smile. I also thank Emily Hawkins for her insightful guidance and advice, kind support, and great sense of understanding through tough times. I would also like to thank Jewel Abbate for her illuminating personality, ideas, and masterful lab skills, which greatly contributed to the experimental setup and data analysis for my thesis. My thanks go out to Cy David as well, whose genius and talents have been instrumental in completing this thesis. Additionally, I want to express my appreciation to Miranda Chang, Nika Eskandari, Rachel Tripoli, Hearth Yager, Taylor Lonner, David James, Jake Ehret, Robert Long, Tao Cai, and Sietze Oostveen for their help, friendship, and support.

I am immensely grateful to my colleagues, especially my former roommate and dear friend, Akash Gupta, for constantly humbling me with his countless bets, advisor-like guidance, and encouragement. I extend my appreciation to Tyler Powell and Ariel Graykowski,

whose boundless creativity never ceases to amaze me. I want to acknowledge Han Bao for his courage in pivoting careers and serenading us with his Mongolian song. Special thanks go to Xiyuan Bao for providing valuable feedback on my research. Lastly, I would like to express my gratitude to all my other friends and colleagues for their unwavering emotional support throughout the years.

The heroic EPSS staff deserves special recognition for their invaluable assistance on multiple fronts of this work. I extend my thanks to Eric Wessenauer, the building manager, for his handy help in troubleshooting essential components of the experiments. I am grateful to Brad Stewart for manufacturing parts for the experiment, to Peter Yu for designing the electronic components, to Roderic O'Connor of the IT department, and to the EPSS purchasing team. I want to thank Emmanuel Masongsong for his machining advice and musical talent, and to Henry Gonzalez for his help with acrylic. I would also like to acknowledge Lauri for her advice and support during important events throughout my Ph.D.

I want to thank Tobias Vogt for his help and guidance on the UDV system, and many inspiring conversations contributing to this thesis. I want to thank Hao Cao for his career advice and support, and also for his insightful feedback on the thesis. I would also like to thank Jing Li and David Jewitt for generously sharing their family dinners and providing encouragement. I am grateful to all the faculty members I have served as a teaching assistant for.

My deepest gratitude goes to my parents, who never had the opportunity to attend college. They have selflessly devoted their unconditional love and life savings to support me. Their wisdom and guidance have encouraged me to embark on new adventures in life. They have taught me the importance of facing challenges with calmness and persistence. I also want to thank the rest of my family for their constant encouragement, love, and support. Lastly, I would like to sincerely thank my lovely wife, Weixin Yang. You have been the brightest star and the endless source of happiness and positivity in my life. Thank you for enduring my dreadful presentations but still being my biggest supporter. Your mindful

feedback on my writing has been invaluable. Without you, completing this thesis would not have been possible.

I would like to gratefully acknowledge the support of the NSF Geophysics Program (EAR awards #1620649, #1853196, and #2143939) for funding this thesis work.

VITA

- 2013-2017 B.Sc. Applied Math, Engineering and Physics (AMEP), University of Wisconsin-Madison.
- 2015 Hilldale Undergraduate/Faculty Research Fellowship, University of Wisconsin-Madison.
- 2017-2023 Graduate Student Researcher, Teaching Assistant, University of California, Los Angeles.
- 2022 UCLA Dissertation Year Fellowship, University of California, Los Angeles.

PUBLICATIONS

1. **Xu, Y.**, Abbate, J., David, C., Horn, S., Vogt, T., & Aurnou, J. (2023). Large-scale vortices in liquid metal rotating convection. *Science*. In-prep.
2. **Xu, Y.**, Horn, S., & Aurnou, J. (2023). The Transition from Wall Mode to Multimodal Magnetoconvection in Liquid Gallium. *Physics Review Fluids*. In review.
3. **Xu, Y.**, Horn, S., & Aurnou, J. (2022). Thermoelectric Precession in Turbulent Magnetoconvection. *Journal of Fluid Mechanics*, 930, A8.
4. Grannan, A., Cheng, J., Aggarwal, A., Hawkins, E., **Xu, Y.**, Horn, S., Sanchez-Alvarez, J., & Aurnou, J. (2022). Experimental pub crawl from Rayleigh-Bénard to magnetostrophic convection. *Journal of Fluid Mechanics*, 939, R1.
5. Abbate, J., **Xu, Y.**, Vogt, T., Horn, S., Julien, K. & Aurnou, J. (2023). Diffusivity-free heat and momentum transfer in liquid metal rotating convection experiments. In prep.

6. David, C. S., Hester, E. W., **Xu, Y.**, & Aurnou, J. M. (2023). Magneto-Stokes Flow in a Shallow Free-Surface Annulus. *Journal of Fluid Mechanics*. In prep.

CHAPTER 1

Introduction

*“Of course she’s not afraid. She knows
that the Sun will rise again tomorrow.”*
— Cixin Liu, *The Dark Forest*

This chapter introduces the grand scheme of the geophysical and astrophysical context for magnetic field generation processes in planetary bodies. This chapter sets the motivations for our laboratory experiments on the magnetic influences of planetary core-style convection. Section 1.1 describes the Earth’s and planetary magnetic fields. Section 1.2 explains the challenges of studying geodynamo from inversion via the example of the South Atlantic Anomaly. Section 1.3 discusses forward modeling methods for core dynamics. It also covers the mathematical description of the rotating magnetoconvection (RMC) system and its subsystem magnetoconvection (MC) that are explored in this thesis. Section 1.3.5 shows that the inverse cascade can be an important pathway to explain large-scale structures in the core. Section 1.4 sets fundamental research questions for this thesis.

1.1 Earth’s and planetary magnetic fields

The mysterious attraction between two lodestones has intrigued humanity’s curiosity ever since the dawn of civilization. Although early records of natural magnetism can be found in ancient Greek and Chinese manuscripts, it was not until the English physicist William Gilbert (1540-1603) that magnetism was investigated systematically using scientific methods.

In his famous publication in 1600, *De Magnete*, Gilbert intuitively explained that the origin of the dipole geomagnetic field is similar to that of a static bar magnet. However, with the accumulation of geomagnetic data collected from marine navigators and global magnetic surveys, our view on the geomagnetic field has changed dramatically since. The geomagnetic field has exhibited complex time-dependent characteristics such as secular variations in field strength and orientations, first proposed and measured by Edmund Gunter, 1622 and Henry Gellibrand, 1635. This fascinating phenomenon, now precisely measured and monitored by near-Earth satellites (e.g., [Finlay *et al.*, 2012](#)), strongly indicates that our geomagnetic field has a fluid dynamic origin – the molten outer core must be generating and creating temporal changes in the geomagnetic field (e.g., [Roberts & Scott, 1965](#); [Bloxham *et al.*, 1989](#)). The Earth’s liquid outer core is located 2890 km below the surface and extends 2265 km in thickness. The outer core is mainly composed of electrically conducting liquid metals, such as iron (78 – 88%), nickel (5%), and some lighter elements (5 – 10%) ([McDonough & Sun, 1995](#); [Stacey & Davis, 2008](#)). Moreover, the geotherm exceeds the Curie point of any natural ferromagnetic materials below merely $\sim 10 - 50$ km (e.g., [Schlinger, 1985](#); [Frost & Shive, 1986](#)). Thus, the remnant magnetic materials in the Earth’s crust only contribute locally to the Earth’s magnetic field.

Paleomagnetic studies (e.g., [Hale & Dunlop, 1984](#); [Tarduno *et al.*, 2010](#)) reveal that the Earth’s dynamo has been operated for over 3.4 billion years. The longevity of Earth’s magnetic field also suggests that the field must be self-sustaining and constantly generated against magnetic diffusion ([Stevenson, 2003](#)) because the magnetic diffusion timescale of the Earth is estimated to be $\sim 65,000$ years ([Roberts & King, 2013](#)), only a fraction of Earth’s geomagnetic record. Without active magnetic generation processes, the Earth would quickly lose its magnetic field over a few magnetic diffusion timescales.

Joseph Larmor proposed in 1919 that a self-exciting dynamo, powered by the internal motion of conducting material, could give birth to the Sun’s and Earth’s magnetic fields ([Larmor, 1919](#)). Later this idea was furthered by [Elsasser \(1939\)](#) and [Bullard \(1949\)](#), which laid

the fundamental theory for convection-driven dynamos. Their work demonstrated that the combination of convective and rotational motions could maintain the dynamo. The current view on Earth’s magnetic field generation processes remains magnetohydrodynamic. The most popular idea is that turbulent thermal and compositional convection provides kinetic energy to the core flows and drives fluid motions inside planets (Jones, 2011, 2015). The kinetic energy of electrically conducting fluids at the interior of bodies converts into magnetic energy through dynamo processes. Moreover, rotational and magnetic forces interact with these turbulent convective motions.

The astrophysical-scale magnetic field is non-unique to the Earth. Many celestial bodies, including galaxies, stars (e.g., Brandenburg & Subramanian, 2005), planets, icy moons (e.g., Stevenson, 2003; Tikoo & Evans, 2022), and even asteroids (Nimmo, 2009; Fu *et al.*, 2012), can generate self-sustained magnetic fields at different stages of their existence. The first evidence of a planetary magnetic field outside the Earth was only found about seven decades ago by Burke & Franklin (1955) through the observation of the Jovian radio waves. Understanding the magnetic field generation processes inside planets is crucial in the search for life on other bodies in the solar system and exoplanetary systems (e.g., Kochukhov, 2021). On Earth, turbulent convective flows in the molten metal outer core generate a planetary-scale, dipole-dominated magnetic field. This magnetic field partially shields the Earth from high-energy solar wind (Kivelson, 1995) and cosmic radiation (Grießmeier *et al.*, 2009). Moreover, without this global-scale magnetic field, high-energy charged particles from space will result in atmospheric loss, making the planetary bodies inhospitable for life (e.g., Moore & Khazanov, 2010; Lazio *et al.*, 2018; Ramstad & Barabash, 2021).

Understanding the magnetic field generation processes on planets, besides its significance in habitability, will elucidate the fundamental dynamics of the planetary interiors, which gives valuable information on the composition and evolution of the bodies. Recent Juno and Cassini missions have revealed that gas giants such as Jupiter and Saturn generate strong yet very different magnetic fields flux density and

structures (e.g. Moore *et al.*, 2018; Dougherty *et al.*, 2018; Cao *et al.*, 2020). This implies that these gas giants’ internal structures and magnetic field generation processes could differ significantly. However, tremendous challenges remain in our investigation of the Earth’s and planetary dynamo processes. Limitations of the current inversion methods and forward modeling methods are discussed in the following sections.

1.2 Investigating the geodynamo through geomagnetic field observation

1.2.1 The induction equation

Studying dynamo processes requires information about the core flows, especially their velocity, length scale, and energetics. So far, although there is no direct measurement of the core flows, estimates of the core flow velocity and scales are derived from geomagnetic secular variation data, the associated field models, and certain assumptions. The connection between the magnetic field’s time variations and their associated core flow velocity is described by the induction equation,

$$\frac{\partial \mathbf{B}}{\partial t} = \eta \nabla^2 \mathbf{B} + \nabla \times (\mathbf{u} \times \mathbf{B}), \quad \nabla \cdot \mathbf{B} = 0, \quad (1.1)$$

where \mathbf{B} is the magnetic field, \mathbf{u} is the fluid velocity, and η is the magnetic diffusivity, which is a material property of the fluid. Here, $\eta = 1/(\sigma\mu)$ is assumed constant, where σ is the electric conductivity and μ is the magnetic permeability. In the core, $\eta \sim 1 \text{ m}^2/\text{s}$ (Roberts & King, 2013). Equation (1.1) shows that the rate of change in the magnetic field involves diffusion and magnetic field generation. The first term on the right-hand side of the eq. (1.1) is magnetic diffusion via Ohmic dissipation. The second term is induction via fluid motions. It is worth noticing that there is a similarity between eq. (1.1) and the fluid vorticity equation.

The dimensionless magnetic Reynolds number characterizes the ratio of the induction to

diffusion:

$$Rm = \frac{UH}{\eta}, \quad (1.2)$$

where U and H are the characteristic system velocity and length scales, respectively. Alternatively, nondimensionalizing eq. (1.1) also leads to Rm ,

$$\frac{\partial \tilde{\mathbf{B}}}{\partial \tilde{t}} = \frac{1}{Rm} \tilde{\nabla}^2 \tilde{\mathbf{B}} + \tilde{\nabla} \times (\tilde{\mathbf{u}} \times \tilde{\mathbf{B}}), \quad (1.3)$$

where $\tilde{\mathbf{B}}$, \tilde{t} , $\tilde{\nabla}$, and $\tilde{\mathbf{u}}$ are dimensionless. A self-generated dynamo driven by steady flows in spherical geometry requires $Rm > 44$ (Chen *et al.*, 2018). Based on the secular variation data and measurements of the electrical conductivity of iron alloys, the Earth has a $Rm \sim \mathcal{O}(10^2)$ with a velocity of the observed core flows and a length scale of the thickness of the outer core. In general, the current view is that $Rm \gg 1$ in bulk is a necessary condition for self-sustaining planetary dynamos (Landeau *et al.*, 2022). Equation (1.1) also gives an essential clue to the origin of the geomagnetic field. Theoretically, any infinitesimal currents in the core can lead to a full-blown dynamo under suitable conditions (Landeau *et al.*, 2022).

In the extreme approximation of $Rm \rightarrow \infty$, the fluid is perfectly conducting. The diffusion term is now insignificant, eq. (1.1) becomes

$$\frac{\partial \mathbf{B}}{\partial t} = \nabla \times (\mathbf{u} \times \mathbf{B}), \quad (1.4)$$

which leads to the famous Alfvén’s theorem, or “frozen flux theorem”: *In a perfectly conducting fluid, the magnetic flux through any material surface is preserved – the flux tube moves with the flow as if frozen to it* (Davidson, 2016; Roberts & King, 2013). It is a linear analog of the Kelvin theorem for vorticity. Equation (1.4) suggests an important method for interpreting core flows via the frozen flux approximation: as $Rm \gtrsim \mathcal{O}(10^2)$ in the Earth’s outer core, the time variation of the radial components of the magnetic flux at the CMB approximately represents the large-scale core flows underneath the thin no-slip boundary layer. The secular variation data and geomagnetic field models are thus crucial to decipher the core dynamics. The secular variation suggests a root-mean-square (RMS) core flow velocity

up to 20 km/yr, or 0.63 mm/s at the CMB (Holme, 2015; Finlay *et al.*, 2016). Even though slower than LA’s traffic (surprisingly!), this sub-mm per second speed flow is lightning fast on the geological timescale. The overturn timescale of the core flow $\tau_{ot} \sim 2R/U \sim 200$ yrs.

1.2.2 Geomagnetic field model

Perhaps the most elegant and significant geophysical contribution by Gauss (1777-1855) is the mathematical model of the geomagnetic field (Gauss, 1877). Assuming the space outside Earth’s surface is electrically insulating, and there is no free current nor change of the electric field. Ampere-Maxwell’s law predicts that $\nabla \times \mathbf{B} = 0$. In this case, the geomagnetic field can be written as the gradient of the magnetic scalar potential,

$$\mathbf{B} = -\nabla V, \quad (1.5)$$

furthermore, $\nabla^2 V = 0$, which stems from the non-monopolar nature of the magnetic field ($\nabla \cdot \mathbf{B} = 0$). With no external source, the geomagnetic field potentials are solutions of Laplace’s equation.

The magnetic vector potential of a dipole can be written as

$$\mathbf{A} = \frac{\mu_0}{4\pi} \frac{\mathbf{m} \times \hat{\mathbf{r}}}{r^3}, \quad (1.6)$$

where \mathbf{m} is the magnetic moment, r is the radius, θ is the colatitude, defined with respect to the dipole axis, $\mu_0 = 4\pi \times 10^{-7} \text{ Hm}^{-1}$ is the vacuum permeability. The magnetic field is the curl of the magnetic vector potential, $\mathbf{B} = \nabla \times \mathbf{A}$. The magnetic scalar potential of a dipole is (Turcotte & Schubert, 2002)

$$V_m = \frac{\mathbf{m} \cdot \mathbf{r}}{4\pi r^3} = \frac{m \cos \theta}{4\pi r^2}, \quad (1.7)$$

in which the magnetic field is its gradient,

$$\mathbf{B} = -\mu_0 \nabla V_m. \quad (1.8)$$

Hence, the orthogonal components of \mathbf{B} in spherical coordinate write (Stacey & Davis, 2008)

$$B_\theta = -\frac{\mu_0}{r} \frac{\partial V_m}{\partial \theta} = \frac{\mu_0 m}{4\pi r^3} \sin \theta, \quad B_r = -\mu_0 \frac{\partial V_m}{\partial r} = \frac{\mu_0 m}{2\pi r^3} \cos \theta, \quad (1.9)$$

where θ is the latitude, and for Earth, $m_{Earth} = 7.768 \times 10^{22} \text{ Am}^2$. The magnetic field strength on the magnetic equator is $B_0 = 3.004 \times 10^{-5} \text{ T}$, or 0.3 Gauss (Stacey & Davis, 2008). The total field strength at the surface, $B = \sqrt{B_\theta^2 + B_r^2} = B_0 \sqrt{1 + 3 \cos^2 \theta}$. The RMS strength of the dipole field over the Earth's surface $\sim 4 \times 10^{-5} \text{ T}$, while the non-dipole field is about a quarter of it. In comparison, Jupiter has a magnetic dipole moment $m_{Jupiter} = 1.23 \times 10^{26} \text{ Am}^2$, and a surface (1 bar) equatorial field strength $4.17 \times 10^{-4} \text{ T}$ (Russell & Dougherty, 2010; Connerney *et al.*, 2018).

The general magnetic scalar potential can be expressed as a linear combination of Legendre polynomials (Gauss, 1877):

$$V_m = \frac{a}{\mu_0} \sum_{\ell=1}^N \left(\frac{a}{r}\right)^{\ell+1} \sum_{m=0}^{\ell} (g_\ell^m \cos m\phi + h_\ell^m \sin m\phi) P_\ell^m(\cos \theta), \quad (1.10)$$

where ℓ is the spherical harmonics degree, and $\ell = 1$ represents the dipole; a is the Earth's mean radius, $a = 6371 \text{ km}$; r , θ , and ϕ are radius, colatitude, and longitude components in a spherical coordinate; g_ℓ^m and h_ℓ^m are Gauss coefficients of degree ℓ and order m . P_ℓ^m is the Schmidt-normalized Legendre polynomials (Schmidt, 1917).

Equation (1.10) is a powerful tool for characterizing geomagnetic fields. Inversions from the secular variations of the geomagnetic fields yield an extrapolated velocity field of the outer core flow. Combining advanced numerical simulations, present-day magnetic field observations from low-Earth-orbit satellites reveal large-scale, short-time advection of the core fluid with increasing resolution and complexity over the last 20 years (Finlay *et al.*, 2023). The largest magnetic field changes are presently occurring at low latitudes (e.g., Olsen *et al.*, 2009; Finlay *et al.*, 2016). The strong secular variation at this region implies a westward speed of the core flow up to 15-50 km/yr (Finlay *et al.*, 2023). Quasi-geostrophic wave dynamics arising from the interplay among Lorentz, Coriolis, and inertia have been

proposed to explain the fluctuations of the outer core’s flow patterns (e.g., Hori *et al.*, 2015; Finlay *et al.*, 2023). However, it is yet unclear the exact pathway where the convective energy enters the system, which makes forward modeling of convection a necessity for understanding the ground truth of turbulent motions in the outer core.

Moreover, two main difficulties arise when attempting to solve the inverse problem of the geomagnetic field generated below the core-mantle boundary (CMB). First, the spatial attenuation of the magnetic field is significant and sets the lower bound for the length scale of the core dynamics that can be interpreted. Equation (1.10) predicts that the potential of an ℓ -th degree harmonic falls off with radius as $r^{-(\ell+1)}$, and the magnetic flux density, as the gradient of the potential, falls off as $r^{-(\ell+2)}$. The potential of a dipole source ($\ell = 1$) drops off as r^{-2} . The dipolar magnetic field, as a derivative of the potential, drops off as r^{-3} . The quadrupole field terms drop off as r^{-4} , and higher order terms drop off increasingly rapidly with the radius.

Second, non-trivial crustal magnetic fields complicate the interpretation and set the wavelength limits for the observable core dynamics. Langel & Estes (1982) have shown that the spectrum of the geomagnetic field below CMB becomes indistinguishable from the crustal field when $\ell \gtrsim 13$. For this reason, there are at least two distinct components in the observed surface geomagnetic field. The first is the main fields generated by dynamo processes which are limited to degree 13 and have a minimum surface length scale of $\sim 2\pi a/\ell_{max} \sim 10^3$ km, where $\ell_{max} = 13$ (Roberts & King, 2013). The second is the remnant magnetization in the crust, such as the oceanic magnetic anomalies, which exist in much shorter wavelengths and lower amplitudes than the main field (Kono, 2015).

Figure 1.1 a) shows a Mauersberger-Lowes spectrum of the geomagnetic field. The power spectrum is defined as (Mauersberger, 1956; Lowes, 1974)

$$R_\ell(r) = \left(\frac{a}{r}\right)^{2\ell+4} (\ell + 1) \sum_{m=0}^{\ell} [(g_\ell^m)^2 + (h_\ell^m)^2], \quad (1.11)$$

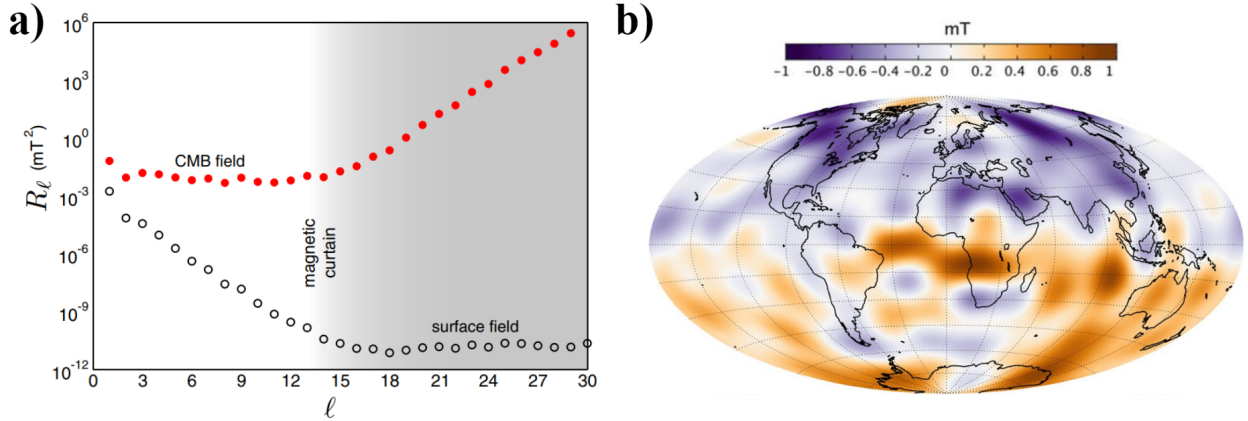


Figure 1.1: a) A Mauerberger-Lowes spectrum depicts the mean-square intensity of the geomagnetic field R_ℓ (mT^2) as a function of harmonic degree ℓ at the Earth’s surface $r = a$ and at the CMB $r = r_c$. The data points on the graph correspond to Gauss coefficients extracted from the xCHAOS model Olsen & Mandea (2008). Figure adapted from Roberts & King (2013). b) A snapshot of the radial magnetic field at CMB from CHAO-7 geomagnetic model (Finlay *et al.*, 2020) in 2019. Figures adapted from Finlay *et al.* (2020).

so that

$$\langle B^2(r) \rangle = \sum_{\ell=1}^{\infty} R_\ell(r), \quad (1.12)$$

where $\langle B^2(r) \rangle$ is the spherical surface average of the geomagnetic field squared at a radius of r .

The hollow symbols in fig. 1.1 a) represent the spectrum observed at Earth’s surface ($r = a$), while solid symbols represent the spectrum extrapolated to the CMB ($r = r_c$), using eq. (1.11). Below $\ell \lesssim 13$, the field intensity at CMB represents the main field generated by geodynamo. At $\ell \gtrsim 13$, however, the spectrum represents the small-scale crustal field. The shaded area in the fig. 1.1 a) indicates where information about the Earth’s core is obscured by the “magnetic curtain” above $\ell = 13$. The drastically increasing power of the larger spherical harmonic degree features at the CMB field, as shown in the upper curve of fig. 1.1 b), comes from incorrectly extrapolating a near-surface local source to a much deeper region. Therefore, these $\ell \gtrsim 13$ CMB data are unphysical (Roberts & King, 2013). However, even

though the time stationary field is restricted to $\ell = 13$, one can still observe secular variation beyond $\ell = 13$ since the crustal field does not change on fast time scales (Finlay *et al.*, 2020).

Regardless, fluxgate magnetometry on modern satellites with advanced geomagnetic field models (e.g., CHAOS-7 model) has provided sufficient accuracy up to spherical harmonics degree $\ell = 13$ for the time-dependent internal field at CMB (Finlay *et al.*, 2020), as shown in fig. 1.1 b). Combining geomagnetic data from the low-Earth orbit satellites and ground observation, CHAOS-7 is the parent model for the International Geomagnetic Reference Field (IGRF-13), which is the leading reference field model that includes magnetic vector measurements. Figure 1.1 b) shows that the magnetic flux patches from the radial magnetic field at the CMB are non-uniform and multi-scale. The symmetric four large-scale lobes at the north and south polar regions with $\sim 120^\circ$ apart contain most of the axial dipole energy and are thought to be long-lasting convection rolls in the outer core (e.g., Gubbins & Bloxham, 1987; Olson & Amit, 2006).

Source-free magnetic fields consist of poloidal and toroidal components (Chandrasekhar, 1961; Roberts & King, 2013). See Chandrasekhar (1961), p.622. The poloidal field contains information about the radial and latitudinal magnetic fields mentioned above. In addition to the difficulties in observing the poloidal field, assuming the mantle has a negligible electrical conductivity, dynamo theory requires toroidal fields restricted inside the source region, making it almost impossible to be observed (Stacey & Davis, 2008). So far, the effects of the toroidal field on the core flow are still poorly understood.

1.2.3 South Atlantic Anomaly: CMB heterogeneity or deeper core origin?

Our observation of the geomagnetic field secular variation is susceptible to only large-scale structures with slow time-scale motions. This low-pass filtering effect makes characterizing core flows challenging. Consequently, it is difficult to identify the dynamic region of the core that is responsible for any features of the geomagnetic field. A good example is the continental-scale magnetic anomaly, namely the South Atlantic Anomaly (SAA) (Gubbins,

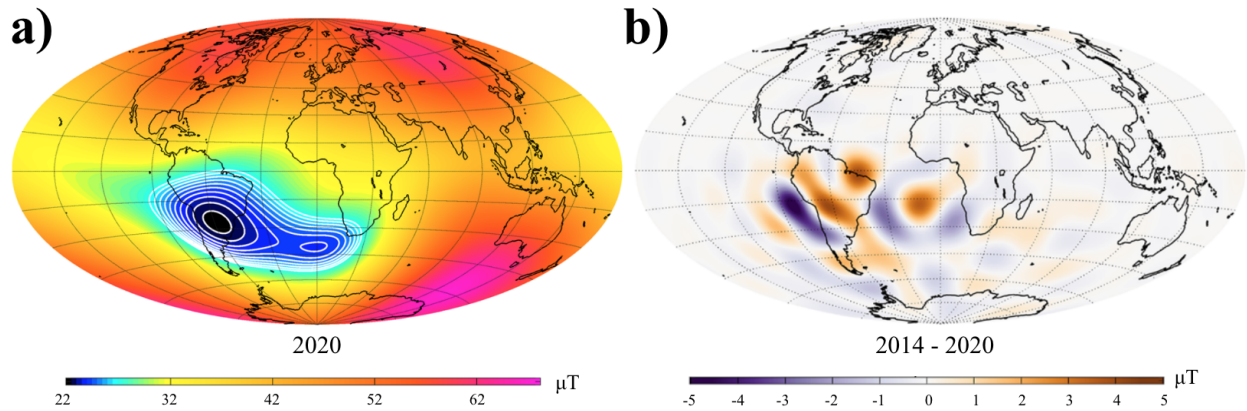


Figure 1.2: a) Magnetic field intensity at Earth’s surface from CHAO-7 geomagnetic model (Finlay *et al.*, 2020). The map is based on 2020’s CHAOS-7 internal field up to degree 20. Contour lines show the field intensity in steps of 500 nT from 22,500 nT. b) Temporal change in the radial magnetic field B_r at the core-mantle boundary focusing on the South Atlantic Anomaly region from 2014 to 2020. Both figures are modified from Finlay *et al.* (2020).

1987; Hulot *et al.*, 2002), which is believed to be originated from core flows below CMB. The SAA is like a ‘dent’ in the Earth’s magnetic field where the field strength is significantly lower than the global average.

Figure 1.2 a) shows the total magnetic field intensity at Earth’s sea-level surface in 2020. The SAA is the distinct low-intensity patch located below the South American continent and South Atlantic Ocean (blue color region). The minimum field strength of the center of the SAA drops to $\sim 22.5 \mu\text{T}$, and $\sim 50\%$ of the global average. The SAA has deepened and shifted westward for over three centuries (Mandea *et al.*, 2007; Hartmann & Pacca, 2009) and is possibly a recurring feature (Engbers *et al.*, 2022). Today, the SAA continues to decrease its field intensity, raising attention to its potential hazard toward space missions (Johnson-Groh & Merzdorf, 2020). With even the reduced protection of the magnetic field, technological systems onboard satellites can suffer from malfunction or even short-circuit by high-energy particles in space.

Figure 1.2 b) shows a processed inversion of the intensity change for the observed radial

magnetic field extrapolated down to the CMB from the 2014's reference field (Finlay *et al.*, 2020). Figure 1.2 reveals that the radial magnetic field intensity changes associated with the SAA are multi-scale, non-uniform, and asymmetric in spatial distribution. The deviation in B_r happens the fastest at SAA's western and southern edges (Finlay *et al.*, 2020). Studies show that the anomalously rapid field decay of the SAA is a reoccurring feature in the region on the time scale of ~ 700 yrs (Tarduno *et al.*, 2015; Trindade *et al.*, 2018; Campuzano *et al.*, 2019).

Despite extensive research, the origin of the SAA remains unclear. Some researchers have proposed that the anomaly comes from deeper interior core flow processes, such as a growth in non-dipolar components during geomagnetic reversal transit (e.g., Laj & Kissel, 2015; Pavón-Carrasco & De Santis, 2016; Terra-Nova *et al.*, 2017). In contrast, others (Tarduno *et al.*, 2015) speculate that the SAA might emerge due to the CMB processes at the edges of African Large low-shear-velocity Provinces (LLSVP), a continental-size anomaly in the lower mantle partially overlapping the SAA region.

The questions surrounding the SAA highlight the challenges and complexities involved in studying planetary dynamos. Since the inversion of the magnetic field at the surface only provides a limited view of the core flow, the interpretation of the core flow dynamics from magnetic field observation is non-unique without making *a priori* assumptions about the core flow dynamics at different regions of the core. The magnetic field observed at the CMB could be from flow induced by boundary heterogeneity, internal dynamics, or a superposition of both. ***Therefore, forward modeling of both the core-mantle dynamics and core flow dynamics is essential to better understand the magnetic anomalies and planetary dynamos as a whole.***

1.3 Forward modeling of core dynamics

For decades, progress in understanding planetary magnetic field generation has been hindered by the need for more validation of the dynamic processes at the planetary fluid layer boundaries and limited knowledge of liquid metal turbulence at extreme parameters. Thus, it is of great interest and necessity to develop forward modeling of the reduced systems with theories, numerical simulations, and laboratory experiments to verify fundamental physics related to dynamo processes. *This thesis is focused on the forward modeling approach via liquid metal laboratory experiments.*

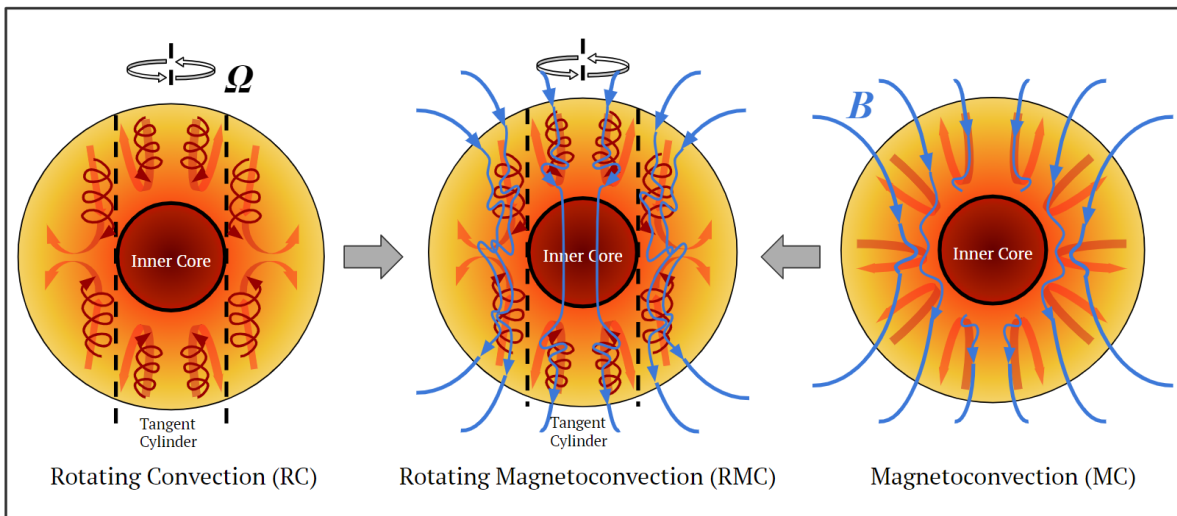


Figure 1.3: Schematics of the Earth's outer core convection models. Rotating convection (left) and magnetoconvection without rotation (right) are two end-member reduced models of the rotating magnetoconvection (center) system. The blue line represents the magnetic field generated from the fluid motion. The thick orange arrows represent the buoyancy convection due to the temperature/composition gradient from the inner core to the core-mantle boundary. The thin dark red spiral lines with arrows are the traces of fluid motion that might take place in the outer core. The schematics are not to scale.

1.3.1 Governing equations

First, it is important to introduce a fundamental MHD model of the core flow. This model, called “liquid metal rotating magnetoconvection (RMC)”, prescribes a conducting convective flow that is subject to magnetic field and rotation. A simple schematic of RMC is shown in the center of fig. 1.3. The flow is reasonably assumed to be incompressible, and the Boussinesq approximation can be applied (Oberbeck, 1879; Boussinesq, 1903; Gray & Giorgini, 1976; Tritton, 1977; Chillà & Schumacher, 2012) such that the density variation only affects the buoyancy forcing in the system. Moreover, chemical convection is excluded from the buoyancy, and Poincaré forces are excluded from rotation. The dimensional governing equations for an RMC system are then:

$$\text{Induction equation: } \frac{\partial \mathbf{B}}{\partial t} = \eta \nabla^2 \mathbf{B} + \nabla \times (\mathbf{u} \times \mathbf{B}), \quad (1.13a)$$

$$\text{Gauss's law for magnetism: } \nabla \cdot \mathbf{B} = 0, \quad (1.13b)$$

$$\text{Ohm's law: } \mathbf{J} = \sigma (-\nabla \Phi + \mathbf{u} \times \mathbf{B}), \quad (1.13c)$$

$$\text{Charge conservation: } \nabla \cdot \mathbf{J} = 0, \quad (1.13d)$$

$$\text{Navier-Stokes: } \frac{\partial \mathbf{u}}{\partial t} + (\mathbf{u} \cdot \nabla) \mathbf{u} + 2\boldsymbol{\Omega} \times \mathbf{u} = -\frac{1}{\rho} \nabla p + \frac{1}{\rho} (\mathbf{J} \times \mathbf{B}) + \nu \nabla^2 \mathbf{u} + \alpha_T \Delta T \mathbf{g}, \quad (1.13e)$$

$$\text{Continuity: } \nabla \cdot \mathbf{u} = 0, \quad (1.13f)$$

$$\text{Energy equation: } \frac{\partial T}{\partial t} + (\mathbf{u} \cdot \nabla) T = \kappa \nabla^2 T + \mathcal{H}, \quad (1.13g)$$

where \mathbf{J} is current density, σ is the electric conductivity, Φ is the electric potential, $\boldsymbol{\Omega}$ is the angular velocity of the applied rotation, ρ is the density of the fluid, p is non-hydrostatic pressure, ν is the kinematic viscosity of the fluid, α_T is the thermal expansivity, ΔT is the superadiabatic temperature difference across the fluid layer, $\mathbf{g} = g \hat{\mathbf{e}}_z$ is the gravitational acceleration, T is the temperature, κ is the thermal diffusivity, and \mathcal{H} is the source or sink internal energy term. It can represent radiogenic heating, compositional flux, and cooling in some scenarios. It is assumed that η is uniform through the volume and is commonly

applied to terrestrial planets. However, this does not apply to gas giants where the internal electrical conductivity varies significantly with radius.

An important step to simplify this complex system is the “low- Rm approximation”. In a low- Rm system, where magnetic diffusion dominates, the influence of fluid motions on the magnetic field is small (Sarris *et al.*, 2006; Davidson, 2016; Knaepen & Moreau, 2008). Additionally, we apply quasistatic approximation, which means the magnetic field can reach a steady state so that magnetic field \mathbf{B} is invariant in time. This is possibly true on a small local scale of Earth’s liquid metal core (Aurnou & King, 2017). The consequence of the approximation is: the full magnetic induction equation (eq. (1.13a)) need not be solved; \mathbf{B} now only represents the external field. The external field is $\mathbf{B} = B\hat{\mathbf{e}}_b$; the Ohm’s law (1.13c) has been simplified such that the rotational part of the electric field and perturbative second-order terms from $\mathbf{u} \times \mathbf{B}$ are not considered. Accordingly, in the bulk fluid, the quasistatic Lorentz force is $\mathbf{J} \times \mathbf{B} = \sigma(\mathbf{u} \times \mathbf{B}) \times \mathbf{B} \approx -\sigma\mathbf{u}_\perp B^2$, where \mathbf{u}_\perp is the velocity perpendicular to the direction of the magnetic field. Therefore, the low- Rm Lorentz force acts as a drag that opposes bulk fluid velocities directed perpendicular to \mathbf{B} (Sarris *et al.*, 2006; Davidson, 2016). This quasistatic Lorentz drag depends only on B^2 .

Another simplification has been made here that the source/sink term \mathcal{H} in the energy equation is neglected. Since we only consider thermal convection, \mathcal{H} represents the internal radiogenic heating. On Earth, the internal heating by the radiogenic elements is mainly from the mantle (~ 18 TW) (McDonough & Sun, 1995). Only a fraction of the heat ($\lesssim 2$ TW) is estimated to be generated by radioelements within the core (Labrosse, 2015). This is approximately $\sim 4\%$ of the total heat flow ($\sim 46 \pm 3$ TW) escaping the CMB (Jaupart *et al.*, 2007; Landeau *et al.*, 2022).

The terms in eq. (1.13e), from left to right, are the change of momentum in time, the advection term, the Coriolis term, the modified pressure gradient, the Lorentz term, the viscous diffusion, and the thermal buoyancy term. The terms in eq. (1.13g), from left to right, are the change rate in temperature, the advection term, and the thermal diffusion

term.

The majority of the current research for core convection has been focused on the reduced sub-systems such as rotating convection (RC) without magnetic field (e.g., [Gastine *et al.*, 2016](#); [Guervilly *et al.*, 2019](#)). The schematics for an RC system are shown on the left in [fig. 1.3](#). Although large-scale dynamics of the planetary cores are indeed dominated by rotation, the magnetic field can also be important in the convective dynamics of the core ([Roberts & King, 2013](#); [Soderlund *et al.*, 2015](#); [Aurnou & King, 2017](#)). The other end-member reduced model is magnetoconvection (MC), as shown on the right in [fig. 1.3](#). MC is also relevant to many magnetically dominated geophysical and astrophysical convection systems (e.g., [Proctor & Weiss, 1982](#); [Schüssler & Vögler, 2006](#); [Rempel *et al.*, 2009](#)). However, its essential behavioral regimes and heat transfer are less understood than in RC. See [chapter 3](#) and [chapter 4](#) for more details on MC systems.

In non-rotating magnetoconvection (MC), all the rotational influences are removed in the governing equation. Equation (1.13e) then becomes

$$\frac{\partial \mathbf{u}}{\partial t} + (\mathbf{u} \cdot \nabla) \mathbf{u} = -\frac{1}{\rho} \nabla p + \frac{1}{\rho} (\mathbf{J} \times \mathbf{B}) + \nu \nabla^2 \mathbf{u} + \alpha_T \Delta T \mathbf{g}, \quad (1.14)$$

In this simplified system, I can address the core flow dynamics at the CMB affected by the electromagnetic influences due to the boundary heterogeneity by modifying Ohm's law in [eq. \(1.13c\)](#) ([Xu *et al.*, 2022](#)). This problem is further discussed in [chapter 4](#).

1.3.2 Nondimensional parameters

Main control parameters arise from non-dimensionalizing the governing equations of low- Rm RMC. The Prandtl number Pr describes the thermal properties of the fluid in ratio of viscous to thermal diffusion,

$$Pr = \nu / \kappa, \quad (1.15)$$

In liquid gallium, our working fluid for this thesis study, $Pr \sim 0.025$.

Related to the Prandtl number, the magnetic Prandtl is the ratio of the fluid's viscous and magnetic diffusion,

$$Pm = \frac{\nu}{\eta}. \quad (1.16)$$

In liquid gallium, $Pm \sim 1.7 \times 10^{-6}$, which is a realistic value for the core flow.

Re is the Reynolds number, which denotes the ratio of inertial and viscous effects,

$$Re = \frac{UH}{\nu} \quad (1.17)$$

and is often used to describe the vigor of the fluid motions. The magnetic Reynolds number $Rm = RePm$. In Earth's core, $Pm \sim 10^{-6}$ (e.g., [Pozzo *et al.*, 2012](#)), and $Rm \gtrsim 10^2$, which leads to $Re \gtrsim 10^8$. Usually, the flow is considered turbulent at $Re > 10^4$, in which it shows a broad range of scales in length and time, and cross-scale energy transfers (e.g., [Mininni & Pouquet, 2010](#); [Davidson, 2016](#); [Schaeffer *et al.*, 2017](#)). Therefore, the liquid core has been treated as a turbulent system. In the lab, Re rises up to $\approx 5 \times 10^4$ in the 40-cm tank. Thus, laboratory experiments can conveniently reach turbulence.

The Rayleigh number Ra characterizes the buoyancy forcing with respect to the thermal and viscous diffusion:

$$Ra = \frac{\alpha_T g \Delta T H^3}{\nu \kappa}. \quad (1.18)$$

The Chandrasekhar number Ch is the ratio of Lorentz force to viscous diffusion with quasistatic approximation:

$$Ch = \frac{\sigma B^2 H^2}{\rho \nu} \approx 10^{15} \text{ (Earth core)}, \quad (1.19)$$

The Ekman number, Ek , describes the ratio of viscous diffusion to Coriolis force:

$$Ek = \frac{\nu}{2\Omega H^2} \approx 10^{-15} \text{ (Earth core)}, \quad (1.20)$$

where Ω is the angular rotation rate of the system.

Conveniently, by grouping some of these dimensionless numbers mentioned above, there are a few commonly used dimensionless numbers. The interaction parameter N is the ratio

of quasistatic Lorentz drag and fluid inertia. It is defined as:

$$N = \frac{\sigma B^2 H}{\rho U} = \frac{Ch}{Re}. \quad (1.21)$$

When $N > 1$, the Lorentz force will tend to damp buoyancy-driven convective turbulence.

The Rossby number is essential for describing the importance of Coriolis in a system's dynamics. It is the ratio between inertia and Coriolis:

$$Ro = \frac{U}{2\Omega H} = ReEk, \quad (1.22)$$

which shows up as a collapse parameter in a broad array of rotating convection problems (e.g. Gastine *et al.*, 2014; Aurnou *et al.*, 2020; Landin *et al.*, 2023).

In parallel to Ro , the magnetic Rossby number, Ro_m , which formally describes the ratio of convective inertia and the Lorentz force:

$$Ro_m = \frac{\rho U}{\sigma B^2 H} = \frac{Re}{Ch} = \frac{1}{N}. \quad (1.23)$$

When these Rossby numbers exceed order unity, buoyancy-driven inertial forces should be dominant.

Lastly, the ratio between Lorentz and Coriolis is defined as the linear Elsasser number Λ ,

$$\Lambda = \frac{\sigma B^2}{2\rho\Omega} \sim ChEk \sim 0.1 - 10 \text{ (Earth core)}, \quad (1.24)$$

which is later discussed in section 1.3.4. Table 1.1 summarizes all the important dimensionless parameters for the low- Rm RMC.

1.3.3 Boundary heterogeneity

It has been long argued that the large-scale magnetic flux anomalies may be caused by large-scale boundary heterogeneities (e.g., Gubbins & Richards, 1986; Bloxham & Gubbins, 1987; Johnson & Constable, 1998). Numerical simulation from Calkins *et al.* (2012) suggests small-scale flow structures (wavenumber $m \sim \mathcal{O}(10^2 - 10^3)$) in the core can be excited

by topographic heterogeneity. Moreover, by coupling inner-core and mantle, [Aubert *et al.* \(2013\)](#) explored the effects of heterogeneous buoyancy-flux on geodynamo modeling.

Other MHD effects, such as thermoelectricity, have been considered to drive planetary dynamo in Mercury ([Stevenson, 1987](#); [Giampieri & Balogh, 2002](#)). However, the effect of thermoelectricity on the heterogeneous boundary on the core flow is still poorly understood ([Xu *et al.*, 2022](#)). To simplify the system, I remove rotation from the model so it becomes MC, focusing only on the magnetic influence of the system. This is further discussed in detail in chapter 4.

1.3.4 Interior core dynamics

Dynamos are prone to complexity. [Cowling \(1933\)](#) demonstrated an anti-dynamo theorem, showing that dynamo action could not maintain a purely axisymmetric magnetic field. [Zeldovich \(1957\)](#) established that plane two-dimensional motion could not lead to dynamo action. These findings indicate that dynamo action is inherently three-dimensional. The classical theory, commonly referred to as “mean field dynamo theory,” is a quasi-linear theory based on the induction equation ([Hughes & Tobias, 2010](#)). An underlying assumption for the mean-field theory is the separation of length scales for both velocity and magnetic fields. The velocity and magnetic field can be decomposed into a mean component with a scale of L and a fluctuating component with a scale of l with $l \ll L$. This theory postulates that the small-scale driving flow generates a large-scale mean magnetic field (e.g., [Steenbeck *et al.*, 1966](#); [Rädler, 1980](#); [Moffatt, 1978](#)). However, both magnetic field observation and secular variation analysis point to the existence of the large-scale flow in the core (e.g., [Gubbins & Bloxham, 1987](#)), which is not addressed in mean field theory.

The large-scale flow appears in another linear theory approach, which is through understanding the MHD flow field. The linear analysis of the RMC system ([Chandrasekhar, 1961](#)) predicts that the rotational and magnetic forces partially cancel each other out when both are present in the electrically conducting fluid, leading to an optimally efficient, large-scale

steady mode called “magnetostrophic mode” for magnetic field generation. This has been a popular idea for the dynamo community to explain the large-scale flow structures in the core (Roberts & King, 2013). This process can be shown by a relaxation of the geostrophic constraint, in which Coriolis balances the pressure.

When the magnetic field balances with the rotation, the dominant force balance becomes magnetostrophic (MS). Assuming Boussinesq and incompressibility, the leading term balance is

$$2\boldsymbol{\Omega} \times \mathbf{u} = -\nabla p + \frac{1}{\rho} \mathbf{J} \times \mathbf{B}, \quad (1.25)$$

where $\boldsymbol{\Omega}$ is assumed to be in the vertical direction. The curl of eq. (1.25) yields (Soderlund *et al.*, 2015)

$$\frac{\partial \mathbf{u}}{\partial z} = -\frac{1}{2\rho\Omega} \nabla \times (\mathbf{J} \times \mathbf{B}). \quad (1.26)$$

In contrast, in a rapidly rotating system, the geostrophic balance requires the Taylor-Proudman theorem where $\partial_z \mathbf{u} = 0$ (e.g., McWilliams, 2006). The flow in geostrophic balance is invariant in the flow direction. With convection, quasi-geostrophic balance still requires $\partial_z \mathbf{u} \approx 0$, and the flow is organized in columnar structures (e.g., Gastine *et al.*, 2016; Cheng *et al.*, 2015). As a result, eq. (1.26) shows that a magnetic field can relax the geostrophic constraint, allowing large-scale structures to form as the magnetostrophic modes.

However, because it is from the linear theory at $Rm \ll 1$, there is a fundamental “flaw” in the linear Elsasser number as shown in eq. (1.24), which has been used to predict the large-scale magnetostrophic mode in the core. The linear Elsasser number is appropriate for a steady imposed magnetic field (low- Rm). The Elsasser number is, in its nature, the ratio of Lorentz to Coriolis,

$$\Lambda = \frac{\mathbf{J} \times \mathbf{B}}{2\rho\boldsymbol{\Omega} \times \mathbf{u}} \sim \frac{JB}{2\rho\Omega U} \quad (1.27)$$

If the magnetic field is not strongly time-variant, the electric field is irrotational, and Ohm’s law can be used to predict $J \sim \sigma UB$ so that eq. (1.27) becomes eq. (1.24). Unless otherwise specified, the Elsasser number Λ used in this thesis is based on low- Rm

laboratory experiments and conveniently refers to the linear Elsasser number defined in eq. (1.24). However, geodynamo exhibits a significant time variance from secular variation data. It is thus more accurate to use the current density approximated from Ampere’s law, $\mathbf{J} = \nabla \times \mathbf{B}/\mu_0 \sim B/(\mu_0\ell_B)$, where ℓ_B is the characteristic scale of the magnetic field structures (Cardin *et al.*, 2002; Christensen, 2010; Soderlund *et al.*, 2012, 2015; Aurnou & King, 2017). Substitute into eq. (1.27), the dynamic Elsasser number is defined,

$$\Lambda_d = \frac{B^2}{2\mu_0\rho\Omega\ell_B} \approx \frac{\Lambda}{Rm} \left(\frac{H}{\ell_B} \right), \quad (1.28)$$

where H is the length scale of the entire system. Equation (1.28) shows when the magnetic length scale ℓ_B is small, the Lorentz force is more dominant in the dynamic of the core flow (Soderlund *et al.*, 2015; Aurnou & King, 2017). Further, at global scale when $\ell_B \sim H$, Λ_d is at least $\mathcal{O}(Rm^{-1})$ of the linear Λ .

Further, to estimate the typical value for ℓ_B , we can assume the induction happens due to a large-scale core flow H , whereas the magnetic diffusion happens on the magnetic scale ℓ_B . Equating the induction and diffusion terms in the induction equation (eq. (1.13a)) using different length scales for each term yields (Soderlund *et al.*, 2015; Aurnou & King, 2017)

$$\frac{UB}{H} \sim \frac{\eta B}{\ell_B^2}, \quad (1.29)$$

and thus,

$$\ell_B \sim Rm^{-1/2}H, \quad \Lambda_d \sim \Lambda Rm^{-1/2}. \quad (1.30)$$

In the Earth core, $Rm \sim \mathcal{O}(10^2)$, thus, $\Lambda_d \sim 10^{-1}$ is approximately two orders of magnitude smaller than the linear Elsasser at the global scale in the core.

Equation (1.30) suggests that the Lorentz force is dynamically subdominant on the global large scale of the core flow. Coriolis force, therefore, is considered dominant in the large-scale dynamics of the core (Jones, 2011; Gastine *et al.*, 2014; Aurnou *et al.*, 2015a). It is worth noting that the ensemble of small-scale fluid motions may also lead to a large-scale dynamo (e.g., Calkins *et al.*, 2015), yet this is unlike the multi-scaled, patchy geomagnetic field

from observation (Aurnou *et al.*, 2015a). Consequently, the attempts to explain large-scale magnetic flux patches with linear steady magnetostrophic modes at $\Lambda \sim 1$ are, therefore, at least questionable.

Although numerical simulation of the dynamo has been the primary tool for current investigating the dynamo processes (e.g., Gastine *et al.*, 2016; Yadav *et al.*, 2016; Schaeffer *et al.*, 2017; Aubert, 2019), many of their dynamic parameters are still many orders of magnitudes away from the planetary dynamo, with significant differences in the defining time scales. As a result, it remains uncertain whether the existing numerical dynamo models accurately represent the fundamental physical processes occurring in planetary cores (Aurnou *et al.*, 2015a).

1.3.5 Inverse cascade as a possible pathway

Large-scale turbulent structures, beyond linear theory, have been proposed to generate large-scale magnetic structures in the core. I have discussed that, at the global scale, rotating convection could adequately represent the Earth’s core flows. In fact, turbulent convection with rapid rotation, where Coriolis force is dominant, can result in an inverse kinetic energy cascade (e.g., Smith & Waleffe, 1999; Seshasayanan & Alexakis, 2018; Maffei *et al.*, 2021). This dynamic process facilitates the transfer of kinetic energy from small-scale convection to large-scale flows, which is in reverse of a classical forward energy cascade in non-rotating turbulence (Kolmogorov *et al.*, 1942). The inverse cascade in kinetic energy leads to the formation of large-scale vortices (LSVs) in 2D (McWilliams, 1984), which has also been demonstrated by various recent 3D numerical simulations of turbulent rotating convection (e.g., Julien *et al.*, 2012; Favier *et al.*, 2014; Guervilly *et al.*, 2014; Rubio *et al.*, 2014; Stellmach *et al.*, 2014).

Figure 1.4 shows an example of a pair of LSVs born out of a direct numerical simulation (DNS) at $Ek = 10^{-7}$, $Pr = 1$, with free-slip boundary. The domain width is $20\ell_{conv}$. The convective length scale is defined as the convective length scale in RC (Chandrasekhar, 1961;

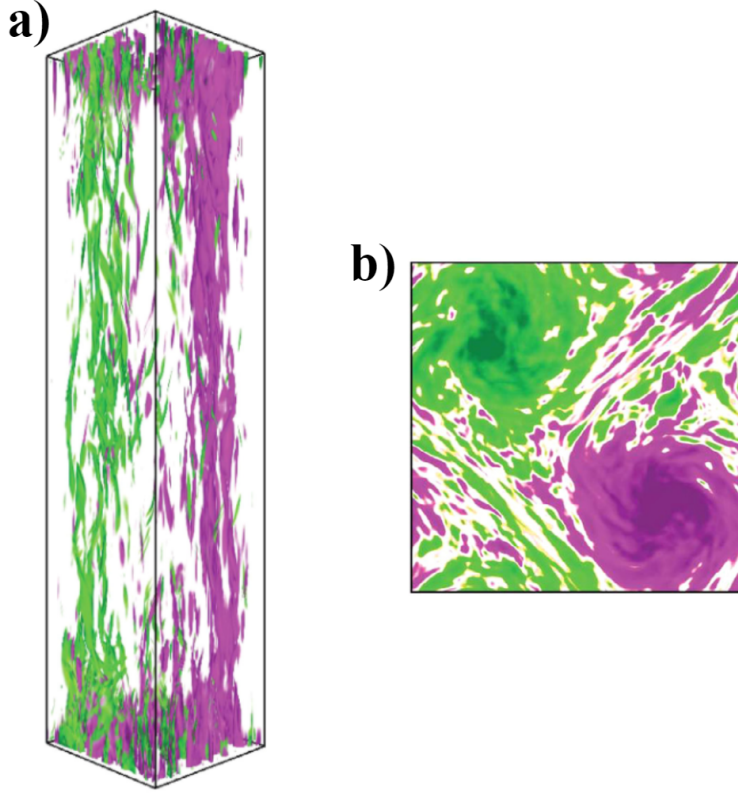


Figure 1.4: a) A pair of large-scale vortices (LSVs) appear in the axial vorticity field of DNS with free-slip boundary (Stellmach *et al.*, 2014), at $Ek = 10^{-7}$, $Pr = 1$, $Ra/Ra_c = 11.5$ and with a domain width of $20\ell_{conv}$. b) Axial integration of vertical vorticity in a). Figures adapted from Stellmach *et al.* (2014) and Aurnou *et al.* (2015a).

Aurnou *et al.*, 2015a), and $\ell_{conv} = 2.4Ek^{1/3}H$ in the $Ek \rightarrow 0$ limit. This case was carried out in the geostrophic turbulent regime at $Ra/Ra_c = 11.5$, where Ra_c is the critical Ra corresponding to the onset of bulk flow in RC. The axial vorticity field integration indicates a pair of two counter-rotating, barotropic, large-scale vortices across the entire domain.

It is found that the LSVs formed at relatively high $Re \gtrsim 20$ and low $Ro \lesssim 1$ (Favier *et al.*, 2014), which is suitable for core flows. However, the required convective supercriticality for the onset of LSVs (Ra/Ra_c) and the effect of fluid properties (e.g., Pr and Pm) remain poorly understood. The thermal Prantl number in the liquid core $Pr \sim 10^{-2}$ and the magnetic Prantl number $Pm \sim 10^{-6}$. The supercriticality for the RC onset is also related

to Pr . The convective onset in fluids with $Pr \lesssim 0.68$ and $Ek \gtrsim 10^{-7}$ is via bulk thermal-inertial oscillations (Horn & Schmid, 2017; Aurnou *et al.*, 2018; Vogt *et al.*, 2021) instead of the steady column onset implied above.

The LSVs seem to hold across compressible and incompressible RC. Recent efforts in small Pr numerical simulations of RC in solar and astrophysical contexts have reached metal-like parameters. Studies have found the existence of LSVs in compressible $Pr = 0.24 - 1.20$ rotating convection relevant to sunspots (Käpylä *et al.*, 2011) and Jovian vortices (Chan & Mayr, 2013). Cai (2021) simulated $Pr = 0.1$ rapidly rotating convection of liquid metal-like incompressible fluid with stress-free boundary conditions in a rectangular geometry. This study found the formation of LSVs must satisfy the vertical Reynolds number $Re_z \geq 400$ and $Ro \leq 0.4$ (in $\Gamma = 1$). The Ro threshold increases with an increasing aspect ratio. Nevertheless, the lack of laboratory evidence indicates that there is still great uncertainty regarding whether the existing LSV simulations accurately depict the liquid metal turbulence occurring in planetary cores.

To hunt for the existence of liquid metal LSVs in the lab, I carry out laboratory experiments of turbulent RC and RMC in liquid gallium, which has much more realistic material properties ($Pr \approx 0.025$, $Pm \approx 10^{-6}$) and high Re , which is discussed in detail in chapter 5. To the best of my knowledge, no liquid metal LSV has ever been found experimentally. This has been the missing link to extrapolate the inverse cascade of LSVs to the planetary core dynamics. Therefore, ***I propose that characterizing liquid metal LSVs via laboratory experiment is a possible pathway to large-scale dynamics in the core.***

Number Names	Symbol	Definition	Equivalence	RoMag (Ga)	Earth
Magnetic Prandtl	Pm	$\frac{\nu}{\eta}$		1.7×10^{-6}	$\sim 10^{-6}$
Magnetic Reynolds	Rm	$\frac{UH}{\eta}$	$Re Pm$	$\lesssim 10^{-2}$	$\sim 10^2$
Prandtl	Pr	$\frac{\nu}{\kappa}$		$\sim 2.5 \times 10^{-2}$	$\sim 10^{-2}$
Rayleigh	Ra	$\frac{\alpha g \Delta T H^3}{\nu \kappa}$		$\sim 10^6 - 10^9$	$\sim 10^{20} - 10^{30}$
Ekmen	Ek	$\frac{\nu}{2\Omega H^2}$		$\sim 10^{-7} - \infty$	$\sim 10^{-15}$
Chandrasekhar	Ch	$\frac{\sigma B^2 H^2}{\rho \nu}$		$\sim 0 - 10^7$	$\sim 10^{15}$
Aspect Ratio	Γ	$\frac{D}{H}$		0.5, 1, 2, 4, 6, 8	
Elsasser	Λ	$\frac{\sigma B^2}{2\rho\Omega}$	$Ek Ch$	$0 - \infty$	$\sim 0.1 - 1$
Reynolds	Re	$\frac{UH}{\nu}$	$\sqrt{\frac{Ra}{Pr}}^*$	$\lesssim 5 \times 10^4$	$\sim 10^8$
Péclet	Pe	$\frac{UH}{\kappa}$	$\sqrt{Ra Pr}^*$	$\lesssim 10^3$	$\sim 10^6$
Interaction	N	$\frac{\sigma B^2 H}{\rho U}$	$\frac{Ch}{Re}, \sqrt{\frac{Ch^2 Pr}{Ra}}^*$	$0 - \infty$	$\sim 10^7$
Rossby	Ro	$\frac{U}{2\Omega H}$	$Re Ek, \sqrt{\frac{Ra Ek^2}{Pr}}^*$	$0 - \infty$	$\sim 10^{-6}$
Magnetic Rossby	Ro_m	$\frac{\rho U}{\sigma B^2 H}$	$\frac{Re}{Ch}, \sqrt{\frac{Ra Ch^{-2}}{Pr}}^*$	$0 - \infty$	$\sim 10^{-7}$

Table 1.1: Nondimensional parameters in rotating magnetoconvection and their estimated value in experiments in the thesis and the Earth’s outer core. See section 1.3.2 for detailed definitions and descriptions. *The equivalence expressions in the last five numbers assume a characteristic free-fall velocity, U_{ff} , which arises from buoyancy inertia (eq. (4.10)).

1.4 Research questions

In this thesis, I focus on investigating the near-boundary and interior core flow dynamics using reduced models developed primarily through laboratory rotating magnetoconvection experiments.

The fundamental research questions for this thesis are:

1. What are the characteristics of low- Rm liquid metal magnetoconvection (MC)? What are the fundamental behavior regimes of liquid metal MC from its onset to turbulence? How do wall modes in liquid metal MC affect heat transfer behaviors? (Chapter 3)
2. What are the electromagnetic effects on solid-liquid interfaces in a local-scale low- Rm MC system? Can thermoelectricity with magnetic fields affect the near-boundary dynamics in the Earth's core? (Chapter 4)
3. Do large-scale structures such as LSVs exist in turbulent liquid metal rotating convection? Is the magnetostrophic mode dominant in a low- Rm liquid metal rotating magnetoconvection system? (Chapter 5)

CHAPTER 2

Laboratory Analog of Planetary Cores

*“We shape our tools and, thereafter,
our tools shape us.”*

— John Culkin, 1967

In this chapter, I describe the current state of the Rotating Magnetoconvection Device (ROMAG) that I have used for my thesis experiments. This chapter is an extension and a supplement to Chapter 2 of E. King’s (King, 2009) and Chapter 7 of A. Grannan’s (Grannan, 2017) Ph.D. theses. Combining these previous works with this chapter compiles a comprehensive manual for ROMAG. Section 2.1 overviews the design philosophy and motivation behind the apparatus. Section 2.2 describes the apparatus’s main mechanical/electrical components, data acquisition, and control systems. Section 2.3 describes auxiliary systems associated with main ROMAG components. Section 2.4 describes calibration procedures for diagnostics. Section 2.5 lists a catalog of Standard Operating Procedures (SOPs) for safely running ROMAG, which are partially exhibited in the appendix. Moreover, section 2.6 discusses some open issues and potential future upgrades on ROMAG.

Complementary to this written chapter, I have compiled a YouTube video for the taking down procedures of ROMAG with the help of my colleagues Jewel Abbate and Rachel Tripoli. The video link is attached below.

Video link: <https://youtu.be/gOjTy5QXsrA>.

2.1 Laboratory simulation of the planetary cores

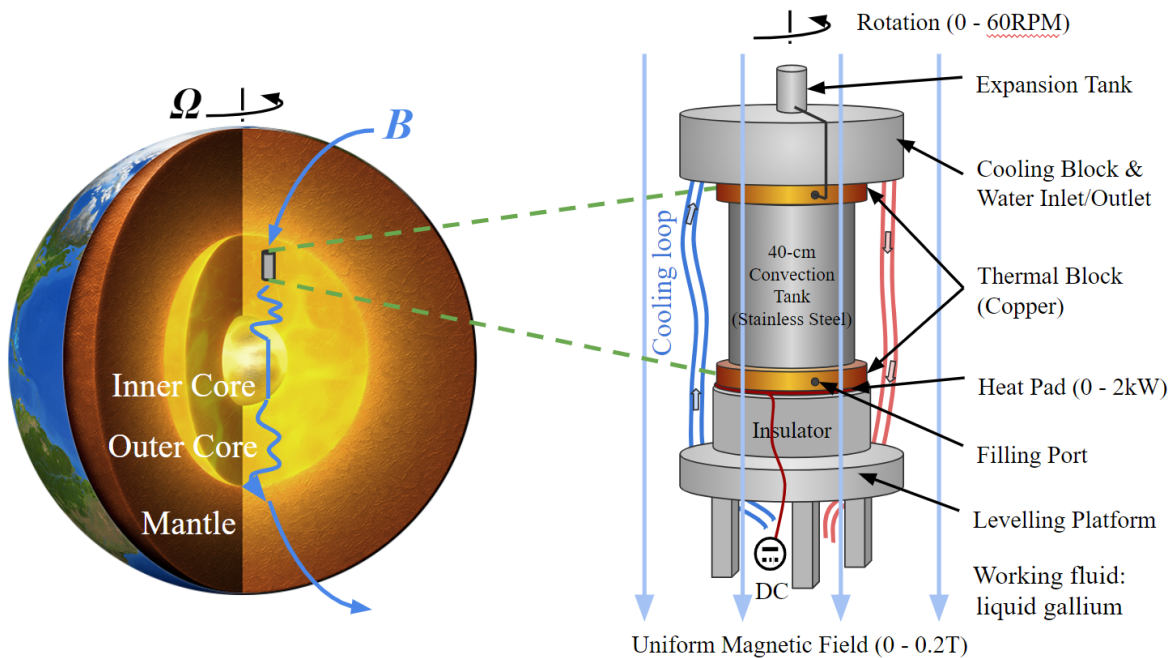


Figure 2.1: Laboratory simulation of the planetary core—the ROMAG device at UCLA. ROMAG simulates a parcel of core fluid inside the Earth’s tangent cylinder region above the solid inner core with applied rotation and a vertical magnetic field.

Numerical simulations are powerful tools capable of directly generating dynamos from convective flows (e.g. Glatzmaiers & Roberts, 1995; Schaeffer *et al.*, 2017). However, limited by computing power, they cannot reach real core flow properties and develop core-style turbulence. Numerical simulations also cannot resolve small-scale dynamics, especially when $Rm \lesssim 1$, leading to its incapability of investigating the small-scale dynamo generation processes (Aurnou & King, 2017).

Liquid metal laboratory experiments, on the other hand, have a number of advantages over numerical simulations. The laboratory experiments can model real core-style fluids – liquid metal and are easier to reach more extreme parameters and higher supercriticality (Cheng *et al.*, 2018; Hawkins *et al.*, 2023). Another advantage is that laboratory experiments can easily operate on a much longer timescale than their numerical counterpart. Therefore

laboratory experiments can be used to study long-period dynamics (e.g., [Brown & Ahlers, 2006](#); [Grannan *et al.*, 2022](#)). The thermal diffusion time is defined as $\tau_\kappa = H^2/\kappa$. In our diameter-to-height aspect ratio 0.5 experiment, 1 thermal diffusion time is 3.4 hours. In contrast, it is rare for direct numerical simulations (DNS) even to reach $0.1 \tau_\kappa$, which is approximately 240 overturn time for our high- Ra cases. Moreover, laboratory experiments help verify critical physical processes that numerical models might neglect, such as the thermoelectric effects on container boundaries due to large temperature gradients in liquid metal convection ([Xu *et al.*, 2022](#)). Limitations of laboratory experiments include challenges in diagnosing information from the flow field, especially in opaque liquid metal. Further, a fully self-sustaining dynamo has yet to be achieved in the lab (cf. [Zimmerman *et al.*, 2014](#); [Rojas *et al.*, 2021](#); [Berhanu *et al.*, 2010](#)). The magnetic Reynolds number in the laboratory scale is usually too small to generate a dynamo.

The laboratory experiments in this thesis do not aim to generate dynamo but instead provide a pathway from local to global dynamics in planetary core convection. The experiments presented in this thesis were carried out on our state-of-art rotating magnetoconvection device (ROMAG), which simulates a parcel of core fluid inside the Earth’s tangent cylinder region above the solid inner core with applied rotation and a vertical magnetic field (fig. 2.1).

Assume the core flow on average moves at $U_c \sim 0.1$ mm/s, a length scale of $H_c \sim 2 \times 10^6$ m, and a viscous diffusivity $\nu_c \sim 10^{-6}$ m²/s ([de Wijs *et al.*, 1998](#)). The core flow is estimated to be $Re \sim 2 \times 10^8$. The maximum length scale in our experiments is the maximum height of the tanks, $H = 0.4$ m. The maximum velocity measured in the most extreme RMC case at $\Lambda = 1.94$ is $U \approx 0.04$ m/s, and the viscous diffusivity of Gallium is $\nu \approx 3 \times 10^{-7}$ m²/s. Thus, Re in our RMC experiments is estimated up to $\sim 5 \times 10^4$. Dimensionally, the ROMAG device filled with Gallium represents the dynamics of a core parcel up to $\sim \mathcal{O}(10^2)$ km in length scale.

This thesis focuses on the low- Rm local dynamics that are likely to happen near bound-

aries and bulk regions of a planetary liquid core. In addition, ROMAG can be used to simulate solid-liquid interfaces in the planetary interiors using different sets of top/bottom boundaries. ROMAG is equipped with advanced diagnostics such as Ultrasonic Doppler Velocimetry, precision thermometry, and a 3-axis magnetometer to diagnose the fluid behaviors.

ROMAG can investigate liquid metal (gallium) RMC in cylindrical confinement over an extensive range of the control parameters Ra , Ek , and Ch . The cylindrical geometry simplifies the complex shell geometry of the core, allowing us to directly compare experimental results with theoretical studies and existing numerical simulations.

2.2 The RoMag Device

First developed in the early 2000s, the rotating magnetoconvection device (ROMAG) at UCLA was designed to investigate the effects of rotation and magnetic field on convective fluids. It is currently the world’s only working rotating magnetoconvection device using liquid metal. Another rotating magnetoconvection experiment called the “Little Earth Experiment” using sulphuric acid has recently been developed in the UK since the 2010s (e.g., Aujogue *et al.*, 2016).

The ROMAG device consists of five major systems. The cooling system regulates the temperature for the top layer of the experimental fluids, maintains the lab chiller’s functionality, and most importantly, prevents magnet solenoid coils from overheating. The power system provides regular AC and high DC currents to the electronics and diagnostics of the apparatus. The rotating system, driven by the Kollmorgen Servo-Drive motor, transfers plumbing and electricity from the lab frame to the rotating frame through a slip ring and a separated rotary union. The Data Acquisition (DAQ) System acquires thermal-velocity-magnetic data from the device and other auxiliary data required for monitoring the experiments. These four major systems are shown in fig. 2.3. The electronic deck is a rotating disk platform under the slip ring where the DAQ System and other electronics are located. It is shown in

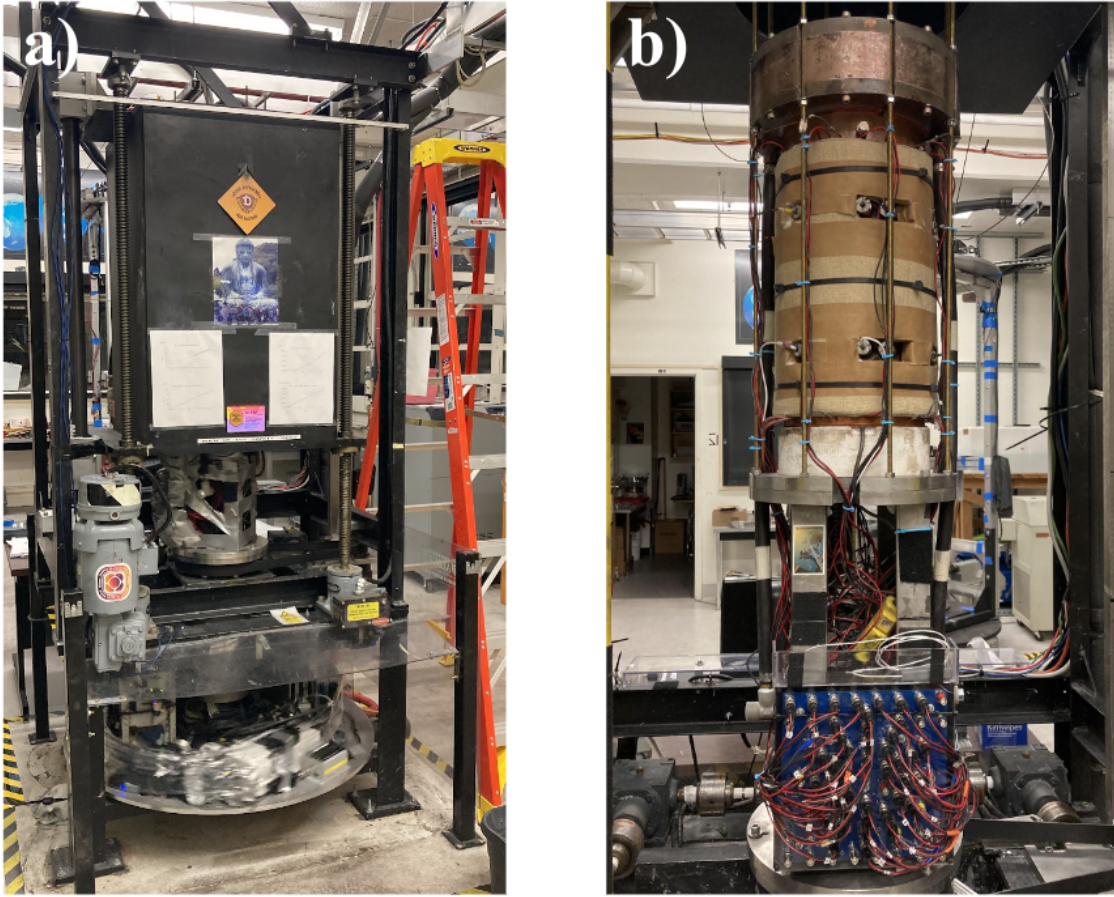


Figure 2.2: Photos of the ROMAG device. a) The ROMAG device at work with lowered magnet and rotation. b) Photos of the ROMAG convection tank with inner layer insulation. The lower box is the upgraded channel terminal connected to the thermometry and the DAQ systems.

fig. 2.2 a) at the bottom of the device. The final system is the control system which is not shown in the schematics here. The Control System comprises I/O interfaces and designated computers for sending command signals to the other four systems.

2.2.1 The cylinder tanks

ROMAG has a collection of different tanks and top/bottom lid boundaries. Different tank heights lead to different parameter ranges in Ra , Ek , and Ch . The tanks consist of a set of top and bottom boundaries and a cylindrical sidewall. All the sidewalls have an inner

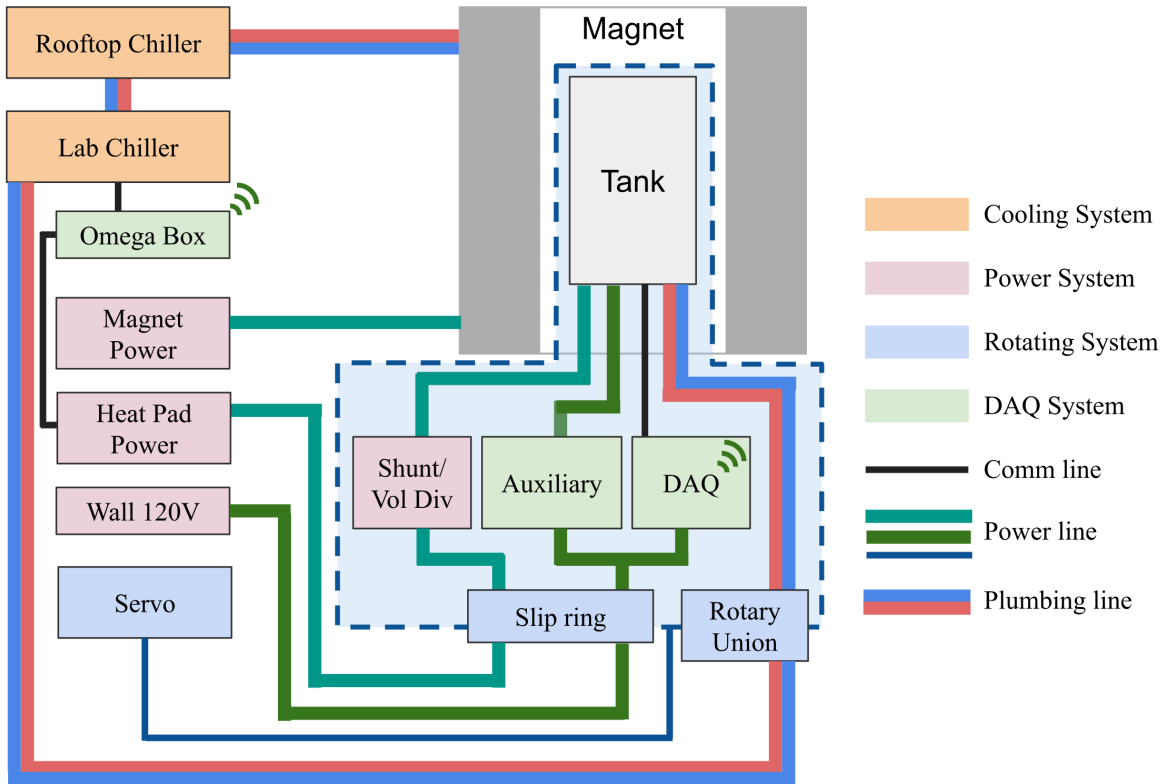


Figure 2.3: Schematics of the ROMAG's major systems.

diameter of 19.685 cm or 7.75 inch. Currently, there are two sets of top/bottom boundaries: copper and Teflon-coated aluminum; two types of sidewalls: stainless steel and acrylic; six different aspect ratios $\Gamma = D/H$: 0.5 (40-cm), 1 (20-cm), 2 (10-cm), 4 (4.9-cm), 6 (3.2-cm), and 8 (2.5-cm). I have also designed a $\Gamma = 0.25$ (80-cm) tank with an improved version of sensor ports. See details in section 2.6.

Figure 2.4 shows a drawing of the 8-port, 40-cm in height, 19.685-cm in diameter, aspect ratio $\Gamma = D/H = 0.492$ stainless steel tank. The thickness of the wall is 3.175 mm. The probe ports on the sidewall are positioned in particular angles so the orientation coincides with each other and with the vertical ports on the top lid (see fig. 2.20). Additional to this tank, I have designed a new set of 10-cm, 60-cm, and 80-cm tank, so that multiple thermometry, Ultrasonic Doppler probes, and magnetometers can be mounted onto the sidewalls and

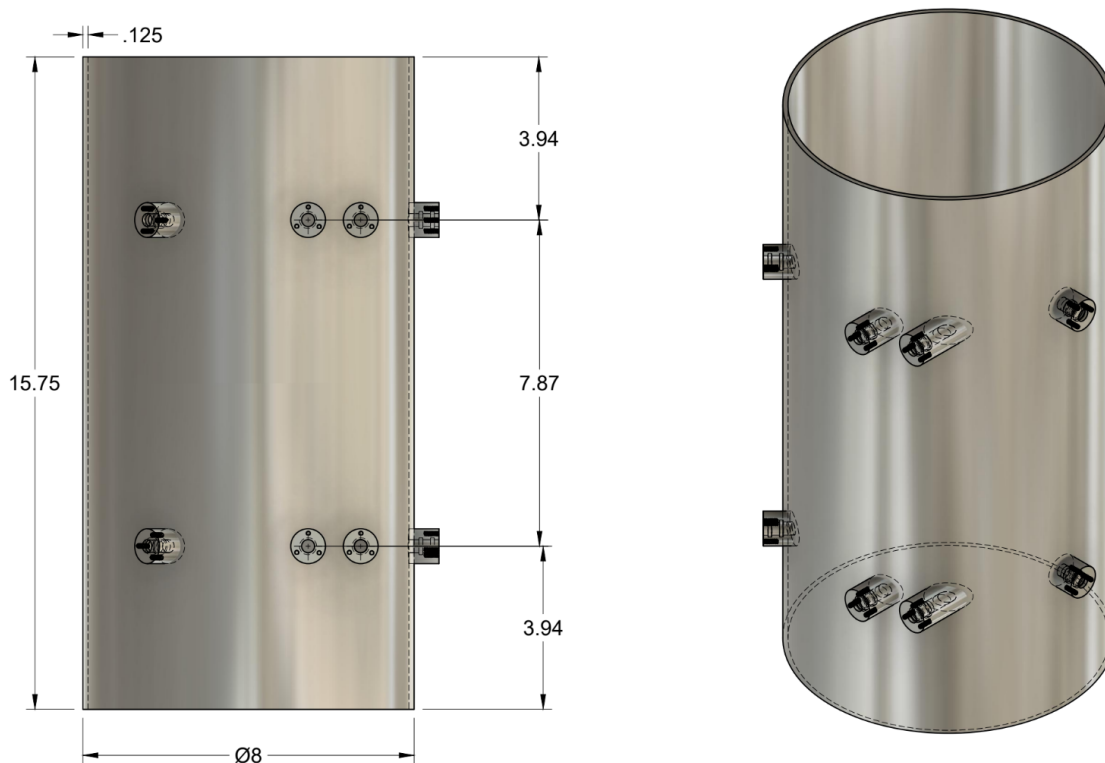


Figure 2.4: Design and dimensions of ROMAG’s 40-cm convection tank. The diameter-to-height aspect ratio of the tank is $\Gamma = D/H = 0.492$. The sensor ports are small cylinders with o-ring grooves and tapped holes mounted to the sidewall at 1/4 and 3/4 of the tank heights. The detailed geometric information of the probe ports’ orientation is shown in fig. 2.20.

extended into the interior with direct contact with the fluid. The probe holders should be brazed on to the stainless steel sidewall in a machine shop. The 80-cm tank in fig. 2.32 has square probe holders which are easier to machine.

The design package is in the lab’s shared Google Drive under the folder “ROMAG”.

2.2.2 Cooling system

The cooling system maintains and regulates the well-being of the experiment. Failure of the cooling system can lead to a meltdown and even fire of the device. Thus, the top priority in lab safety is to carry out regular checkups and maintenance of this system.

The major players in the cooling system are the General Air rooftop chiller and the Thermo Neslab HX300 lab chiller. The rooftop air-cooled General Air recirculating water chiller (Model TAE121) locates directly above the lab. It is cooling the lab chiller, the magnet, and another lab chiller for the NoMag device in the same lab. The chiller has a refrigeration capacity of 128,000 BTU/hr, which is equivalently 37.51 kW. The chiller has a 70 gallon reservoir tank, and its internal pump can circulate up to ~ 26 gallons per minute (GPM) for all the thermal loads. The returning flow is cooled by the hermetic type compressor Maneurop MTZ160HW3, which has 13.5 horsepower. The standard operating procedure (SOP) for setting the rooftop chiller is listed in the SOP section of this chapter.

One of the main functionalities of the rooftop chiller is cooling the magnet. When lowered onto the fluid tank, the magnet can also be used as a thermal blanket to attenuate fluctuations in the room temperature and therefore improves the thermal insulation of the device. It is of future interest to correlate the setting temperature of the rooftop with the temperature of the magnet's inner bore with and without current passing through the coils.

The lab chiller is a Thermo Neslab HX300 precision chiller. It is water-cooled by the rooftop chiller and can extract approximately 10 kW from the thermal load. The chiller has a thermostated range from 5 to 35 Celsius with an accuracy of ± 0.1 K. The chiller has a 15 gallon reservoir and can circulate ~ 15 GPM by a CP-75 centrifugal pump.

The lab chiller passes through a water filter station near the ceiling cable tray and then through the rotary union at the bottom of the apparatus. Afterwards, the water loops through a two-sided double-spiral aluminum heat exchanger block with a diameter of 13 inches, as shown in fig. 2.1. Currently, there is no flow rate monitoring or direct temperature measurements of the inlet and outlet at the heat exchanger. This is addressed in the future upgrade in section 2.6.



Figure 2.5: Argantix XDS 300-17 power supply for providing heating power up to ~ 5 kW into the system. The Magna-Power power supply for the magnet is located directly below this power supply in the same rack.

2.2.3 Power system: heat pad and Argantix power supply

We use an OEM custom fabricated non-inductively wound silicon heating pad to power the convective heat flux into the fluid system in the rotating frame. The heat pad is in direct contact with the bottom block, with a thin layer of thermal paste for better coupling. The heat pad has an electric resistance of $\sim 18 \Omega$, subject to minor changes due to temperature.

An Argantix 300-17 power supply (upper deck of fig. 2.5) outputs up to 300 V and 17 A to the heating element on ROMAG, totals up to 5.1 kW in power. The power supply is connected to the three-phase 208 VAC facility power on the upper North wall. See section 2.2.8 for more details on its voltage control.

2.2.4 Power system: magnet power supply

Below the Argantix, The lower deck of the power supply rack is the Magna-power TSD 250-120 power supply. Newly installed in 2019, the Magna-power supplies 0-240 VDC and 0-120 ADC. It requires a facility power of three-phase 208 VAC and 105 AAC. A customized heavy-duty DC line has been installed on the North wall. A 125A circuit breaker has been installed in the lab's main electric panel to prevent overload.

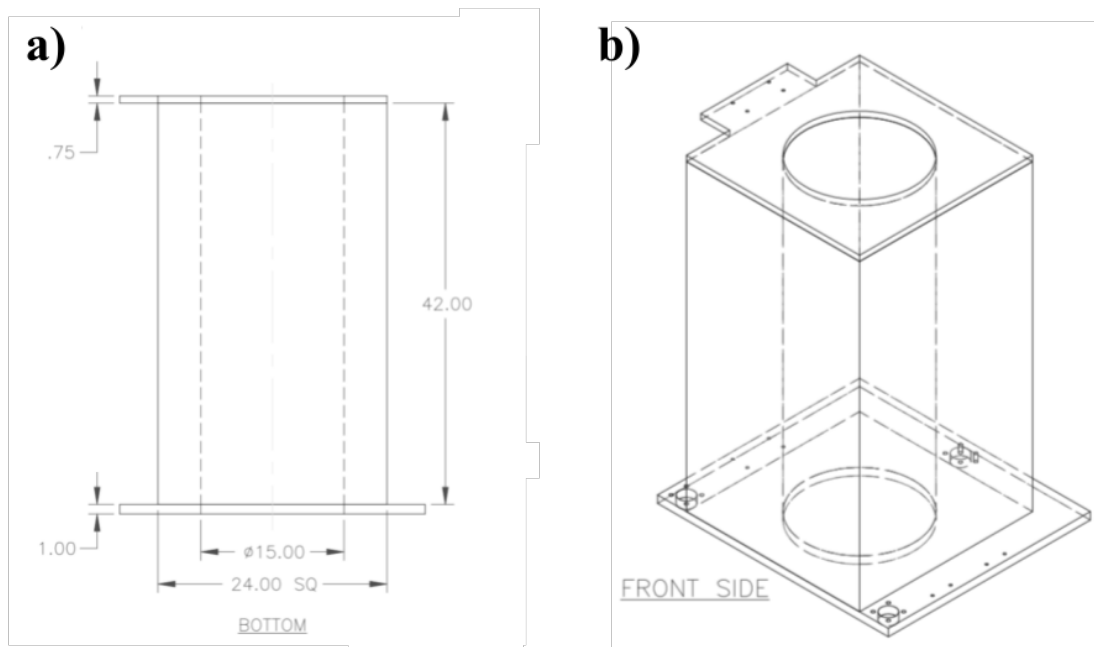


Figure 2.6: Solenoid drawing: a) dimensions; b) three-dimensional view. Figure modified from Joe Neal’s engineering drawing.

A pair of red (V+) and black (V-) quick cable connectors are located on the cable tray near the lab chiller for the polarity switch that changes the direction of the vertical magnetic field in the solenoid. By default, the magnetic field is pointing downwards.

Cautions are needed when operating the magnet power supply because of its high-voltage, high-current hazards. A flow switch will be installed to guarantee the cooling loop is on when the magnet power supply is turned on. This way, the danger when the solenoid overheats in case of rooftop chiller failure can be eliminated. See section 2.2.8 for more detailed control procedures. The magnet power supply is currently under the current control to ensure a stable magnetic field generation by the solenoid.

2.2.5 The solenoid

The magnet solenoid is the main component of the ROMAG device, which currently can generate up to 0.2 T in magnetic flux density. It was fabricated by Walker LDJ and has

basic dimensions 0.61 m wide by 0.61 m deep by 1.07 m high with a 0.38 m diameter hollow inner bore. The lower plate of the magnet is fitted to jack screws and a roller guide so that it can be lowered from above to encapsulate the convection tank.

We were able to measure the upper-half spatial map of the flux density inside the bore with the help of Cy David and Nika Eskandari. The measurement was carried out using a circular acrylic sheet fixed horizontally on top of an acrylic cylinder inside the magnet bore. We used a DC Gaussmeter (Model GM-1-ST, AlphaLab Inc.) to measure B_z , B_ϕ , and B_r at 21 location on the acrylic sheets (a cross pattern). Then the magnet was raised and lowered to access five different heights from inside to outside the bore. Finally, we reconstructed the magnetic field using these three-dimensional components. Figure 2.7 shows the three-dimensional vector field of the upper half (~ 50 cm) inner bore. The vertical distance z is measured from the magnet bore's top ($z = 0$). The azimuthal angle ϕ is increasing counterclockwise. Here, $\phi = 0$ is the direction that faces the workbench and is defined as the front of ROMAG.

Only the vertical component of the magnetic field is needed for the experiment. Therefore, we thus tested the uniformity of the vertical field. Figure 2.8 a) show horizontal cross-section contour of the vertical magnetic field strength at $z/z_b = 0.4$, where $z_b = 1.07$ m. The magnetic field is downward. fig. 2.8 b) is the variation of the magnetic field, $(B_z - \overline{B_z})/\overline{B_z}$. The blue curve in panel c) shows the azimuthally-averaged radial profile of the magnetic field normalized by the maximum. A least-square fit of the radial profile gives

$$\langle B_z \rangle_\theta / B_{z,max} = 1 - 0.450(r/r_b)^6. \quad (2.1)$$

The magnetic field at the center of the inner bore is very uniform. Our convection tank is 51.6% of the inner bore radius, subject to only $< 1\%$ difference from the center. However, the outer edge of the inner bore has a considerable variation. Moreover, the radial component of the magnetic field is large enough at $z \lesssim 10$ cm that the curvature of the magnetic field lines should be considered. Thus, the region where $r/r_b \gtrsim 0.7$, $z/z_b \lesssim 0.1$, and $z/z_b \gtrsim 0.9$ should be avoided for future experiments that assume a uniform vertical magnetic field. In

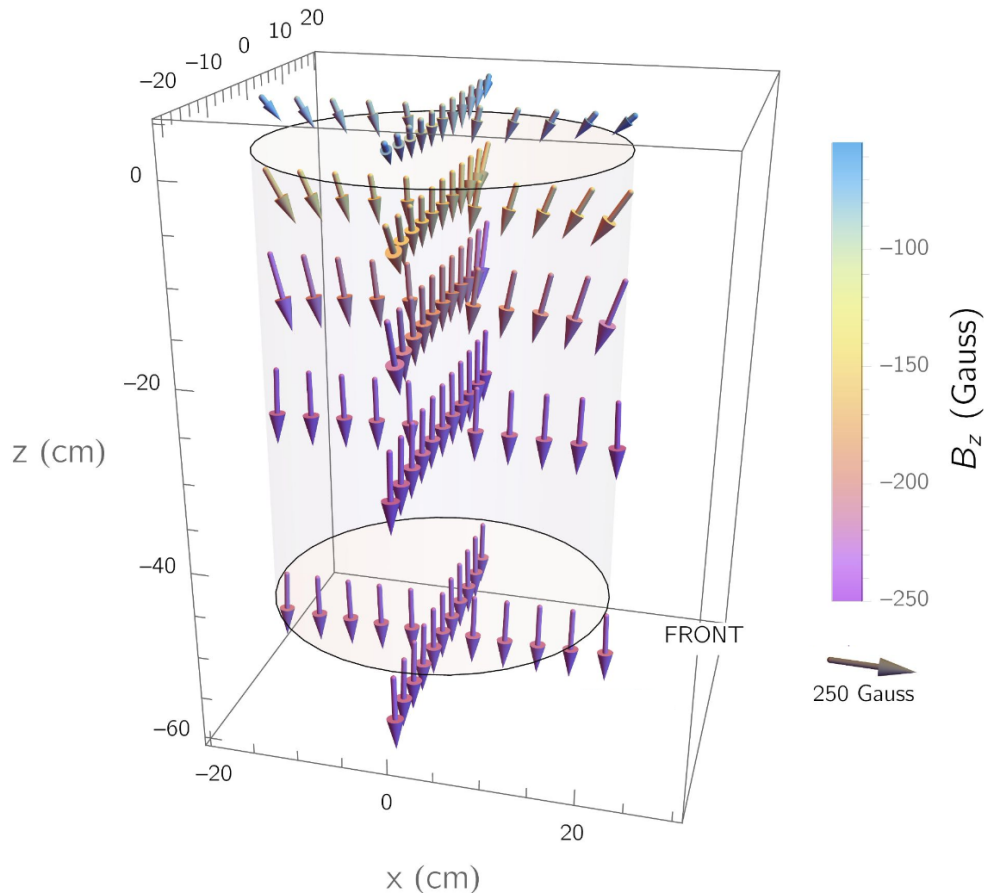


Figure 2.7: Magnetic flux density measurement of ROMAG’s upper-half inner bore. Each vector symbol is a 3D measurement of the magnetic flux density using a hand-held Gaussmeter. Figure made in collaboration with by Cy David.

other words, the ideal dimension of the convection tank should be within the dimension of 27 cm in diameter and 80 cm in height. The red dashed line in fig. 2.8 c) shows a theoretical radial magnetic flux density solution for solenoid in a cylindrical geometry (Derby & Olbert, 2010) agreeing well with our measurements.

Acquiring an accurate estimate of the magnetic flux density is crucial for experiments carried on ROMAG. For this reason, I re-measured the magnetic flux density at different output currents with the new high-precision SENIS magnetometer. The magnetometer is placed at the sidewall of the 40-cm tank at its 3/4 height, which is close to the solenoid’s

midpoint and represents the main field.

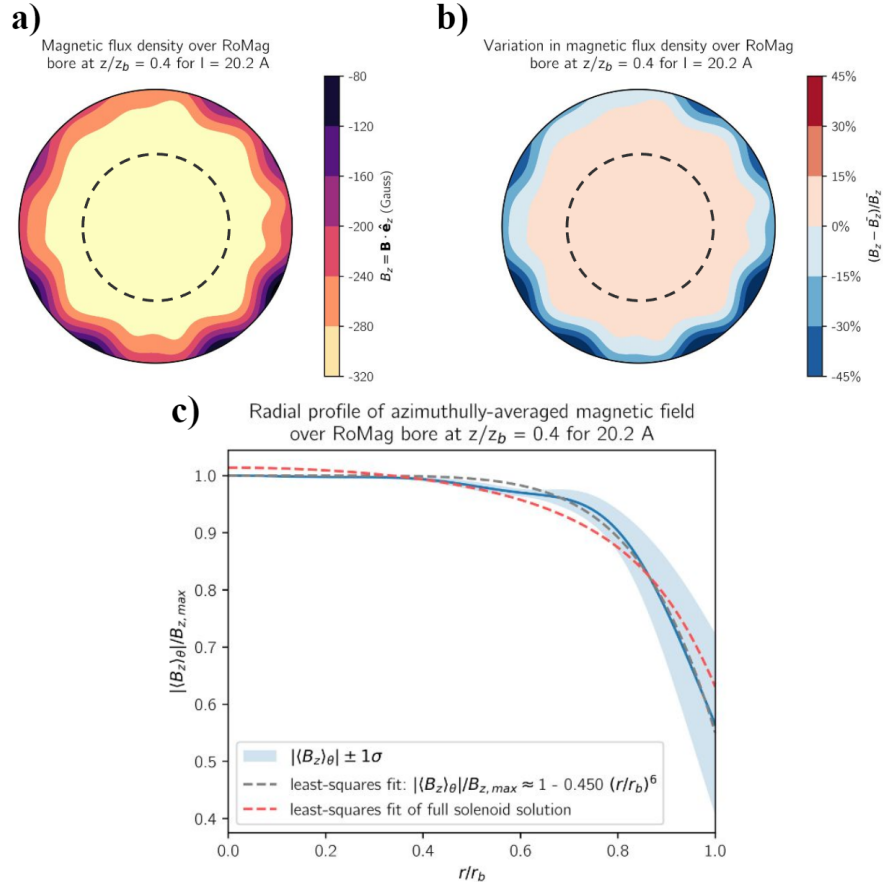


Figure 2.8: a) Horizontal magnetic field flux density contour of 20.2 A at 40 cm from the top. The color represents the flux density in Gauss. b) Variation in magnetic field strength, defined as $(B_z - \overline{B_z})/B_z$ at the same horizontal plane as a). c) Radial profile of azimuthally-averaged magnetic field at 40 cm deep horizontal plane inside the magnet bore. Here, r_b is the radius of the bore, whereas $z_b = 1.07$ m is the height of the bore. Figures made in collaboration with by Cy David.

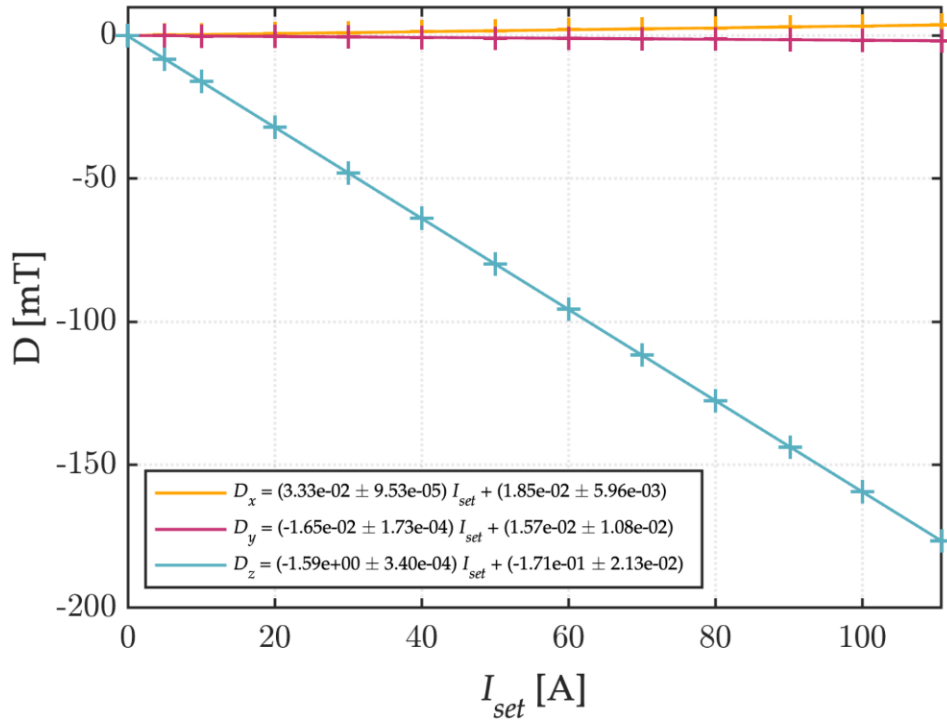


Figure 2.9: Measured B-field as a function of output current from the Magna power supply. Figure made in collaboration with by Jewel Abbate.

Figure 2.9 shows the time-averaged magnetic flux density $\mathbf{D} = \langle \mathbf{B} \rangle_t$ as a function of output current from the Magna power supply. All the cases here were measured with rotation to exclude any background and the Earth’s magnetic field. The best fit for \mathbf{D} ’s vertical component in mT is

$$D_z[\text{mT}] = (-1.59 \pm 3.40 \times 10^{-4})I_{set}[\text{A}] - (0.17 \pm 2.13 \times 10^{-2}), \quad (2.2)$$

where I_{set} is the set current on the magnet power supply. Equation (2.2) predicts the magnetic field strength for the magnetoconvection experiments with or without rotation and should be used to benchmark future magnetometer installation. See section 2.4.5 for more details.

2.2.6 Rotating System

2.2.6.1 Slip ring

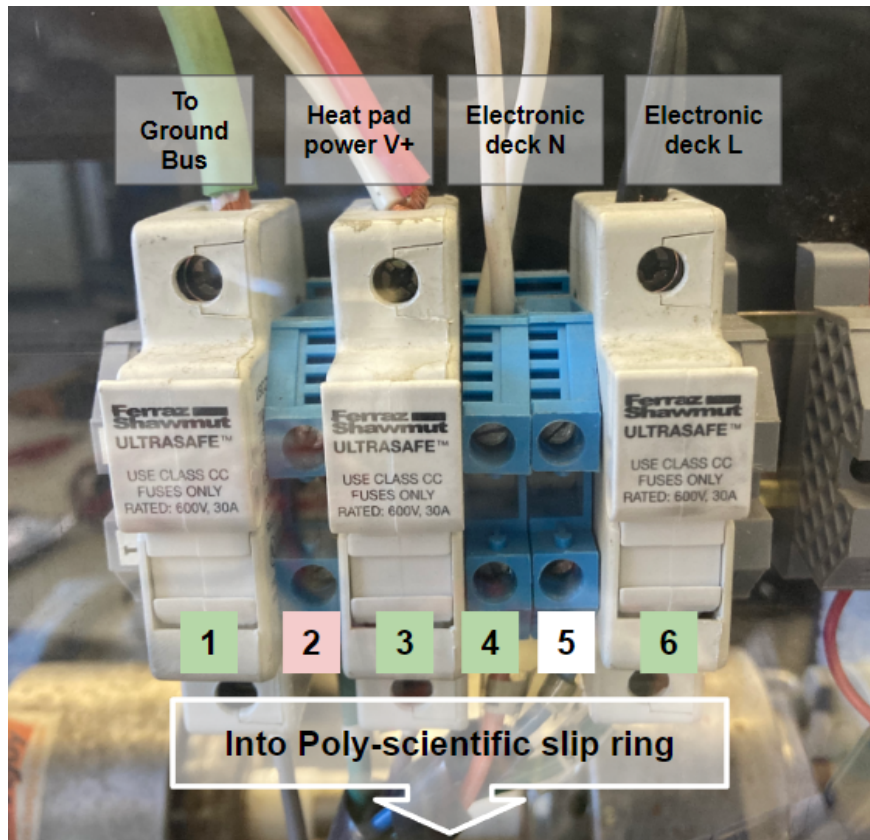


Figure 2.10: ROMAG’s Lab Frame Rail, located on the east side of ROMAG. It passes lab-frame AC and DC power into the rotating frame through the slip ring. The slip ring path connected to terminal 2 is malfunctioning and needs further investigation. Terminal 5 is currently unused.

Electric power is passed into the rotating frame through ROMAG’s heavy-duty slip-rings (model AC6098-24), manufactured by Poly-Scientific of Northrup Grumman. There are six power rings rated to 50 A each, and 54 10-A signal rings which are currently unused. They can maintain connections at up to 250 RPM.

See Grannan’s thesis (section 7.4.2) on the slip ring for more details. There is one update on the system. Figure 2.10 shows the power cables on ROMAG’s Lab Frame Rail with six

terminals. Terminals 1, 3, and 6 have built-in fuses. Terminals 2 and 5 are currently unused. The connection coming from terminal 2 of the Lab Frame Rail (two neutral legs of the electronic deck power cable) through the slip ring had some issues when the rotation is on. For unknown reasons, sometimes there's a short in the circuit to cause an overload in the power strip and trigger its built-in breaker. So the wires have been substituted to terminal 4 which was vacant before. Terminal 5 is still vacant. A future checkup on the condition of the slip ring is required.

As mentioned in Grannan's thesis, the first terminal of the Lab Frame Rail also requires future attention. The fuse should be removed to allow excessive currents to the ground.

2.2.6.2 Rotary union

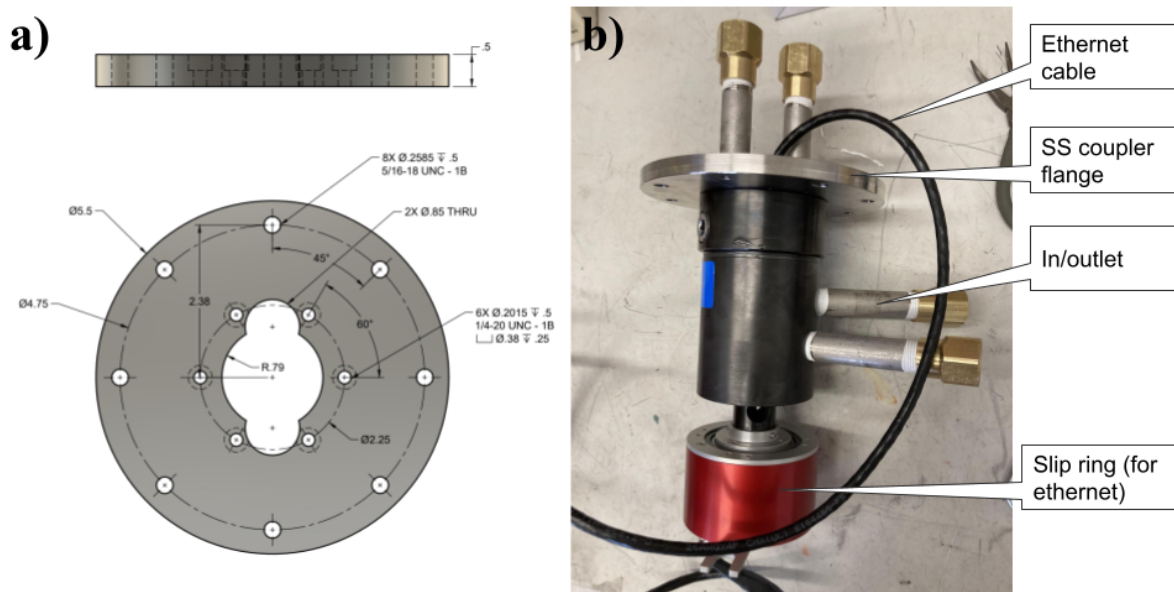


Figure 2.11: Rotary union. a) Stainless steel coupler flange design. b) Rotary union with an Ethernet slip-ring pathway.

ROMAG's new rotary union, shown in fig. 2.11, is manufactured by Rotary Systems. It has two pass unions with 3/8-inch ports that can exchange coolant from the lab frame to the

rotating frame. It also contains a 10MB Ethernet slip ring with a total length of 7.5 inches. In addition to the rotary union with Ethernet, I have designed a stainless steel coupler flange to connect the rotary union to the rotating frame. Water flows from the lab chiller into the inlet at the lower tubing of the rotary union and comes out from the top, which goes into the rotating frame. The cycled water follows a reverse path back to the lab chiller.

2.2.7 Data acquisition system

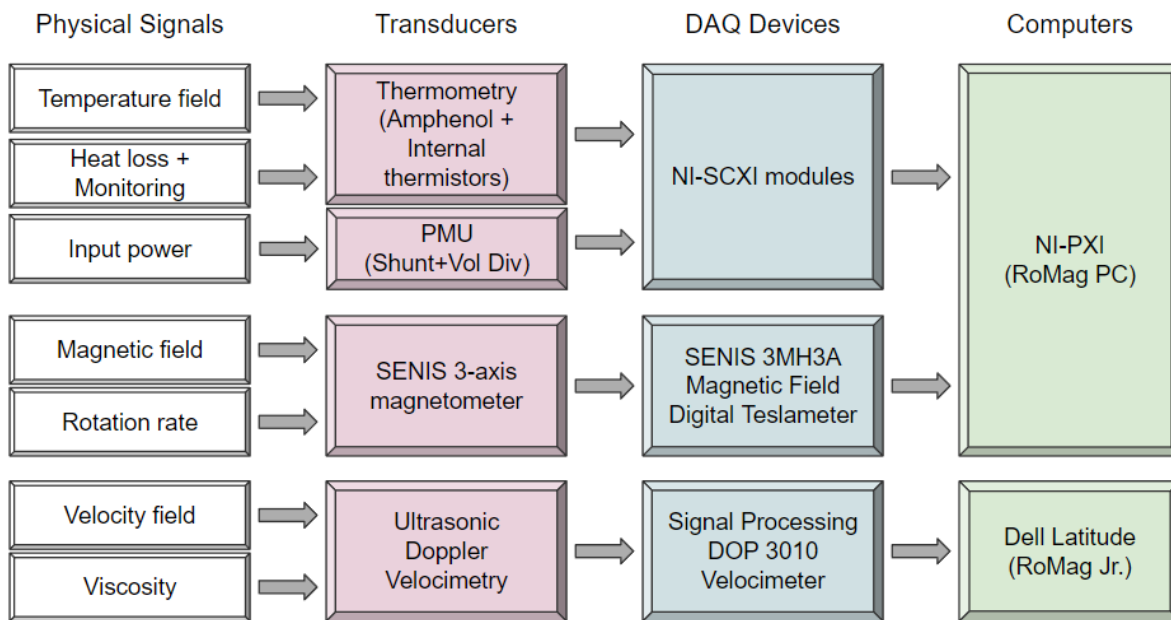


Figure 2.12: Schematics of ROMAG’s DAQ system. Physical signals (first column) are measured by transducers (second column) and then conditioned and converted into digital signals in multiple DAQ devices. Eventually, they will be transmitted to the computers and prepared for analysis.

ROMAG collects power, thermal, velocity, and magnetic field data from its data acquisition (DAQ) system. Figure 2.12 shows a schematic of ROMAG’s DAQ system. The temperature field and heat loss are measured by thermometry, including external Amphenol thermistors and high-precision internal thermistors. A few thermistors are used to monitor room temperature and heating on the expansion tank. PMU measures input power for the heat pad. Both thermometry and PMU send signals to the NI-SCXI modules, which have

current excitation and voltmeters. The NI-SCXI conditions and digitizes the analog signals, then send them to NI-PXI 8105 computer, the “RoMag PC” for further processing. These data are collected and visualized by LabView 2013 software on the NI-PXI.

The SENIS 3-axis magnetometer measures three-dimensional magnetic flux density in the rotating frame. It can also measure the rotation rate of the device by fitting the sinusoidal change in the magnetic field from the rotation. The signals from the transducers are processed with temperature compensation in the 3MH3A Digital Teslameter, which communicates with NI-PXI via a USB cable. A 3MH3A software on the NI-PXI visualizes and writes measurements into data files.

Up to ten ultrasonic Doppler transducers measure velocity field and viscosity from linear spin-up experiments. The signals are processed in a 10-channel DOP 3010 Velocimeter manufactured by Signal Processing. For better stability and larger storage, the DOP 3010 connects to a Dell Latitude 7430 laptop (nickname “RoMag Jr.”) via a USB cable. A UDOP software on the Dell laptop can visualize and convert velocity measurements into data files.

2.2.7.1 The upgraded channel terminal

I have rewired and expanded NI-SCXI modules to increase their channel capacity. The NI-SCXI modules now have a total of 64 available channels, including 56 thermistor channels (9 of which are currently not functional), two PMU channels for the shunt and the voltage divider, two legacy hall probe channels, and three unused $100\ \mu\text{A}$ current source channels. Figure 2.13 shows a schematic of SCXI modules and wires that go into the barring shaft to connect to the transducers. The channel number is half of the wire numbers as one half is the positive side of the loop and the other half is negative.

I have redesigned the channel terminal, as shown in fig. 2.14. The most important feature is the cluster of 67 solid-state BNC connectors, which are hard-soldered onto a four-layer PCB. This design provided a robust connection between the transducer and the terminal,

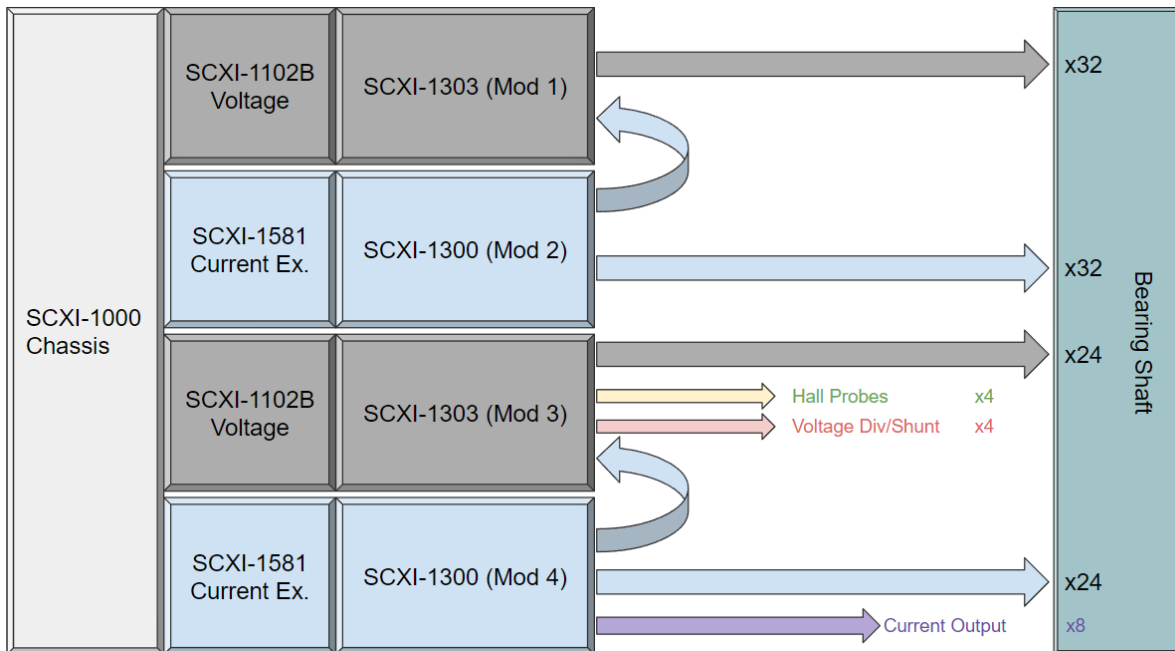


Figure 2.13: National Instruments SCXI modules connection. The NI SCXI-1000 Chassis hosts eight SCXI modules reading the measurements from thermometry and PMU via ribbon cables. The SCXI-1000 Chassis connects to the PXI computer for data visualization and analysis.

even under high-speed rotation.

A total of 67 BNC ports (3 blanks, 9 faults) are arranged in the way that the first 43 channels are in a concentric form. This design creates a direct mapping between the BNC ports and the physical locations of the transducers on a cylindrical tank. For instance, the inner-most cycle has six thermistors. One can map the bottom lid thermistors in the same azimuthal direction. And each circle represents thermometry at different heights on the cylinder. Say the azimuthal degree increases right-handed, then channel 1 correlates to the thermistor at 0 degrees, channel 2 correlates to the thermistor at 60 degrees, and so on. This feature becomes especially helpful when the device is fully insulated, so there is no visual clue where the thermistors are located on the cylinder. Besides channel mapping documents, the terminal box provides redundancy for an accurate callout of the physical location of the transducers.

Figure 2.15 shows the four-layer PCB designed in collaboration with Peter Yu from the UCLA Physics electronic shop. The board connects BNC connectors and bundles the wires into four ribbon cable terminals. Moreover, the circuit board is protected by a 3D-printed plastic box with a polycarbonate clear panel. There is also an extra polycarbonate tray that can be placed on top of the channel box to prevent Gallium erosion.

Note that the terminal box is currently only connected to the SCXI modules through ribbon cables. The other types of transducers are connected directly to their DAQ boxes, such as the magnetometer, or through other BNC cables, such as the Doppler probes.

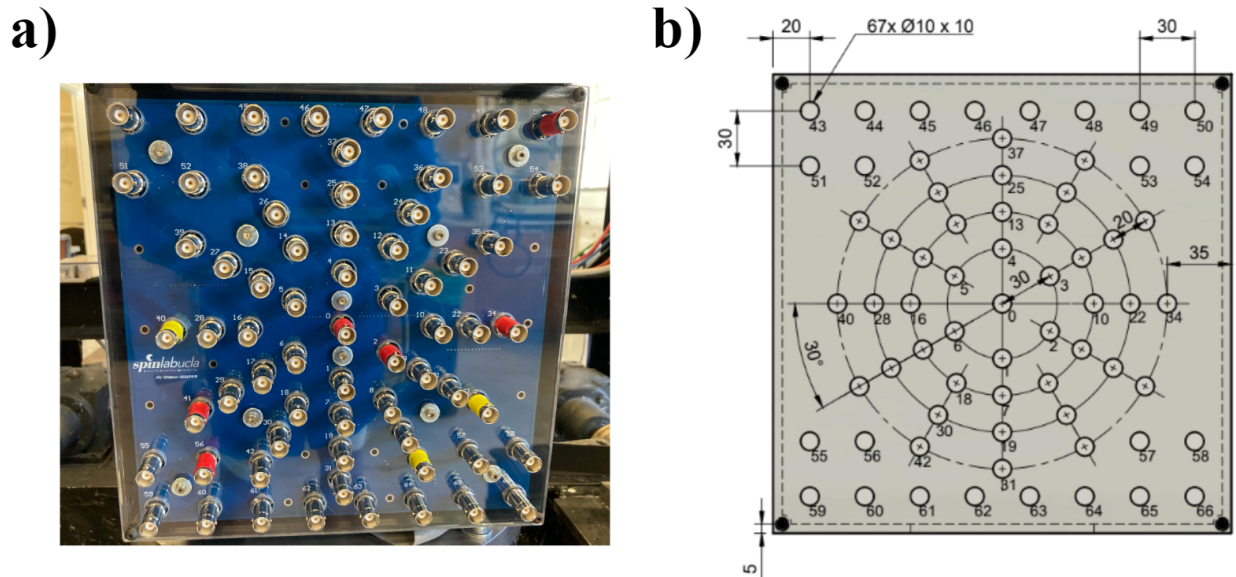


Figure 2.14: The upgraded 67-ports BNC channel terminal. a) Photo of the front view of the terminal box. b) Channel design. The concentric circles of BNC ports can be mapped to azimuthal arrangement of the thermometry on the cylindrical tank.

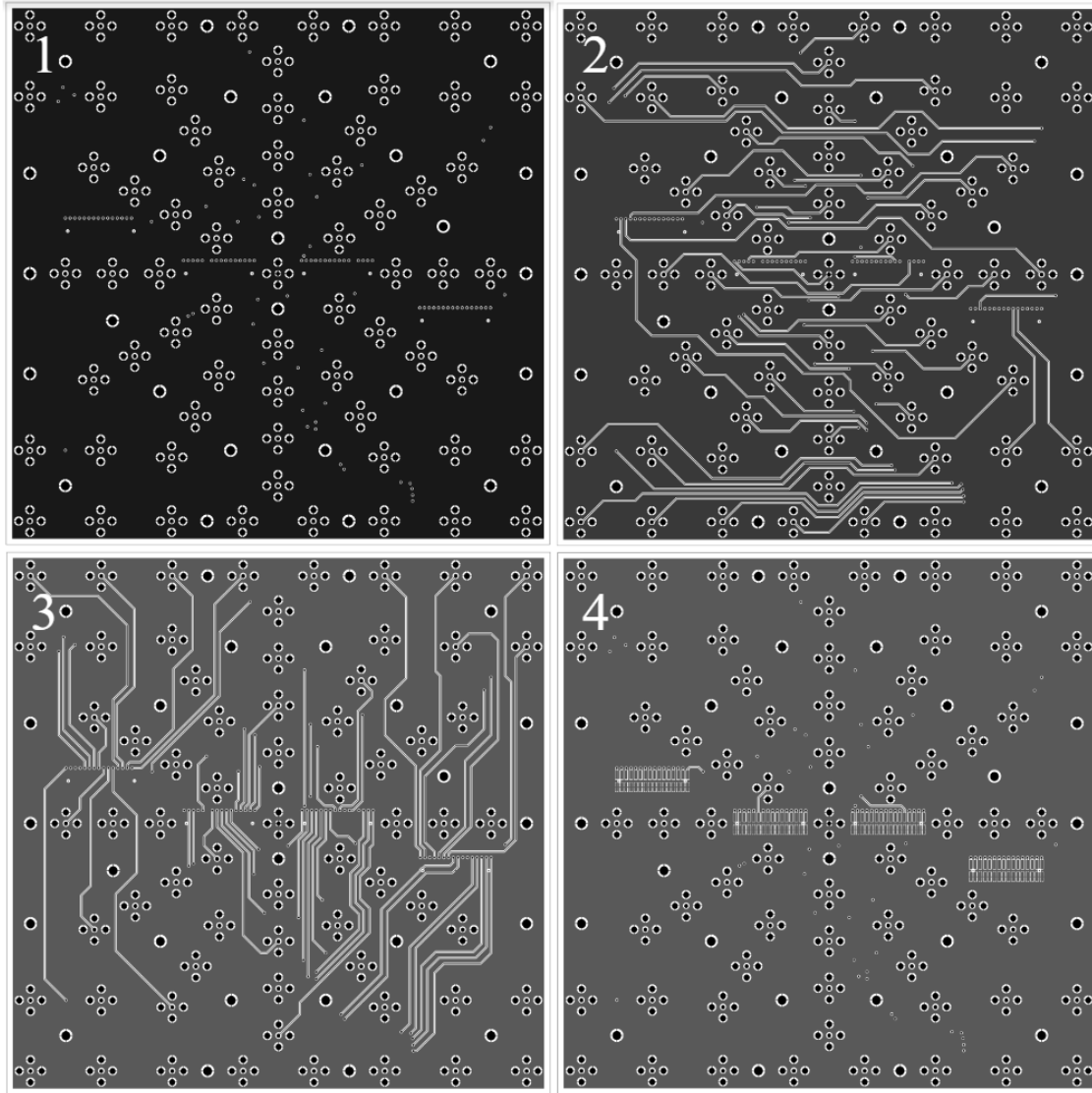


Figure 2.15: Four-layer circuit board designed in collaboration with Peter Yu (UCLA physics electronic shop) for the upgraded 66-port BNC channel terminal. Layers 1 to 4 are stacked and printed as one integrated PCB board.

2.2.7.2 Thermometry

ROMAG's thermometry has two types of sensors. The first type is the Amphenol thermistors (SC50F103V), which are used externally to the fluid. Figure 2.16 shows a simple schematic of the thermistors. Most Amphenol thermistors are on the sidewall, as shown in fig. 2.17 a). One is used to calculate the heat loss through the sidewall, one to measure room temperature, and three to monitor the expansion tank temperature. They are connected to the channel terminal with BNC connectors (fig. 2.17 b)) and have internal resistance around $10\text{ k}\Omega$ at room temperature. They have an averaged error of $\pm 0.1\text{ K}$ before calibration.

The second type is the in-house calibrated high-precision internal thermistors (averaged error $< \pm 0.01\text{ K}$). They have solid thin stems that can extend into the bulk fluid. They are located at the top lid, measuring down into the bulk. A picture of these thermistors is shown in fig. 5.4 a). Figure 2.17 c) shows schematics of the thermometry setup on a 40-cm tank. In most cases, sidewall thermometry is used with internal thermometry to interpret important spatial-temporal characteristics of the liquid metal flows.

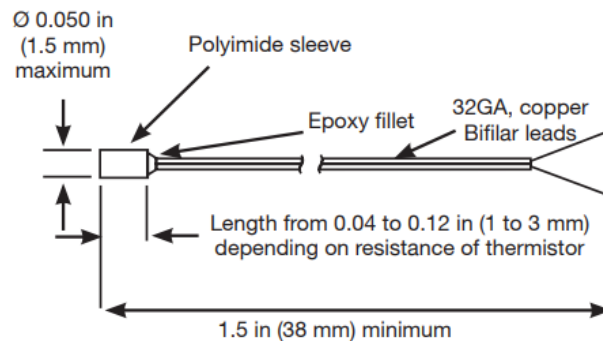


Figure 2.16: Schematics of the Amphenol thermistors, type SC50F103V. Figure adapted from the manual.

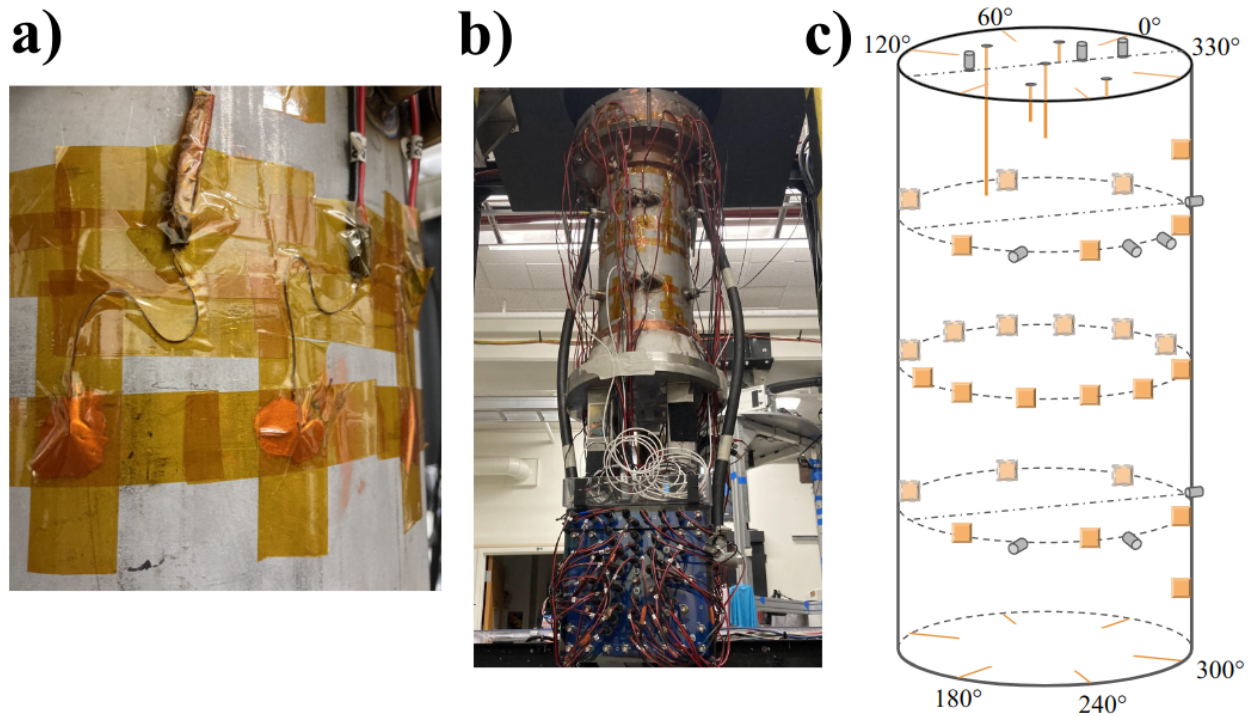


Figure 2.17: a) Sidewall thermometry attachment. Sensors are taped onto the sidewall with thermal grease and Kapton high-temperature tape. The wires are curved under the tape to prevent excess stress. b) A photo of the thermometry with the channel terminal at the bottom. The white wires are Doppler probes. c) Schematic of the thermometry setup for the 40-cm tank. There are five internal thermistors extended below the top lid.

2.2.7.3 Ultrasonic Doppler Velocimetry

Ultrasonic Doppler Velocimetry (UDV) is currently the state-of-art method for measuring velocity in liquid metals (e.g. [Perez & Kelley, 2015](#); [Vogt *et al.*, 2018a, 2021](#); [Cheng *et al.*, 2022b](#)). An ultrasonic transducer generates periodic pulses and listens to the echoes of the pulses from a moving particle. A short ultrasonic burst Doppler shifts its own frequency as it echoes back from a moving object. The time interval dt reveals the particle's position, while the Doppler shift in its frequency reveals the particle's velocity. Transducer can measure the single velocity component at many locations along its emission line. Liquid gallium has small impurities and oxides that naturally form in the bulk. UDVs are sensitive enough to

pick up those particle movements and use them to characterize the flow field. However, these impurities are inclined to settle over time. Doing a spin-up with alternating directions to mix up the fluid before any measurements is always a good idea.

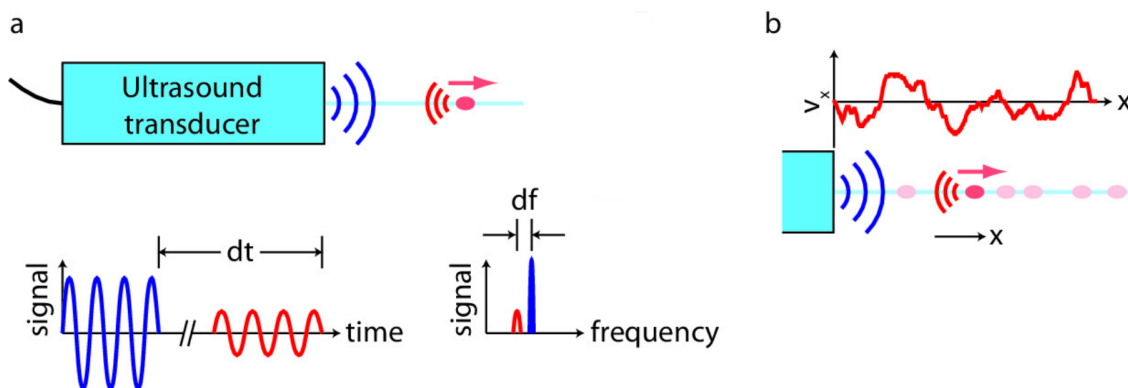


Figure 2.18: Schematics (not to scale) of ultrasonic velocimetry, adapted from [Perez & Kelley \(2015\)](#). a) An ultrasonic transducer generates a pulse and listens to the echos from a moving particle. The time interval dt reveals the particle’s position, while the Doppler shift in its frequency df reveals the particle’s velocity. b) Transducer can also measure one velocity component at many locations along its emission line.

Before using Doppler velocimetry, knowing the transducers’ operating range and maximum temperature is crucial. The Nyquist theorem limits the pulsed Doppler ultrasound transducers. To avoid aliasing, the maximum velocity must be at least

$$v_{max} = \frac{cf_p}{4f_e \cos \Theta}, \quad (2.3)$$

where c is the speed of sound in liquid. The sound speed $c = 2870$ m/s in liquid gallium at 30°C . The pulse repetition frequency (PRF) is marked as f_p , ranging from 0.1 Hz to 15,625 kHz. Next, f_e is the emitted frequency of the sound from the 8MHz transducer, with an adjustable range of 450 kHz to 10.5 MHz. The angle between particle velocity and the beam is Θ , and $0 \leq \Theta \leq \pi/2$. For the lower bound, $\Theta = 0$. See the manual for a detailed derivation. Equation (2.3) shows that increasing f_p or decreasing f_e results in a higher velocity limit.

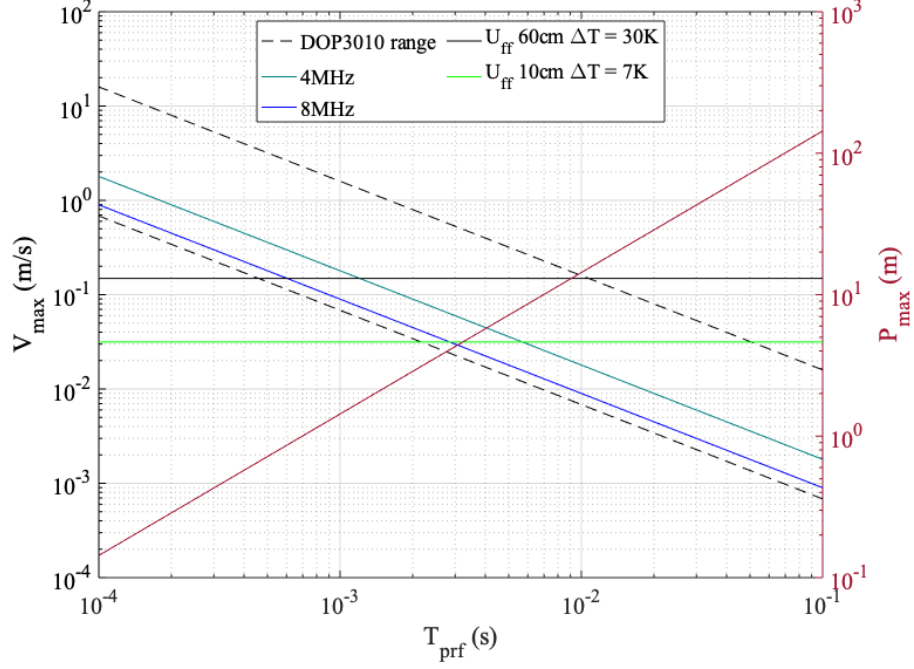


Figure 2.19: Ultrasonic Doppler Velocimetry operating range. The horizontal axis is the pulse-repetition time. The left vertical axis is the maximum velocity. The right axis and the red line show the maximum depths Doppler probes can measure. The black horizontal line shows the estimated convective free-fall velocity as an upper limit in a 60-cm tank with a temperature difference of $\Delta T = 30$ K. The green horizontal line represents the estimated upper limit velocity in a 10-cm tank with $\Delta T = 7$ K. The dark green and blue slopes show the maximum velocity based on emission frequency of 4 MHz and 8 MHz, respectively.

Maximum depth is determined by the time needed for the ultrasonic signal to travel from the transducer to the target and back,

$$P_{max} = \frac{c}{2f_p}. \quad (2.4)$$

Therefore, combining eq. (2.3) and eq. (2.3) yields

$$P_{max}V_{max} = \frac{c^2}{8f_e}. \quad (2.5)$$

Given a fixed f_e , the maximum speed and the maximum depth are inversely proportional to each other. Reducing the f_p will increase the maximum measurable depth but will also

reduce the maximum velocity that the probe can measure at the same f_e .

Figure 2.19 shows the operating range of maximum velocity and depths for both 4 MHz and 8 MHz probes. The pulse repetition time $T_{prf} = 1/f_p$. The typical velocity of the experiments is usually below the black and green horizontal lines ($\lesssim 0.1$ m/s) and overlaps with the DOP3010 velocity range, as shown between the two dashed lines. If $f_e = 8$ MHz, which is a typical value for the 8 MHz probe, the maximum speed here is plotted in the horizontal black line, which intercepts the blue line at $T_{prf} \sim 6 \times 10^{-4}$ s. This value indicates a maximum depth of ~ 0.8 m. The 4 MHz probe can measure up to ~ 2 m.

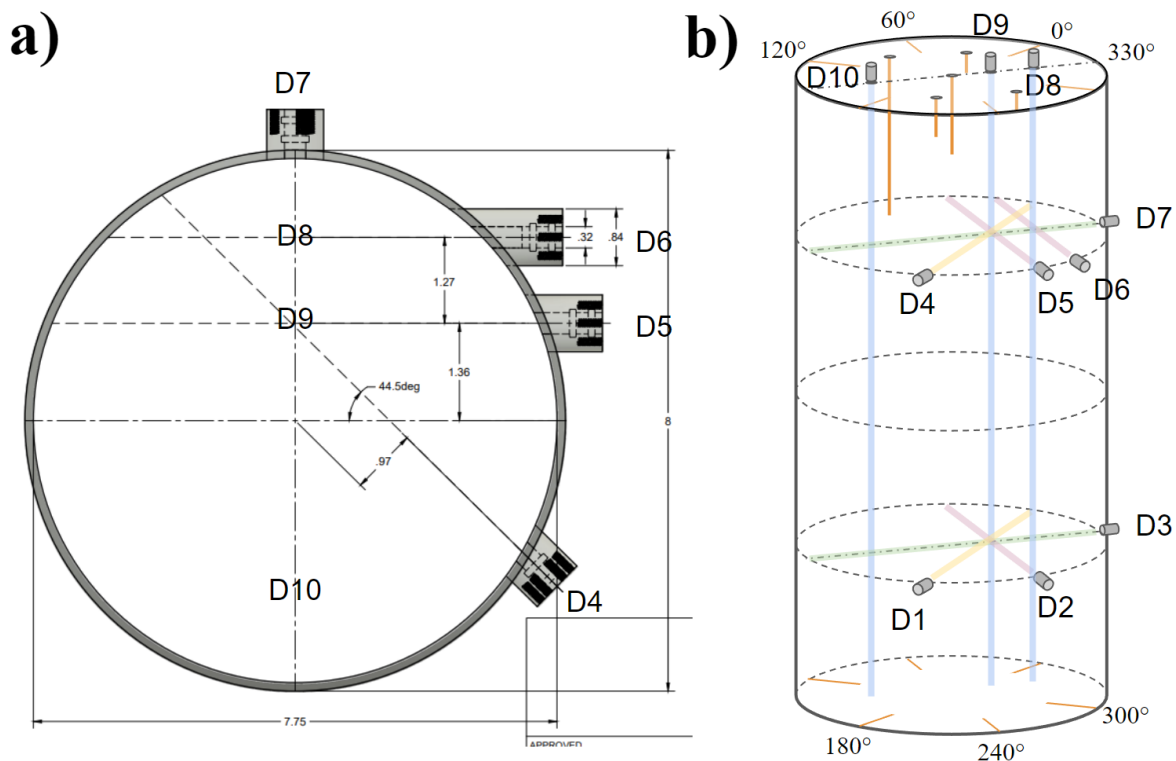


Figure 2.20: Ultrasonic Doppler Velocimetry setup on a 40-cm tank. a) The horizontal cross-section at 3/4 tank height. b) Schematics of ROMAG's velocimetry and thermometry on a 40-cm tank.

UDV on ROMAG gathers velocity information of the fluids and can be used to analyze the dynamic morphology, momentum transport, and kinetic energy of the flow. Doppler probes

can be placed on the sidewall as well as the top lid of the convection tank. I have made new designs for 10-cm, 40-cm, 60-cm, and 80-cm tanks with UDV ports on the sidewall. Due to the height limitation, the Doppler ports on the 10-cm design only locate in the midplane. There is also an existing 10-cm tank with one chord probe port at the sidewall midplane. Both 40-cm and 60-cm designs have Doppler ports at $1/4$ and $3/4$ heights. For the 80-cm tank, I have added up to 15 ports in total at $1/4$, $1/2$, and $3/4$ of the tank height, which will be compatible with future upgraded DOP boxes (see fig. 2.32).

The orientations of the Doppler sensor ports at $3/4H$ in a 40-cm tank are shown in fig. 2.20 a). The chord beam from D4 intersects with chord probes D5, D6, radial probe D7, and top lid D9. This setup allows getting two-dimensional and three-dimensional velocity measurements at the intersection points. D4, D5, and D6 allow estimates of different azimuthal velocities as a function of radius as the beams' distance to the center of the tank increases. Another similar setup at $1/4H$ allows any indication of large-scale structures that could maintain their velocity profile throughout nearly the entire tank domain.

2.2.7.4 Magnetometry

The SENIS 3MH3A 3-axis magnetometer can measure up to 0.2 T with better than 0.1% accuracy. Figure 2.21 shows a schematic of the magnetometer. A 12-V VDC powers the main signal processing box of the magnetometer (module E), which has a display showing the real-time measurement of the 3-axis magnetic field flux density measured by the hall probe (module H). The magnetometer talks to NI-PXI via a USB cable. The probe is currently placed on the sidewall, but future upgrades on the probe holder and encapsulation will allow the probe to be inserted into the fluid from the top lid or from the sidewall sensor ports.

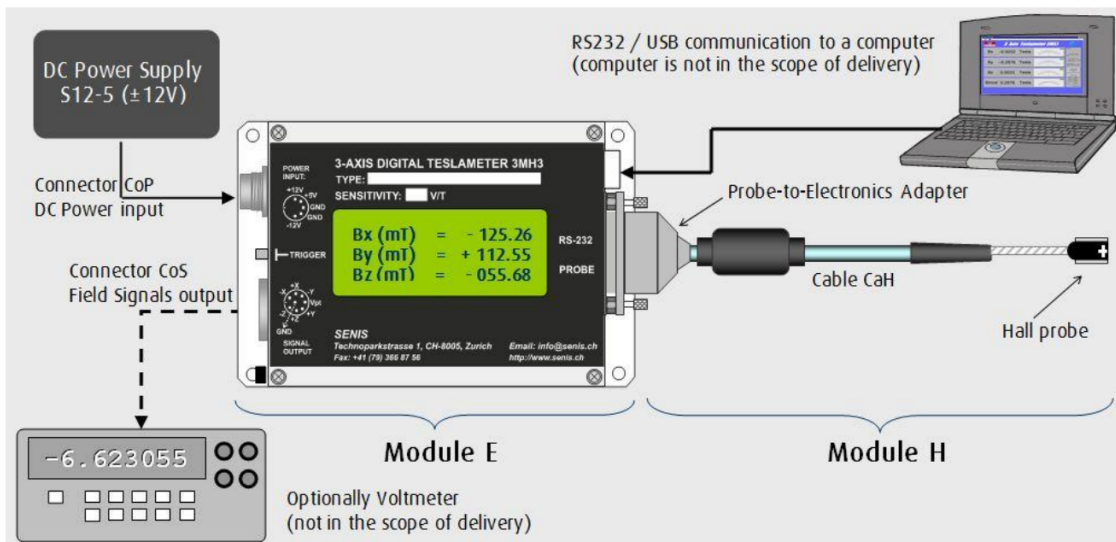


Figure 2.21: 3MH3A Magnetic Field Digital Teslameter. Figure adapted from 3MH3A datasheet by SENIS. Module E is a box with analog/digital electronics for signal conditioning. Module H has the Hall Probe and the CaH cable.

2.2.8 Control systems

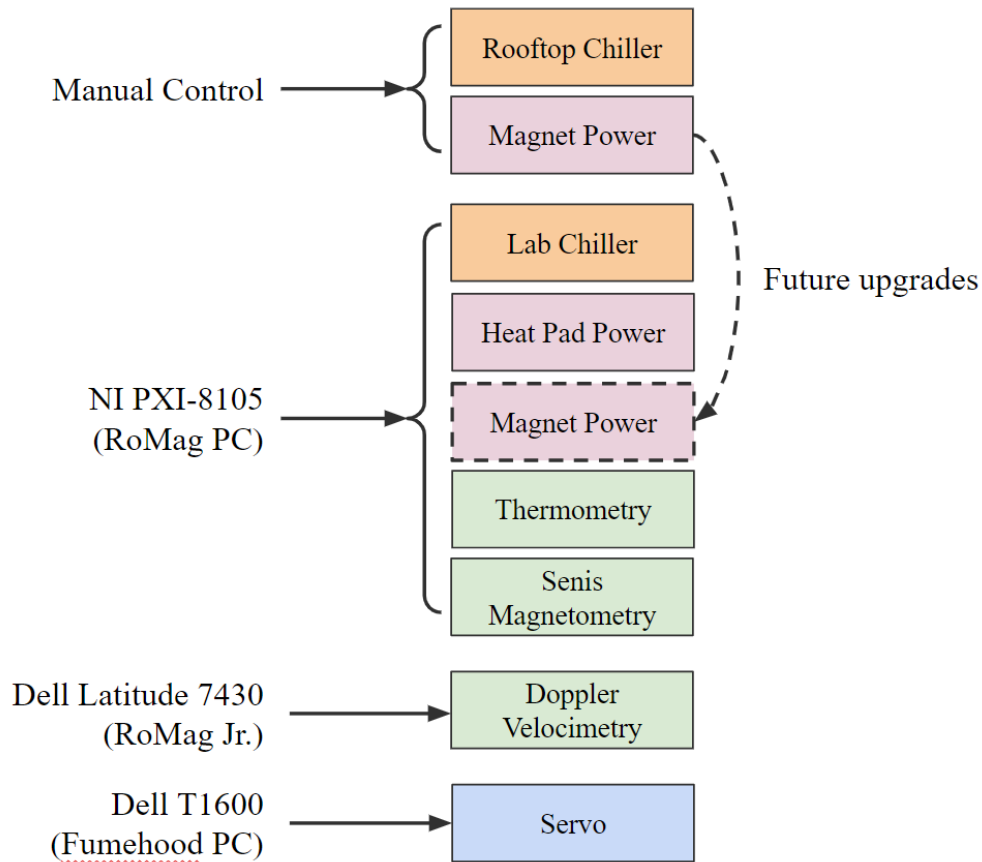


Figure 2.22: Schematics of the control system.

ROMAG’s current control system includes three computers: NI-PXI 8105 computer (nickname “RoMag PC”) located at the electronic deck on ROMAG. It controls the lab chiller temperature setting, heat pad power setting, and thermal data acquisition in the rotating frame. The second computer is a Dell Latitude 7430 laptop (nickname “RoMag Jr.”) located at the electronic deck as well. It controls the Doppler velocimetry system on board. The third computer is a Dell T1600 computer (nickname “fumehood PC”) at the static lab frame next to the fume hood. It controls the servo motor in the static lab frame, monitors the fume hood status, and connects to the lab’s live cameras.

Figure 2.22 shows complete schematics of the control system. Currently, the magnetic

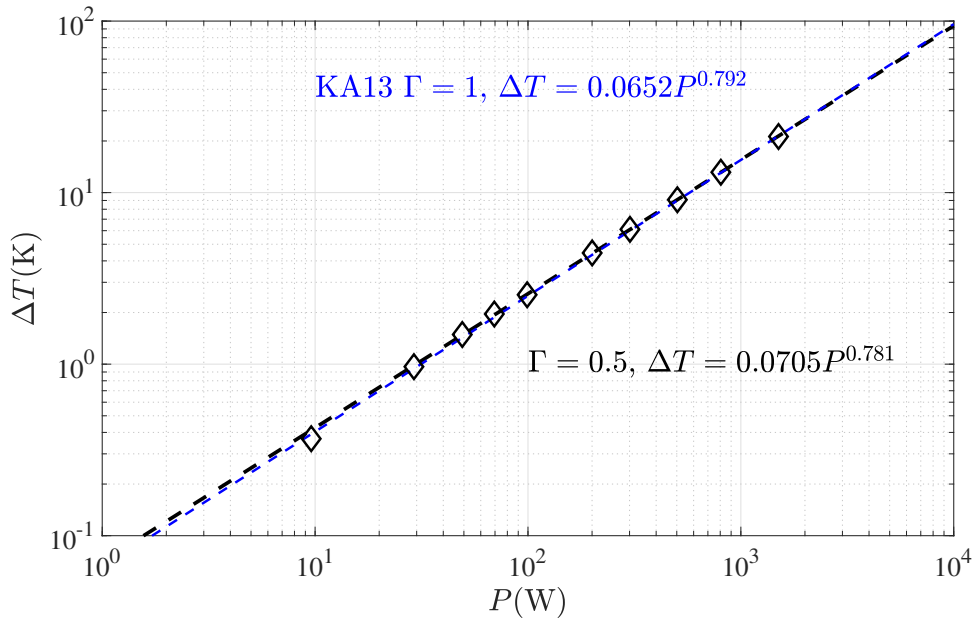


Figure 2.23: Empirical scaling of the Argantix raw output power and resulting temperature difference across a gallium fluid layer with copper boundaries on ROMAG. The fluid undergoes Rayleigh-Bénard convection (RBC). The aspect ratio $\Gamma = 1$ data are from [King & Aurnou \(2013\)](#).

power supply requires manual control (SOP in section 2.2.8.2). But it has the capability of remote control using the analog I/O module. The rooftop chiller requires manual input from its dash panel. See [Grannan \(2017\)](#) for detailed instructions.

2.2.8.1 Thermal and rotation control

Always check cooling systems before using any of the power supplies in the lab. NI-PXI 8105 remotely controls the Argantix power supply via the Omega module. The SCXI voltage module measures the output voltage and current from the Argantix. And because the PXI and the SCXI module can only read small voltages up to 10 V, a shunt and voltage divider are needed for converting the output current and voltage to a readable level. See Chapter 7 of A. Grannan’s thesis ([Grannan, 2017](#)) on the power management unit (PMU) and thermal control for more details.

Figure 2.23 shows temperature difference across gallium fluid layer ΔT with two different



Figure 2.24: Magna Power Supply control panel. The numbers indicate the proper steps for manual current controls.

aspect ratios in ROMAG with Copper boundaries as a function of raw power input, P , from the Argantix power supply. The scaling behavior of the heat transfer of RBC in both aspect ratios agrees with each other. This power law can be used to estimate the upper limit of the system temperatures before the experiments.

The Servostar Motionlink software on the Fumehood PC controls the rotation of the ROMAG devices. The Fumehood PC connects to the servo drive box via three pins of an RS232 cable. See section 7.9 of A. Grannan's thesis (Grannan, 2017) for instructions and more details.

2.2.8.2 Magnetic field control

Because there is no temperature monitoring on the solenoid right now. It is extremely dangerous to leave the manga power supply on. Therefore, any operation on the magnetic control should make sure there is emergency contact, and there are people onsite. The steps for turning on the magnetic field on ROMAG are shown below:

- First, ALWAYS check if the magnet cooling loop is open and the rooftop chiller works properly. The facility will install a flow switch in spring 2023 to ensure that the cooling

loop is operating when the magnet power supply is on.

- Turn on the 125A circuit breaker in the main electric panel.
- Press the display button (1), the power supply will be in standby mode.
- Measure the inlet/outlet on the magnet using a remote infrared temperature sensor and make sure the flow temperature is ideal.
- Press the Start button (2), and wait for a few seconds.
- If the power supply is in constant current mode, only turn the current nob (3) to a desired current setting.
- During operation, constantly check the temperature of the magnet following the previous steps.
- When it's time to shut it down, turn the current nob all the way down, and then press the Stop button. Then the display, and eventually the main breaker.

2.3 Other auxiliary systems

2.3.1 Holiday emergency heating system (HEHS)

Safety has always been the priority of the SpinLab. In case of holidays and other special occasions when no one is physically around ROMAG, one should implement Holiday Emergency Heating System (HEHS). HEHS is consist of a Yeti Lithium Battery, two Inkbird thermostats, and three heating tapes. And the monitoring status can be access remotely from the remote desktop applications or VNC connectors.

When HEHS is in use, as shown in fig. 2.25, the Yeti battery is constantly charging and providing power to the Inkbird thermostats and heating tapes. The Inkbird controls the heating tapes and constantly monitors the heating temperature from the thermistors. Two

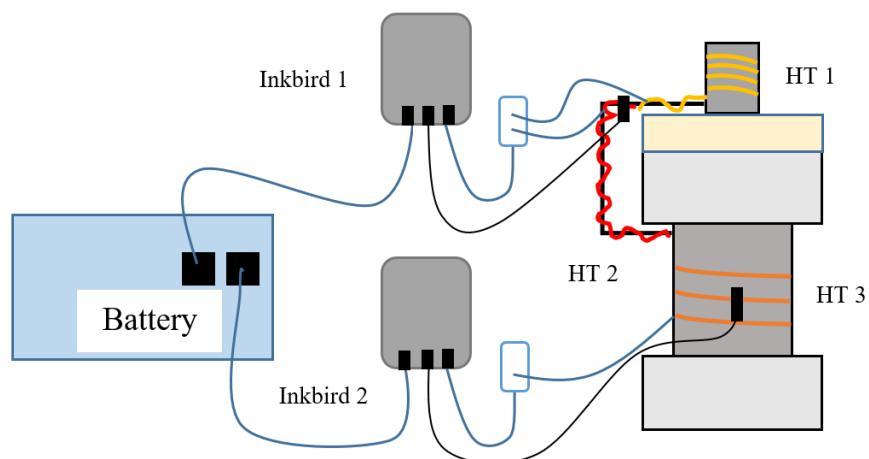


Figure 2.25: Schematics of Holiday Emergency Heating System (HEHS). Three heating tapes (HT1-3) are wrapped around the convection tank, the expansion tubing, and the expansion tank. Sometimes, HT1 and HT2 can be combined using just one heating tape. Two Inkbird modulators are used to control the temperature output of the heating tape. Inkbird 1 is usually set to a higher temperature than Inkbird 2. Inkbird 2 is to prevent the bulk gallium from freezing in case of the heat pad fails.

heating tapes are wrapped around the expansion tank and the cornered expansion tube to prevent freezing from the top. Another heating tape is wrapped around the tank and is set to heat near the 32°C . It only starts heating when the tank's temperature drops below the set temperature to prevent freezing inside the tank. In addition, the SERVO should be turned off from the fuse box to prevent rotation of the apparatus. And the table should be mechanically jammed to prevent rotation. Usually, the gallium will supercool – it remains liquid even below its freezing point. The point of using HEHS is to mitigate any risk of damaging the device or having clogs in expansion tubing.

2.3.2 Remote access

Accessing lab computers remotely gives advantages in monitoring the status of the main parts and taking data on ROMAG without being physically in proximity to the lab. Cyber

security guidelines must be carefully followed before remotely logging into any lab computer. Currently, there are two ways to access ROMAG’s computers remotely. The first and more efficient way is to use a program called “VNC viewer,” which allows multi-platform remote access such as smartphones and iPads. However, it is not recommended by the IT department due to security reasons. Future upgrades on the remote control system should be discussed with the IT department and may utilize campus VPN. More conventionally, one may remotely access via Remote Desktop Applications. For Windows users, “Remote Desktop Connection” is a built-in application that can easily set up the connection. For Mac users, it is the “Microsoft Remote Desktop” application from the app store. A detailed SOP can be found in the SOP folder of the lab’s shared google drive.

The Omega box, located above the Servo-Drive box, transmits control signals from PXI to the lab chiller and the Argantix (heat pad power supply) via Bluetooth. However, the Omega system is clumsy and old. It should be replaced and upgraded in the near future. Moreover, a wireless display module on the electronic deck of ROMAG sends signals from the NI-PXI to a recipient module which connects to a lab frame monitor.

2.3.3 Current protection

Instruments	Measured Current Load (A)
SENIS Magnetometer	0.05
Signal Processing Doppler	0.13
SCXI Modules & Chassis	0.28
Remote Desktop	0.10
Expansion Tank Heater	1.69
NI-PXI	0.75
Total	3.00

Table 2.1: Measured current load (in Ampere) on ROMAG’s electronic deck.

A 360 Electrical Producer 3.4 12-Outlet Surge Strip has been installed onto the electronic deck with 4320 Joules of surge protection. Its maximum working load is 15 A, which is sufficient for powering all the low-power electronics on board. Table 2.1 shows a measured current load from the working devices on ROMAG’s electronic deck. The total current load of the setup is approximately 3 A.

2.3.4 Thermal Insulation

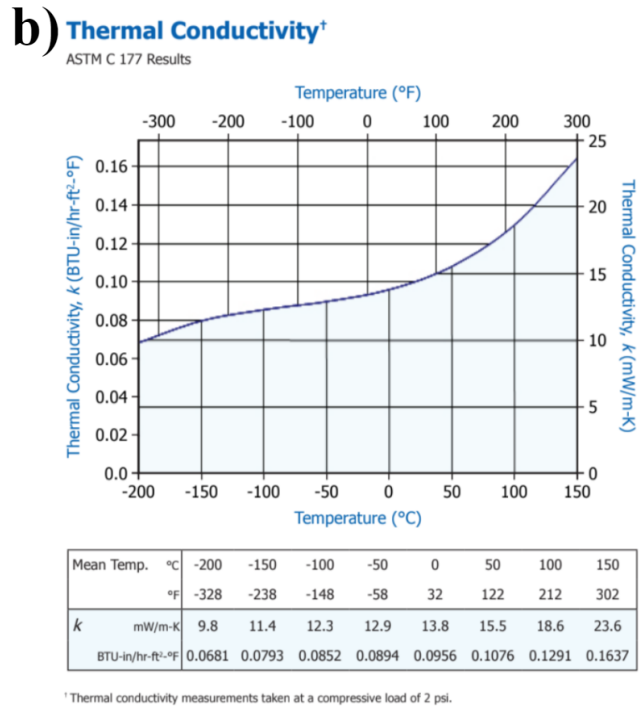


Figure 2.26: a) A photo of the inner layer thermal insulation blanket with a thickness of 2 cm. b) Thermal conductivity of the insulation material – Aspen Aerogels Cryogel x201. Figure modified from the product’s data sheets.

We use a combination of aerogel sheets and Insulfrax fibers for ROMAG’s sidewall insulation. For instance, the sidewall of the 40-cm convection tank is first covered by two layers of aerogel Cryogel x201 with cutout holes for the probe holders. The Insulfrax fibers are then used to fill any gaps. A few more layers of aerogel are applied as the outer insulation layer.

A thermistor is often placed between the inner and outer layers to measure the temperature across the inner insulation layer and gives heat loss estimates at the sidewall. For shorter tanks, pieces of the aerogel sheets are cut out and placed together with Insulfrax.

The heat exchanger at the top has one layer of aerogel sheet wrapped around it. The gaps between the aerogel blanket and the heat exchanger, as well as the heat pad and the bottom ceramic insulation, are filled with Insulfrax fibers.

The main insulating material is the aerogel. The thermal conductivity of the aerogel Cryogel x201 in the experimental temperature range (30-100 °C) is $\approx 15 \text{ mW}/(\text{m} \cdot \text{K})$. This value is assumed to be constant in our heat loss estimates.

2.3.5 Mini-jacks

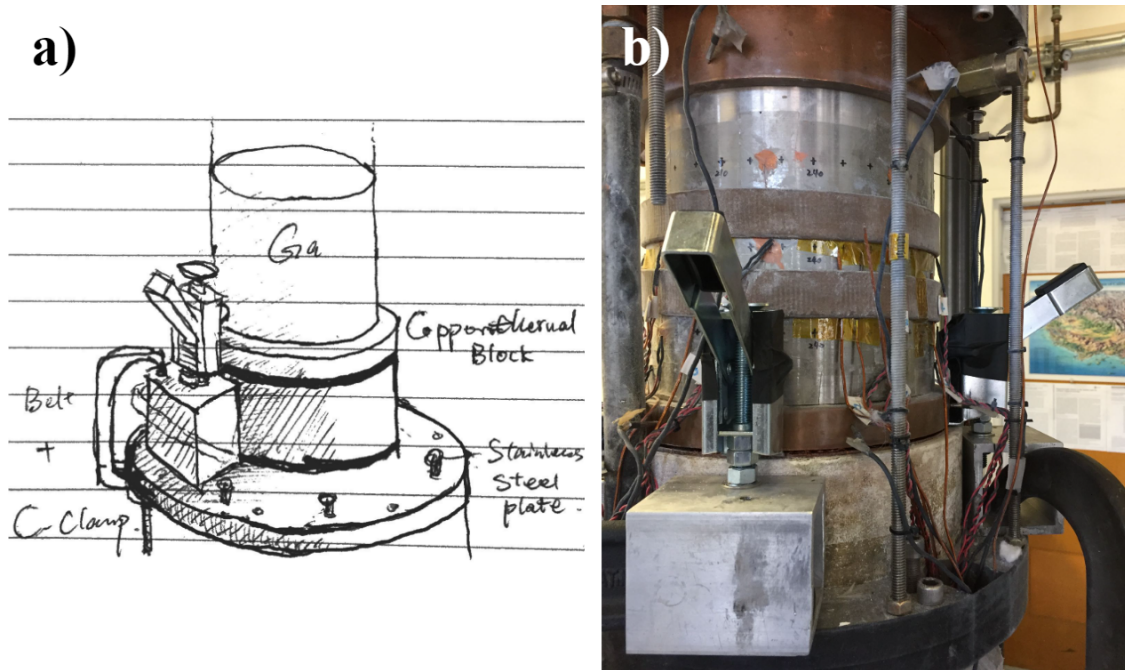


Figure 2.27: a) Schematics of ROMAG's mini-jacks. b) A photo of the mini-jacks with lifting blocks. The belt was not installed in the photo.

A set of three mini-jacks are used to replace the heat pad in case it is broken during experiments. Figure 2.27 a) shows a simple schematic of using min-jacks to lift the tank

from its base. Only one of the jacks is drawn here. Figure 2.27 b) is a photo during the operation. An additional belt was installed later and looped around the aluminum metal blocks to secure them onto the device.

The detailed designs for the lifting blocks and the SOP for replacing the heat pad using mini-jacks are on Google Drive. Be aware that this process may cause permanent damage to the heat pad. Thus, it should be the last resort (if you really need that last data point!)

2.4 Calibration

2.4.1 Thermal conduction profile and heat loss

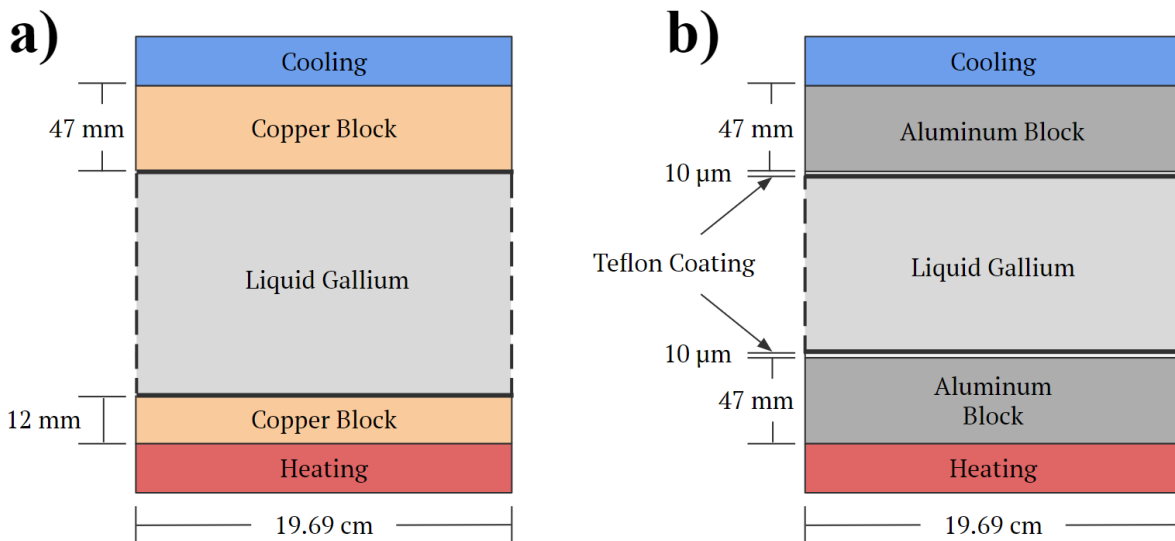


Figure 2.28: Material profile of ROMAG's tanks with a) Copper end-blocks; b) with Teflon-coated end-blocks. The height of the tank is subject to change.

Characterizing heat transfer and calculating essential parameters such as Ra and Nu in ROMAG's experiment requires accurate estimates of the heating power P and vertical temperature difference ΔT across the fluid layer. Heat loss through the sidewall and vertical end-blocks must be compensated from the raw measurements. Figure 2.28 shows material profiles of the tank with two different sets of end-blocks, which requires a slightly different

treatment in calculating their heat loss. Thermal conductivity of the materials commonly used in ROMAG's experiments:

$$\text{Copper: } k_{Cu} = 390 \text{ W}/(\text{m} \cdot \text{K}),$$

$$\text{Gallium: } k_{Ga} = 31.4 \text{ W}/(\text{m} \cdot \text{K}),$$

$$\text{Acrylic: } k_{SW} = 0.2 \text{ W}/(\text{m} \cdot \text{K}),$$

$$\text{Teflon: } k_{Tf} = 0.25 \text{ W}/(\text{m} \cdot \text{K}),$$

$$\text{Aluminum: } k_{Al} = 167 \text{ W}/(\text{m} \cdot \text{K}),$$

$$\text{Cryogel x201 Aerogel: } k_{Ae} = 0.015 \text{ W}/(\text{m} \cdot \text{K}).$$

A 1-D thermal conduction profile can be constructed based on the heating power, thermal conductivity, and heights of each layer, assuming there's no heat loss. For instance, if we consider a material profile of fig. 2.28 a), Fourier's law gives

$$\frac{P}{A} = k_{Cu} \frac{T_0 - T_1}{d_1} = k_{Ga} \frac{T_2 - T_1}{H} = k_{Cu} \frac{T_3 - T_2}{d_2} \quad (2.6)$$

$$\frac{P}{\pi R^2} = k_{Cu} \frac{\Delta T_{top}}{d_1} = k_{Ga} \frac{\Delta T}{H} = k_{Cu} \frac{\Delta T_{bot}}{d_2} \quad (2.7)$$

where $A = \pi R^2$ is the heating area of the fluid at the bottom boundary, and $R = 98.425$ mm is the radius of the horizontal cross-section area of the fluid. The thickness of the top and bottom copper end-blocks are d_1 and d_2 , respectively. The temperature at the top of the top copper lid, the top of the gallium fluid layer, the bottom of the gallium fluid layer, and the bottom of the bottom copper lid are T_0 , T_1 , T_2 , and T_3 , respectively. Note that $T_2 - T_1 = \Delta T$. Figure 2.29 shows an example of a one-dimensional temperature conduction profile of the Cu-Ga-Cu system at $P = 20$ W in a 40-cm tank. The top of the copper top lid is maintained by the lab chiller at 35°C . The thickness of the copper boundaries is shown in the schematics of fig. 2.28 a). The gallium is assumed to be subcritical to any convective behavior, perhaps under the strong constraint of rapid rotation. This conductive profile provides a background reference temperature for the convective heat transfer.

Without convection, the bottom lid temperature rises up to 43.45°C , making the temperature difference across the gallium fluid layer $\Delta T = 8.38\text{ K}$. This is significantly larger when the same system undergoes Rayleigh-Bénard convection, in which $\Delta T = 0.73\text{ K}$ according to the scaling laws from fig. 2.23.

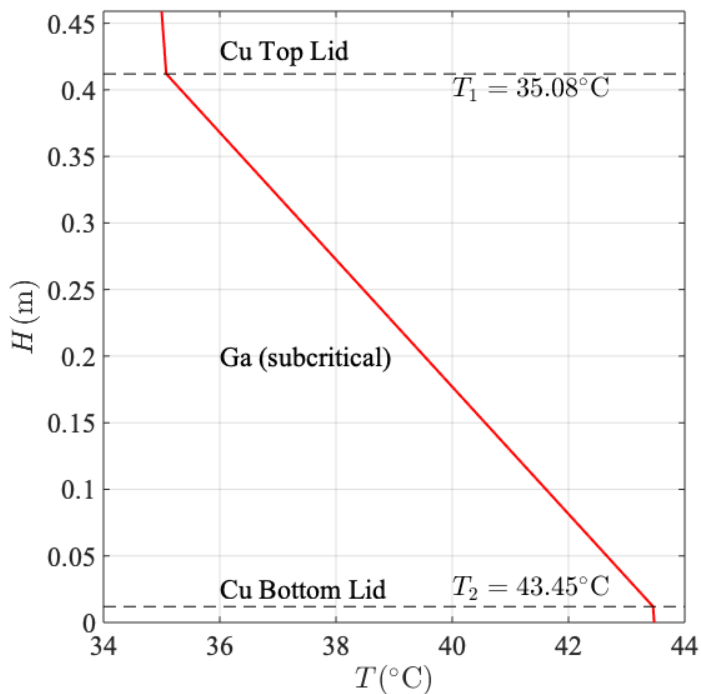


Figure 2.29: One-Dimensional thermal conduction profile of ROMAG’s 40-cm tanks with gallium and copper boundaries at $P = 20\text{ W}$. The horizontal axis is the temperature, and the vertical axis is the height of the tank from 0 to 40 cm. The temperature of the top of the top lid, T_0 , is maintained at 35°C .

Because heat dissipates via conduction at the boundaries in our system, we can estimate the total power loss through the sidewall insulation layer and top/bottom end-block boundaries. First, we calculate the heat loss at the sidewall, P_{SW} , through aerogel insulation in 1D concentric cylindrical geometry. The temperature difference between the insulation layer with a thickness of δR is measured by two thermistors on both sides of the insulation,

$\delta T_{SW} = T_{in} - T_{out}$. The sidewall heat loss is

$$P_{SW} = \frac{2\pi\delta T_{SW}k_{Ae}H}{\log(R + \delta R) - \log(R)}, \quad (2.8)$$

where $k_{Ae} = 1.5 \times 10^{-2} \text{ W}/(\text{m} \cdot \text{K})$ is the thermal conductivity of the aerogel. The corrected input power is

$$P_{corr} = P_{raw} - P_{SW}, \quad (2.9)$$

where P_{raw} is the raw power input from the bottom heater and measured by the shunt and the voltage divider of the PMU (section 2.2.3).

The second step is to subtract power loss through the vertical boundaries. If the end-blocks have only one single material, such as the copper lids, the vertical ΔT across the fluid-lid interface to the lid thermistors is then

$$\Delta T_{lid} = \frac{2P_{corr}d}{k_{Cu}A}, \quad (2.10)$$

where d is the distance from the fluid-lid interface to the lid thermistors. In most cases, $d = 2 \text{ mm}$. Note that the thickness of the lids does not matter here since the lid thermistors are always approximately a distance of d away from the fluid layer in both end-blocks. If the lids have two layers, e.g., Aluminum end-blocks with Teflon coating, the conduction profile is a superposition of each material. The temperature correction through the lids is, therefore,

$$\Delta T_{lid} = 2 \left(\frac{P_{corr}d}{k_{Al}A} + \frac{P_{corr}d_{Tf}}{k_{Al}A} \right), \quad (2.11)$$

where $d_{Tf} = 10^{-5} \text{ m}$ is the thickness of the Teflon coating. As a result, the corrected total vertical temperature difference is

$$\Delta T = T_{top} - T_{bottom} - \Delta T_{lid}. \quad (2.12)$$

lastly, the power is conducted vertically through the sidewall

$$P_{\perp,SW} = \frac{k_{SW}\Delta T A_{SW}}{H}, \quad (2.13)$$

where A_{SW} is the total cross-section base area of the sidewall $A_{SW} = \pi(R_{out}^2 - R_{in}^2)$. Here R_{out} and R_{in} are the outer and inner radius of the tank, respectively. The thermal conductivity of the sidewall material is k_{SW} . Therefore, the net power transferred through the fluid layer after correction is

$$P = P_{corr} - P_{\perp,SW}. \quad (2.14)$$

The heat loss results in an uncertainty in measured Nu , in which the leading order error comes from P and ΔT . We can write the error in Nu as a combination of statistical and systematic errors. By propagating the error associated with heat loss, the error in Nu can be written as

$$\delta Nu \approx \sqrt{\sigma(Nu)^2 + \overline{Nu}^2 \left[\left(\frac{\delta P}{P} \right)^2 + \left(\frac{\delta T}{\overline{T}} \right)^2 + \left(\frac{\delta H}{H} \right)^2 + \left(\frac{2\delta D}{A} \right)^2 + \left(\frac{\delta k}{k} \right)^2 + \dots \right]}, \quad (2.15)$$

where σ is the standard deviation, and δ is the absolute error for these variables.

2.4.2 Material properties

2.4.2.1 Viscosity

The viscosity of the gallium can be determined from the spin-up cases, in which the azimuthal velocity of the flow during a slight change ($< 10\%$) in rotation rate is measured by a chord Ultrasonic Doppler probe. The resulting velocity time series can then be compared to linear theory. The detailed operation and analysis are in E. King's thesis (King, 2009) and Aurnou *et al.* (2018).

However, if corrosion or crystallization occurs at the boundary, it will create some roughness on the boundaries, which can lead to a false estimation of the viscosity (Hawkins, 2020). The existence of boundary roughness can be easily found by doing several spin-up cases with different rotation rates. The general trend should follow the scaling law of the linear spin-up. Therefore, without boundary plating, it is generally a good practice to ensure that the

experiments can be finished within a short period (approximately a few months).

2.4.2.2 Thermal diffusivity

When the system is subcritical (pure conduction), the top lid thermistor will pick up oscillations around the set temperature (i.e., 35°C) from the lab chiller loop. This oscillation can be used to estimate the thermal diffusivity of the system through thermal skin depth measurement.

The solution of the 1D heat diffusion of conduction in \hat{z} ,

$$\frac{\partial T}{\partial t} = \kappa \frac{\partial^2 T}{\partial z^2} \quad (2.16)$$

is in the form of

$$T = T_0 + \delta T \exp\left(-z\sqrt{\frac{\omega}{2\kappa}}\right) \cos\left(\omega t - z\sqrt{\frac{\omega}{2\kappa}}\right), \quad (2.17)$$

where κ is the thermal diffusivity of the conductive material, T_0 is the initial temperature at $z = 0$, and $\omega = 2\pi f$ is the angular frequency of the applied temperature change at the boundary $z = 0$. Define the temperature fluctuations decrease to $1/e$ of the surface value at a skin depth d_ω :

$$z\sqrt{\frac{\omega}{2\kappa}} = 1, \quad z = d_\omega = \sqrt{\frac{2\kappa}{\omega}}. \quad (2.18)$$

Then the thermal diffusivity can be expressed in the thermal skin depth

$$\kappa = 0.5d_\omega^2\omega = \pi d_\omega f. \quad (2.19)$$

In experiments, the periodic signals from the chiller are picked up by the lid and internal thermistors for a subcritical case. The thermistors at different heights can then be used to interpolate/extrapolate the thermal skin depth based on the power of their FFTs. Finally, the thermal diffusivity of the fluid can be estimated using eq. (2.19). Additionally, the phase shifts between each height can also be used to find thermal diffusivity.

We have only tested eq. (2.19) once by Fourier transforming the chiller loop temperature fluctuation at the top lid and comparing several thermistors' spectral peaks. Figure 2.30

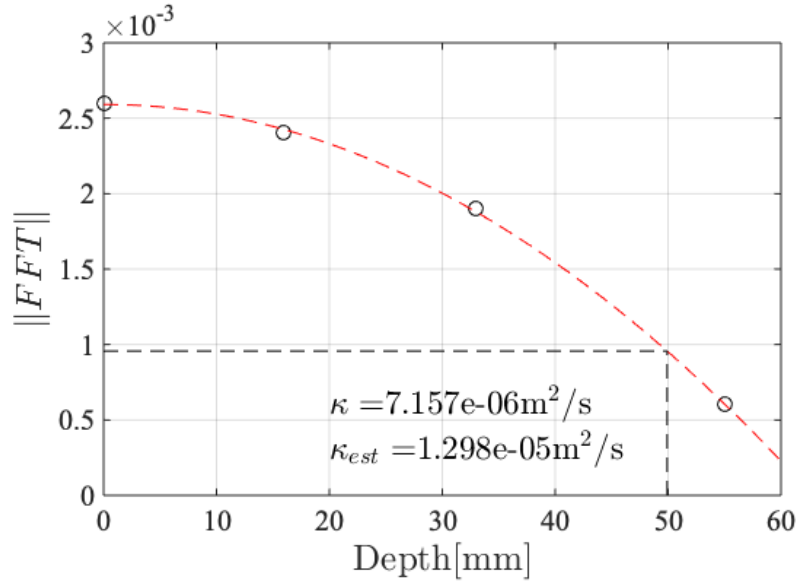


Figure 2.30: FFT power as a function of thermistor depths. The top lid temperature fluctuates with the lab chiller’s periodic control loop. The top lid and interior thermistors pick up the fluctuation, which gradually decreases its amplitude over depth. Black circles mark the peak frequencies of all the thermistors. The peaks are best fitted by a 2nd-order polynomial which is shown in a red dashed line. The horizontal and vertical black dashed lines mark the thermal skin depth of the top lid fluctuation, which has an FFT power $1/e$ of the top at zero depth. The resulting skin depth can be used to estimate the thermal diffusivity of the fluid, κ . In comparison, κ_{est} is the estimate based on the standard thermal conductivity of Gallium.

shows spectral powers of one top-lid thermistor and three internal thermistors at different depths but in proximity to each other in radius and azimuth. In this case, a total of 2.87 W was supplied to the system to compensate for the heat loss. The system was below convective onset and was measured overnight. The result shows a fluctuation frequency of $\omega \approx 0.0057 \text{ rad/s}$, and $d_\omega \approx 0.0499 \text{ m}$, then $\kappa = 7.157 \times 10^{-6} \text{ m}^2/\text{s}$. This value is 44.86% smaller than the estimated value based on the standard thermal conductivity value of gallium.

This test result seems sensible enough, however, requires further scrutiny and development in the future. Specifically, the thermistor at different heights should be in close proxim-

ity, even sharing the same sensor port. This is possible because there is a special thermistor holder that can house two thermistors at the same location. Moreover, the physical meaning of the 2nd-order best-fit curve remains unclear. Finally, a thorough error analysis of this method and finding a better-controlled conduction case would be ideal.

2.4.3 Thermometry calibration

The thermometry system is calibrated using an isothermal bath and an accurate reference thermistor. Thermistors such as Amphenols are not water-proof so should be handled with care. They can be bundled and sealed in a ziploc bag and put inside the isothermal bath along with the reference thermistor. It is common to use the reservoir of another smaller chiller in the lab as the isothermal bath.

The bath then changes to various set temperature measured by the reference thermistor. The other thermistor data are recorded and best fitted by the extended Steinhart-Hart equation:

$$\frac{1}{T} = A + B \ln R + C (\ln R)^2 + D (\ln R)^3, \quad (2.20)$$

where T is the measured temperature, R is the resistance measured by the DAQ. Constants A , B , C , and D are four coefficients from the calibration fitting.

2.4.4 Doppler velocimetry calibration

Before taking Doppler data, we carried calibration in water and did spin-up tests before and after the experiment. See E. King's thesis for detailed procedures ([King, 2009](#)).

2.4.5 Magnetometry calibration

Three calibration processes should be carried out before operation. The first step is the elimination of the background field. By placing the SENIS 3-axis magnetometer inside a Lakeshore zero-Gauss chamber, we can measure the initial offsets in each component.

Then the magnetometer should be placed onto the empty tank without any conducting fluids. We then rotate the tank with a slow but constant angular velocity. With no applied magnetic field, the magnetometer should pick up an oscillation in all three axes. These are the background magnetic field mostly from the Earth.

When a magnetic field is applied and the set current is I_{set} , each component of the net magnetic field can be fitted with a sinusoidal function of current and time,

$$B(I_{set}, t) = \alpha \sin \left[\frac{2\pi}{\beta} t + \frac{2\pi}{\gamma} \right] + D, \quad (2.21)$$

$$\alpha = m_{\alpha} I_{set} + b_{\alpha}, \quad (2.22)$$

$$D = m_D I_{set} + b_D. \quad (2.23)$$

where m_{α} , m_D , b_{α} , b_D , β , and γ are constants from the best fitting. The initial instrumental offset is b_D , which can be compared with the data measured in a zero-Gauss chamber. The background magnetic field has an amplitude of

$$B_{bg} = b_{\alpha} \sin \phi - b_D, \quad (2.24)$$

where $\phi = 2\pi t/\beta + 2\pi/\gamma$ is the phase angle of the rotation. The non-vertical components of the magnetic field from the solenoid or any misalignment of the probe will be shown in $m_{\alpha} I_{set} \sin \phi - b_D$. The leading order term should be the vertical component of $m_D I_{set}$, which measures the azimuthally averaged magnetic field generated from the solenoid (eq. (2.2)).

2.4.6 Rotation rate calibration

The rotation rate of the ROMAG device mainly depends on the set RPM value on the Servo motor (see A. Grannan’s thesis). However, it can also be affected by the weight of the fluid, the applied magnetic field, and even the condition of the belt. For this reason, it is highly recommended to measure the rotation rate using magnetometry before each experiment with a different rotation rate. A dedicated Matlab program called “rotationrate.m” can be found in the data analysis folder in ROMAG’s Google Drive and also on ROMAG’s Github.

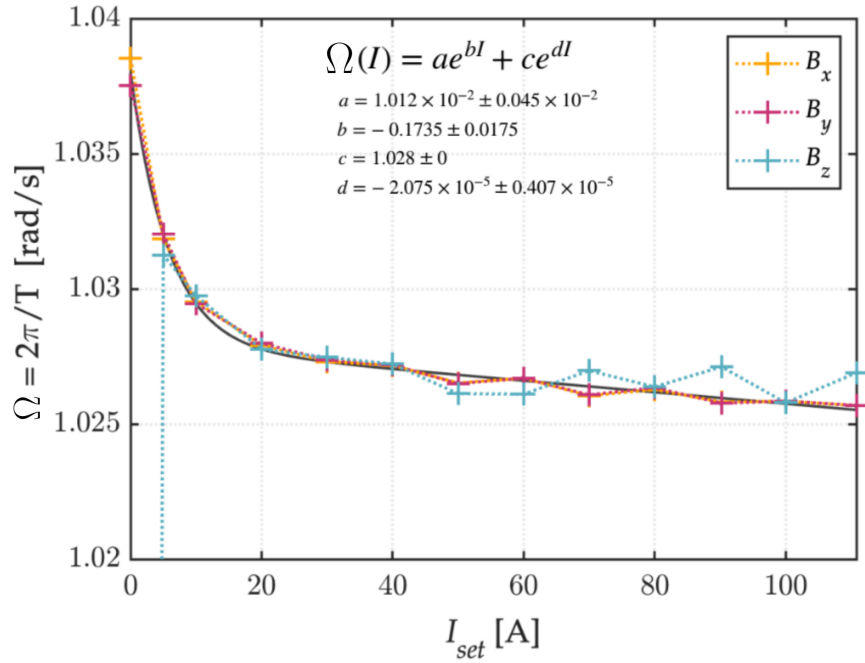


Figure 2.31: Rotation rate (Ω) of the device slightly varies exponentially with magnet power supply output current (I_{set}). Figure made in collaboration with by Jewel Abbate.

For instance, fig. 2.31 shows a weak magnetic field effect on rotation rate. There is an exponential dependence of the rotation rate for the different applied magnetic fields under the same Servo motor RPM setting. Since the output current of the magnet power supply is more accurate than the magnetic field measurements in this calibration, the rotation rate is plotted as a function of the output current. With a larger current and larger magnetic field strength, the rotation rate exponentially decays by 1% of its original angular speed.

2.5 A catalog of RoMag’s Standard Operating Procedures (SOPs) and manuals

The following list includes all the essential SOPs and manuals for safely operating the ROMAG device and its components. All the Standard Operating Procedures (SOPs) and manuals can be found on the lab’s shared google drive and physically inside the file cabinet of

the lab foyer. Going through these SOPs and manuals before operating the ROMAG device is highly recommended.

SOPs:

1. *Remote access to ROMAG's computers*
2. *Raising and lowering the magnet using Duff-Norton control box*
3. *Instruction for operating ROMAG's sleep mode*
4. *Holiday Emergency Heating System (HEHS)*
5. *Gallium cleaning*
6. *Replacing heat pad using mini-jacks*
7. *Legacy SOPs*
8. *Chapter 2 of E. King's thesis*
9. *Chapter 7 of A. Grannan's thesis*

The electronic address for these SOPs are located on the Spinlab shared Google drive → “RoMag” → “SOPs”.

Hard copy manuals can be found in the foyer file cabinet and a RoMag manual folder on the bookshelf:

1. *Rooftop Chiller*
2. *Lab Chiller*
3. *Argantix*
4. *Magna-Power*
5. *Dopplers*

6. *Omega Box*

7. *Kollmorgen Servo-Drive motor*

8. *Rotary Union*

9. *Slip Ring*

The electronic address for these manuals are located on the Spinlab shared Google drive → “RoMag” → “RoMag Manuals”.

All the data analysis tools for thermometry, Doppler velocimetry, magnetometry, and SOPs have been uploaded to ROMAG’s Github:

<https://github.com/RoMagSpinlab>.

2.6 Open issues and future upgrades

2.6.1 Open issues

Here I list a few open issues on the current ROMAG setup, ranked by priority.

- A flow switch relay needs to be installed for the Magna-Power power supply. This is a safety measure against overheating the magnetic solenoid. Lab frame temperature monitoring sensors should be installed on the solenoid cooling loop and its exterior.
- A more elegant solution is needed for the expansion tank heater, which has unstable heating power during the experiments. A new thermostated heating tape has been purchased. It could be used in parallel with the HEHS system.
- The plumbing system near the bottom rotary union region has leaks and should be fixed. The filtering system of the plumbing line should be reinstalled, and the leaking should be fixed.

- The top/bottom copper boundaries are subject to gallium corrosion and perhaps should be Silver-plated (via private communication with researchers at PPPL). Silver has similar thermal and electrical properties to copper and robustness as a plating material.
- A metal heater with resistance wires should be built to replace the commercial silicon heat pads, which have limited power output and tend to burn out after a long period of high-power experiments. A metal heater with resistance wire that could potentially utilize full range of the Argantix power supply (up to ~ 5 kW) would be ideal. I have made a few designs uploaded in the shared Google Drive.
- The temperature and flow rate at the inlet and outlet on the heat exchangers should be measured to better estimate the isothermality of the top thermal boundary.

2.6.2 Future upgrades

Here I list a few future upgrades that could improve the performance of the current ROMAG setup.

- Remote control of the magnet power supply should be implemented. See Magna-Power power supply's manual for instructions.
- DAQ using LabView can be clumsy sometimes. A new Python version of the DAQ program that can integrate all the transducers on ROMAG would be ideal.
- The monitoring system and alarm system can be transformed into apps on mobile device platforms to provide real-time conditions of the experiments.
- Auto-filling function of the lab chiller can be reinstalled.
- Manufacture a new 80-cm tank with radial fins to suppress wall modes (Terrien *et al.*, 2023). The design is shown in fig. 2.32.
- We can purchase a new DOP box with more sensor capacity.

- We should purchase new and more magnetometers for multi-point magnetic field measurements. They need to be calibrated to compensate for temperature fluctuations during the experiments. Find magnetometers with better accuracy.
- To use magnetometry for fluid bulk's induced fields, we need to customize probe holders for the hall probe.
- The aerogel is dusty and hard to deal with. It will be nice to find better insulation blankets materials and make them custom-fit to all the devices.
- We need an elegant solution for switching the polarity of the large current lines for the magnet.

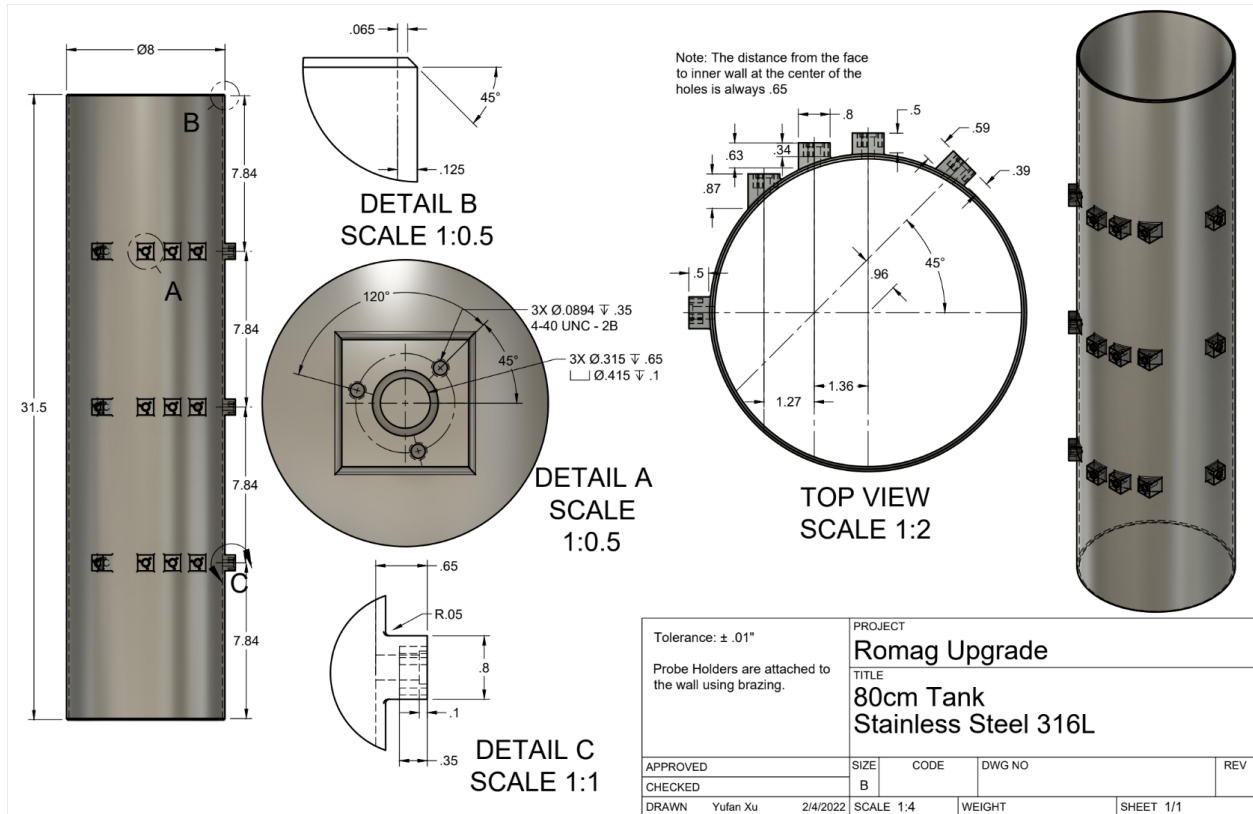


Figure 2.32: 80-cm tank design drawing. This design can house up to 15 Doppler transducers on the sidewall. This design includes a mid-plane array to better characterize any large-scale structures. With improved rectangular sensor ports, it is easier to braze onto the sidewall instead of welding and thus will greatly improve the tolerance on the angle orientations. This design can measure up to five points with two-dimensional components in the horizontal planes at each of three vertical heights and up to a total of nine points with three-dimensional components measurement. In addition, radial fins are shown to suppress wall modes in recent numerical study (Terrien *et al.*, 2023). Since we are interested in the interior flow of the planet, it might be helpful to add a radial rim on the inner wall to eliminate wall modes and their influences on the bulk.

CHAPTER 3

The Transition from Wall Mode to Multimodal Magnetoconvection in Liquid Gallium

“Walls don’t fall without effort.”

— Neal Shusterman, *Bruiser*

Reproduced from: **Xu, Y.**, Horn, S., & Aurnou, J. (2023). The Transition from Wall Mode to Multimodal Magnetoconvection in Liquid Gallium, *Physics Review Fluids*. In review.

Magnetoconvection is one end-member system of the rotating magnetoconvection that describes the core dynamics and the underlying physics for many astrophysical and engineering systems. In answering the first research question in section 1.4, I investigate behaviors of liquid metal magnetoconvection using coupled laboratory-numerical experiments from onset to supercriticality. With increasing supercriticality, the experimental and numerical data reveal transitions between wall modes and from wall-dominated convection to wall-interior multimodality. I correlate transient heat transfer behaviors to dynamic wall modes developed in cylindrical geometry. Combined with previous studies, this study connects onset to supercritical turbulent behaviors in liquid metal magnetoconvection over a large parameter space. The gross heat transfer behaviors between magnetoconvection and rotating convection in liquid metals are compared and discussed. Investigation of the liquid metal magnetoconvection lays the groundwork for studying more complicated systems, including MHD effects at the planetary boundary and rotating magnetoconvection.

3.1 Introduction

Convection influenced by ambient magnetic fields is called magnetoconvection (MC), which arises in many areas of fluid dynamics. In geophysics and planetary physics, motions of turbulent convective flows in planetary liquid metal outer cores generate planetary-scale magnetic fields via dynamo processes. Studying the effects of magnetic fields in MC is essential to understand these processes (e.g., Jones, 2011; Roberts & King, 2013; Aurnou & King, 2017; Moffatt & Dormy, 2019a). In astrophysics, MC is associated with the sunspot umbra on the outer layer of the Sun and other stars (e.g., Proctor & Weiss, 1982; Schüssler & Vögler, 2006; Rempel *et al.*, 2009). Furthermore, MC has an essential role in numerous industrial and engineering applications including but not limited to liquid metal batteries (Kelley & Weier, 2018; Cheng *et al.*, 2022a), crystal growth (Moreau, 1999; Rudolph, 2008), nuclear fusion liquid-metal cooling blanket designs (Barleon *et al.*, 1991; Abdou *et al.*, 2001; Salavy *et al.*, 2007), and induction heating and casting (Taberlet & Fautrelle, 1985; Davidson, 1999). These systems have drastically different ratios between electromagnetic and inertial forces. Therefore, it is crucial to investigate the effects of a wide range of magnetic forces in MC systems.

The canonical model of MC is a convection system with an electrically-conducting fluid layer heated from below, cooled from above, and in the presence of an external vertical magnetic field Chandrasekhar (1961); Yan *et al.* (2019). It is most fundamentally understood in an extended plane layer geometry (e.g., Chandrasekhar, 1961; Nakagawa, 1955; Yan *et al.*, 2019). But there is an increasing interest in MC systems with defined sidewall boundaries because of their many experimental and industrial applications. Various numerical and laboratory studies have been carried out in rectangular (Schüssler & Vögler, 2006; Liu *et al.*, 2018) and cylindrical geometries (Cioni *et al.*, 2000a; Akhmedagaev *et al.*, 2020; Zürner *et al.*, 2019, 2020).

In weakly supercritical, near-onset regimes, MC systems tend to develop steady wall

modes in the sidewall Shercliff boundary layer (Houchens *et al.*, 2002; Busse, 2008; Liu *et al.*, 2018; Zürner *et al.*, 2020; Akhmedagaev *et al.*, 2020) while the bulk remains quiescent. As the magnetoconvective supercriticality increases, convective flows self-organise into multi-cellular bulk flow structures (Yan *et al.*, 2019; Zürner *et al.*, 2020). Eventually, at very large supercriticalities, the buoyancy forces dominate and magnetic field effects become subdominant. Large-scale circulations (LSCs) then form and the heat and momentum transfer asymptote to that of turbulent RBC (e.g. Lim *et al.*, 2019; Zürner *et al.*, 2020; Xu *et al.*, 2022; Grannan *et al.*, 2022).

The pathway from the onset of convection to fully developed turbulence in liquid metal MC is not well characterised. To address this deficit, we present a suite of laboratory-numerical coupled MC experiments in liquid gallium to investigate how MC transitions from near-onset wall modes to turbulent multimodality in cylindrical cells. The paper is organised as follows. Section 3.2 introduces control parameters, and reviews established onset predictions for the magnetoconvection system. Section 3.3 presents our experimental setup, numerical schemes, diagnostics, and the physical properties of liquid gallium. Section 3.4 compares different theoretical onsets and observations of the transition to multimodality in a survey with fixed magnetic field strength and varying convective vigor. Section 3.5 shows heat transfer results combining previous studies of MC and compares the gross heat transfer behaviors between liquid metal magnetoconvection and liquid metal rotating convection systems.

3.2 Control parameters and linear prediction

Laboratory-scale liquid metal magnetoconvection usually has a negligible induced magnetic field \mathbf{b} with respect to the external applied magnetic field \mathbf{B}_0 , so that $|\mathbf{b}| \ll |\mathbf{B}_0|$. Moreover, any induced field is considered temporally invariant, $\partial_t \mathbf{b} \approx 0$. The magnetic Reynolds number, defined as $Rm = UH/\eta$ (Julien *et al.*, 1996; Glazier *et al.*, 1999; Davidson, 2016;

(Akhmedagaev *et al.*, 2020), is well below unity, where U and H are the characteristic velocity and length scales, respectively, and η is the magnetic diffusivity. This parameter represents the ratio between induction and diffusion of the magnetic field. Thus, the so-called low- Rm quasistatic approximation is valid in most liquid metal experimental and industrial applications (Sarris *et al.*, 2006; Knaepen & Moreau, 2008; Davidson, 2016; Cioni *et al.*, 2000a). In the quasistatic limit, Rm and magnetic Prandtl number Pm formally drop out of the problem, so it is not necessary to solve the magnetic induction equation explicitly, and the system is greatly simplified. In addition, the Oberbeck-Boussinesq approximation is commonly applied in the governing equations for liquid metal MC systems (e.g. Cioni *et al.*, 2000a; Liu *et al.*, 2018; Vogt *et al.*, 2018a; Yan *et al.*, 2019; Xu *et al.*, 2022).

Four nondimensional control parameters govern quasistatic Oberbeck-Boussinesq magnetoconvection (Liu *et al.*, 2018; Yan *et al.*, 2019; Xu *et al.*, 2022). The Prandtl number Pr describes the thermo-mechanical properties of the fluid,

$$Pr = \frac{\nu}{\kappa}, \quad (3.1)$$

where ν is the kinematic viscosity and κ is the thermal diffusivity. In this study, $Pr \approx 0.027$ for liquid gallium. The Rayleigh number Ra characterises the buoyancy forcing with respect to thermo-viscous diffusion and is defined as

$$Ra = \frac{\alpha g \Delta T H^3}{\kappa \nu}. \quad (3.2)$$

Here, α is the thermal expansion coefficient, g is the magnitude of the vertically oriented ($\hat{\mathbf{e}}_z$) gravitational acceleration, ΔT is the bottom-to-top vertical temperature difference across the fluid layer, and the characteristic length scale is the layer height H . The Chandrasekhar number Ch denotes the ratio of quasistatic Lorentz forces and viscous forces,

$$Ch = \frac{\sigma B_0^2 H^2}{\rho_0 \nu}, \quad (3.3)$$

where σ is the electric conductivity of the fluid, B_0 is the magnitude of the applied vertical magnetic field, and ρ_0 is the mean density of the fluid. The Chandrasekhar number is the

square of the Hartmann number, $Ch = Ha^2$ (e.g. Davidson, 2016; Moreau, 1999; Roberts, 1967). Additionally, the cylindrical container has a diameter-to-height aspect ratio

$$\Gamma = \frac{D}{H}, \quad (3.4)$$

where D is the diameter of the container. Here, Γ is fixed to 1.0 and 2.0, respectively.

The onset of convection is controlled by the critical Rayleigh denoted as Ra_{crit} , which characterises the buoyancy forcing needed for a particular convective mode in the system (Plumley & Julien, 2019). Figure 3.1 shows different Ra_{crit} predictions. Linear analysis has shown that the convection driven by buoyancy forces must balance the viscous and Joule dissipation (Chandrasekhar, 1961). Thus, in general, the magnetic field inhibits the onset of the convection. Chandrasekhar (1961) derived the onset for the bulk stationary magnetoconvection in an infinite plane layer (∞). With free-slip (FS) boundaries on both ends, the dispersion relation expresses the marginal Rayleigh number Ra_M as,

$$Ra_M = \frac{\pi^2 + a^2}{a^2} \left[(\pi^2 + a^2)^2 + \pi^2 Ch \right], \quad (3.5)$$

where a is the characteristic cell aspect ratio (Davidson, 2016), defined as $a \equiv \pi H/L$, where H is the height of the fluid layer, and $2L$ is the horizontal wavelength of the convection flow, assuming the form of two-dimensional rolls with each roll having diameter L . By minimizing equation (3.5), setting $\partial Ra/\partial a = 0$, we obtain the critical Rayleigh number for the bulk stationary magnetoconvection in an infinite layer with free-slip boundaries on both ends, Ra_{FS}^∞ , and its critical mode number a_{FS} . In the limit of $Ch \rightarrow \infty$, we have $Ra_{FS}^\infty \rightarrow \pi^2 Ch$, and $a_{FS} \rightarrow (\pi^4 Ch/2)^{1/6}$ (Chandrasekhar, 1961; Davidson, 2016).

Magnetoconvection with no-slip (NS) rigid horizontal boundaries has a dispersion relation (Chandrasekhar, 1952)

$$Ra_M = \frac{(\pi^2 + a^2) \left[(\pi^2 + a^2)^2 + \pi^2 Ch \right]}{a^2 \left[1 - 4\pi^2 \delta (q_1^2 - q_2^2) / (\pi^2 + q_1^2) (\pi^2 + q_2^2) \right]} \quad (3.6)$$

where

$$q_1 = \frac{1}{2} \left(\sqrt{Ch + 4a^2} + \sqrt{Ch} \right), \quad q_2 = \frac{1}{2} \left(\sqrt{Ch + 4a^2} - \sqrt{Ch} \right), \quad (3.7)$$

and

$$\delta = (q_1 \tanh(q_1/2) - q_2 \tanh(q_2/2))^{-1}. \quad (3.8)$$

By assuming a single structure in the vertical direction and minimizing Ra in (3.6), we obtain the first approximation of critical Ra of magnetoconvection with two rigid boundaries Chandrasekhar (1952). Equation (3.6) also predicts that $Ra_{NS}^\infty \rightarrow \pi^2 Ch$ and $a_{NS} \rightarrow (\pi^4 Ch/2)^{1/6}$ with $Ch \rightarrow \infty$. Thus, both critical Rayleigh numbers with free-slip boundaries Ra_{FS}^∞ and no-slip boundaries Ra_{NS}^∞ asymptote to $\pi^2 Ch$ above $Ch \gtrsim 10^4$, as shown in figure 3.1a). These asymptotic bulk onset predictions agree with previous experimental results (Nakagawa, 1955; Cioni *et al.*, 2000a; Yan *et al.*, 2019; Zürner *et al.*, 2020).

Busse (2008) theoretically analysed the side wall modes in MC and derived an asymptotic solution along a straight vertical sidewall in a semi-infinite domain with free-slip top-bottom boundaries. The critical Rayleigh number Ra_W for these so-called magnetowall modes is,

$$Ra_W = 3\pi^2 \sqrt{3\pi/2} \left(1 + 3Ch^{-1/4} \sqrt{3\pi/2}\right) Ch^{3/4}. \quad (3.9)$$

The asymptotic onset of the wall modes is generally lower than the onset in the bulk fluid at large Ch , since $Ch^{3/4} \ll Ch$ as $Ch \rightarrow \infty$. These magnetowall modes are non-drifting and extend into the fluid bulk with a distance that scales as the magnetic boundary layer thickness, which scales with the Shercliff boundary layer thickness $\delta_{Sh} \sim Ch^{-1/4}$ (Shercliff, 1953; Liu *et al.*, 2018). The stationary wall modes of MC differ from those found in rotating convection, where wall modes drift in azimuth (Ecke *et al.*, 1992; Herrmann & Busse, 1993; Horn & Schmid, 2017).

Houchens *et al.* (2002) performed a hybrid linear stability analysis combining the analytical solution for the $\delta_{Ha} \sim Ch^{-1/2}$ Hartmann layers (Hartmann & Lazarus, 1937) at top-bottom boundaries and numerical solutions for the rest of the domain in $\Gamma = 1$ and 2 cylindrical geometries. They also presented a linear asymptotic analysis for large Ch . Their asymptotic solutions for critical Ra for $\Gamma = 1$ and 2 are, respectively,

$$Ra_{cyl,\Gamma=1} = 8.302Ch^{3/4}; \quad Ra_{cyl,\Gamma=2} = 67.748Ch^{3/4}. \quad (3.10)$$

Figure 3.1 summarises all the critical Rayleigh predictions mentioned above. Houchens *et al.* (2002)’s $Ra_{cyl, \Gamma=1}$ values (marked by the purple dashed line) are approximately an order of magnitude lower than the rest of the onset predictions that are not aspect-ratio dependent. To test the validity of these predictions, we combine laboratory experiments and direct numerical simulations (DNS) to investigate the five different Ch shown by the vertical dashed lines in figure 3.1b). The values of these five Ch numbers and their corresponding critical Ra are summarised in table 3.1.

Ch	Ra_{FS}^{∞}	Ra_{NS}^{∞}	Ra_W	$Ra_{cyl, \Gamma=1}$	$Ra_{cyl, \Gamma=2}$
1×10^4	1.20×10^5	1.25×10^5	1.06×10^5	8.30×10^3	6.77×10^4
4×10^4	4.46×10^5	4.54×10^5	2.66×10^5	2.35×10^4	1.92×10^5
1×10^5	1.08×10^6	1.09×10^6	4.94×10^5	4.67×10^4	3.81×10^5
3×10^5	3.15×10^6	3.17×10^6	1.05×10^6	1.06×10^5	8.68×10^5
1×10^6	1.03×10^7	1.03×10^7	2.45×10^6	2.63×10^5	2.14×10^6

Table 3.1: Values of different predicted critical Ra at $Ch = \{10^4, 4 \times 10^4, 10^5, 3 \times 10^5, 10^6\}$, which have been examined experimentally.

3.3 Methods

Our experiments are conducted using UCLA’s ROMAGdevice King *et al.* (2012a); Cheng *et al.* (2015); Vogt *et al.* (2018a); Grannan *et al.* (2022); Xu *et al.* (2022). Figure 3.2a) - c) show schematics of the diagnostics and the apparatus. The container consists of two copper end blocks and a stainless steel sidewall. Two sets of sidewalls, $\Gamma = 1.0$ and 2.0 , have been used in this study to investigate MC heat transfer from $10^5 \lesssim Ra \lesssim 10^8$. An external solenoid generates a steady vertical magnetic field, $0 < |\mathbf{B}_0| < 800$ Gauss, with a vertical

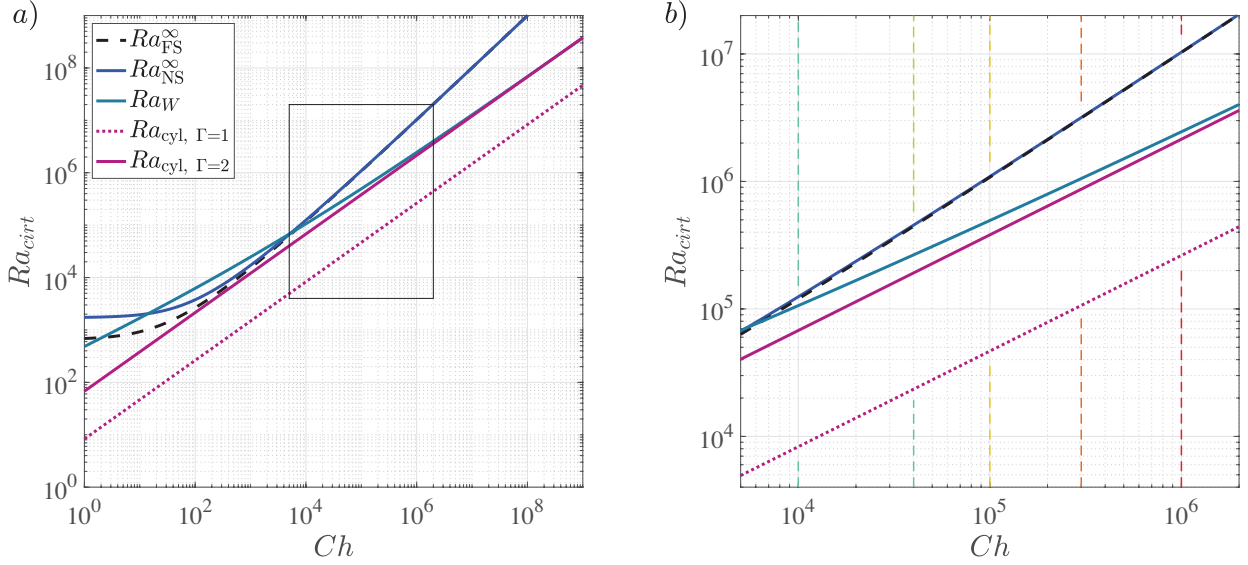



Figure 3.1: a) Different prediction of critical Rayleigh number (Ra_{crit}) as a function of the Chandrasekhar number. The black dashed curve shows the Ra_{crit} . For infinite plane MC system with free-slip boundaries at the top and bottom, $Ra_{crit} = Ra_{FS}^{\infty}$ (Chandrasekhar, 1961), as shown in the black dashed curve; for infinite plane MC system with no-slip boundaries, $Ra_{crit} = Ra_{NS}^{\infty}$ (Chandrasekhar, 1952), as shown in the blue curve. Note that both Ra_{FS}^{∞} and Ra_{NS}^{∞} asymptote to $\pi^2 Ch$ as $Ch \rightarrow \infty$; the grayish-blue curve shows that Ra_W is the asymptotic Ra_{crit} for the wall-mode onset in a half-infinite plane with a vertical boundary Busse (2008); the purple curve and the purple dotted curve are Houchens *et al.* (2002)'s predicted Ra_{crit} , namely $Ra_{cyl, \Gamma=2}$ and $Ra_{cyl, \Gamma=1}$, for MC in cylindrical containers with aspect ratio 1 and 2, respectively. b) The zoom-in view of the region circumscribed by the black rectangular box in panel a). The colored vertical dashed lines correspond to five Ch numbers employed in our study.

component that varies within $\pm 0.5\%$ over the field volume (King & Aurnou, 2015). The tank is placed at the center of the solenoid’s bore. A non-inductively wound electrical resistance pad heats the bottom of the lower copper end block at a constant rate, $0 < P \lesssim 2000\text{W}$, and a thermostated water-cooled heat exchanger maintains a constant temperature at the top of the upper copper end block. This setup can reach up to $Ra \approx 10^9$ and $Ch = 3 \times 10^5$ in the $\Gamma = 1.0$ tank.

Twelve thermistors in total are placed inside the top and bottom boundaries about 28.9 mm radially inwards from the sidewall, as shown in figure 3.2a). These end-block thermistors are used to measure the heat transfer efficiency of the system, characterised by the Nusselt number,

$$Nu = \frac{qH}{\lambda\Delta T}, \quad (3.11)$$

where $q = 4P/(\pi D^2)$ is the heat flux, P is the heating power, and $\lambda = 31.4 \text{ W}/(\text{m} \cdot \text{K})$ is the thermal conductivity of gallium Aurnou *et al.* (2018). The Nusselt number describes the total to conductive heat transfer ratio across the fluid layer, and $Nu = 1$ corresponds to the conductive state. The vertical temperature difference across the fluid layer, ΔT , is indirectly controlled by the constant basal heat flux. Six thermistors are attached to the sidewall midplane to detect wall modes and any thermal imprints of the bulk fluid structures at the sidewall.

We have also conducted direct numerical simulations (DNS) using the finite volume code GOLDFISH  (Horn & Shishkina, 2015; Shishkina *et al.*, 2015; Shishkina & Horn, 2016; Horn & Schmid, 2017; Horn & Aurnou, 2018, 2019, 2021). The nondimensional equations governing quasi-static, Oberbeck-Boussinesq (Oberbeck, 1879; Boussinesq, 1903) magneto-

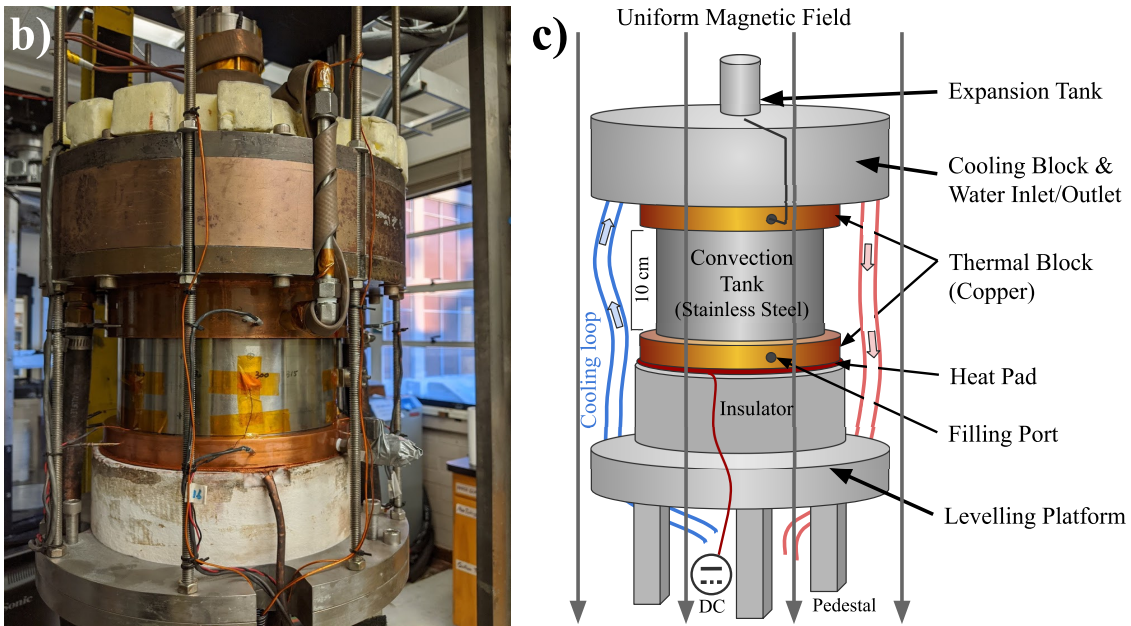
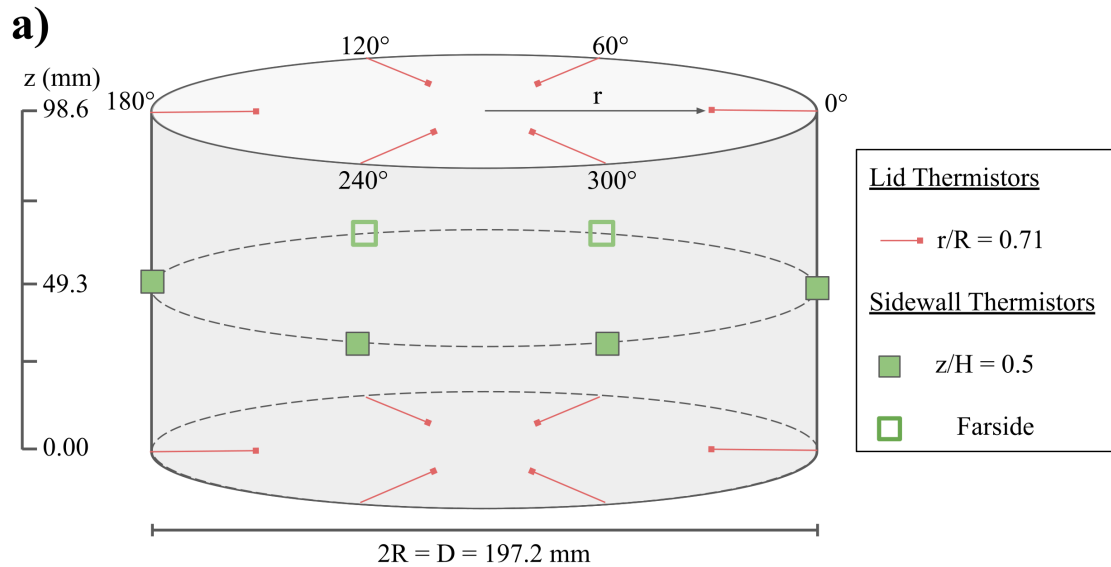


Figure 3.2: : there are six thermistors in the top lid at $0.71R$, six thermistors at the midplane sidewall, and six thermistors in the bottom lid at $0.71R$. These thermistors at different heights align with each other azimuthally. The thermometry is in a similar layout on the aspect ratio one tank ($\Gamma = 1.0$). b) Photo of the convection cell of the ROMAGdevice. c) Schematics of the convection cell of the ROMAGdevice. For further device details, see [Xu *et al.* \(2022\)](#).

convection are:

$$\nabla \cdot \tilde{\mathbf{u}} = 0, \quad (3.12)$$

$$D_t \tilde{\mathbf{u}} = -\nabla \tilde{p} + \sqrt{\frac{Pr}{Ra}} \nabla^2 \tilde{\mathbf{u}} + \sqrt{\frac{Pr}{Ra Ek^2}} \tilde{\mathbf{u}} \times \hat{\mathbf{e}}_z + \sqrt{\frac{Ch^2 Pr}{Ra}} \tilde{\mathbf{j}} \times \hat{\mathbf{e}}_z + \tilde{T} \hat{\mathbf{e}}_z, \quad (3.13)$$

$$D_t \tilde{T} = \sqrt{\frac{1}{Ra Pr}} \nabla^2 \tilde{T}, \quad (3.14)$$

$$\left. \begin{aligned} \nabla \cdot \tilde{\mathbf{j}} &= 0 \\ \tilde{\mathbf{j}} &= -\nabla \tilde{\Phi} + (\tilde{\mathbf{u}} \times \hat{\mathbf{e}}_z) \end{aligned} \right\} \nabla^2 \tilde{\Phi} = \nabla \cdot (\tilde{\mathbf{u}} \times \hat{\mathbf{e}}_z), \quad (3.15)$$

where $\tilde{\mathbf{u}}$ denotes nondimensional velocity, \tilde{T} the temperature, \tilde{p} the pressure, $\tilde{\mathbf{j}}$ the current density, and $\tilde{\Phi}$ the electrostatic potential. The scales used for the nondimensionalisation are the free-fall speed $U_{ff} = \sqrt{\alpha g \Delta T H}$ (Aurnou *et al.*, 2020), the temperature difference between top and bottom ΔT , the reference pressure $\rho_0 U_{ff}^2$, the reference current density $\sigma B_0 U_{ff}$ and the reference potential $B_0 H U_{ff}$.

Our non-linear DNS solves these equations in a cylindrical domain (r, ϕ, z) with $\Gamma = 2.0$. The sidewall is assumed to be perfectly thermally insulating, $\partial_r T|_{r=R} = 0$, and the top and bottom plates are isothermal with $T_t = -0.5$ and $T_b = 0.5$, respectively. All boundaries are assumed to be impermeable and no-slip, $\mathbf{u}|_{\text{wall}} = 0$, and electrically insulating, $\mathbf{j}|_{\text{wall}} = 0$, i.e. the current forms closed loops inside the domain. The DNS control parameters are set to $Pr = 0.027$, $Ch = 4.0 \times 10^4$, and $Ra = \{1.5 \times 10^5, 2.0 \times 10^5, 3.0 \times 10^5, 4.0 \times 10^5, 7.0 \times 10^5, 1.0 \times 10^6, 1.5 \times 10^6, 4.0 \times 10^6\}$. The numerical mesh resolution is $N_r \times N_\phi \times N_z = 240 \times 256 \times 240$. This choice of mesh was verified by running simulations at twice the resolution for the highest Ra for a shorter time, indicating the grid independence of the solution.

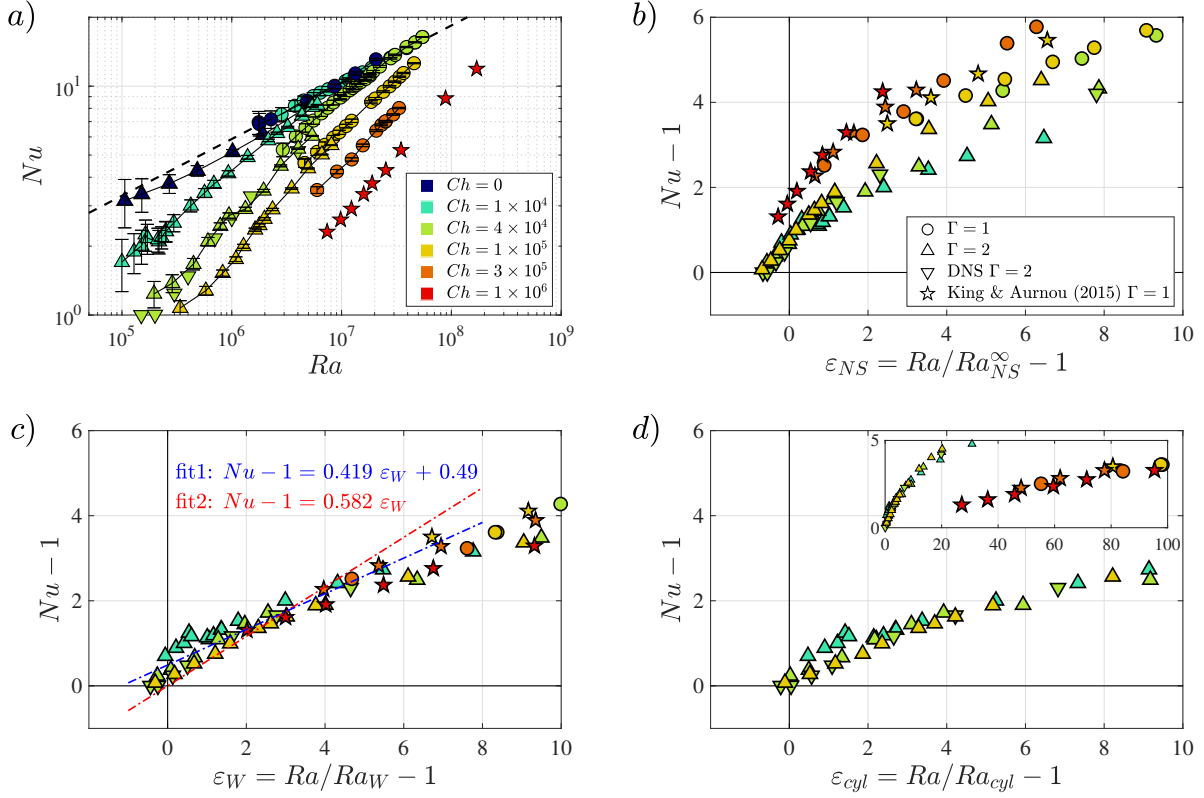


Figure 3.3: a) $Nu - Ra$ survey with various Ch from current study and one set of $Ch = 10^6$ data by King & Aurnou (2015). Different colors correspond to different Ch values. Different shapes correspond to different aspect ratios and sets of experiments, marked in the legend of panel b). Error bars are shown on the experimental data from the current study. The dashed line is the heat transfer scaling acquired from non-magnetic Rayleigh-Bénard convection data in the $\Gamma = 1.0$ tank, marked by dark blue circles. See equation (3.18a). Panel b)-d) show ratios of convective heat transfer to conduction ($Nu - 1$) versus the reduced bifurcation parameter (Zhong *et al.*, 1993; Horn & Schmid, 2017) using three different predicted critical Rayleigh numbers: b) infinite-plane stress-free critical Ra defined in Chandrasekhar (1961); c) magnetowall mode critical Ra by Busse (2008). d) Houchens *et al.* (2002)'s critical Ra for magnetowall modes in two different aspect ratios, $\Gamma = 1$ and 2. The linear fit in panel c) uses data close to onset at $\varepsilon_W \leq 5$. The $\Gamma = 1.0$ data in panel d) are shown in the smaller subplot, which only appears at $\varepsilon \gtrsim 25$.

3.4 Results

3.4.1 Comparing onset predictions

The validity and accuracy of the onset predictions discussed in Section 3.2 are tested here using both laboratory and DNS data at $10^5 \lesssim Ra \lesssim 10^8$, $0 \lesssim Ch \lesssim 3 \times 10^5$, and in $\Gamma = 1.0$ and 2.0 cylindrical cells.

Figure 3.3a) shows measurements of heat transfer efficiency, Nu , as a function of the buoyancy forcing Ra . (All the detailed measurement data are provided in the tables in the Appendix). Vertical error bars based on heat loss and accuracy of the thermometry, are shown in the lab data from this study. We also include King & Aurnou (2015)'s $Ch = 10^6$ data (red stars) made in the same $\Gamma = 1.0$ experimental setup used in this study. Figure 3.3b) - d) show convective heat transfer data ($Nu - 1$) as a function of supercriticality of the convection, as described by the reduced bifurcation parameter $\varepsilon = (Ra - Ra_{crit})/Ra_{crit}$, following the convention of (Ecke *et al.*, 1992; Zhong *et al.*, 1993; Horn & Schmid, 2017). Three different Ra_{crit} are examined in panel b) to d): for convection in an infinite plane layer with two rigid boundaries, Ra_{NS}^∞ (3.6), wall-attached convection, Ra_W^∞ (3.9), and convection in a cylinder with aspect ratio 1 and 2, Ra_{cyl} (3.10). If the Ra_{crit} prediction is accurate, the onset of convection occurs at $\varepsilon = 0$, and Nu and follows an approximate linear scaling for sufficiently small ε .

Figure 3.3b) presents the convective heat transfer data, $Nu - 1$, as a function of the reduced bifurcation parameter $\varepsilon_{NS} = (Ra - Ra_{NS}^\infty)/Ra_{NS}^\infty$ calculated using eq. (3.6). The laboratory-numerical $Nu - 1$ data exceeds 0 at $\varepsilon_{NS} < 0$. This implies that the Ra_{NS}^∞ predictions do not capture the onset of MC in our system. Moreover, the increased scatter and variation in Nu for different Ch as ε_{NS} increases suggest a low correlation between the data and the expected linear ε_{NS} scaling. As the infinite-plane Ra_{crit} is associated with the bulk onset of convection, our heat transfer data implies that the MC flow does not initiate in the fluid bulk.

Figure 3.3c) tests Busse (2008)’s asymptotic onset predictions for magnetowall modes as a function of $\varepsilon_W = (Ra - Ra_W)/Ra_W$ calculated using (3.9). The nonzero $Nu - 1$ data start approximately at the origin of the graph, being only slightly below $\varepsilon_W = 0$ and show a good data collapse up to moderately high supercriticalities of $\varepsilon \lesssim 10$. Thus, our data provide evidence that in our system the onset of convection occurs in the form of wall-attached modes. This is further quantified by two different linear least-square fits for the nonzero $Nu - 1$ data for $\varepsilon_W \leq 5$. The first fit ‘fit1’ (blue line) makes no assumptions on the onset and yields $Nu - 1 = 0.419 \varepsilon_W + 0.490$. The second ‘fit2’ (red line) is forced to pass through the origin, i.e. it assumes the onset prediction $\varepsilon_W = (Ra - Ra_W)/Ra_W$ is exact and yields $Nu - 1 = 0.582 \varepsilon_W$. Thus, in agreement with the theoretical predictions and as also found by Zürner *et al.* (2020), our MC onset data is consistent with the wall mode predictions. Furthermore, both linear fits hold well up to $\varepsilon_W \lesssim 10$, suggesting that the dynamics and the heat transfer in our system are largely controlled by linear magnetowall modes within this supercriticality range (cf. Ecke *et al.*, 1992; Zhong *et al.*, 1993; Horn & Schmid, 2017; Lu *et al.*, 2021).

Figure 3.3d) tests the hybrid theoretical-numerical predictions of Houchens *et al.* (2002) for magnetowall modes in cylindrical geometries by plotting $Nu - 1$ versus $\varepsilon_{cyl} = (Ra - Ra_{cyl})/Ra_{cyl}$ calculated using (3.10). The underlying assumptions for these predictions best match the experimental and numerical setup. Therefore, they should best capture the measured onset of convection. The $\Gamma = 2.0$ data (green and yellow hues) show an excellent agreement with theory. The $\Gamma = 1.0$ data (inset, red and orange hues) does not have a low enough supercriticality ($\varepsilon_{cyl} > 28$) to reliably test the exact Ra_{cyl} value. Thus, we are currently unable to disambiguate which magnetowall mode onset predictions are more accurate, even though Houchens *et al.* (2002)’s $\Gamma = 1.0$ predictions differ from Busse (2008)’s by nearly an order of magnitude.

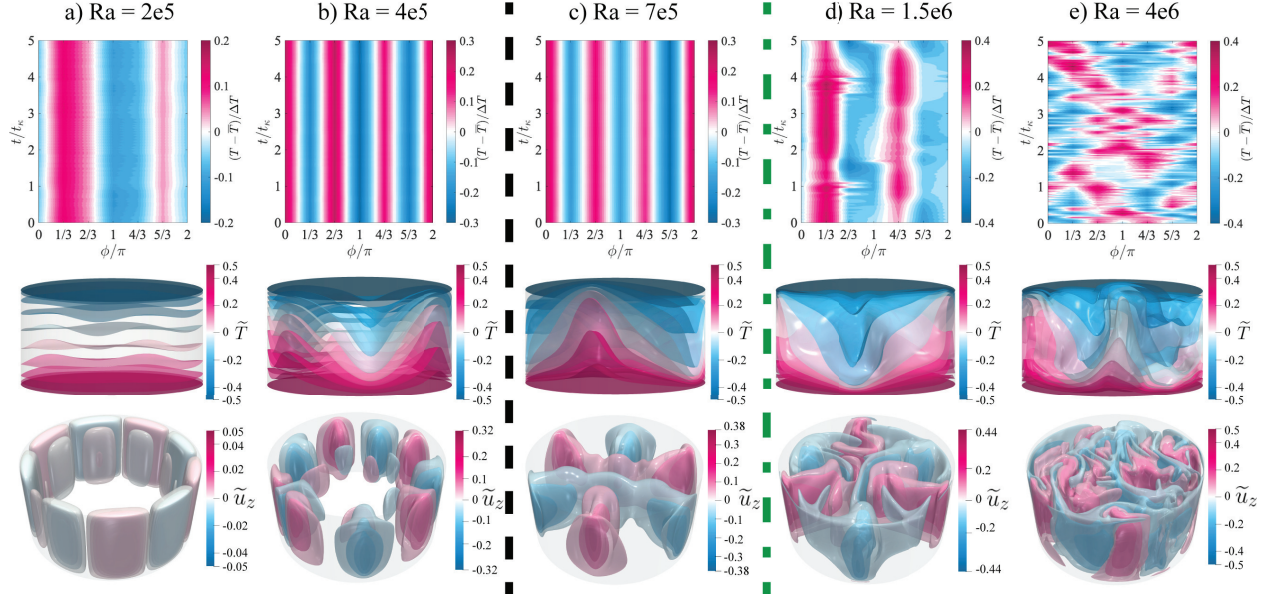


Figure 3.4: Temperature and velocity fields from $\Gamma = 2.0$ laboratory experiments at $Ch = 4.0 \times 10^4$. The vertical columns show cases at a) $Ra = 2.0 \times 10^5$, b) $Ra = 4.0 \times 10^5$, c) $Ra = 7.0 \times 10^5$, d) $Ra = 1.5 \times 10^6$, and e) $Ra = 4.0 \times 10^6$, respectively (Ra is only approximate for the laboratory cases; their exact values are given in tables 3.2 and 3.3). The first row shows the azimuthal-temporal temperature contours at the midplane interpolated by lab data over 5 thermal diffusion times, $\tau_\kappa = H^2/\kappa$. The color represents the dimensionless temperature, $(T - \bar{T})/\Delta T$, where \bar{T} is the mean temperature obtained by averaging the top and bottom temperatures. The second row consists of snapshots of the normalised DNS temperature field \tilde{T} and the third row presents snapshots of normalised DNS vertical velocity fields \tilde{u}_z at the same moment in time as the temperature field. The vertical black dashed line between b) and c) separates between cases below bulk onset (based on Ra_{NS}^∞) to the left and above bulk onset to the right. The vertical green dash-dotted line between c) and d) indicates the transition from an azimuthal mode number of $m = 3$ to $m \leq 2$ seen in the laboratory cases.

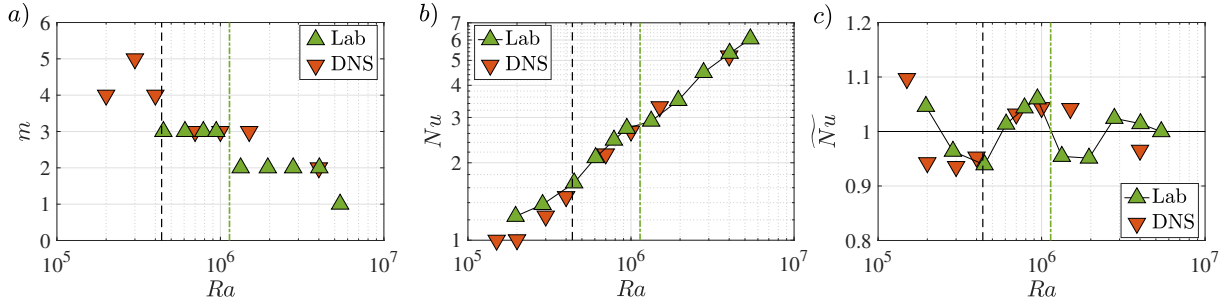


Figure 3.5: a) Azimuthal mode number m as a function of Ra at $Ch = 4 \times 10^4$, $\Gamma = 2.0$ case for both lab (green triangles) and numerical data (red triangles). b) Nusselt number Nu as a function of Ra for both laboratory experimental and numerical data. c) Nu - Ra Data plotted on detrended curves. Here, \widetilde{Nu} is Nu normalised by the linear fits (3.16, 3.17) of each respective data set in panel b). In parallel to figure 3.4, the black dashed line between b) and c) indicates the predicted Ra_{NS}^∞ , whereas the green dash-dotted line between c) and d) marks the average Ra between two adjacent laboratory data with $m = 3$ and $m = 2$. The kinks in Nu - Ra data in b) are shown as the fluctuations around $\widetilde{Nu} = 1$ in the $\widetilde{Nu} - Ra$ trend, likely associated with mode switching.

3.4.2 Transition to multimodality

We analysed temperature and velocity field data to elucidate both the wall modes and the transition to multi-modal flow at higher supercriticality. Figure 3.4 shows temperature and velocity fields of five laboratory numerical cases with $Ch \simeq 4 \times 10^4$ in the $\Gamma = 2.0$ tank. Each column represents the laboratory case (top row) and its corresponding numerical case (middle and bottom rows) at a similar Ra . The detailed parameters are given in table 3.2 and 3.3 in the appendix. The top rows show nondimensional temperature $(T - \bar{T})/\Delta T$ Hovmöller diagrams, a time evolution of the sidewall midplane temperature field. The temperature fields T are interpolated by the mid-plane thermistor data taken 60° apart in azimuth. The mean temperature \bar{T} is measured by averaging the top and bottom boundaries' temperature; the vertical temperature difference across the fluid layer is denoted as ΔT . The second and third rows of figure 3.4 show snapshots of numerical 3D isosurfaces of the dimensionless temperature fields $\widetilde{T} = (T - \langle T \rangle)/\Delta T$ and corresponding vertical velocity fields $\widetilde{\mathbf{u}}_z$ at the same

instant in the time. The mean temperature $\langle T \rangle$ is calculated by averaging the temperature fields over the entire domain.

The velocity and temperature fields in figure 3.4 all show magnetowall modes, manifesting as azimuthally alternating upwelling warm and downwelling cold patches located close to the sidewall. The snapshots of the DNS velocity fields in figures 3.4a) and b) further reveal that the magnetowall modes have a two-layer, ‘nose-like’ flow pattern attached to the sidewall with alternating $\pm \tilde{u}_z$. Liu *et al.* (2018) observed similar structures in their simulations in a rectangular box at $Ra = 10^7$, $Ch = 4 \times 10^6$. They found that these noses scale approximately with a Shercliff boundary layer thickness $\delta_{sh} \propto Ch^{-1/4}$ (Liu *et al.*, 2018).

Figure 3.4a) to b) show that these noses also grow gradually towards the interior as the supercriticality increases, while the interior remains otherwise quiescent. This “Pinocchio effect” persist until $Ra \gtrsim Ra_{NS}^\infty$, when the bulk fluid starts convecting from the top and bottom boundaries and then interacts with the inward-extended wall modes.

Figure 3.4c) shows this extending nose behavior for $Ra = 7 \times 10^5$, which is just above the bulk onset $Ra > Ra_{NS}^\infty$. The DNS velocity field visualises how two noses with positive/negative u_z (pink/blue) connect across the entire diameter of the tank via the convecting upwelling/downwelling fluid in the interior. The laboratory and numerical temperature field on the sidewall agree perfectly and show that close to the sidewall the wall modes are virtually unaffected by this interior dynamics. In total there are six alternating cold and hot patches along the sidewall azimuth, i.e., the azimuthal mode number is $m = 3$. The magnetowall mode number m is defined as the number of repeating azimuthal structures along the lateral surface.

Figure 3.4d) and e) show that these nonlinear interactions become more complicated and chaotic as Ra increases further. The nose-like structures interact and impinge on each other. The nonlinear behaviour also affects the flow close to the sidewall as visible in the temperature Hovmöller diagram from sidewall thermometry in d) for $Ra = 1.5 \times 10^6$ and even more so in e) for $Ra = 4.0 \times 10^6$.

For $Ra = 4.0 \times 10^6$ (Figure 3.4e), the experimental temperature Hovmöller diagram shows that the magnetowall modes are transient between $m = 1$ and $m = 2$ in a chaotic sequence. The velocity field of the DNS further demonstrates that the bulk flow dominates the dynamics, and, hence the flow for $Ra = 4.0 \times 10^6$ significantly differs from the ones at lower Ra shown in figure 3.4a) to d).

There is, however, a small discrepancy between the number of azimuthal structures between the lab and DNS data, being $m = 2$ and $m = 3$, respectively for $Ra = 1.5 \times 10^6$ (Figure 3.4d). This may be because m is sensitive to small changes in Ra and Γ , and there are slight differences in parameters between the lab and the DNS, or because of the sidewall boundary conditions which are not perfectly adiabatic in the experiment. It is also possible that the DNS snapshots do not capture fully equilibrated flow patterns whilst the lab experiments revealed more averaged dynamics of MC, as, unlike the DNS, they can be run for many thermal diffusion times.

Figure 3.5a) shows how the time-averaged azimuthal mode numbers m observed in the laboratory experiment and the DNS velocity fields depend on the Rayleigh number Ra . The m values generally decrease with increasing Ra , which qualitatively agrees with previous studies (Liu *et al.*, 2018; Akhmedagaev *et al.*, 2020; Zürner *et al.*, 2020). For $Ra < 10^4$, we only present DNS data in this plot and no lab data due to a combination of both precision and spatial aliasing issues of the sidewall thermistor array. The temperature variation between each wall mode structure near the midplane is $\lesssim 0.2$ K, which is too small to be resolved by our thermometers. Additionally, with only six thermistors evenly spaced at the azimuth, we can only resolve up to $m = 3$ according to the Nyquist-Shannon sampling theorem. Thus, even though the first-row temperature contour in figure 3.5b) shows an $m = 3$ structure, it was omitted in figure 3.5a) and only the $m = 4$ from the velocity field from the DNS is shown.

The changes in mode number also affect the global heat transport. Figure 3.5b) shows that Nu increases monotonically with Ra , but not at a constant rate. Instead, kinks exist

in the Nu - Ra trends in both lab experiments and DNS for $Ch = 4 \times 10^4$ (and $Ch = 10^5$, see figure 3.3a), a phenomenon which has not been reported in previous MC experiments (Cioni *et al.*, 2000a; Zürner *et al.*, 2020). To further investigate this behaviour, we normalised Nu by power laws obtained by separate fits to the $Ch = 4 \times 10^4$ laboratory and DNS Nu - Ra data sets. For the laboratory data, the best fit is

$$\widetilde{Nu} = Nu / (0.0029 Ra^{0.493}), \quad (3.16)$$

whereas for the DNS, it is found that

$$\widetilde{Nu} = Nu / (0.0014 Ra^{0.541}). \quad (3.17)$$

Figure 3.5c) shows the normalised \widetilde{Nu} . The non-monotonicity of the trend manifests as fluctuations around $\widetilde{Nu} \approx 1$ with an amplitude of approximately 0.05. The increase after the first local minimum in the experimental \widetilde{Nu} data curve coincides with the bulk onset, $Ra = Ra_{NS}^\infty$, and is marked by the vertical black dashed line. This suggests that bulk convection enhances heat transfer efficiency. The decrease after the first local maximum in the experimental \widetilde{Nu} data curve coincides with the change of mode numbers from $m = 3$ to $m = 2$ observed in the laboratory cases (cf. figure 3.4) and is marked by the green dash-dotted line. The transition to a smaller mode number appears to suppress the heat transfer efficiency temporarily. A similar behaviour was observed in Horanyi *et al.* (1999)'s liquid metal Rayleigh-Bénard convection experiments. The second enhancement in \widetilde{Nu} after the second local minimum happens when the highly-nonlinear flow structures in the bulk fluid start to dominate the convective dynamics. This corresponds to flow behaviors somewhere between $Ra = 1.5 \times 10^6$ (figure 3.4d) and $Ra = 4 \times 10^6$ (figure 3.4e). The DNS data in figure 3.5c) match the first enhancement near $Ra = Ra_{NS}^\infty$. Because no mode switch from $m = 3$ to $m = 2$ was found in the DNS, no kink shows up in the Nu - Ra trend in the DNS data at this point.

3.5 Discussion

3.5.1 Wall modes stability and the cellular flow regime

In our laboratory-numerical experiments, the magnetowall modes are stationary and do not drift over dynamically long time scales ($\gg 5\tau_\kappa$), in contrast to the drifting wall modes in rotating convection systems (e.g., [Ecke *et al.*, 1992](#)). This is because the quasi-static Lorentz force ($f_L \propto B_0^2$) does not break the system's azimuthal symmetry, unlike the Coriolis force ([Ecke *et al.*, 1992](#)). The stationarity of magnetowall modes has been confirmed in both numerical simulations ([Liu *et al.*, 2018](#)) and laboratory experiments ([Zürner *et al.*, 2020](#)). Furthermore, [Liu *et al.* \(2018\)](#) showed that the magnetowall modes can inject jets into the bulk. This phenomenon was also found in the numerical MC simulations of [Akhmedagaev *et al.* \(2020\)](#), where strong, axially invariant wall mode injections were accompanied by a net azimuthal drift of the flow field with random orientations. We believe that the collisional interaction of the jets in a small aspect ratio cylinder ($\Gamma = 1.0$), rather than any innate azimuthal motion of magnetowall modes, is responsible for the drifting motions observed by [Akhmedagaev *et al.* \(2020\)](#).

The fully three-dimensional flow fields from our DNS facilitated the investigation of the bulk flow patterns in this study. Thus, we are also able to compare multiple cases at similar parameters with [Zürner *et al.* \(2020\)](#) who inferred the interior structure solely from line-wise Ultrasonic Doppler Velocimetry (UDV) and pointwise temperature measurements along the sidewalls and within the top and bottom plate. Our identified flow structures and corresponding flow changes match well with their observations. Specifically, what they denoted as the 'cellular regime' corresponds to our case with extended wall mode noses with interior bulk modes. Our $Ra = 7 \times 10^5$ and $Ra = 1.5 \times 10^6$ cases (figure 3.4c, d) resemble the inferred '3-cell' and '4-cell' patterns of figure 3 in [Zürner *et al.* \(2020\)](#). Our $Ra = 1.5 \times 10^6$, $m = 2$ thermal data in figure 3.4d) also agrees with their '2 cell' pattern on the sidewall. Moreover, the transition range from the 'cellular regime' to the non-rotating

LSC regime in their experiment occurred approximately at $Ra \gtrsim 4 \times 10^6$ for $Ch = 4 \approx 10^4$, which is consistent with our observation of a more chaotic interior and unsteady and irregular wall mode behaviour, as shown in figure 3.4e).

3.5.2 The Nu vs. Ra MC party

Figure 3.6 presents a broad compilation of laboratory MC heat transfer measurements in different aspect ratios and geometries, all in the presence of an external vertical magnetic field. Cioni *et al.* (2000a) (open circles) studied liquid mercury in a $\Gamma = 1.0$ cylindrical cell up to $Ch \approx 4 \times 10^6$ and $Ra \approx 3 \times 10^9$. Aurnou & Olson (2001) (open triangles pointing right) carried out near onset liquid gallium experiments in a $\Gamma = 8$ rectangular cell. Burr & Müller (2001) (open triangles pointing left) investigated sodium-potassium alloy in a 20 : 10 : 1 rectangular cell. King & Aurnou (2015) studied liquid gallium MC in a $\Gamma = 1.0$ cylinder on the same device (ROMAG) as this study. Zürner *et al.* (2020) studied both heat and momentum transfer behaviors of liquid GaInSn in a $\Gamma = 1$ cylinder. The results from our current $\Gamma = \{1.0, 2.0\}$ cylindrical liquid gallium experiments and simulations are demarcated by the filled symbols.

In addition, we have included the Nusselt number data for $Ch = 0$, i.e. pure Rayleigh-Bénard convection (RBC). Best fits to the RBC cases yield

$$Nu_0 \approx (0.191 \pm 0.088) Ra^{0.248 \pm 0.025} \quad \text{for } \Gamma = 1.0, \quad (3.18a)$$

$$Nu_0 \approx (0.176 \pm 0.081) Ra^{0.246 \pm 0.028} \quad \text{for } \Gamma = 2.0, \quad (3.18b)$$

which are in good agreement with previous studies on the same device (ROMAG) (King & Buffett, 2013; King & Aurnou, 2015; Vogt *et al.*, 2018a; Aurnou *et al.*, 2018). The differences between these two scaling laws lie within their error bars but may be due to the different tank aspect ratios (King & Aurnou, 2013; Vogt *et al.*, 2018a; Aurnou *et al.*, 2018).

As discussed in section 3.4, our data show that the onset of MC in a cylinder occurs via wall modes. The five-point stars at $Nu = 1$ mark the magnetowall mode onset predictions

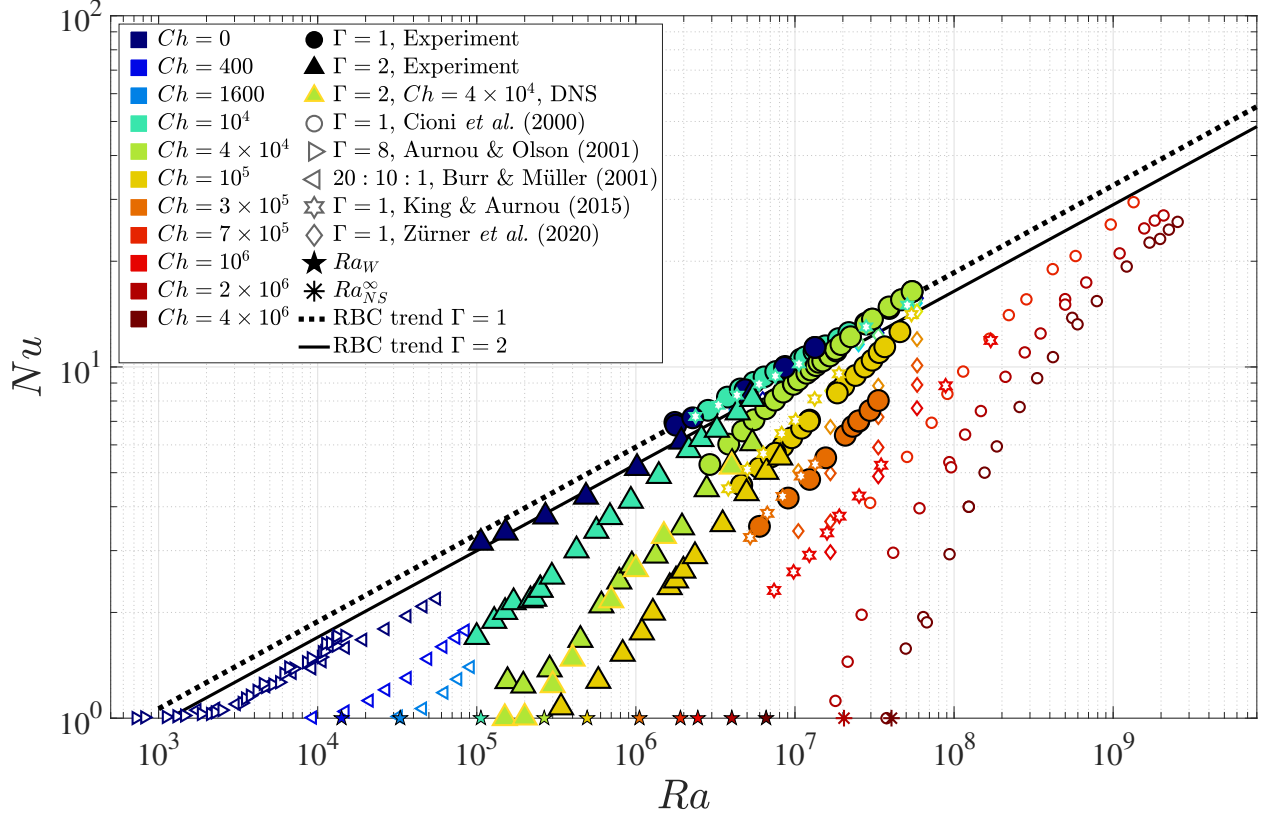


Figure 3.6: Collection of Nu - Ra data from this study and previous MC laboratory experiments in liquid metal Chandrasekhar (1961); Cioni *et al.* (2000a); Aurnou & Olson (2001); Burr & Müller (2001); King & Aurnou (2015); Zürner *et al.* (2020). Color represents Ch . The filled symbols mark the data in this study. The five-pointed stars at $Nu = 1$ mark the Ra_W (3.9) for all different $Ch > 0$. The two asterisk symbols from left to right mark Ra_{NS}^∞ for $Ch = 2 \times 10^6$ and 4×10^6 , respectively, and corresponding to the Cioni *et al.* (2000a)'s two Ch data set. The non-filled color symbols are selected heat transfer data from prior liquid metal laboratory experiments. All data displayed here are included in appendix tables 3.2 - 3.6.

Ra_W (3.9) for the different Ch . Our near-onset data at $Ch = 10^5$ (yellow triangles) is in good agreement with the onset prediction by Busse (2008) (yellow star). However, Cioni *et al.* (2000a)'s heat transfer data at $Ch = 2 \times 10^6$ and $Ch = 4 \times 10^6$ have $Ra_{crit} \approx 3Ra_W$. The lowest Nu data from Cioni *et al.* (2000a)'s $Ch = 2 \times 10^6$ and $Ch = 4 \times 10^6$ align well with the bulk onset prediction, Ra_{NS}^∞ . Zürner *et al.* (2020) have analysed the Nu - Ra trends and also found a large deviation between the experimental results of Cioni *et al.* (2000a) and King & Aurnou (2015). This discrepancy is likely due to Cioni *et al.* (2000a)'s thermometry setup, which used a single thermistor at the center of each top and bottom boundary to measure ΔT . This setup was not designed to characterise wall modes and could only detect the convective heat transfer occurring near the center of the tank. Thus, top and bottom end wall temperature measurements nearer to the sidewall are required in order to detect the onset of wall modes and to measure their contributions to the total heat transfer (cf. Akhmedagaev *et al.*, 2020; Zürner *et al.*, 2020; Grannan *et al.*, 2022).

3.5.3 Comparison between magnetoconvection and rotating convection in liquid metal

The goal of this work is to provide a better understanding of the pathway from convective onset to multimodal turbulence in liquid metal magnetoconvection. Thus far, we have compared our laboratory-numerical data with the results of other MC studies. Here we expand on this by comparing our MC data against rotating convection data. Although the Lorentz and Coriolis forces both act to constrain the convection in these systems (Julien & Knobloch, 2007), their data are rarely closely compared since the vast majority of rotating convection (RC) studies are carried out in moderate to high Prandtl fluids (non-metals), whereas MC studies are nearly always made using low Pr liquid metals (cf. Aujogue *et al.*, 2018).

Figure 3.7 shows a side-by-side comparison of the convective heat transfer efficiency Nu/Nu_0 as a function of the normalised buoyancy forcing in a) our present liquid gallium $\Gamma = 1.0$ and 2.0 MC experiments and b) the liquid gallium $\Gamma = 1.0$ rotating convection data

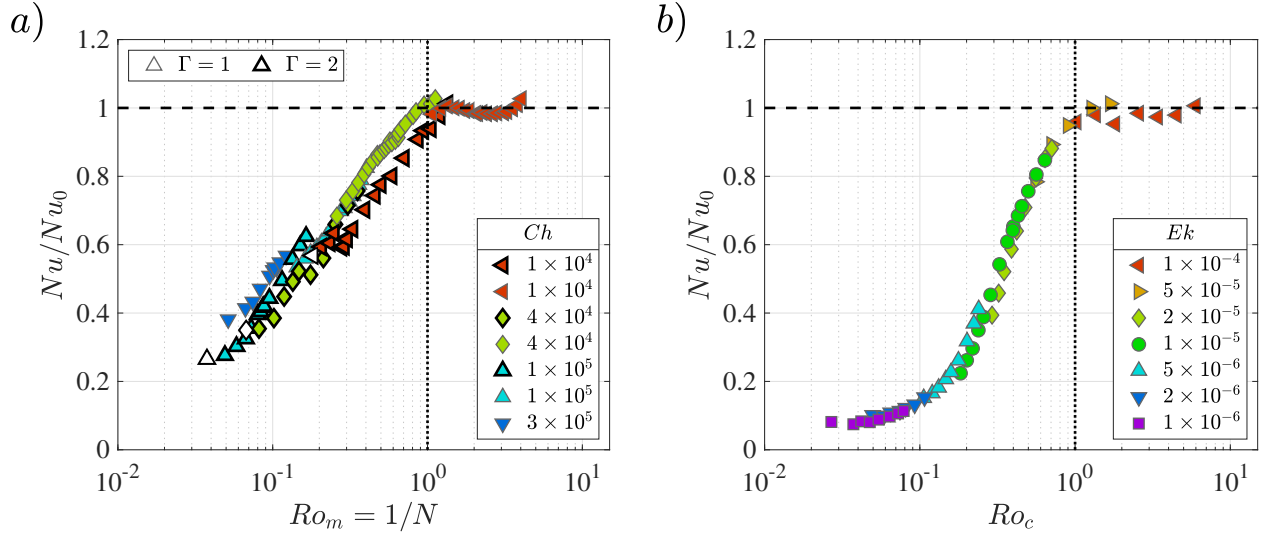


Figure 3.7: a) Normalised Nusselt number (Nu/Nu_0) versus magnetic Rossby number (Ro_m) for MC lab data in $\Gamma = 1.0$ and 2.0 tanks. Here, Nu_0 are the best-fit power laws in (3.18) and Ro_m is the inverse of interaction parameter N , as defined in (3.19). Symbols in thick black outlines represent $\Gamma = 2.0$ data, and those in thin grey outlines are $\Gamma = 1.0$ data. The color of the symbols indicates $\log_{10}(Ch)$. The white symbols are subcritical cases according to wall mode onset ($Ra < Ra_W$). The symbol shapes do not contain information but help differentiate different Ch . b) Rotating convective heat transfer data adapted from the $\Gamma = 1.0$ liquid gallium experiments of King & Aurnou (2013). The color indicates $\log_{10}(Ek^{-1})$. The vertical axis shows a reduced Nusselt number $Nu/Nu_0 = Nu/(0.185Ra^{0.25})$, following (King & Aurnou, 2013). The horizontal axis is convective Rossby number Ro_c , as defined in (3.19).

from King & Aurnou (2013) King & Aurnou (2013). The thicker outlined symbols in panel a) demarcate the $\Gamma = 2.0$ MC cases. The liquid gallium convection data in Figure 3.7 was all obtained using the same experimental apparatus and setup. The fill color in a) denotes $\log_{10}(Ch)$, whereas it denotes $\log_{10}(Ek^{-1})$ in panel b). The Ekman number, $Ek = \nu/2\Omega H^2$, is the ratio of viscous and Coriolis forces in rotating systems and Ω is the RC system's angular rotation rate.

The best co-collapse of the Nu/Nu_0 data sets was found when the buoyancy force was normalised by the appropriate constraining force, that being Lorentz in MC and Coriolis forces in RC. In MC, this non-dimensional ratio is called the magnetic Rossby number, Ro_m , which formally describes the ratio of convective inertia and the Lorentz force:

$$Ro_m = \frac{\text{Inertia}}{\text{Lorentz}} = Re_{ff}Ch^{-1} = \sqrt{\frac{RaCh^{-2}}{Pr}}, \quad (3.19)$$

where $Re_{ff} = U_{ff}H/\nu$. In the MHD literature, the reciprocal of this ratio, which is called the interaction parameter $N = Ro_m^{-1}$ is often employed (e.g., Xu *et al.*, 2022). In RC, this non-dimensional ratio is called the convective Rossby number, Ro_c ,

$$Ro_c = \frac{\text{Inertia}}{\text{Coriolis}} = Re_{ff}Ek = \sqrt{\frac{RaEk^2}{Pr}}, \quad (3.20)$$

which shows up as a collapse parameter in a broad array of rotating convection problems (e.g. Gastine *et al.*, 2014; Aurnou *et al.*, 2020; Landin *et al.*, 2023). Lorentz forces dominate in MC when $Ro_m = 1/N$ is small; Coriolis forces dominate in RC when Ro_c is small. When these Rossby numbers exceed unity, buoyancy-driven inertial forces should be dominant and the convection is expected to be effectively unconstrained on all available length scales in the system.

Comparing Figures 3.7a) and 3.7b), it is clear that the liquid metal MC and RC data have similar gross morphologies. The Nu/Nu_0 is near unity and effectively flat for both $Ro_m \gtrsim 1$ and $Ro_c \gtrsim 1$. Thus, when the constraining Lorentz or Coriolis forces become subdominant to inertia in either system, the heat transfer is similar to that found in unconstrained RBC experiments.

The basic structures of MC and RC data are also similar at $Ro_m \lesssim 1$ and $Ro_c \lesssim 1$: the normalised heat transfer trends relatively sharply downwards with decreasing Rossby number. However, the detailed structures of the low Ro_m and low Ro_c data differ substantively. The data fall off more steeply with Rossby in the rotating case, then it greatly flattens out in the lowest Nu/Nu_0 RC cases. The differences in slope may be due to the difference in Ekman pumping (EP) effects in both systems (Julien *et al.*, 2016), although heat transfer enhancement by EP is typically weak in metals since it is hard to modify the thermal boundary layers in low Pr flows.

Alternatively, these differences may be caused by the differences in critical Ra values and their scalings. For instance, in the parameter ranges explored in Figure 3.7, oscillatory bulk convection first onsets in RC (Aurnou *et al.*, 2018), whereas it is the wall modes that develop first in MC. Further, the bulk magnetoconvective onset scales asymptotically as $Ra_{crit} \sim Ch^1$ whereas bulk oscillatory convective onset asymptotically scales as $Ra_{crit} \sim Ek^{-4/3}$. This 1/3 difference in the scaling exponents may imply that the available range of Nu/Nu_0 will be larger in the RC cases. Further, the flat tail in the lowest Nu/Nu_0 RC data is likely due to the low convective heat transfer efficiency of oscillatory rotating convection.

Thus, the gross structures of the two data compilations are similar in Figure 3.7. We hypothesise that their differences in our current data are likely due to the various modal onset phenomena, as are clearly present in Figure 3.5, that alter the low Rossby branches of each figure panel. However, it may be that differences in MC and RC supercritical dynamics better explain these data (cf. Yan *et al.*, 2019; Oliver *et al.*, 2023). Regardless of the root cause, these low Rossby differences have thus far thwarted our attempts to create a unified plot in which all the Nu/Nu_0 data are simultaneously collapsed (cf. Chong *et al.*, 2017).

3.5.4 Summary

We have conducted a suite of laboratory thermal measurements of liquid gallium magnetoconvection in cylindrical containers of aspect ratios $\Gamma = 1.0$ and 2.0 . Our data allow us

to characterise liquid metal MC from wall mode onset to multimodality. We performed a fixed $Ch = 4 \times 10^4$ survey of direct numerical simulation for the same system in a $\Gamma = 2.0$ cylindrical geometry. Both laboratory and numerical methods obtained similar heat transfer behaviors, with possible subtle differences in flow morphology. Together with previous studies, our liquid metal heat transfer data comprise a convective heat transfer survey over six orders of magnitude in both Ra and in Ch (Figure 3.6).

Busse (2008)’s asymptotic solutions for magnetowall modes best collapse all our MC heat transfer data, whereas the hybrid theoretical-numerical solutions by Houchens *et al.* (2002) captures the exact onset for $\Gamma = 1.0$, but the onset for $\Gamma = 2.0$ remains unverified. Better theoretical onset predictions are needed for liquid metal MC in a cylindrical cell as a function of Γ . This differs from liquid metal rotating convection where accurate theoretical predictions currently exist for low- Pr fluids in cylindrical geometries (Zhang & Liao, 2009, 2017).

The MC flow morphology was characterised experimentally using a sidewall thermistor array as well as the DNS temperature and velocity fields. The onset of convection was verified to occur in the form of stationary (non-drifting) magnetowall modes. These magnetowall modes develop nose-like protuberances that extend into the fluid bulk with increasing supercriticality. At Rayleigh numbers beyond the critical value for steady bulk convection, the noses interact with the interior bulk modes, likely resulting in the apparent cell-like flow patterns observed by Zürner *et al.* (2020). Our data show that MC convective heat transport is sensitive to the flow morphology, with the Nusselt number $Nu-Ra$ data containing distinct kinks at these points where the dominant convection mode appears to change.

Lastly, liquid metal heat transfer trends in magnetoconvection were compared with rotating convection. The gross behavior of the heat transfer is controlled by the magnetic and convective Rossby numbers, Ro_m and Ro_c , in the respective systems, with the normalised heat transport Nu/Nu_0 approaching the RBC scaling as Ro_m and Ro_c approach unity from below. The detailed trends at Rossby values less than unity show clear differences between

MC and RC. We have not yet deduced a scheme by which it is possible to collapse all the liquid metal MC and RC data in a unified way. Nevertheless, all these important findings lay the foundation for understanding other more complex MC, RC, and RMC systems.

3.6 Appendix: Tables

<i>Ch</i>	<i>Ra</i>	<i>Nu</i>	<i>Ch</i>	<i>Ra</i>	<i>Nu</i>	<i>Ch</i>	<i>Ra</i>	<i>Nu</i>
0	1.93E+06	6.13	1.00E+04	5.64E+05	3.41	3.98E+04	1.93E+06	3.52
0	1.02E+06	5.16	1.01E+04	6.87E+05	3.74	4.00E+04	2.79E+06	4.48
0	4.86E+05	4.27	1.00E+04	9.30E+05	4.16	4.02E+04	4.03E+06	5.33
0	2.70E+05	3.75	1.02E+04	1.39E+06	4.89	4.15E+04	5.40E+06	6.06
0	1.52E+05	3.37	1.03E+04	2.15E+06	5.79	9.40E+04	1.65E+05	1.20
0	1.06E+05	3.16	1.04E+04	2.58E+06	6.23	9.40E+04	2.10E+05	1.15
0	3.81E+04	3.24	1.04E+04	3.23E+06	6.62	9.42E+04	3.39E+05	1.07
0	5.69E+04	3.99	1.06E+04	4.37E+06	7.42	9.44E+04	5.81E+05	1.28
0	5.26E+06	8.31	1.05E+04	5.40E+06	8.11	9.49E+04	8.26E+05	1.52
1.06E+04	9.98E+04	1.70	1.09E+04	6.01E+06	8.28	9.47E+04	1.09E+06	1.75
1.06E+04	1.29E+05	1.89	3.87E+04	9.24E+04	1.47	9.48E+04	1.28E+06	2.00
1.01E+04	1.51E+05	2.01	3.72E+04	1.56E+05	1.27	9.70E+04	1.63E+06	2.36
1.00E+04	1.64E+05	2.25	3.88E+04	1.96E+05	1.24	9.73E+04	1.79E+06	2.47
1.01E+04	1.70E+05	2.17	3.89E+04	2.87E+05	1.38	9.76E+04	1.92E+06	2.59
1.01E+04	2.17E+05	2.10	3.89E+04	4.48E+05	1.67	9.76E+04	1.99E+06	2.63
1.01E+04	2.13E+05	2.14	3.91E+04	6.07E+05	2.09	9.81E+04	2.35E+06	2.89
1.01E+04	2.30E+05	2.19	3.92E+04	7.86E+05	2.45	9.91E+04	3.51E+06	3.57
1.01E+04	2.50E+05	2.33	3.91E+04	9.43E+05	2.72	1.01E+05	4.96E+06	4.37
1.01E+04	2.52E+05	2.32	3.92E+04	1.33E+06	2.90	1.04E+05	6.61E+06	5.03
1.01E+04	2.96E+05	2.53	3.93E+04	1.33E+06	2.90	1.05E+05	8.08E+06	5.52
1.01E+04	4.23E+05	3.00	3.97E+04	1.95E+06	3.49			

Table 3.2: Current study. Liquid gallium. $Pr = 0.027$, $\Gamma = 2$.

<i>Ch</i>	<i>Ra</i>	<i>Nu</i>	<i>Ch</i>	<i>Ra</i>	<i>Nu</i>	<i>Ch</i>	<i>Ra</i>	<i>Nu</i>
4.00E+04	1.5E+05	1.000	4.00E+04	4.0E+05	1.477	4.00E+04	1.50E+06	3.302
4.00E+04	2.0E+05	1.004	4.01E+04	7.0E+05	2.165	4.00E+04	4.0E+06	5.202
4.00E+04	3.0E+05	1.241	4.00E+04	1.0E+06	2.635			

Table 3.3: Current study. DNS. $Pr = 0.025$, $\Gamma = 2$.

<i>Ch</i>	<i>Ra</i>	<i>Nu</i>	<i>Ch</i>	<i>Ra</i>	<i>Nu</i>	<i>Ch</i>	<i>Ra</i>	<i>Nu</i>
0	1.76E+06	6.95	1.11E+04	5.45E+07	16.40	4.43E+04	5.45E+07	16.40
0	1.78E+06	6.83	3.83E+04	1.88E+06	4.53	9.13E+04	4.63E+06	4.61
0	2.28E+06	7.17	3.84E+04	2.92E+06	5.28	9.13E+04	4.60E+06	4.61
0	4.86E+06	8.61	3.86E+04	3.83E+06	6.03	9.17E+04	5.98E+06	5.16
0	8.61E+06	9.98	3.86E+04	4.69E+06	6.57	9.21E+04	7.07E+06	5.54
0	1.33E+07	11.37	3.89E+04	5.53E+06	7.07	9.15E+04	8.40E+06	5.95
0	2.06E+07	13.10	3.85E+04	6.55E+06	7.61	9.10E+04	9.55E+06	6.29
9.55E+03	1.11E+06	5.66	3.86E+04	7.46E+06	8.04	9.12E+04	1.10E+07	6.69
9.35E+03	1.40E+06	6.10	3.86E+04	8.43E+06	8.48	9.19E+04	1.24E+07	7.06
9.60E+03	2.84E+06	7.53	3.91E+04	9.74E+06	8.99	9.53E+04	1.86E+07	8.53
9.65E+03	3.76E+06	8.21	3.86E+04	9.79E+06	8.92	9.44E+04	2.03E+07	8.83
9.61E+03	4.53E+06	8.66	3.87E+04	1.05E+07	9.19	9.55E+04	2.40E+07	9.46
9.60E+03	5.52E+06	9.04	3.88E+04	1.19E+07	9.59	9.62E+04	2.74E+07	9.99

Table 3.4: Current study. Liquid gallium. $Pr = 0.027$, $\Gamma = 1$.

<i>Ch</i>	<i>Ra</i>	<i>Nu</i>	<i>Ch</i>	<i>Ra</i>	<i>Nu</i>	<i>Ch</i>	<i>Ra</i>	<i>Nu</i>
9.55E+03	6.39E+06	9.37	3.89E+04	1.26E+07	9.80	9.65E+04	3.05E+07	10.45
9.58E+03	7.57E+06	9.70	3.88E+04	1.36E+07	10.09	9.82E+04	3.38E+07	10.99
9.62E+03	8.67E+06	10.04	3.92E+04	1.41E+07	10.31	9.89E+04	3.67E+07	11.41
9.75E+03	1.09E+07	10.52	3.90E+04	1.49E+07	10.40	1.02E+05	4.57E+07	12.60
9.77E+03	1.15E+07	10.68	3.93E+04	1.64E+07	10.83	2.88E+05	5.98E+06	3.43
9.94E+03	1.16E+07	10.88	3.95E+04	1.66E+07	10.75	2.75E+05	9.07E+06	4.13
9.78E+03	1.32E+07	11.07	3.97E+04	1.82E+07	11.10	2.88E+05	1.24E+07	4.67
9.92E+03	1.55E+07	11.49	3.95E+04	1.80E+07	11.22	2.90E+05	1.56E+07	5.38
1.00E+04	1.88E+07	12.04	3.96E+04	1.94E+07	11.58	2.90E+05	2.07E+07	6.24
1.01E+04	2.18E+07	12.53	3.98E+04	2.24E+07	12.19	2.90E+05	2.31E+07	6.61
1.03E+04	2.78E+07	13.31	4.09E+04	2.81E+07	13.24	2.89E+05	2.52E+07	6.84
1.03E+04	3.05E+07	13.68	4.13E+04	3.07E+07	13.69	2.96E+05	2.96E+07	7.34
1.07E+04	3.91E+07	14.67	4.26E+04	3.90E+07	14.82	2.97E+05	3.34E+07	7.83
1.09E+04	4.68E+07	15.53	4.31E+04	4.67E+07	15.55	2.88E+05	2.51E+07	6.86

Table 3.5: Current study. Liquid gallium. $Pr = 0.027$, $\Gamma = 1$. Continued.

<i>Ch</i>	<i>Ra</i>	<i>Nu</i>	<i>Ch</i>	<i>Ra</i>	<i>Nu</i>	<i>Ch</i>	<i>Ra</i>	<i>Nu</i>
0	8.06E+06	8.676	0	2.53E+09	48.527	2.00E+06	4.99E+08	15.051
0	1.27E+07	9.620	0	2.67E+09	51.986	2.00E+06	6.77E+08	17.400
0	1.82E+07	10.667	7.22E+05	2.97E+07	4.103	2.00E+06	1.10E+09	21.055
0	2.35E+07	11.930	7.22E+05	5.06E+07	5.545	2.00E+06	1.57E+09	24.800
0	3.71E+07	13.228	7.22E+05	7.22E+07	6.936	2.00E+06	1.83E+09	26.111
0	3.81E+07	12.562	7.22E+05	9.08E+07	8.382	2.00E+06	2.07E+09	27.000
0	5.30E+07	14.542	7.22E+05	1.14E+08	9.703	3.93E+06	3.76E+07	1.000
0	6.83E+07	15.986	7.22E+05	1.67E+08	12.033	3.93E+06	4.97E+07	1.578
0	1.08E+08	17.879	7.22E+05	2.21E+08	14.050	3.93E+06	6.41E+07	1.940
0	1.54E+08	18.989	7.22E+05	2.85E+08	15.578	3.93E+06	6.74E+07	1.875
0	2.09E+08	21.055	7.22E+05	4.17E+08	18.989	3.93E+06	9.37E+07	2.930
0	2.44E+08	21.055	7.22E+05	5.81E+08	20.696	3.93E+06	1.24E+08	3.998
0	2.77E+08	22.556	7.22E+05	9.66E+08	25.445	3.93E+06	1.24E+08	4.000

Table 3.6: Cioni *et al.* (2000a). Liquid mercury. $Pr = 0.025$, $\Gamma = 1$.

<i>Ch</i>	<i>Ra</i>	<i>Nu</i>	<i>Ch</i>	<i>Ra</i>	<i>Nu</i>	<i>Ch</i>	<i>Ra</i>	<i>Nu</i>
0	3.40E+08	23.347	7.22E+05	1.34E+09	29.455	3.93E+06	1.55E+08	5.001
0	4.98E+08	25.011	2.00E+06	1.80E+07	1.120	3.93E+06	1.86E+08	5.940
0	5.11E+08	25.665	2.00E+06	2.14E+07	1.448	3.93E+06	2.58E+08	7.691
0	5.80E+08	26.564	2.00E+06	2.62E+07	1.970	3.93E+06	3.33E+08	9.290
0	6.59E+08	27.259	2.00E+06	4.14E+07	2.958	3.93E+06	4.18E+08	10.667
0	7.67E+08	27.972	2.00E+06	6.06E+07	3.960	3.93E+06	5.53E+08	13.800
0	8.72E+08	28.458	2.00E+06	9.34E+07	5.358	3.93E+06	5.97E+08	13.228
0	9.90E+08	28.952	2.00E+06	9.58E+07	5.180	3.93E+06	7.90E+08	15.400
0	1.28E+09	31.284	2.00E+06	1.17E+08	6.419	3.93E+06	1.22E+09	19.319
0	1.57E+09	32.103	2.00E+06	1.47E+08	7.490	3.93E+06	1.69E+09	22.600
0	1.87E+09	35.904	2.00E+06	2.10E+08	9.375	3.93E+06	1.97E+09	23.147
0	2.29E+09	36.843	2.00E+06	2.78E+08	11.000	3.93E+06	2.24E+09	24.600
0	2.35E+09	40.155	2.00E+06	3.50E+08	12.455	3.93E+06	2.54E+09	25.887
0	2.41E+09	43.764	2.00E+06	4.99E+08	15.600			

Table 3.7: Cioni *et al.* (2000a). Liquid mercury. $Pr = 0.025$, $\Gamma = 1$. Continued

<i>Ch</i>	<i>Ra</i>	<i>Nu</i>	<i>Ch</i>	<i>Ra</i>	<i>Nu</i>	<i>Ch</i>	<i>Ra</i>	<i>Nu</i>
0	7.21E+02	1.00	0	5.76E+03	1.27	670	1.52E+03	1.00
0	8.18E+02	1.01	0	6.13E+03	1.34	670	2.74E+03	1.01
0	1.12E+03	1.01	0	7.09E+03	1.38	670	4.24E+03	1.00
0	1.30E+03	1.01	0	6.57E+03	1.40	670	6.00E+03	1.01
0	1.46E+03	1.02	0	8.49E+03	1.44	670	7.04E+03	1.01
0	1.86E+03	1.03	0	9.10E+03	1.48	670	9.17E+03	1.01
0	2.12E+03	1.03	0	1.05E+04	1.49	670	8.26E+03	1.01
0	2.27E+03	1.04	0	1.07E+04	1.54	670	1.16E+04	1.03
0	2.50E+03	1.05	0	1.11E+04	1.55	670	1.03E+04	1.02
0	3.35E+03	1.11	0	1.31E+04	1.61	670	1.25E+04	1.03
0	3.52E+03	1.14	0	1.12E+04	1.63	670	1.34E+04	1.04
0	3.77E+03	1.16	0	1.20E+04	1.64	670	1.37E+04	1.05
0	4.15E+03	1.20	0	1.30E+04	1.68	670	1.44E+04	1.05
0	4.71E+03	1.23	0	1.32E+04	1.71	670	1.48E+04	1.06
0	4.55E+03	1.25	0	1.48E+04	1.71	670	1.53E+04	1.08
0	5.22E+03	1.25						

Table 3.8: Aurnou & Olson (2001). Liquid gallium. $Pr = 0.023$, $\Gamma = 6$.

<i>Ch</i>	<i>Ra</i>	<i>Nu</i>	<i>Ch</i>	<i>Ra</i>	<i>Nu</i>	<i>Ch</i>	<i>Ra</i>	<i>Nu</i>
0	1.74E+03	1.05	0	2.65E+04	1.80	400	4.92E+04	1.48
0	2.29E+03	1.06	0	3.64E+04	1.95	400	6.13E+04	1.60
0	3.08E+03	1.10	0	4.59E+04	2.08	400	7.39E+04	1.69
0	4.72E+03	1.23	0	5.58E+04	2.19	400	8.46E+04	1.78
0	6.92E+03	1.35	400	9.27E+03	1.00	1600	3.22E+04	1.01
0	9.19E+03	1.39	400	1.49E+04	1.05	1600	4.56E+04	1.07
0	1.07E+04	1.45	400	2.11E+04	1.12	1600	6.22E+04	1.18
0	1.49E+04	1.59	400	2.68E+04	1.20	1600	7.60E+04	1.29
0	1.92E+04	1.67	400	3.65E+04	1.30	1600	9.10E+04	1.40

Table 3.9: Burr & Müller (2001). Liquid Na-K alloy. $0.017 < Pr < 0.021$, rectangular box 20 : 10 : 1.

<i>Ch</i>	<i>Ra</i>	<i>Nu</i>	<i>Ch</i>	<i>Ra</i>	<i>Nu</i>	<i>Ch</i>	<i>Ra</i>	<i>Nu</i>
9.46E+03	2.37E+06	7.23	4.74E+04	8.44E+06	8.40	2.85E+05	1.09E+07	4.89
9.50E+03	3.30E+06	7.78	9.35E+04	3.81E+06	4.50	2.85E+05	1.34E+07	5.29
9.54E+03	4.32E+06	8.31	9.39E+04	5.02E+06	5.11	9.35E+05	7.39E+06	2.31
9.60E+03	5.95E+06	8.94	9.43E+04	6.33E+06	5.67	9.40E+05	9.80E+06	2.61
9.58E+03	7.53E+06	9.42	9.49E+04	8.25E+06	6.46	9.46E+05	1.23E+07	2.91
9.58E+03	1.06E+07	10.20	9.48E+04	1.01E+07	7.05	9.54E+05	1.59E+07	3.37
9.74E+03	2.80E+07	13.00	9.47E+04	1.33E+07	8.11	9.54E+05	1.90E+07	3.76
1.01E+04	5.08E+07	15.00	9.53E+04	1.89E+07	9.56	9.57E+05	2.53E+07	4.29
4.68E+04	3.10E+06	5.52	9.96E+04	5.40E+07	14.10	9.67E+05	3.48E+07	5.25
4.70E+04	4.11E+06	6.24	2.80E+05	5.23E+06	3.27	1.02E+06	8.85E+07	8.84
4.72E+04	5.13E+06	6.99	2.81E+05	6.70E+06	3.83	1.24E+06	1.70E+08	11.90
4.75E+04	6.81E+06	7.81	2.83E+05	8.37E+06	4.28			

Table 3.10: King & Aurnou (2015). Liquid gallium. $Pr = 0.025$, $\Gamma = 1$.

<i>Ch</i>	<i>Ra</i>	<i>Nu</i>	<i>Ch</i>	<i>Ra</i>	<i>Nu</i>	<i>Ch</i>	<i>Ra</i>	<i>Nu</i>
1.73E+02	4.18E+06	7.59	1.73E+04	2.51E+07	11.80	2.12E+05	3.34E+07	8.84
1.73E+02	6.27E+06	8.10	1.73E+04	3.34E+07	12.30	2.12E+05	5.85E+07	12.00
1.73E+02	1.05E+07	9.19	1.74E+04	5.78E+07	15.50	4.32E+05	1.05E+07	3.18
1.73E+02	1.67E+07	11.00	1.74E+04	5.82E+07	15.50	4.32E+05	1.05E+07	3.67
1.72E+02	3.34E+07	12.50	1.73E+04	5.84E+07	15.00	4.32E+05	1.05E+07	3.18
1.74E+02	5.82E+07	15.70	3.89E+04	1.05E+07	7.67	4.32E+05	1.05E+07	3.41
1.78E+02	5.91E+07	15.70	6.92E+04	6.26E+06	5.48	4.32E+05	1.67E+07	4.98
4.32E+03	4.18E+06	7.49	6.92E+04	1.05E+07	6.62	4.33E+05	3.34E+07	7.20
4.32E+03	6.27E+06	7.71	6.92E+04	1.67E+07	8.55	4.33E+05	5.86E+07	10.10
4.32E+03	1.05E+07	9.23	6.92E+04	2.51E+07	9.77	7.31E+05	1.67E+07	3.63
4.33E+03	1.67E+07	10.90	6.93E+04	3.34E+07	11.00	7.31E+05	3.34E+07	5.90
4.33E+03	2.51E+07	11.60	6.93E+04	3.34E+07	10.80	7.32E+05	5.86E+07	8.89
4.33E+03	3.34E+07	12.30	6.94E+04	5.84E+07	14.40	1.11E+06	1.67E+07	2.97
4.34E+03	5.81E+07	15.20	6.94E+04	5.85E+07	14.00	1.11E+06	3.34E+07	4.75
1.73E+04	4.18E+06	5.99	6.94E+04	5.85E+07	14.40	1.11E+06	3.34E+07	5.12
1.73E+04	6.27E+06	7.28	6.94E+04	5.86E+07	14.30	1.11E+06	3.34E+07	4.88
1.73E+04	1.05E+07	9.07	2.12E+05	1.05E+07	5.05	1.11E+06	5.85E+07	7.63
1.73E+04	1.67E+07	10.90	2.12E+05	1.67E+07	6.75			

Table 3.11: Zürner *et al.* (2020). Liquid GaInSn. $Pr = 0.029$, $\Gamma = 1$.

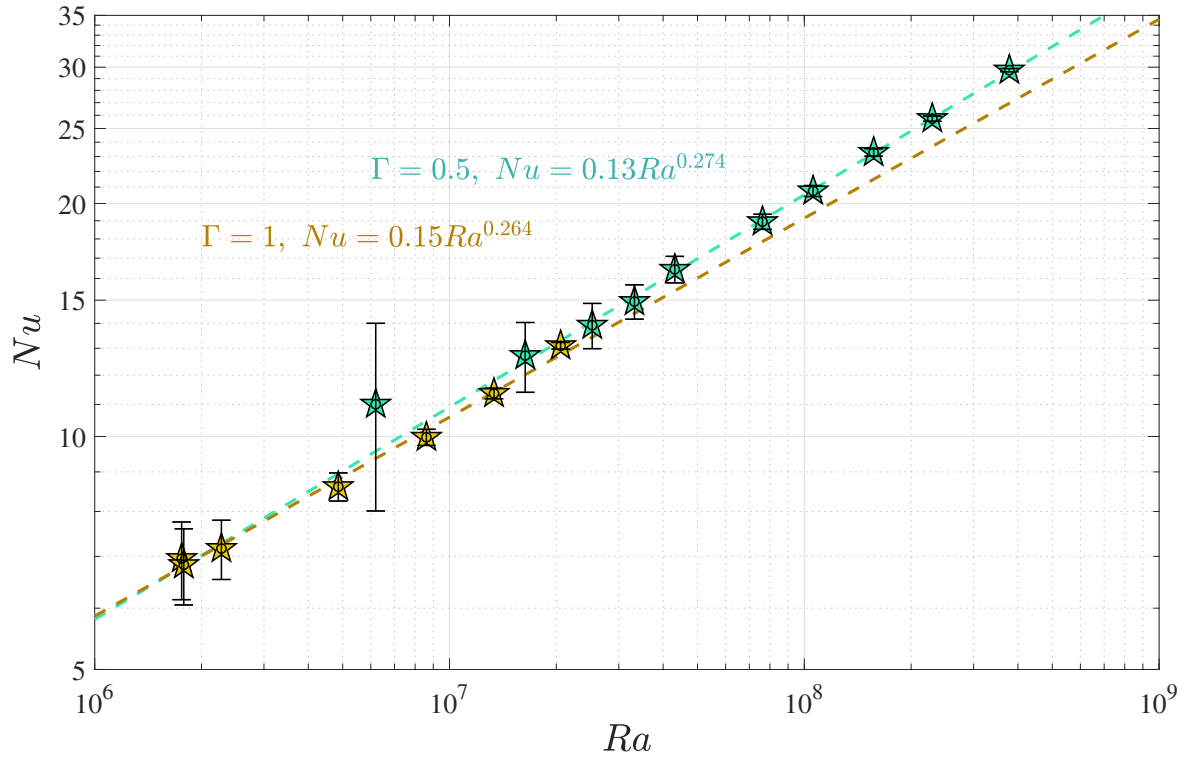


Figure 3.8: Nu vs. Ra Rayleigh-Bénard convection of liquid gallium with error bars on the data. The $\Gamma = 0.5$, 40 cm tank data are in teal, and $\Gamma = 1$, 20 cm tank data are in brown.

3.7 Appendix: RBC heat transfer in the 40-cm tank

Figure 3.8 shows that the RBC heat transfer behavior in the $\Gamma = 0.5$, 40 cm tank approximately follows the scaling behaviors derived from $\Gamma = 1$, 20 cm tank.

CHAPTER 4

Thermoelectric Magnetoconvection at Planetary Boundaries

“Realize that everything connects to everything else.”

— Leonardo da Vinci

Reproduced from: **Xu, Y.**, Horn, S., & Aurnou, J. (2022). Thermoelectric Precession in Turbulent Magnetoconvection. *Journal of Fluid Mechanics*, 930, A8. [\[Link\]](#)

Understanding the MHD dynamics near the planetary boundaries, such as the core-mantle boundary (CMB), are essential to interpreting the geomagnetic data and, thus, a crucial step in studying planetary dynamo processes. In answering the second question in section 1.4, I conducted laboratory magnetoconvection experiments in liquid gallium. In this study, I find that a self-sustaining thermoelectric current at the solid-liquid boundary interfaces interacts with the vertical magnetic field and causes a slow axial precession in the turbulent large-scale circulation of the liquid MC. My experiments demonstrate that this LSC precession occurs only when electrically conducting boundary conditions are employed and that the precession direction reverses when the axial magnetic field direction is flipped. I developed a thermoelectric magnetoconvection (TEMC) model that successfully predicts the zeroth-order magnetoprecession dynamics. This model yields precession frequency predictions that agree with the experimental observations. This study postulates that thermoelectric effects in convective flows may have dynamical influences on the core flows near the CMB. More broadly, this study suggests that core-mantle current systems

may exist in a variety of planetary/exoplanetary settings (e.g., Giampieri & Balogh, 2002).

Section 4.2.1 introduces the fundamentals of thermoelectric effects. Section 4.2.2 presents the governing equations and non-dimensional parameters that control the TEMC system. Section 4.2.3 reviews the established stability analysis and previous research related to the MC system. Section 4.3 addresses the experimental setup, the diagnostics used, and the physical properties of the working fluid, liquid gallium. Section 4.4 shows the experimental results with electrically-insulating boundary conditions. Section 4.5 presents the results of experiments made with electrically-conducting boundary conditions and the appearance of the magnetoprecessional mode. Section 4.6 presents an experimental survey in which I fix the convective forcing and vary the strength of the applied magnetic field. Following these laboratory results, in section 4.7, I develop an analytical model of the magnetoprecessional mode driven by thermoelectric currents generated by horizontal temperature gradients that exist along the top and bottom electrically-conducting boundaries. Finally, in section 4.8, I discuss the findings and potential future applications.

4.1 Introduction

The classical set-up for magnetoconvection (MC) is that of Rayleigh-Bénard convection (RBC) in an electrically-conductive fluid layer occurring in the presence of an externally imposed magnetic field (Chandrasekhar, 1961; Nakagawa, 1955). The electrically conducting fluid layer is heated from below and cooled from above, typically with the assumption that the top and bottom horizontal boundaries are isothermal and electrically insulating. The imposed magnetic field is usually vertically- (Cioni *et al.*, 2000*b*; Aurnou & Olson, 2001; Zürner *et al.*, 2020) or horizontally-oriented (Tasaka *et al.*, 2016; Vogt *et al.*, 2018*b*). MC is employed as an idealized model for many physical systems (Weiss & Proctor, 2014). In geophysics, MC is considered an essential sub-system of the thermocompositionally driven turbulent convection that generates the magnetic fields in molten metal planetary cores (e.g.,

Jones, 2011; Roberts & King, 2013; Aurnou & King, 2017; Moffatt & Dormy, 2019b). In astrophysics, MC is associated with the sunspot umbra structure, where the strong magnetic field suppresses the thermal convection in the outer layer of the Sun and other stars (e.g., Proctor & Weiss, 1982; Schüssler & Vögler, 2006; Rempel *et al.*, 2009). MC is also related to the X-ray flaring activities on magnetars with extremely large magnetic flux densities estimated from 10^9 to 10^{11} T (Castro-Tirado *et al.*, 2008). Furthermore, MC has an essential role in numerous industrial and engineering applications such as crystal growth (Moreau, 1999; Rudolph, 2008), design of liquid-metal-cooled blankets for nuclear fusion reactors (Barleon *et al.*, 1991; Abdou *et al.*, 2001; Salavy *et al.*, 2007) as well as induction heating, casting (Taberlet & Fautrelle, 1985; Davidson, 1999), and liquid metal batteries (Kelley & Weier, 2018; Cheng *et al.*, 2022a).

In sharp contrast to the ideal theoretical MC system, liquid metals employed in many laboratory and industrial MC systems have different thermoelectric properties from the boundary materials. This is also the case in natural systems where the properties significantly differ across a material interface, such as at the Earth’s core-mantle boundary (e.g., Lay *et al.*, 1998; Mao *et al.*, 2017; Mound *et al.*, 2019). When an interfacial temperature gradient is present, thermoelectric currents are generated that can form current loops across the interface (Shercliff, 1979; Jaworski *et al.*, 2010). When in the presence of magnetic fields that are not parallel to the currents, Lorentz forces arise that can stir the liquid metal (Jaworski *et al.*, 2010). Such phenomena can be explained by the thermoelectric magnetohydrodynamics (TE-MHD) theory first developed by Shercliff (1979), which focussed on forced heat transfer in nuclear fusion blankets. Although other applications of TE-MHD exist in solidification processes and crystal growth (Boettinger *et al.*, 2000; Kao *et al.*, 2009), we are unaware of any previous applications of TE-MHD where the convection itself sets the boundary thermal gradients (Zhang *et al.*, 2009), as occurs in the experiments presented here.

Our laboratory experiment focuses on the canonical configuration of turbulent MC in

a cylindrical volume of liquid gallium in the presence of vertical magnetic fields and with different electrical boundary conditions. Three behavioral regimes are identified primarily using sidewall temperature measurements: i) a turbulent large-scale circulation ‘jump rope vortex (JRV)’ regime in the weak magnetic field regime (Vogt *et al.*, 2018a); ii) a magnetoprecessional (MP) regime in which the large-scale circulation (LSC) precesses around its vertical axis is found for moderate magnetic field strengths and electrically conducting boundary conditions; iii) a multi-cellular magnetoconvection (MCMC) regime is found in the highest magnetic field strength cases. Although this is the first systematic study of the magnetoprecessional mode, this is not the first time that it has been experimentally observed. This behavior was first observed in our laboratory in the thesis experiments of (Grannan *et al.*, 2017). In addition, what appears to be a similar precession was reported in the MC experiments of (Zürner *et al.*, 2020).

4.2 Background

4.2.1 Thermoelectric Effects

Thermoelectric effects enable conversions between thermal and electric energy in electrically conducting materials. There are three different types: the Seebeck, Peltier, and Thomson effects (Terasaki, 2011). The Peltier and Thomson effects in our experimental system produce temperature changes of order μK , which are not resolvable with our present thermometric capabilities. Moreover, such small temperature variations will not affect the dynamics of our system. Thus, Peltier and Thomson effects are not considered further.

The Seebeck effect describes the net spatial diffusion of electrons towards or away from a local temperature anomaly (Kasap, 2001). As a consequence of this effect, positive and negative charges tend to become sequestered on opposite sides of a regional temperature gradient in the material, leading to the development of a thermoelectric electrical potential.

Ohm's law then becomes (Shercliff, 1979):

$$\mathbf{J} = \sigma (\mathbf{E} + \mathbf{u} \times \mathbf{B} - S \nabla T), \quad (4.1)$$

where $-\sigma S \nabla T$ encapsulates the thermoelectric current. The variables in eq. (4.1) are the electric current density \mathbf{J} , the electric conductivity σ ($\simeq 3.85 \times 10^6$ S/m in gallium), the electric field \mathbf{E} , the fluid velocity \mathbf{u} , the magnetic flux \mathbf{B} , the Seebeck coefficient S , and temperature T .

Mott & Jones (1958) derived the following expression for the Seebeck coefficient of a homogeneous and electrically conducting material as below:

$$S = -\frac{\pi^2 k_B^2 x_0}{3e E_{F0}} T, \quad (4.2)$$

where T is measured in Kelvin ($T \approx 300$ K for room temperature), k_B is the Boltzmann constant, $k_B = 1.38 \times 10^{-23}$ kg m²s⁻²K⁻¹ is the Boltzmann constant, x_0 is an $O(1)$ dimensionless constant that depends on the material properties, $e = 1.60 \times 10^{-19}$ C is the elementary electron charge, and E_{F0} is the material's Fermi energy (~ 10 eV = 1.6×10^{-18} J for metals). In a uniform medium, S is a function only of T . In this case, ∇S is parallel to ∇T such that $\nabla S \times \nabla T = 0$, which then requires that $S \nabla T$ is irrotational in a uniform medium.

As figure 4.1 shows, however, a temperature gradient at the interface of two materials with different Seebeck coefficients can generate a net thermoelectric potential. In this case, the Seebeck coefficient S discontinuously varies across the interface of the two materials, \mathcal{A} and \mathcal{B} . Near r_0 and r_1 , ∇S is no longer parallel to ∇T , so a thermoelectric current can form a closed-looped circuit.

The thermoelectric potential, Φ_{TE} , can be calculated via the circuit integral

$$\Phi_{TE} = \oint \frac{\mathbf{J}_{TE} \cdot d\mathbf{r}}{\sigma_{AB}}, \quad (4.3)$$

where σ_{AB} is the effective electric conductivity of the two-material system. The effective

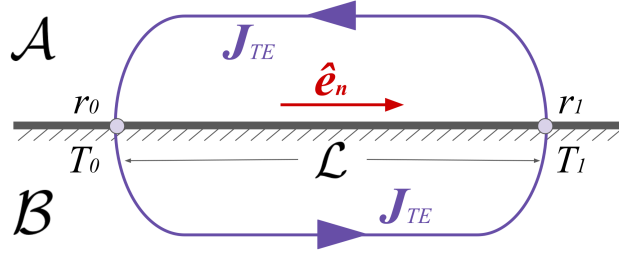


Figure 4.1: A thermoelectric current loop, \mathbf{J}_{TE} , forms across two different conducting materials \mathcal{A} and \mathcal{B} with a horizontal temperature gradient in the $\hat{\mathbf{e}}_n$ -direction. The locations where the thermoelectric current flows in and out the interface are labeled as r_0 and r_1 , respectively. A temperature gradient exists between r_0 and r_1 , where the corresponding temperatures are $T_0 < T_1$. The distance between r_0 and r_1 is defined as the characteristic length $\mathcal{L} = |r_1 - r_0|$. The direction of the current depends on the Seebeck coefficients of both materials, $S_{\mathcal{A}}$ and $S_{\mathcal{B}}$, following eq. (4.6).

electrical resistivity $\tilde{\rho}_{AB}$ is the sum of the resistivities in each material:

$$\tilde{\rho}_{AB} = \tilde{\rho}_{\mathcal{A}} + \tilde{\rho}_{\mathcal{B}}, \quad (4.4)$$

where we assume that the current travels through comparable cross-sectional areas and lengths in each material. Since $\sigma = 1/\tilde{\rho}$, the effective electrical conductivity for the thermoelectric circuit is

$$\sigma_{AB} = \frac{1}{\tilde{\rho}_{AB}} = \frac{1}{\tilde{\rho}_{\mathcal{A}} + \tilde{\rho}_{\mathcal{B}}} = \frac{\sigma_{\mathcal{A}} \sigma_{\mathcal{B}}}{\sigma_{\mathcal{A}} + \sigma_{\mathcal{B}}}. \quad (4.5)$$

Isolating the thermoelectric current density in the current loop, \mathbf{J}_{TE} , in eq. (4.1) yields

$$\mathbf{J}_{TE} = -\sigma_{AB} \tilde{S} \nabla T \approx -\sigma_{AB} \tilde{S} \left(\frac{T_1 - T_0}{\mathcal{L}} \right), \quad (4.6)$$

where \tilde{S} is the net Seebeck coefficient of the two-material system, and the temperature gradient in the $\hat{\mathbf{e}}_n$ -direction is approximated by $(T_1 - T_0)/\mathcal{L}$ (see figure 4.1). Substituting eq. (4.6) into eq. (4.3), one can show that the net thermoelectric potential Φ_{TE} is the difference between the thermoelectric potentials in each material,

$$\Phi_{TE} = \Phi_{\mathcal{A}} - \Phi_{\mathcal{B}} = - \int_{r_0(T_0)}^{r_1(T_1)} S_{\mathcal{A}} \nabla T \cdot d\mathbf{r} + \int_{r_0(T_0)}^{r_1(T_1)} S_{\mathcal{B}} \nabla T \cdot d\mathbf{r}, \quad (4.7)$$

where r_0 and r_1 denotes the location where the thermoelectric current flows in and out the interface, and T_0 and T_1 are the temperatures at r_0 and r_1 , respectively. We set $T_0 < T_1$, so that the temperature gradient is positive from r_0 to r_1 , following figure 4.1. Here $S_{\mathcal{A}}$ and $S_{\mathcal{B}}$ are the Seebeck coefficients of materials \mathcal{A} and \mathcal{B} , respectively.

Substituting eq. (4.2) into eq. (4.7) then yields

$$\Phi_{TE} = \int_{r_0(T_0)}^{r_1(T_1)} (S_{\mathcal{B}} - S_{\mathcal{A}}) \nabla T \cdot d\mathbf{r} = \frac{\pi^2 k_B^2}{6e} \left[\frac{x_{\mathcal{B}}}{E_{F\mathcal{B}}} - \frac{x_{\mathcal{A}}}{E_{F\mathcal{A}}} \right] (T_1^2 - T_0^2), \quad (4.8)$$

where $x_{\mathcal{A}}$, $x_{\mathcal{B}}$, $E_{F\mathcal{A}}$, and $E_{F\mathcal{B}}$ are numerical constants and Fermi energies of the materials \mathcal{A} and \mathcal{B} , respectively.

The system's *net Seebeck coefficient* is then written as

$$\tilde{S} = \frac{\Phi_{TE}}{T_1 - T_0} = \frac{\pi^2 k_B^2}{3e} \left[\frac{x_{\mathcal{B}}}{E_{F\mathcal{B}}} - \frac{x_{\mathcal{A}}}{E_{F\mathcal{A}}} \right] \left(\frac{T_0 + T_1}{2} \right), \quad (4.9)$$

where $(T_1 + T_0)/2$ is the mean temperature of the material interface. Note the structural similarity between the expressions for the Seebeck coefficient for a single material eq. (4.2) and the net Seebeck coefficient across a material interface eq. (4.9).

4.2.2 Governing Equations and Nondimensional Parameters

The magnetic Reynolds number, Rm , estimates the ratio of magnetic induction and diffusion in an MHD system. In our laboratory experiments, upper bounding values of Rm are estimated by using the convective free-fall velocity (Julien *et al.*, 1996; Glazier *et al.*, 1999),

$$U_{ff} = \sqrt{\alpha_T \Delta T g H}, \quad (4.10)$$

leading to

$$Rm = \frac{U_{ff} H}{\eta} = Re Pm, \quad (4.11)$$

where Re is the Reynolds number, which denotes the ratio of inertial and viscous effects,

$$Re = \frac{U_{ff} H}{\nu}, \quad (4.12)$$

the magnetic Prandtl number is the ratio of the fluid's magnetic diffusivity η and its kinematic viscosity ν ,

$$Pm = \frac{\nu}{\eta}, \quad (4.13)$$

and α_T is the thermal expansivity of the fluid, ΔT is the vertical temperature difference across the fluid layer of depth H , g is the gravitational acceleration. In our experiments, $Re \lesssim 9 \times 10^3$ and $Pm \simeq 1.7 \times 10^{-6}$. Thus, $Rm \lesssim 0.015 \ll 1$ for our system, in good agreement with estimates made using ultrasonic velocity measurements in this same setup by Vogt *et al.* (2018a). Further, the free-fall timescale can be defined as

$$\tau_{ff} = H/U_{ff}. \quad (4.14)$$

The estimates above show that magnetic diffusion dominates induction in our experiments. In this low- Rm regime, the influence of fluid motions on the magnetic field can be neglected and the full magnetic induction equation need not be solved amongst the governing equations. This results in both Rm and Pm dropping out of the problem (Davidson, 2016). This so-called ‘quasistatic approximation’ is commonly applied in low- Rm fluid systems and is valid in most laboratory and industrial liquid metal applications (Sarris *et al.*, 2006; Davidson, 2016; Knaepen & Moreau, 2008).

In addition to quasistaticity, the Boussinesq approximation is applied (Oberbeck, 1879; Boussinesq, 1903; Gray & Giorgini, 1976; Tritton, 1977; Chillà & Schumacher, 2012). The governing equations of thermoelectric magnetoconvection (TEMC) are then

$$\mathbf{J} = \sigma (-\nabla\Phi + \mathbf{u} \times \mathbf{B} - S\nabla T), \quad (4.15a)$$

$$\nabla \cdot \mathbf{J} = 0, \quad (4.15b)$$

$$\frac{\partial \mathbf{u}}{\partial t} + (\mathbf{u} \cdot \nabla)\mathbf{u} = -\frac{1}{\rho}\nabla p + \frac{1}{\rho}(\mathbf{J} \times \mathbf{B}) + \nu\nabla^2\mathbf{u} + \alpha_T\Delta T\mathbf{g}, \quad (4.15c)$$

$$\nabla \cdot \mathbf{u} = 0, \quad (4.15d)$$

$$\frac{\partial T}{\partial t} + (\mathbf{u} \cdot \nabla)T = \kappa\nabla^2T, \quad (4.15e)$$

where ρ is fluid density, p is non-hydrostatic pressure, $\mathbf{g} = g\hat{\mathbf{e}}_z$ is the gravity vector, and κ is the thermal diffusivity. The external field is $\mathbf{B} = B\hat{\mathbf{e}}_b$. Note that Ohm's law (4.15a) has been simplified via the quasistatic approximation, such that the rotational part of electric field and perturbative second-order terms from $\mathbf{u} \times \mathbf{B}$ are not considered. Accordingly, in the bulk fluid, far from material interfaces, where net Seebeck effects are small, the quasistatic Lorentz force is $\mathbf{J} \times \mathbf{B} \sim -\sigma\mathbf{u}_\perp B^2$, where \mathbf{u}_\perp is the velocity perpendicular to the direction of the magnetic field. Therefore, the low- Rm Lorentz force acts as a drag that opposes bulk fluid velocities that are directed perpendicular to \mathbf{B} (Sarris *et al.*, 2006; Davidson, 2016). This quasistatic Lorentz drag depends only on B^2 . In sharp contrast, the thermoelectric component of the Lorentz force, $-\sigma S\nabla T \times \mathbf{B}$, varies linearly with \mathbf{B} . Therefore, the thermoelectric Lorentz force changes sign when the direction of the applied magnetic field is flipped.

The governing equations (4.15) can be nondimensionalized using H as length scale and U_{ff} as the velocity scale, such that the free-fall time $\tau_{ff} = H/U_{ff}$ is the time scale. Moreover, the external magnetic flux density B is the magnetic field scale, the bulk current density is scaled by $\sigma U_{ff} B$, the electric potential scale is $U_{ff} B H$, and ΔT is the temperature scale. The dimensionless governing equations of Oberbeck-Boussinesq thermoelectric magnetoconvection (TEMC) are

$$\nabla \cdot \mathbf{J} = 0, \quad (4.16a)$$

$$\mathbf{J} = -\nabla\Phi + \mathbf{u} \times \hat{\mathbf{e}}_b - Se\nabla T, \quad (4.16b)$$

$$\nabla \cdot \mathbf{u} = 0, \quad (4.16c)$$

$$\frac{\partial \mathbf{u}}{\partial t} + \mathbf{u} \cdot \nabla \mathbf{u} = -\nabla p + \sqrt{\frac{Ch^2 Pr}{Ra}} (\mathbf{J} \times \hat{\mathbf{e}}_b) + \sqrt{\frac{Pr}{Ra}} \nabla^2 \mathbf{u} + T \hat{\mathbf{e}}_z, \quad (4.16d)$$

$$\frac{\partial T}{\partial t} + \mathbf{u} \cdot \nabla T = \sqrt{\frac{1}{Ra Pr}} \nabla^2 T, \quad (4.16e)$$

where here \mathbf{u} is the dimensionless velocity of the fluid, p is the dimensionless non-hydrostatic pressure, \mathbf{J} is the dimensionless electric current density, $\mathbf{B} = \hat{\mathbf{e}}_b$ is the dimensionless flux

density of the external magnetic field, and T is the nondimensional temperature. The nondimensionalized vertical magnetic field is constant and uniform, $\hat{\mathbf{e}}_b = \pm \hat{\mathbf{e}}_z$.

This nondimensional control group may be decomposed into four parameters: the Prandtl number Pr , the Rayleigh number Ra , the Chandrasekhar number Ch , and the Seebeck number Se . The Prandtl number describes the thermo-mechanical properties of the fluid:

$$Pr = \frac{\nu}{\kappa}; \quad (4.17)$$

in liquid gallium, $Pr \approx 0.027$ at 40°C. The Rayleigh number characterizes the buoyancy forcing relative to thermoviscous damping:

$$Ra = \frac{\alpha_T \Delta T g H^3}{\nu \kappa}. \quad (4.18)$$

The Chandrasekhar number describes the ratio of quasistatic Lorentz and viscous forces:

$$Ch = \frac{\sigma B^2 H^2}{\rho \nu}. \quad (4.19)$$

The Seebeck number estimates the ratio of thermoelectric currents in the fluid and currents induced by fluid motions:

$$Se = \frac{|\tilde{S}| \Delta T / H}{U_{ff} B}. \quad (4.20)$$

Alternatively, Se can be cast as the ratio of the thermoelectrical potential and the motionally-induced potential in the fluid. Typical values of Se in our experiments with gallium-copper interfaces range from $O(10^{-2})$ to $O(1)$, implying that the Seebeck effect can generate dynamically significant experimental thermoelectric currents.

Lastly, the aspect ratio acts to describe the geometry of the fluid volume:

$$\Gamma = \frac{D}{H}, \quad (4.21)$$

where D is the inner diameter of the cylindrical container. We focus on $\Gamma = 2$ in this study, similar to Vogt *et al.* (2018a), and present only two $\Gamma = 1$ case results for contrast in section 4.11.

Number Names	Symbol	Definition	Equivalence	Current Study
Magnetic Reynolds	Rm	$\frac{U_{ff}H}{\eta}$	$RePm$	$\lesssim 10^{-2}$
Magnetic Prandtl	Pm	$\frac{\nu}{\eta}$		1.7×10^{-6}
Prandtl	Pr	$\frac{\nu}{\kappa}$		2.7×10^{-2}
Rayleigh	Ra	$\frac{\alpha g \Delta T H^3}{\nu \kappa}$		$\sim 2 \times 10^6$
Chandrasekhar	Ch	$\frac{\sigma B^2 H^2}{\rho \nu}$		$[0, 8.4 \times 10^4]$
Seebeck	Se	$\frac{ \tilde{S} \Delta T / H}{U_{ff} B}$		$\sim [10^{-2}, 1]$
Aspect Ratio	Γ	$\frac{D}{H}$		2.0
Reynolds	Re	$\frac{U_{ff}H}{\nu}$	$\sqrt{\frac{Ra}{Pr}}$	$\lesssim 8.7 \times 10^3$
Péclet	Pe	$\frac{U_{ff}H}{\kappa}$	\sqrt{RaPr}	$\lesssim 2.2 \times 10^2$
Convective Interaction	N_c	$\frac{\sigma B^2 H}{\rho U_{ff}}$	$\sqrt{\frac{Ch^2 Pr}{Ra}} = \frac{Ch}{Re}$	$\lesssim 10$
Thermoelectric Interaction	N_{TE}	$\frac{\sigma B \tilde{S} \Delta T}{\rho U_{ff}^2}$	$Se N_c$	$\lesssim 10$

Table 4.1: Nondimensional parameters and parameter groups in thermoelectric magnetoconvection (TEMC). The low values of the top two parameters show that the current experiments fall within the quasistatic approximation. The next five are the base parameters used to describe most of the experimental cases. The next four parameters are alternative groupings that arise in the nondimensional version of eq. (4.15).

Alternatively, the groups of the above parameters that exist in (4.16) and (4.25) are the Péclet number Pe , the Reynolds number Re , the convective interaction parameter N_C and the thermoelectric interaction parameter $N_C Se$. The Péclet number,

$$Pe = \frac{U_{ff} H}{\kappa} = \sqrt{RaPr}, \quad (4.22)$$

estimates the ratio of thermal advection and thermal diffusion in the thermal energy equation. The convective interaction parameter N_C is the ratio of quasistatic Lorentz drag and fluid inertia. It is defined as:

$$N_C = \frac{\sigma B^2 H}{\rho U_{ff}} = Ch \sqrt{\frac{Pr}{Ra}} = \frac{Ch}{Re}. \quad (4.23)$$

When $N_C \gtrsim 1$, the Lorentz force will tend to strongly damp buoyancy-driven convective turbulence. Lastly, the thermoelectric interaction parameter, N_{TE} is the product of the convective interaction parameter N_C and the Seebeck number Se . This parameter approximates the ratio between the thermoelectric Lorentz force and the fluid inertia, and is given by

$$N_{TE} = \frac{\sigma B |\tilde{S}| \Delta T}{\rho U_{ff}^2} = Se N_C. \quad (4.24)$$

Thus, when $Se \sim 1$, the thermoelectric forces can become comparable to the MHD drag, at least in the vicinity of the material interfaces where the thermoelectric currents are maximal.

The physical meanings of N_{TE} and N_C can be found in the Lorentz term of the governing equation. The $(Ra/Pr)^{-1/2}$ grouping in (4.16d) is the reciprocal of the Reynolds number Re . The $(RaPr)^{-1/2}$ group in (4.16e) is the reciprocal of the Péclet number. Further, using (4.16b), the Lorentz term in (4.16d) expands to:

$$\begin{aligned} \sqrt{\frac{Ch^2 Pr}{Ra}} (\mathbf{J} \times \hat{\mathbf{e}}_b) &= [N_C (-\nabla \Phi + \mathbf{u} \times \hat{\mathbf{e}}_b) - N_{TE} \nabla T] \times \hat{\mathbf{e}}_b \\ &= N_C [(\hat{\mathbf{e}}_b \times \nabla \Phi) - \mathbf{u}_\perp] + N_{TE} (\hat{\mathbf{e}}_b \times \nabla T), \end{aligned} \quad (4.25)$$

where \mathbf{u}_\perp is the velocity perpendicular to the vertical direction \mathbf{e}_z . The first term on the right-hand side is due to irrotational electric fields in the fluid, which are likely small in our experiments. The second term is the quasi-static Lorentz drag, and the third term is due to

thermoelectric currents in the fluid. The nondimensional groups in (4.25) are the convective interaction parameter, $N_C = Ch\sqrt{Pr/Ra}$, and the thermoelectric interaction parameter, $N_{TE} = Se N_C$.

All the nondimensional parameters and their estimated values for our study are summarized in Table 4.1.

4.2.3 Previous Studies of Turbulent Magnetoconvection

Despite its broad relevance to natural and industrial systems, magnetoconvection has not been studied in great detail relative to non-magnetic RBC (Ahlers *et al.*, 2009) and rotating convection (Aurnou *et al.*, 2015b). Further, laboratory and numerical studies of turbulent MC have largely neglected thermoelectric effects to date (cf. Zhang *et al.* (2009)). Thus, in reviewing the current state of turbulent MC studies, TE effects will not be considered.

In the limit of weak magnetic fields, such that $N_C \rightarrow 0$, turbulent MC behaves similarly to RBC (Cioni *et al.*, 2000b; Zürner *et al.*, 2016), with the flow self-organizing into a large-scale circulation (LSC). Thus, the LSC is the base flow structure in turbulent MC when the dynamical effects of the magnetic field are subdominant (Zürner *et al.*, 2020). LSCs, the largest turbulent overturning structure in the bulk fluid, have been studied extensively in RBC systems (Xia *et al.*, 2003; Xi *et al.*, 2004; Sun *et al.*, 2005; Von Hardenberg *et al.*, 2008; Brown & Ahlers, 2009; Ahlers *et al.*, 2009; Chillà & Schumacher, 2012; Pandey *et al.*, 2018; Stevens *et al.*, 2018; Vogt *et al.*, 2018a; Zürner *et al.*, 2020).

Vogt *et al.* (2018a) carried out turbulent RBC laboratory (and associated numerical) experiments in a $\Gamma = 2$ liquid gallium cell using the same laboratory device as we employ in this study. Coupling the DNS outputs to laboratory thermo-velocimetric data, Vogt *et al.* (2018a) found that the turbulent liquid metal convection was dominated by a so-called jump rope vortex (JRV) LSC mode, instead of the sloshing and torsional modes found in the majority of $\Gamma = 1$ experiments (Funfschilling & Ahlers, 2004; Funfschilling *et al.*, 2008;

Brown & Ahlers, 2009; Xi *et al.*, 2009; Zhou *et al.*, 2009). The JRV had a characteristic oscillation frequency \tilde{f}_{JRV} of

$$\tilde{f}_{JRV} = f_{JRV}/f_\kappa = 0.027Ra^{0.419}, \quad (4.26)$$

where f_κ is the inverse of the thermal diffusion timescale

$$\tau_\kappa = H^2/\kappa. \quad (4.27)$$

Ultrasonic measurements yielded an LSC velocity scaling corresponding to

$$Re_{JRV} = 0.99 (Ra/Pr)^{0.483}, \quad (4.28)$$

formulated using their mean Prandtl number value, $Pr \simeq 0.027$. These velocity measurements approach the free-fall velocity scaling in which $Re = U_{ff}H/\nu = (Ra/Pr)^{1/2}$. Thus, we will use U_{ff} as the characteristic velocity scale when nondimensionalizing our equations and in the model of thermoelectric LSC precession developed in §4.7.

The quasistatic Lorentz force does, however, impede the convective motions in finite N_C cases. Zürner *et al.* (2020) used ultrasonic velocimetry measurements to develop an empirical scaling law for the global characteristic velocity, U_{MC} , in GaInSn MC experiments:

$$U_{MC} = \left(\frac{1}{1 + 0.68 N_C^{0.87}} \right) U_{ff}. \quad (4.29)$$

In §4.7, we will test both U_{MC} and U_{ff} in our model for thermoelectrical precession of the LSC, and show that the U_{MC} -based predictions better fit our precessional frequency measurements.

The turbulent LSC mode breaks down in MC when $N_C \gtrsim 1$ (Cioni *et al.*, 2000b; Zürner *et al.*, 2019, 2020). This is roughly analogous to the loss of the LSC in rotating convection when the Rossby number is decreased below unity (Kunnen *et al.*, 2008; Horn & Shishkina, 2015). In the supercritical $N_C \gtrsim 1$ regime, the convection in the fluid bulk should then become multi-cellular, akin to the flows shown in Yan *et al.* (2019).

Near the onset of the magnetoconvection, wall modes appear near the vertical boundaries and will become unstable before bulk convection in many geometrically-confined MC systems (Busse, 2008).

It is important to stress that MC wall modes do not drift along the wall, in contrast to rotating convection (Ecke *et al.*, 1992), since the quasistatic Lorentz force does not break azimuthal reflection symmetry (Houchens *et al.*, 2002). The multi-cellular and magneto-wall mode regimes were both investigated in the numerical MC simulations of Liu *et al.* (2018). The wall modes were found not to drift in their large-aspect ratio simulations, similar to the experimental findings of Zürner *et al.* (2020). Further, Liu *et al.* (2018) showed that the wall modes could become unstable and inject nearly axially-invariant jets into the fluid bulk.

Strong wall mode injections are also found in the numerical MC simulations of Akhmedagaev *et al.* (2020). These injected axially-invariant jets are accompanied by a net azimuthal drift of the flow field, whose drift direction appears to be randomly set. We interpret these drifting flows as being controlled by the collisional interaction of the jets, qualitatively similar in nature to the onset of the shearing flows in the plane layer simulations of Goluskin *et al.* (2014). Therefore, we argue that the drifting effect found in the $N_C > 1$ near-onset numerical simulation by Akhmedagaev *et al.* (2020) fundamentally differs from the LSC precession found in the thermoelectrically-active $N_C \lesssim 1$ experiments reported herein.

4.3 Experimental Set-up and Methods

Laboratory MC experiments are conducted using UCLA’s ROMAGdevice, as shown in figure 4.2. See the appendix of King *et al.* (2012b) for device details. Here, a vertical magnetic field is applied to an upright, non-rotating cylindrical tank filled with liquid gallium ($Pr \simeq 0.027$). The magnetic field vector is

$$\mathbf{B} = B\hat{\mathbf{e}}_{\mathbf{b}}, \quad \text{where} \quad \hat{\mathbf{e}}_{\mathbf{b}} = \pm\hat{\mathbf{e}}_{\mathbf{z}}, \quad (4.30)$$

such that $\hat{\mathbf{e}}_{\mathbf{b}} = +\hat{\mathbf{e}}_z$ corresponds to an upward magnetic field vector and $\hat{\mathbf{e}}_{\mathbf{b}} = -\hat{\mathbf{e}}_z$ corresponds to a downward magnetic field vector. The magnetic field is generated by an hourglass solenoid. With the tank centered along the bore of the solenoid, the vertical component of the magnetic field is constant over the fluid volume to within $\pm 0.5\%$ (King & Aurnou, 2015). The magnetic field strength can be varied from 0 to 650 gauss, corresponding to a maximum Chandrasekhar value of $Ch = 8.4 \times 10^4$.

The material properties of liquid gallium are adapted from Aurnou *et al.* (2018). The container is made up of a cylindrical sidewall and a set of top and bottom end-blocks; the sidewall has an inner diameter $D = 2R = 196.8$ mm and the fluid layer height is fixed at $H = 98.4$ mm such that $\Gamma = 2.0$. We control the thermoelectric effects by changing the materials of these bounding elements. In specific, two different sets of boundaries are used. The first set is made up of an acrylic sidewall and Teflon coated aluminum end-blocks, in order to achieve electrically-insulated boundary conditions. The second set uses a stainless steel 316L sidewall and copper end-blocks, which provide electrically-conducting boundary conditions. The copper is uncoated and has been allowed to chemically interact with the gallium. This copper interface is not perfectly smooth due to gallium corrosion, allowing gallium to fully wets the surface. This is important as liquid metals often fail to make good surface contact with extremely smooth, pristine surfaces, likely due to strong surface tension effects.

The bottom of the convection stack is heated with a non-inductively wound electrical resistance pad (figure 4.2(c)), with the heating power held at a fixed value, P_{input} , in each experiment. Heat is extracted at the top of the convection stack by circulating thermostated cooling fluid through an aluminum heat exchanger that contains a double-spiral internal channel. Although the double wound channel minimizes the temperature gradients within the heat exchanger, the inlet and outlet ports must be at different temperatures due to the extraction of heat from the tank. The locations of the cooler inlet and warmer outlet are marked by arrows and triangles in figure 4.2(d), and in later figures just by the triangles.

By maintaining the time-mean difference between the horizontally averaged temperatures on the top and bottom boundaries, we are able to fix $Ra \approx 2 \times 10^6$ for all the experiments in this study. The sidewall of the tank is thermally insulated by a 5-cm thick Aspen Aerogels' Cryogel X201 blanket (not shown), which has a thermal conductivity of 0.015 W/(m K). The heating power lost from the sidewall and endwalls, P_{loss} , is estimated and then subtracted from the total input power, so that the effective heating power is $P = P_{input} - P_{loss}$.

Twelve thermistors are embedded in the top and bottom end-blocks roughly $\delta z = 2$ mm from the fluid-solid interface, and at cylindrical radius $r = 0.71R$. These are shown as the red probes in figure 4.2(d)). These thermistors are evenly separated 60° apart from each other in azimuth. Another six thermistors, shown in green in figure 4.2(d), are located on the exterior wall of the sidewall in the tank's midplane. The midplane thermistors are located at the same azimuth values as the top and bottom block thermistors, forming six vertically aligned thermistor triplets. Temperature data are simultaneously acquired at a rate of 10 Hz. The top and bottom thermistors are located 2 mm from the fluid surfaces and extend horizontally 28.9 mm into the lids from the side.

This thermometry data is discretized in both space and time. The discrete temperature time series data is expressed as

$$T_{ij}^k = T(\phi_i, t_j, z_k). \quad (4.31)$$

The index i ranges from 1 to 6, corresponding to the thermistor locations at 0° , 60° , 120° , 180° , 240° , and 300° azimuth, respectively. The time step in the data acquisition is denoted by the index j , which ranges from 1 to a final index value N for a given time series. Thermistor height is labeled via index $k = 1, 2$, or 3 , corresponding to the bottom block thermistors, the midplane thermistors and the top block thermistors, respectively. The bottom block thermistors are located at $z_1 = -2$ mm = '*bot*'; the midplane thermistors are at $z_2 = 49.3$ mm = '*mid*'; and the top block thermistors are set at $z_3 = 100.6$ mm = '*top*'. No index is given for the radial position of the thermistors, so we reiterate that the end-block thermistors ($k = 1, 3$) are located at $r = 69.7$ mm = $0.71R$, whereas the midplane

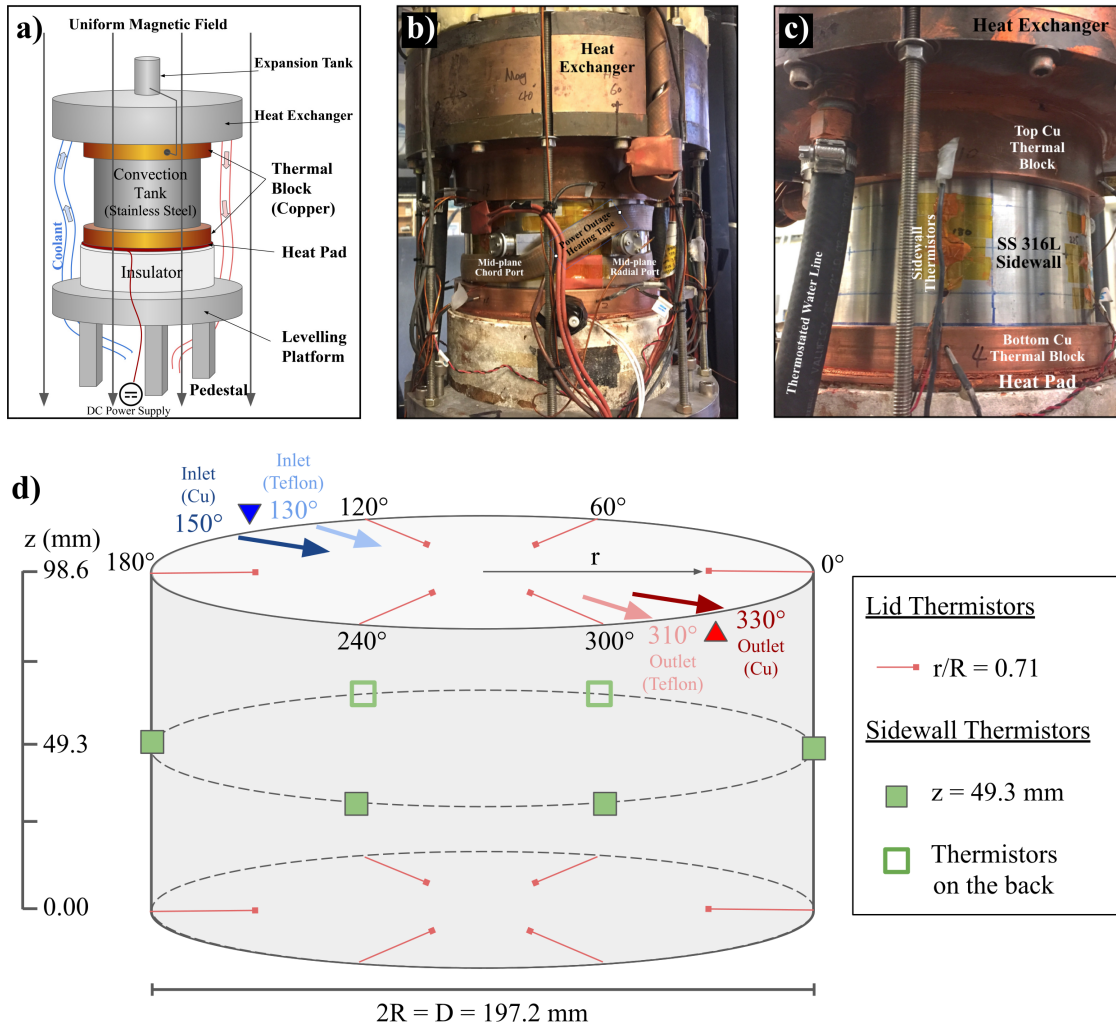


Figure 4.2: a) Schematic of the laboratory apparatus. b) Image of the convection tank with heat exchanger and safety heating tape in case of a power outage. c) Closer in image of the sidewall and top and bottom thermal end-blocks. The device is thermally insulated by an aerogel blanket that is not shown here. d) Schematic showing the top, bottom, and midplane thermistor placements. The blue and red arrows on the top mark the azimuth position of the inlet (cooler coolant) and outlet (warmer coolant) locations on the heat exchanger. In the following figures, these azimuthal angles are marked by the downward blue triangle and the upward red triangle.

thermistors ($k = 2$) are on the exterior of the sidewall at $r = 100 \text{ mm} = 1.02R$.

The thermometry data is used to calculate the time-averaged temperature difference across the height of the fluid layer, ΔT , defined as

$$\Delta T = T^{bot} - T^{top}, \quad (4.32)$$

where T^{bot} and T^{top} are the time and azimuthal mean temperatures of the bottom and top end-block boundaries. These horizontal means are calculated via

$$T^{bot} = \frac{1}{6N} \sum_{i=1}^6 \sum_{j=1}^N T_{ij}^{bot} \quad \text{and} \quad T^{top} = \frac{1}{6N} \sum_{i=1}^6 \sum_{j=1}^N T_{ij}^{top}. \quad (4.33)$$

This indexing convention will be used throughout this treatment. Further, T^k denotes the time-azimuthal mean temperature on the index k horizontal plane.

The material properties of the working fluid are determined using the mean temperature of the fluid volume

$$\bar{T} = (T^{bot} + T^{top}) / 2. \quad (4.34)$$

These, in turn, can then be used to measure the heat transfer efficiency of the system, characterized by the Nusselt number,

$$Nu = \frac{qH}{\lambda\Delta T}, \quad (4.35)$$

where $q = 4P/(\pi D^2)$ is the heat flux, and $\lambda = 31.4 \text{ W}/(\text{m K})$ is the thermal conductivity of gallium. The Nusselt number describes the ratio of the total and conductive heat transfer across the fluid layer (Cheng & Aurnou, 2016).

The physical properties of the boundary are also very important in this study. The isothermality of the bounding end-blocks is typically characterized by the Biot number,

$$Bi = \frac{Nu(\lambda/H)}{\lambda_s/D_s}, \quad (4.36)$$

where λ_s and D_s are the solid end-block's thermal conductivity and thickness, respectively. This parameter estimates the effective thermal conductance of the convective fluid layer

to that of the solid bounding block. When $Bi \ll 1$, it is typically argued that boundary conditions are nearly isothermal, since the thermal conductance in the solid so greatly exceeds that of the fluid. We estimate $Bi = 0.07$ for the top copper lid and $Bi = 0.22$ for the bottom Cu end-block. A similar estimation suggests that $Bi = 0.24$ for both Teflon-coat aluminum boundaries. These Bi values would suggest that boundary thermal anomalies are approximately 10% of ΔT (Verzicco, 2004).

This estimate, however, is not accurate in moderate Pe , low Pr liquid metal convection (Vogt *et al.*, 2018a), where the convective flux is predominantly carried by large-scale inertial flows with thermal anomalies that approach ΔT . These large amplitude thermal anomalies tend to generate significant signals on the container boundaries.

Furthermore, in low to moderate Pe liquid metal convection, higher Nu implies larger interior temperature gradients since the convective heat flux is carried by large-scale, large amplitude temperature anomalies, instead of via small-scale turbulent plumes (Grossmann & Lohse, 2004). These temperature anomalies imprint on the top and bottom boundaries and create non-isothermal interfacial conditions. We infer from our T_{ij}^k data that significant interfacial non-isothermality exists in our experiments and that these interfacial thermal anomalies can generate thermoelectric currents that drive long-period dynamics in our TE-MC cases at $0.1 \lesssim N_C \lesssim 1$.

4.4 Magnetoconvection with Electrically Insulating Boundaries

A baseline experiment is presented first in which the boundaries are electrically insulating. Aluminum end-blocks coated in Teflon ($\sigma \approx 10^{-24}$ S/m) are used in conjunction with an acrylic sidewall. The Rayleigh number is fixed at $Ra = 1.61 \times 10^6$ and the equilibrated experiment is run continuously for $t = 42.8 \tau_\kappa = 9.6 \times 10^3 \tau_{ff}$. During this 8.9-hour data acquisition, three separate sub-experiments are carried out. During the first $13.6 \tau_\kappa$, an 120 gauss downwardly directed ($\hat{\mathbf{e}}_b = -\hat{\mathbf{e}}_z$) magnetic field is applied, such that $Ch =$

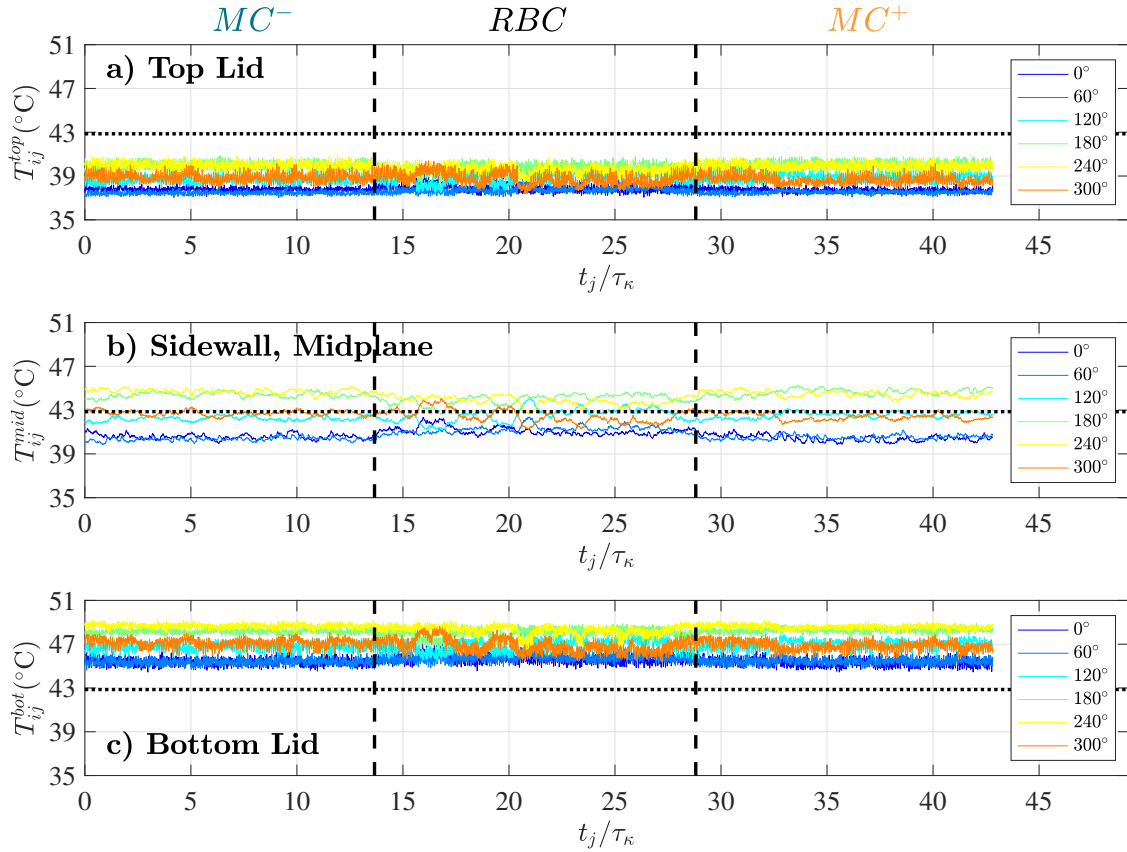


Figure 4.3: Temperature time series for the $Ra = 1.61 \times 10^6$, $Nu = 5.8$ electrically-insulated (Teflon) boundary conditions experiment. Data from thermistors, with locations shown in Figure 4.2d, embedded in the top boundary T_{ij}^{top} in (a); located on the exterior of the acrylic sidewall midplane T_{ij}^{mid} in (b); and embedded in the bottom boundary T_{ij}^{bot} in (c). The mean fluid temperature is $\bar{T} = 42.90^\circ\text{C}$, as marked by the horizontal dotted lines in each panel. The abscissa shows the time normalized by the thermal diffusion time scale t/τ_κ . This experiment contains three successive subcases that are divided by two dashed vertical lines: *Insulating MC⁻*, *Insulating RBC*, and *Insulating MC⁺*. No significant differences are found between the *Insulating MC⁻* and *Insulating MC⁺* cases, as is expected for non-thermoelectric, quasistatic magnetoconvection.

2.42×10^3 , and $N_C = 0.31$. This sub-case is called *Insulating MC⁻*. The magnetic field is set to zero in the next sub-case, *Insulating RBC*, which extends from $t = 13.6 \tau_\kappa$ to $28.8 \tau_\kappa$. The 120 gauss magnetic field is turned back on, but its direction is flipped such that it is directed upwards ($\hat{\mathbf{e}}_b = +\hat{\mathbf{e}}_z$) in the last sub-case, *Insulating MC⁺*, which runs from $t = 28.8 \tau_\kappa$ to $42.8 \tau_\kappa$. The Nusselt number is approximately constant, $Nu \simeq 5.8$, in all three sub-cases.

Figure 4.3 shows the temperature time series from the electrically-insulating experiment on a) the top end block T_{ij}^{top} , (b) the sidewall midplane T_{ij}^{mid} , and (c) the bottom end block T_{ij}^{bot} . The horizontal axis shows time normalized by the nondimensional thermal diffusion time t/τ_κ . In each panel, the line color represents an individual thermistor, each spaced 60 degrees apart in each layer (as shown in Figure 4.2).

The temperature time series in the midplane contains less high-frequency variance relative to the top and bottom block thermistor signals because the measurement is taken outside the acrylic sidewall, and thus is damped by skin effects. The temperatures in the top block are all well below the mean temperature of the fluid (black dotted line); the midplane temperatures are adequately situated around the mean temperature line, and the bottom block temperatures are all well above the mean temperature. However, the temperature range in each panel covers nearly 50% of the mean temperature difference ΔT across the fluid layer. This implies strong horizontal temperature anomalies exist in the end blocks, even though the Biot numbers for this experiment is well below unity ($Bi \simeq 0.24$). The RBC case features slightly lower peak-to-peak temperature variations in the midplane thermistors, along with a slightly higher variance in each time series. This suggests that the RBC case carries more of the convective heat flux via higher speed, magnetically undamped flows with regards to the *MC⁻* and *MC⁺* cases. Importantly for later comparisons to cases with electrically-conducting boundaries, the *MC⁻* and *MC⁺* cases are essentially identical in all their statistical properties and behaviors. Thus, these two MC cases are not sensitive to the direction of \mathbf{B} , as is expected in quasi-static, non-thermoelectrically-active magneto-

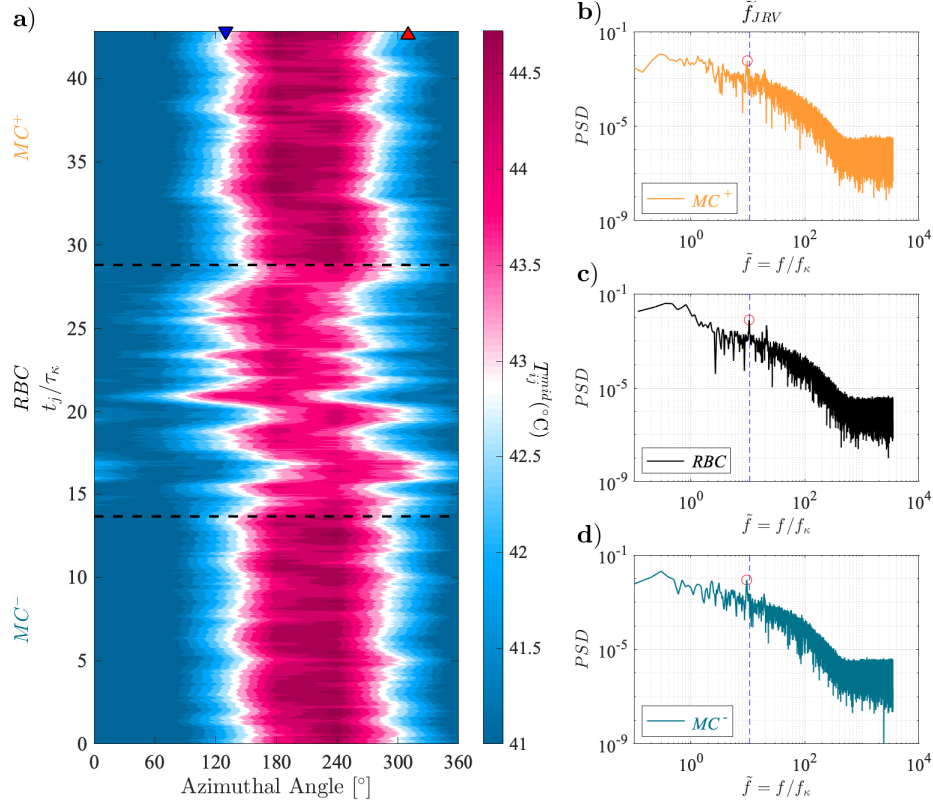


Figure 4.4: Electrically-insulating boundary study: (a) a contour map of the mid-plane sidewall temperature field T_{ij}^{mid} in the $Ra = 1.61 \times 10^6$ case (i.e., corresponding to fig. 4.3(b)). The horizontal axis shows the azimuthal angle around the tank; the vertical axis shows time normalized by τ_κ . The blue, downward (red, upward) triangle on the top axis denotes the azimuth of the heat exchanger inlet (outlet) location. The black dashed lines separate the *Insulating MC⁻*, *Insulating RBC* and *Insulating MC⁺* subcases. Hann-windowed FFTs of the temperature data from the midplane thermistor located at 120° are shown for (b) the *Insulating MC⁺* subcase; (c) the *Insulating RBC* subcase; (d) the *Insulating MC⁻* subcase. The red circles mark the lowest frequency sharp spectral peaks that correspond to the empirical characteristic frequency prediction for turbulent RBC (Vogt *et al.*, 2018a), $\tilde{f}_{JRV} = f_{JRV}/f_\kappa \approx 10.77$, shown as the blue dashed vertical lines in each spectrum.

convection.

Figure 4.4(a) shows the spatiotemporal evolution of the midplane temperature data T_{ij}^{mid} in the electrically insulating experiment. The colormap represents the temperature, in which red (blue) regions are hotter (colder) relative to the mean value (white). The midplane temperature field contains a warmer region on one side of the tank and a downwelling region antipodal to that, as found in RBC cases with a single LSC (Brown & Ahlers, 2007; Vogt *et al.*, 2018a; Zürner *et al.*, 2019). Thus, we argue based on figure 4.4(a) that a turbulent LSC is present in these electrically-insulating boundaries $N_C \lesssim 1$ experiments, and that it maintains a nearly fixed azimuthal alignment for over $40 \tau_\kappa$.

Figures 4.4(b)-(d) show the spectral power density of the averaged temperature signals from each horizontal plane plotted versus normalized frequency, $\tilde{f} = f/f_\kappa$. The vertical dashed lines denote the normalized frequency predictions, \tilde{f}_{JRV} , for the jump rope LSC described in Vogt *et al.* (2018a). The lowest frequency sharp spectral peaks correspond to the JRV frequency and are marked with red circles, $f_{peak}/f_\kappa \approx 10.51$, matching that of Vogt *et al.* (2018a) to within 2.5% in the *Insulating RBC* case. (The broad lower frequency peaks correspond to the slow meanderings of the LSC plane.) The distinct sharp peaks in both the *Insulating MC⁺* and the *Insulating MC⁻* FFTs are $\approx 25\%$ lower than \tilde{f}_{JRV} . We infer then, based on figure 4.4, that a quasi-stationary turbulent LSC flow is maintained in these electrically insulating, $N_C < 1$ experiments. The magnetic field does, however, cause a roughly 25% decrease in the LSC oscillation frequency, likely because magnetic drag reduces the characteristic flow speeds. This agrees adequately with eq. (4.29), which predicts a 20% decrease in flow speed at $N_C = 0.31$.

Following prior LSC studies (Cioni *et al.*, 1997; Brown & Ahlers, 2009; Xi *et al.*, 2009; Zhou *et al.*, 2009), we approximate the horizontal temperature profile as a sinusoid varying with azimuth angle ϕ at each point in the time series:

$$T_{fit}^k(t_j) = A_j^k \cos(\phi - \xi_j^k) + T_j^k. \quad (4.37)$$

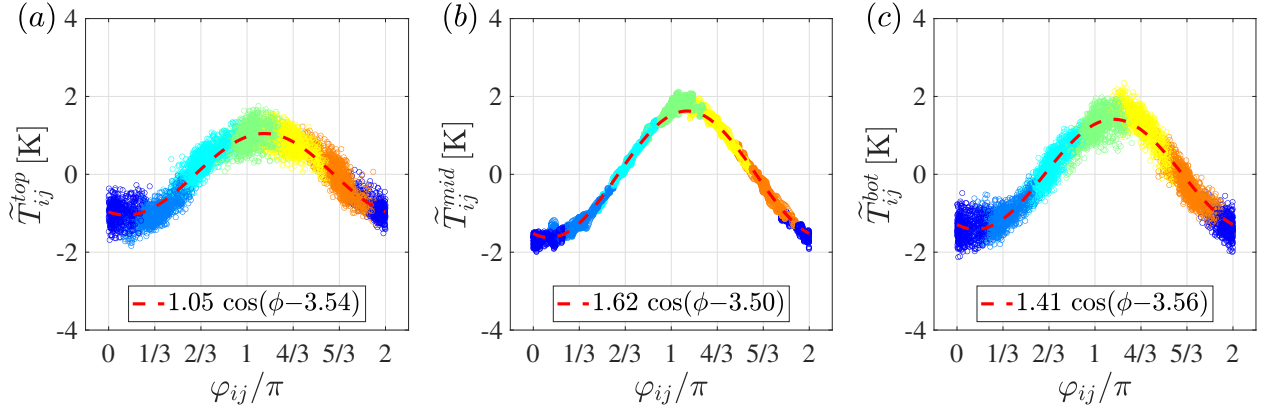


Figure 4.5: Temperature data of the *Insulating RBC* case shifted azimuthally into the best fit LSC frame, \tilde{T}_{ij}^k , in (a) the top block; (b) the sidewall midplane; and (c) the bottom block. The vertical axis is the temperature minus the azimuthal mean temperature at each time step. Different colors are used to label the location of the thermistors in the lab frames as the LSC fluctuates around its mean position following the color scale convention used in figure 4.3. The colors from left (blue) to right (orange) correspond to thermistors $i = 1$ to 6 , respectively. The time-averaged best fit sinusoidal temperature profile is shown via the dashed red line in each panel.

On each z -level, A_j^k is the instantaneous amplitude of the sinusoidal temperature variation, ξ_j^k denotes the instantaneous azimuthal orientation of the LSC plane, and the instantaneous azimuthal-mean temperature is T_j^k . Using eq. (4.37), we best fit each z -level's temperature data at every time step.

Figure 4.5 shows the *insulating RBC* temperature anomaly on the top plane (a), midplane (b), and bottom planes (c), but with the data at each time step azimuthally-shifted into the best-fit LSC frame. This is accomplished by plotting \tilde{T}_{ij}^k , defined as

$$\tilde{T}_{ij}^k \equiv T_{ij}^k(\varphi_{ij}^k, t_j) - T_j^k \quad \text{where} \quad \varphi_{ij}^k \equiv \phi_{ij}^k - [\xi_j^k - \xi] . \quad (4.38)$$

The new azimuth variable φ_{ij}^k shifts each instantaneous thermistor measurement T_{ij}^k to its azimuthal location relative to the best fit LSC azimuthal orientation angle ξ_j^k in eq. (4.37). The best fit LSC orientation angle averaged over time and over z -level is $\xi = 3.55$ rad for this case. The time-mean best fit sinusoid for the data on each z -level is plotted as a dashed

red in each panel, with the best fit given in the legend box. The color of each thermistor follows the convention used in figure 4.3. The well-defined patches of color in figure 4.5 are aligned with the individual thermistor locations, producing a rainbow color pattern. The relative fixity of these color patches shows that the approximately sinusoidal temperature pattern does not drift significantly in time in this sub-case. Although they are not shown here, similar rainbow patterns also exist for the two insulating MC sub-cases.

In sum, we take figures 4.3 through 4.5 as evidence of a quasi-stationary, container-scale LSC in all three electrically insulating sub-cases made with $N_C \lesssim 0.3$.

4.5 Thermoelectric Magnetoconvection with Conducting Boundaries

Another approximately $48\tau_\kappa$ experiment has been carried out, but with all the boundaries electrically conducting such that thermoelectric effects can now affect the system, in contrast to the electrically insulating experiment presented in §4.4. The end-blocks used here are copper and the sidewall is stainless steel 316L. The heating power is fixed at 396.2W, leading to $Ra \simeq 1.8 \times 10^6$ and $Nu \simeq 5.9$. The experiment is made up of three successive sub-cases, *Conducting MC⁺*, *Conducting RBC*, and *Conducting MC⁻*, having an upward 120 gauss applied magnetic field $+\hat{e}_z$, no magnetic field, and then a downward 120 gauss magnetic field $-\hat{e}_z$, respectively. This corresponds to $N_C \simeq 0.3$ in the two MC sub-cases and $N_C = 0$ in the RBC case, similar to the prior insulating sub-cases. Figure 4.6 - 4.8 correspond to figure 4.3 - 4.5. The exact parameters are given in the Appendix of Xu *et al.* (2022).

Figure 4.6 presents the T_{ij}^k thermistor time series data from this electrically conducting experiment, following the same plotting conventions as figure 4.3. The time series shows that the *Conducting RBC* sub-case generates a nearly stationary LSC structure, similar to the time series in figure 4.3. In the *Conducting MC⁺* and *Conducting MC⁻* cases, the temperature signals oscillate periodically around the mean temperature of the same layer

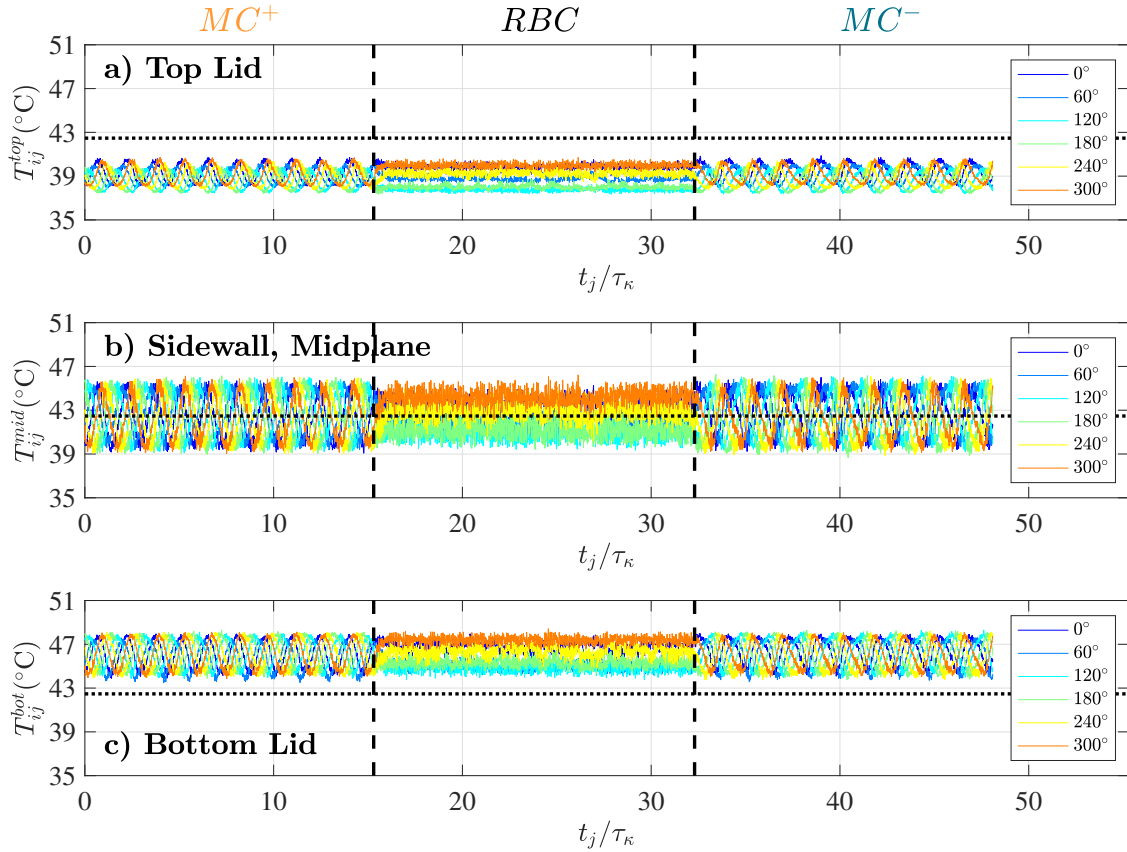


Figure 4.6: Temperature time series for the $Ra \simeq 1.82 \times 10^6$, $Nu \simeq 5.86$ electrically-conducting boundary conditions experiment. Data from thermistors, with locations shown in Figure 4.2d, embedded in the top boundary T_{ij}^{top} in (a); located on the exterior of the acrylic sidewall mid-plane T_{ij}^{mid} in (b); and embedded in the bottom boundary T_{ij}^{bot} in (c). The mean fluid temperature is $\bar{T} = 42.47^\circ \text{C}$, as marked by the horizontal dotted lines in each panel. The abscissa shows the time normalized by the thermal diffusion time scale t/τ_κ . This experiment contains three successive subcases that are divided by two dashed vertical lines: *Conducting* MC^- , *Conducting* RBC and *Conducting* MC^+ . Large amplitude, low frequency thermal oscillations are observed at all thermistor locations in the *Conducting* MC^+ and *Conducting* MC^- subcases, which differs greatly with respect to the corresponding *Conducting* MC subcases in figure 4.3.

height. Moreover, the oscillation of different heights are in phase at each azimuthal position. The temperature measurements indicate the presence of a container scale, coherent thermal structure that precesses in time.

Figure 4.7 follows the same plotting conventions as figure 4.4. Figure 4.7(a) shows a temperature contour map of the midplane sidewall thermistors, T_{ij}^{mid} for the electrically-conducting experiment. In the *Conducting RBC* case, the temperature pattern remains roughly fixed in place, similar to the insulating case. In contrast to this, the temperature field is found to coherently translate in the $-\hat{e}_\phi$ direction in the *Conducting MC⁺* sub-case and to translate in the $+\hat{e}_\phi$ direction in the *Conducting MC⁻* sub-case. However, at any instant in time, t_j , the azimuthal temperature pattern is similar to that of the LSC-like pattern found in the electrically-insulating experiment, with one warmer region and an antipodal cooler region.

Comparing figures 4.4(a) and 4.7(a) shows that the instantaneous LSC-like temperature pattern precesses around the container only in MC cases with electrically conducting boundaries. Further, the precession direction depends on the sign of the magnetic field, as cannot be the case for standard quasi-static MHD processes. Thus, we hypothesize that an LSC exists in these electrically-conducting sub-cases, and that thermoelectric current loops exist across the container's electrically conducting boundaries which drive the LSC to precess azimuthally in time. Our model for this thermoelectric magnetoprecession (MP) process is presented in §4.7.

The figure 4.7(a) contour map also reveals that a slight asymmetry in the precession rate of *Conducting MC⁻* case which does not exist in the *Conducting MC⁺* case. The precessional banding of the temperature field is uniform in the *Conducting MC⁺* case. In contrast, the bands have a slight variation in thickness in the *Conducting MC⁻* case. We do not currently have an explanation for this difference between the *MC⁻* and *MC⁺* cases.

Figures 4.7(b)-(d) show the time-averaged, thermal spectral power density plotted versus normalized frequency for the *Conducting MC⁺*, *Conducting RBC*, and *Conducting MC⁻*

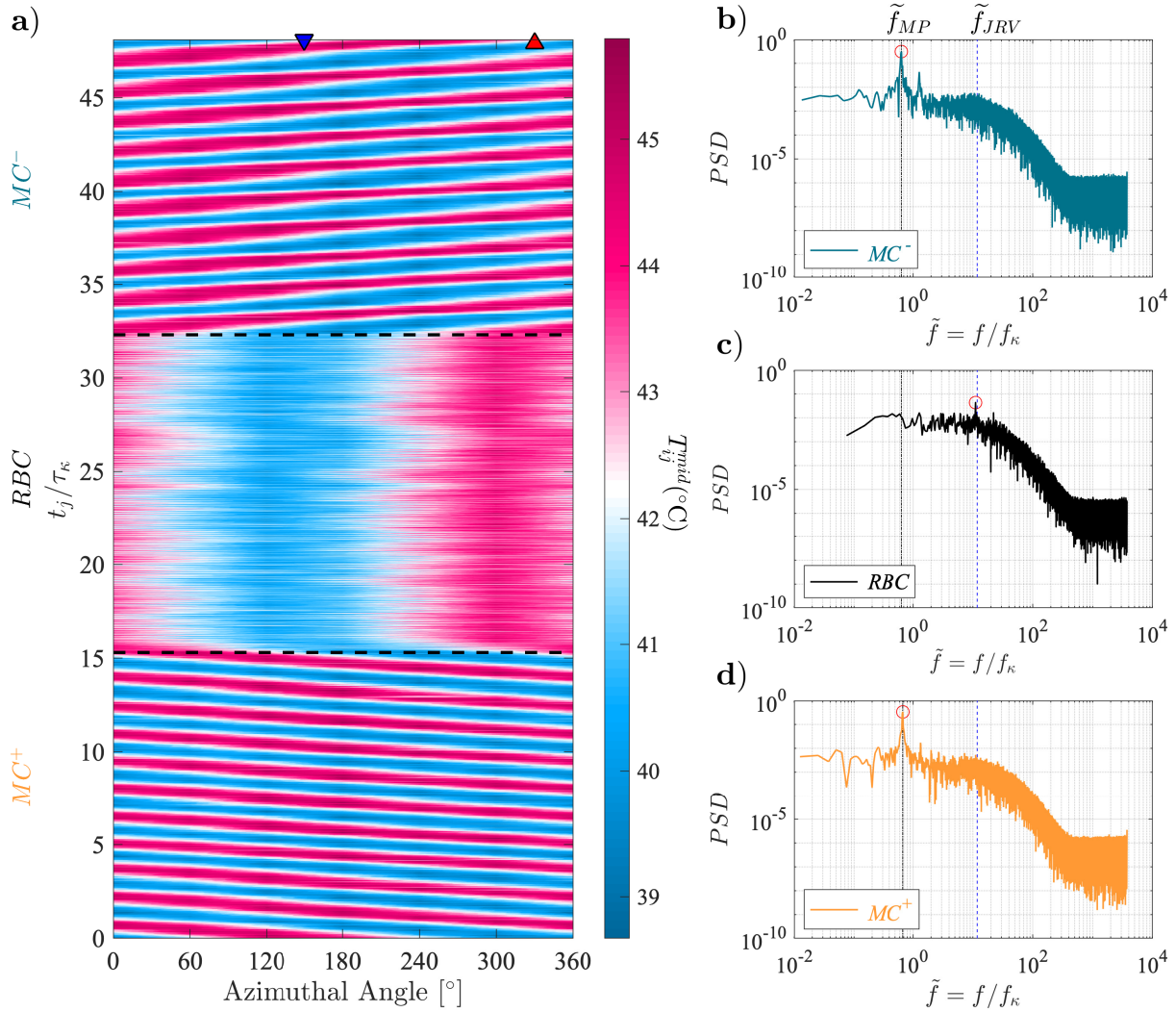


Figure 4.7: Identical to figure 4.4, but showing the $Ra \approx 1.8 \times 10^6$, $Nu \approx 5.8$ *Conducting* MC^+ , *Conducting* RBC , *Conducting* MC^- subcases experiment. However, all the FFTs here are analyzed using the *Long* version of the same experiments. The averaged low frequency spectral peak in the *Conducting* MC subcases is marked by the vertical black dot-dashed lines in (b), (c) and (d). This corresponds to the magnetoprecessional (MP) mode and its nondimensional frequency is labeled \tilde{f}_{MP} .

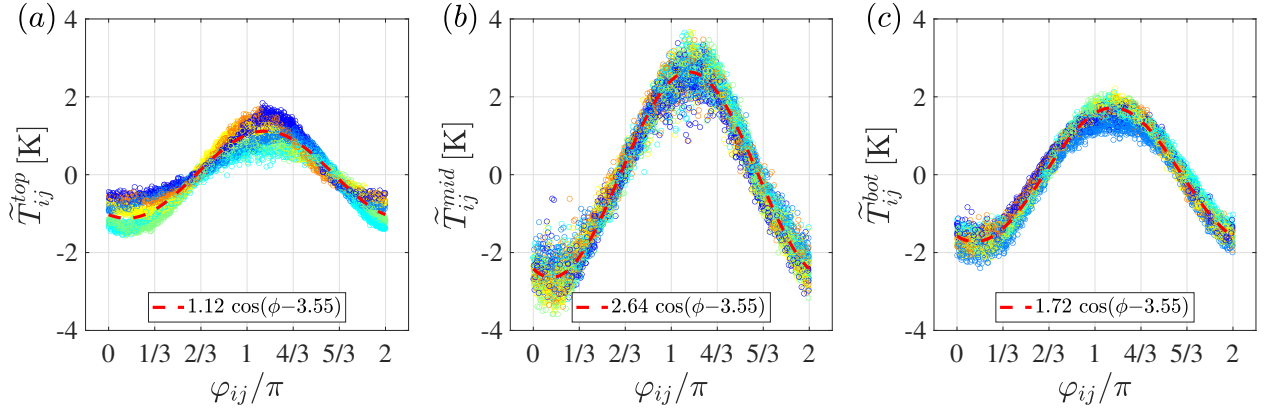


Figure 4.8: Temperature anomaly \tilde{T}_{ij}^k as defined eq. (4.38) on the a) top; b) midplane; and c) bottom horizontal planes in the LSC frame of the *Conducting MC⁻* subcase. For ease of comparison, we set $\xi = 3.55$, which is the same as the *Insulating RBC* case, since the precessing case does not have a meaningful time-averaged LSC position. The same colors are also used to label the location of the thermistors in the lab frames as figure 4.5. Contrary to figure 4.5, where the same color data cluster near a fixed azimuth, here each color is spread out and covers the entire azimuth relative to the LSC plane, which occurs because the LSC plane is constantly precessing through all the azimuthal angles. Panels (a) – (c) show that a sinusoidal temperature profile exists at each horizontal level k , with the largest amplitude in the midplane. The time-averaged best fit sinusoidal temperature profile is shown via the dashed red line in each panel.

sub-cases. To better identify the spectral peaks, these FFTs are made using three longer experimental cases, each up to $\approx 100\tau_\kappa$ in duration but employing the same control parameters. The frequencies are normalized by the thermal diffusion frequency $\tilde{f} = f/f_\kappa = f\tau_\kappa$. Red circles mark the peak frequency in each spectrum. The peak of the *Conducting RBC* sub-case is in good agreement with the predicted jump rope vortex frequency $\tilde{f}_{JRV} = 11.79$ (dashed blue vertical line). The magnetoprecessional frequency dominates the *Conducting MC⁻* and *Conducting MC⁺* spectra in figures 4.7 (b) and (d), respectively. The peak frequencies are nearly identical in *Conducting MC⁻* and *Conducting MC⁺* cases, with a mean value $\tilde{f}_{MP} = 0.66$ (black dot-dashed vertical line). Thus, magnetoprecession is slow relative to the jump rope mode, with $\tilde{f}_{MP} = 0.06\tilde{f}_{JRV}$.

Figure 4.8 is constructed parallel to figure 4.5, but plots the horizontal temperature anomalies of the *Conducting MC⁻* thermistor data azimuthally-shifted into the best fit LSC reference frame. Since the LSC continually precesses in the $+\hat{e}_\phi$ direction in this sub-case, there is no mean location of the best fit LSC plane. For ease of comparison with figure 4.5, we set $\xi = 3.55$. In figure 4.5, each thermistor's data exists in an azimuthally-localized cloud since the LSC maintains its position over time. In contrast, each thermistor's data points form an approximately continuous sinusoid in this magnetoprecessional case. This occurs since the thermal field precesses past each of the spatially fixed thermistors and, thus, each thermistor samples every part of the sinusoidally precessing temperature field over time.

The top block thermistor data sets in figure 4.8(a) deviate from that of a sinusoid. This is caused by spatially fixed $\simeq 0.5$ K temperature anomalies in the top block that are co-located with the inlet and outlet positions of the top block heat exchanger's cooling loop, which are located at $\phi = 150^\circ$ and 330° , respectively. These fixed temperature anomalies are likely not evident in figure 4.5 because the orientation angle of the LSC remains nearly aligned with the heat exchanger inlet and outlet angles in the electrically-insulating experiment. In addition, we note that the midplane has a larger temperature variation in figure 4.8(b) than in the corresponding *Insulating RBC* case. This may be due to differences in Bi for the

differing experiments.

4.6 Fixed Rayleigh Number TEMC Survey

To characterize the system's behavioral regimes, we have conducted a survey of turbulent TEMC with the Rayleigh number fixed at approximately 2×10^6 and the Chandrasekhar number varying from 0 to 8×10^5 all with a vertically downward applied magnetic field ($\hat{\mathbf{e}}_b = -\hat{\mathbf{e}}_z$). Three regimes are found: (i) the jump rope vortex (*JRV*) regime; (ii) the magnetoprecessional (*MP*) regime; and (iii) the multi-cellular magnetoconvection (*MCMC*) regime.

Figure 4.9(a) shows a thermal spectrogram made using the T_{ij}^{mid} data, plotted as functions of f/f_κ on the vertical axis and the Chandrasekhar number Ch on the horizontal axis. Here, we use $Pr = 0.027$, and the RBC case's $Ra_0 = 2.12 \times 10^6$ value to calculate N_C for all the cases. The interaction parameter is calculated here as $N_C = \sqrt{Ch^2 Pr / Ra_0}$, where $Ra_0 = 2.12 \times 10^6$ corresponds to the case with no magnetic field. The peak frequency at each Ch -value is marked by an open black circle. The black square marks the peak frequency of the *Conducting MC⁻* case, and the white cross marks the peak frequency of the *Insulating MC⁻* case. The black dashed curve denotes the second-order fit to the experimental data in the MP regime. The white stars are magnetoprecession frequency estimates calculated using eq.(4.60) for each MP case, and the white dotted curve is the second-order fit of these theoretical estimates developed in §4.7.5.

Starting from the left of the figure, the predicted peak RBC frequency, \tilde{f}_{JRV} derived from equation eq. (4.26), is marked by the white, horizontal dashed line. In the JRV regime, the $0 < N_C \lesssim 10^{-1}$ experimental data are in good agreement with \tilde{f}_{JRV} , with sidewall thermal fields that correspond to that of an LSC-like flow (e.g., figure 4.9(b)). In this regime, buoyancy-driven inertia is the dominant forcing in the system. As N_C increases and exceeds unity, it is expected that the LSC will weaken and eventually disappear (Cioni

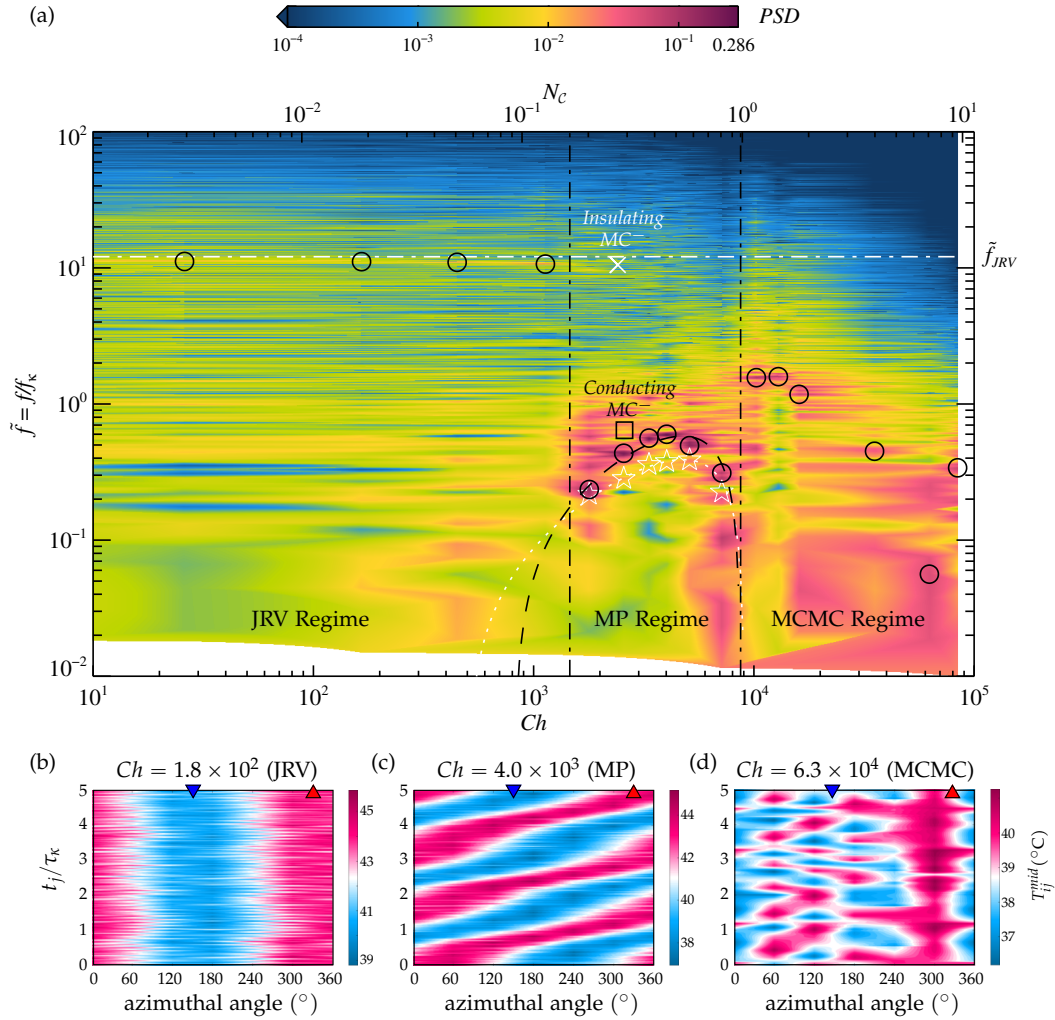


Figure 4.9: Spectrogram (a) Power spectral density (PSD) of the T_{ij}^{mid} temperature data versus Ch and N_C for the $Ra \approx 2 \times 10^6$ cases. The peak frequency for each case is marked with black open circles. The jump rope vortex (JRV), the magnetoprecession (MP), and the multi-cellular magnetoconvection (MCMC) regimes are separated by the two black vertical dot-dashed lines. The JRV frequency (Vogt *et al.*, 2018a), \tilde{f}_{JRV} , is shown as the white horizontal dotted line near $\tilde{f} \approx 12.1$. The lower panels show sidewall midplane temperature contour maps in (b) JRV, (c) MP, and (d) MCMC regimes. The blue downwards and red upwards triangles in the lower panels denote the heat exchanger inlet and outlet azimuth locations, respectively.

et al., 2000b; Zürner *et al.*, 2020). However, the MP regime exists in the intermediate N_C TEMC system. In this regime, the spectral peak switches from near to \tilde{f}_{JRV} to the slow magnetoprecessional frequency above $N_C \approx 0.1$, corresponding to the magnetoprecessional sidewall thermal signal shown in figure 4.9(c)). The MP frequency grows with N_C , reaching a value of $0.60 f_\kappa$ near $N_C \approx 0.4$. At higher N_C , the peak frequency decays, becomes unstable, and mixes with other complex modes at $N_C \gtrsim 1$ (e.g., figure 4.9(d)). The single, turbulent LSC likely gives way to multi-cellular bulk flow in this $N_C \gtrsim 1$ MCMC regime.

We contend that it is the existence of coherent thermoelectric current loops existing across the top and bottom horizontal interfaces of the fluid layer that drive the magnetoprecessional mode observed in the MP regime. Following the arguments of §4.2.1, this requires horizontal temperature gradients to exist along on these bounding interfaces as shown schematically in figure 4.1. To quantify this, the horizontal temperature difference at height z_k and time t_j is estimated using the best fit of the data to eq. (4.37) as

$$\delta T_j^k = \max(T_{fit}^k(t_j)) - \min(T_{fit}^k(t_j)) = 2A_j^k. \quad (4.39)$$

Its time-mean value is denoted by

$$\delta T^k = \frac{2}{N} \sum_{j=1}^N A_j^k, \quad (4.40)$$

where j is the j^{th} step in the discrete temperature time series and N is the total number of time steps. Thus, δT^{top} estimates the time-averaged, maximum horizontal temperature difference in the top block thermistors located at $z = 100.6 \text{ mm} = 1.022H$ and $r = 0.71R$. Similarly, δT^{bot} estimates this value using the bottom block thermistors located at $z = -2.0 \text{ mm} = -0.020H$ and $r = 0.71R$.

Figure 4.10(a) shows time series of the maximum *horizontal* temperature variations in the top and bottom boundaries in the reference frame of the fitted LSC plane, δT_j^k , calculated using eq. (4.39). This data is from our canonical *Conducting MC⁻* case at $Ra = 1.83 \times 10^6$, $Ch = 2.59 \times 10^3$, and $N_C = 0.31$. The temperature time series for this case has been shown in

figure 4.6. In the top block, the time-averaged maximum horizontal temperature variation, plotted in blue, is 2.24 K, which is 1.2 K smaller than that of the bottom block (in red), 3.44 K. Moreover, the top has a larger magnitude of fluctuation of ~ 2 K, while the bottom remains relatively stable with a fluctuation of ~ 1 K. The difference in top and bottom δT_j^k fluctuation amplitudes is likely due to the structure of the heat exchanger, in which the inlet and the outlet of the cooling water are antipodal to one another. This imposes a small (~ 1 K), spatially fixed temperature gradient along the line connecting these two points. This causes the horizontal temperature variation at the top boundary to fluctuate as the LSC precesses across the top block's spatially fixed temperature gradient. We hypothesize that this fluctuation propagates to the bottom boundary, generating a smaller fluctuation there than on the top block and lagging the top fluctuation by about 0.6 thermal diffusion times.

Figure 4.10(b) shows δT^k , the time-mean horizontal temperature differences calculated via eq. (4.40) on the top block (blue triangles) and on the bottom block (red triangles) for the $N_c < 1$ experiments in the fixed Ra survey ($Ra \approx 2 \times 10^6$). The *Conducting MC⁻* case in panel (a) corresponds to the square markers on the right in panel (b). The horizontal dashed and dotted lines show the mean values of δT^k for the *Conducting MC⁻* case. The two vertical dot-dashed lines denote the boundaries between the JRV, MP and MCMC regimes. In the lowest N_c case shown in figure 4.10(b), it is found that $\delta T^{top} \approx \delta T^{bot} \approx 2.6$ K. This value is nearly 40% of the vertical temperature gradient across the tank, and is similar to values found for comparable RBC cases. We argue that this 2.6 K value is predominantly generated by the jump rope vortex imprinting its thermal anomalies onto the top and bottom boundary thermistors. The values of δT^{bot} exceed δT^{top} in the MP regime ($0.1 \lesssim N_c \lesssim 1$). For $N_c \gtrsim 1$, the jump rope-style LSC breaks down into multi-cellular flow (Zürner *et al.*, 2020) and it is not possible to fit a sinusoidal function of the form (4.37) to the thermistor data in the top and bottom blocks.

The right hand vertical axis in figure 4.10(b) shows thermal block temperature differences normalized by the vertical temperature difference, $\delta T^k / \Delta T$. The fixed Ra survey cases have

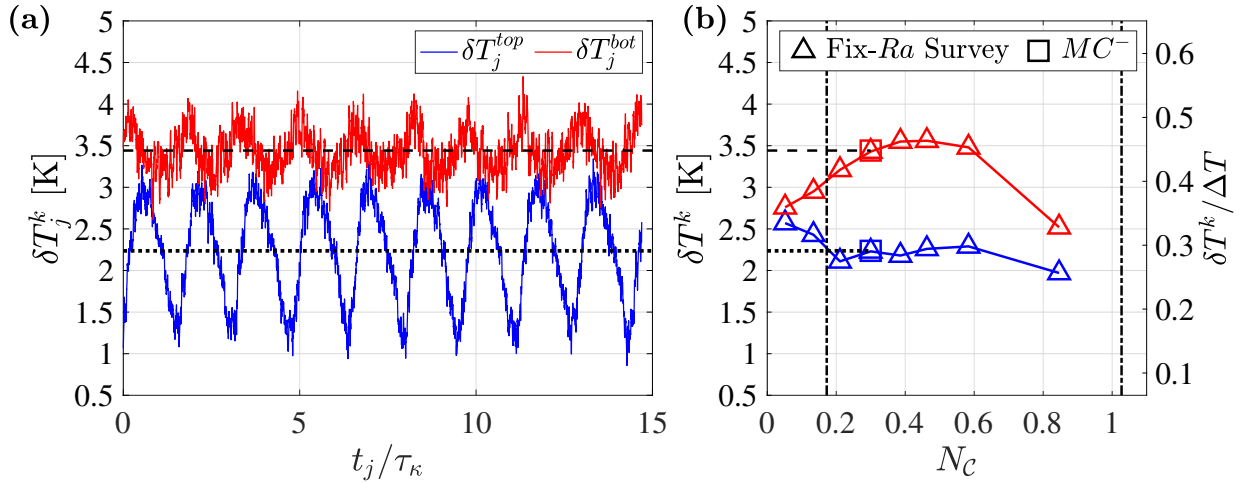


Figure 4.10: (a) Time series of the horizontal temperature difference at different heights, δT_j^k , defined in eq. (4.39), from the *Conducting* MC^- case at $Ra = 1.83 \times 10^6$, $Ch = 2.59 \times 10^3$, and $N_C = 0.31$. The horizontal axis is normalized time t_j/τ_κ . The black dotted line denotes the mean values of $\delta T^{top} = 2.24$ K, and the black dashed line denotes $\delta T^{bot} = 3.44$ K. (b) Time-averaged horizontal temperature difference estimates δT^k on the top and bottom boundaries for the fixed- Ra cases ($Ra \approx 2 \times 10^6$) at $N_C < 1$. The fixed- Ra cases are marked by triangles; blue (red) color represents top (bottom) boundary measurements. The magnetoprecessional (MP) regime lies between the two vertical dot-dashed lines. The right hand y -axis denotes δT^k normalized by the averaged vertical temperature difference $\Delta T = 7.68$ K of the fixed- Ra cases shown here. Values of δT_j^k for the *Conducting* MC^- case are marked by the square symbols.

$\delta T^k/\Delta T$ values ranging from roughly 0.3 to 0.5, demonstrating that low Pr convective heat transfer occurs via large-scale, large amplitude thermal anomalies that may alter the thermal boundary conditions in finite Bi experiments. Such conditions differ from those typically assumed in theoretical models of low Prandtl number convection (Clever & Busse, 1981; Thual, 1992).

The slow magnetoprecessional modes only appear in MC experiments with electrically conducting boundaries for $0.1 \lesssim N_c \lesssim 1$. Strong, coherent horizontal temperature gradients exist along the top and bottom boundaries in these cases, as shown in figure 4.10. This suggests that magnetoprecession is controlled by the material properties of the boundaries and the horizontal temperature gradients on the liquid-solid interfaces. Based on these arguments, we develop a simple model for thermoelectrically-driven magnetoprecession of the LSC in the following section.

4.7 Thermoelectric Precession Model

This study presents the first detailed characterization of the large-scale, long-period magnetoprecessional (MP) mode that appears in turbulent MC cases with conducting boundaries. We hypothesize that the MP mode emerges from an imbalance between the thermoelectric Lorentz forces at the top and bottom boundaries of the fluid layer. This imbalance, which arises due to the differing thermal gradients on the top and bottom boundaries, creates a net torque on the overturning LSC. This net torque causes the LSC to precess like a spinning top. To test this hypothesis, a simple mechanistic model of such a thermoelectrically-driven magnetoprecessing LSC is developed, and is shown to be capable of predicting the essential behaviors in our MP system.

4.7.1 Angular Momentum of the LSC Flywheel

A Cartesian coordinate frame is used in our model of thermoelectrically-driven magnetoprecession of the LSC. This Cartesian frame is fixed in the LSC plane such that $\hat{\mathbf{e}}_y$ always points along the $\xi_j = 0$ direction. The thermal gradient is also aligned in the same direction, yielding $\hat{\mathbf{e}}_n = \hat{\mathbf{e}}_y$. The magnetic field direction is oriented in $\pm\hat{\mathbf{e}}_z$, and the right-handed normal to the LSC plane is oriented in the $\hat{\mathbf{e}}_x$ -direction.

We treat the LSC as a solid cylindrical flywheel that spins around a midplane $\hat{\mathbf{e}}_x$ -axis, as shown in figure 4.11. The LSC is taken to have the same cross-sectional area as the LSC plane, $A_{LSC} = \Gamma H^2$. The corresponding radius of the solid LSC cylinder is then

$$R^* = \sqrt{A_{LSC}/\pi} = \sqrt{\Gamma H^2/\pi}. \quad (4.41)$$

which corresponds to $R^* \approx 0.8H$ for the $\Gamma = 2$ experiments carried out here. The volume of the turbulent LSC is V_{LSC} . For convenience, we take the depth of the LSC in $\hat{\mathbf{e}}_x$ to be R^* so that $V_{LSC} = \pi R^{*3}$, noting that the assumed depth and V_{LSC} both drop out of our eventual prediction for the LSC's magnetoprecession rate ω_{MP} . The LSC flywheel, as constructed, does not physically fit within the tank since $R^* > H/2$, as shown in figure 4.11. (It is not shown to scale in figure 4.13(b).)

The angular momentum of the flywheel is taken to be that of a uniform-density solid cylinder with mass $M_{LSC} = \rho V_{LSC}$ and radius R^* , rotating around $\hat{\mathbf{e}}_x$. Its moment of inertia with respect to the $\hat{\mathbf{e}}_x$ -axis is

$$I = \frac{1}{2} M_{LSC} R^{*2} = \frac{1}{2} \rho V_{LSC} R^{*2}. \quad (4.42)$$

We use the upper bounding free-fall velocity as an estimate of the angular velocity vector for the LSC flywheel:

$$\boldsymbol{\omega}_{LSC} \approx U_{ff}/R^* \hat{\mathbf{e}}_x. \quad (4.43)$$

Thus, the angular momentum due to the overturning of the flywheel, \mathbf{L}_{LSC} , is oriented along

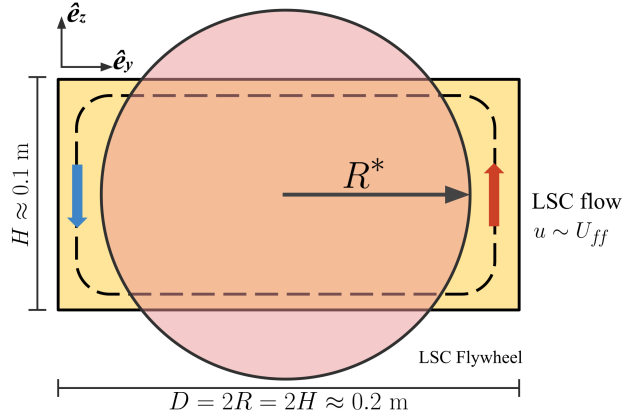


Figure 4.11: Cross-section view of the precessional flywheel model (pink) in the LSC plane (yellow). The precessional flywheel is assumed to have the same cross-sectional area as the LSC plane, $\pi(R^*)^2 = 2H^2$. The angular velocity of the overturning LSC flywheel is estimated by assuming it rotates at the free-fall speed $\omega_{LSC} \approx U_{ff}/R^*$.

\hat{e}_x and is estimated as:

$$\mathbf{L}_{LSC} = I\boldsymbol{\omega}_{LSC} \approx \left(\frac{1}{2}\rho V_{LSC} R^{*2} \right) \left(\frac{U_{ff}}{R^*} \right) \hat{e}_x = \frac{1}{2}\rho V_{LSC} U_{ff} R^* \hat{e}_x. \quad (4.44)$$

4.7.2 Thermoelectric Currents at the Electrically Conducting Boundaries

Figure 4.12(a) shows a schematicized vertical slice through our experimental tank in the low N_C regime. The LSC generates horizontal thermal gradients on both horizontal boundaries. Thus, the end-blocks have a higher temperature near the upwelling branch of the LSC, which carries warmer fluid upwards, and the end-blocks are cooler near the downwelling branch of the LSC, which carries cooler fluid downwards. These temperature gradients on the top and bottom fluid-solid interfaces generate thermoelectric current loops. Eq. (4.7) is used to calculate the net Seebeck coefficient of such a thermoelectric current loop in our Cu-Ga system:

$$\Phi_{TE} = \int_{r_0(T_0)}^{r_1(T_1)} (S_{Cu} - S_{Ga}) \nabla T \cdot d\mathbf{r} = \frac{\pi^2 k_B^2}{6e} \left[\frac{x_{Cu}}{E_{FCu}} - \frac{x_{Ga}}{E_{FGa}} \right] (T_1^2 - T_0^2), \quad (4.45)$$

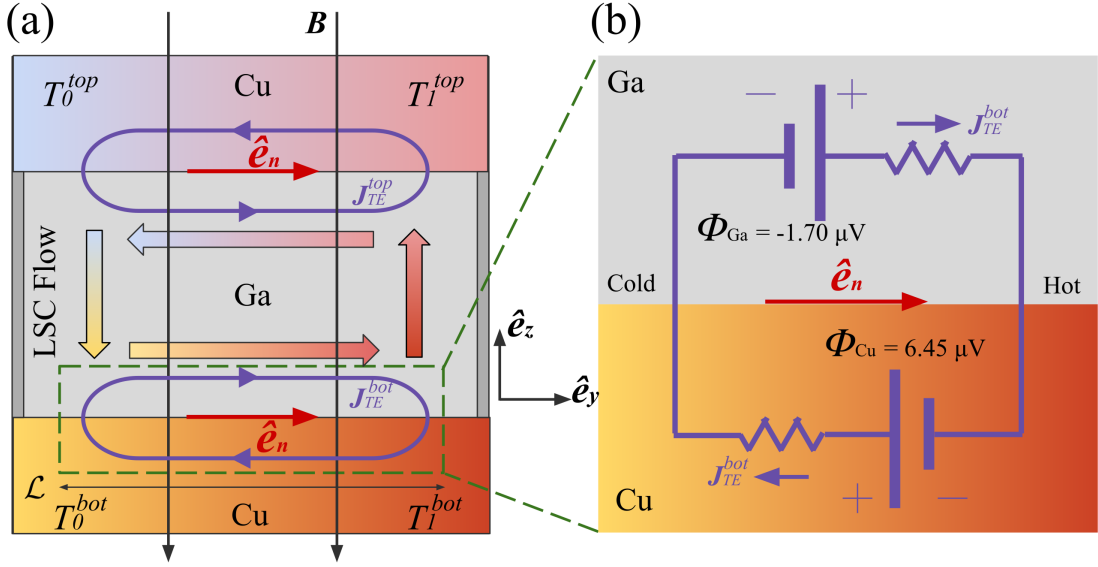


Figure 4.12: (a) Cross-sectional schematics of the experimental MC system with electrically conducting boundaries. In the plane of LSC, the turbulent LSC imprints large scale thermal anomalies onto the boundaries: the top boundary has a minimum temperature T_0^{top} and a maximum temperature T_1^{top} ; the bottom boundary has a minimum temperature T_0^{bot} and a maximum temperature T_1^{bot} . Thermoelectric potentials are generated at the Cu-Ga interfaces and form current density loops across the boundaries, \mathbf{J}_{TE}^{top} and \mathbf{J}_{TE}^{bot} , with a width of $\mathcal{L} \approx \Gamma H$. (b) Circuit diagram of the Cu-Ga system at the bottom boundary. The thermoelectric potential in gallium is denoted as Φ_{Ga} , which is smaller in magnitude and has an opposite sign as the thermoelectric potential in copper, Φ_{Cu} . Thus, the thermoelectric current flows from cold to hot in liquid gallium (in $+\hat{e}_n$), and from hot to cold in copper (in $-\hat{e}_n$).

where S_{Ga} and S_{Cu} are Seebeck coefficients for gallium and copper, respectively, calculated via eq. (4.2). For gallium, the numeric coefficient x_0 is $x_{Ga} = 0.7$ (Cusack, 1963) and the Fermi energy is $E_{FGa} = 10.37$ eV (Kasap, 2001). For copper, $x_{Cu} = -1.79$ and $E_{FCu} = 7.01$ eV. The temperatures T_0 and T_1 represent the minimum and maximum temperatures, respectively, in a given horizontal plane (e.g., figure 4.1).

Following eq. (4.9), the net Seebeck coefficient on the k -level Cu-Ga interface is:

$$\tilde{S}^k = \frac{\pi^2 k_B^2}{3e} \left[\frac{x_{Cu}}{E_{FCu}} - \frac{x_{Ga}}{E_{FGa}} \right] T^k \equiv X_0 T^k \text{ [V/K]}, \quad (4.46)$$

where T^k is the time-azimuthal mean temperature on the k -interface. The Cu-Ga Seebeck prefactor X_0 collects all the constant and material properties in eq. (4.46). Its value in our system is

$$X_0 \approx -7.89 \times 10^{-9} \text{ V/K}^2. \quad (4.47)$$

Unlike the net Seebeck coefficient, X_0 does not depend on temperature.

The thermoelectric current density vector in liquid gallium is approximated via eq. (4.6):

$$\mathbf{J}_{TE}^k \approx \sigma_0 X_0 T^k \left(\frac{\delta T^k}{\mathcal{L}} \right) \hat{\mathbf{e}}_y, \quad (4.48)$$

where $\sigma_0 = 3.63 \times 10^6 \text{ S/m}$ is the effective electric conductivity for the Cu-Ga system, calculated by substituting the conductivity of gallium ($\sigma_{Ga} \approx 3.88 \times 10^6 \text{ S/m}$) and copper ($\sigma_{Cu} \approx 5.94 \times 10^7 \text{ S/m}$) into eq. (4.5). The horizontal temperature gradient is approximated by the maximum temperature difference across the k -interface, δT^k , divided by a characteristic width of the current loop, \mathcal{L} . We assume this width is the same as the diameter D of the tank, $\mathcal{L} \approx \Gamma H = 2H = 197.2 \text{ mm}$. (Effects of possible TE currents in the stainless steel sidewall ($\sigma_{St.Stl.} \approx 1.4 \times 10^6 \text{ S/m}$) are not accounted for here.)

Figure 4.12(b) shows a circuit diagram for the thermoelectric current loop near the experiment's bottom liquid-solid interface at $\approx 40^\circ \text{ C}$. The thermoelectric potential in gallium has a negative sign, so the currents within the fluid are always aligned in the direction of the thermal gradient $\hat{\mathbf{e}}_n = \hat{\mathbf{e}}_y$. In contrast, the thermoelectric potential in copper has a positive sign, so the current flows from the hot to the cold region in $-\hat{\mathbf{e}}_n$.

4.7.3 Thermoelectric Forces and Torques

The thermoelectric component of the mean Lorentz forces density on the index k horizontal interface can be calculated, using eq. (4.48), as

$$\mathbf{f}_{TE}^k = \mathbf{J}_{TE}^k \times \mathbf{B} = \sigma_0 X_0 T^k \left(\frac{\delta T^k}{\Gamma H} \hat{\mathbf{e}}_y \right) \times B \hat{\mathbf{e}}_b = \frac{\sigma_0 X_0 B T^k \delta T^k}{\Gamma H} (\hat{\mathbf{e}}_y \times \hat{\mathbf{e}}_b), \quad (4.49)$$

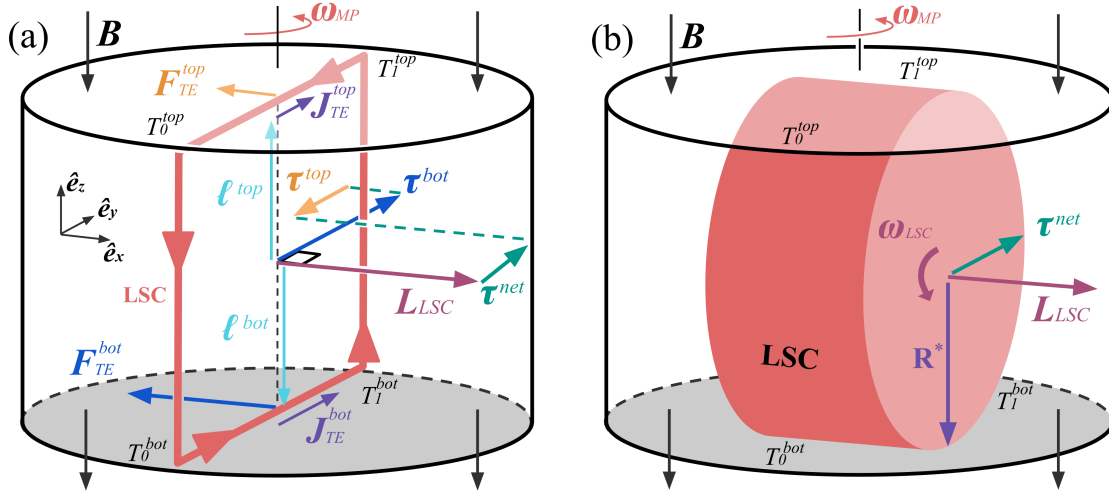


Figure 4.13: (a) Free-body diagram of thermoelectric LSC precession. The red arrows enclosed inside the tank represents the LSC. The thermoelectric potentials generate current in the liquid gallium at top and bottom boundaries: \mathbf{J}_{TE}^{top} and \mathbf{J}_{TE}^{bot} with $J_{TE}^{top} < J_{TE}^{bot}$. The thermoelectric Lorentz forces, \mathbf{F}_{TE}^{top} and \mathbf{F}_{TE}^{bot} , create a net torque $\boldsymbol{\tau}_{net}$ perpendicular to the LSC's angular momentum vector, \mathbf{L}_{LSC} , which drives the LSC to precess around the tank's vertical \hat{e}_z -axis. (b) Precessional flywheel schematic (not to scale). The LSC is simplified into a flywheel-like cylinder of radius R^* , with angular velocity $\omega_{LSC} \lesssim U_{ff}/R^*$ and angular momentum $\mathbf{L}_{LSC} = \omega_{LSC} M R^{*2} \hat{e}_x/2$. The LSC is assumed to respond to $\boldsymbol{\tau}_{net}$ in a solid-body manner.

where we have taken $\mathcal{L} \approx \Gamma H$. Since the thermoelectric currents are predominantly in the LSC plane and are aligned parallel to the thermal gradient, the thermoelectric Lorentz forces point in the $+\hat{\mathbf{e}}_x$ -direction for upward directed \mathbf{B} , and in the $-\hat{\mathbf{e}}_x$ -direction for downward directed \mathbf{B} (corresponding to figure 4.13(a)).

The Lorentz force is the volume integral of the force density:

$$\mathbf{F}_{TE}^k = \int \mathbf{f}_{TE}^k dV = \int \mathbf{J}_{TE}^k \times \mathbf{B} dV. \quad (4.50)$$

We coarsely assume that each thermoelectric current loop exists in the top half or bottom half of the LSC, and generates uniform Lorentz forces that act, respectively, on the upper or lower half of the LSC. With these assumptions, we take each hemicylindrical integration volume to be $V_{LSC}/2$. The Lorentz forces due to thermoelectric currents generated across the k -level Cu-Ga interface are then estimated to be

$$\mathbf{F}_{TE}^k = \frac{1}{2} V_{LSC} \mathbf{f}_{TE}^k. \quad (4.51)$$

In order to estimate the torques due to each thermoelectric current loop, we assume that the thermoelectric Lorentz forces act on the LSC via a moment arm $\boldsymbol{\ell}$ of approximate length $H/2$. Thus, $\boldsymbol{\ell}^{top} = H/2 \hat{\mathbf{e}}_z$ and $\boldsymbol{\ell}^{bot} = -H/2 \hat{\mathbf{e}}_z$. The net thermoelectric torque on the LSC then becomes

$$\boldsymbol{\tau}^{net} = \boldsymbol{\tau}^{top} + \boldsymbol{\tau}^{bot} \quad (4.52a)$$

$$= (\boldsymbol{\ell}^{top} \times \mathbf{F}_{TE}^{top}) + (\boldsymbol{\ell}^{bot} \times \mathbf{F}_{TE}^{bot}) \quad (4.52b)$$

$$= (H/2) \hat{\mathbf{e}}_z \times (\mathbf{F}_{TE}^{top} - \mathbf{F}_{TE}^{bot}) \quad (4.52c)$$

$$= (HV_{LSC}/4) \hat{\mathbf{e}}_z \times (\mathbf{f}_{TE}^{top} - \mathbf{f}_{TE}^{bot}). \quad (4.52d)$$

Substituting eq. (4.49) into eq. (4.52d) yields the net thermoelectric torque on the LSC to be

$$\begin{aligned} \boldsymbol{\tau}^{net} &= \frac{\sigma_0 V_{LSC} X_0 B (T^{bot} \delta T^{bot} - T^{top} \delta T^{top})}{4\Gamma} (\hat{\mathbf{e}}_x \times \hat{\mathbf{e}}_b) \\ &= \frac{\sigma_0 V_{LSC} X_0 B \mathcal{T}}{4\Gamma} (\hat{\mathbf{e}}_x \times \hat{\mathbf{e}}_b), \end{aligned} \quad (4.53)$$

where

$$\mathcal{T} \equiv (T^{bot} \delta T^{bot} - T^{top} \delta T^{top}) \quad (4.54)$$

describes the difference in thermal conditions on the bottom relative to top horizontal Cu-Ga interfaces. Since $T^{bot} > T^{top}$ in all our convection experiments, the data in figure 4.10(b) implies that $\mathcal{T} > 0$ in the MP regime. Since all the other parameters in eq. (4.53) are positive, the net thermoelectric torque is directed in $-\hat{e}_y$ for upwards directed magnetic fields ($\hat{e}_b = +\hat{e}_z$) and, as shown in figure 4.13, the net torque is directed in $+\hat{e}_y$ for downwards directed magnetic fields ($\hat{e}_b = -\hat{e}_z$). Eq. (4.53) also shows that the bottom torque will tend to dominate even when $\delta T^{bot} \approx \delta T^{top}$ since $T^{bot} > T^{top}$ in all convectively unstable cases.

4.7.4 Thermoelectrically-driven LSC Precession

The net thermoelectric torque on the LSC acts in the direction perpendicular to \mathbf{L}_{LSC} . The LSC must then undergo a precessional motion in order to conserve angular momentum. This precession can be quantified via Euler's equation (Landau & Lifshitz, 1976), in which the net torque is the time derivative of the angular momentum:

$$\boldsymbol{\tau}^{net} = \frac{d\mathbf{L}_{LSC}}{dt} = I \frac{d\boldsymbol{\omega}}{dt} + \boldsymbol{\omega} \times \mathbf{L}_{LSC}, \quad (4.55)$$

The angular velocity vector $\boldsymbol{\omega}$ is comprised of two components here

$$\boldsymbol{\omega} = \omega_{LSC} \hat{e}_x + \boldsymbol{\omega}_{MP}, \quad (4.56)$$

where ω_{LSC} is the angular velocity component of the flywheel in \hat{e}_x and $\boldsymbol{\omega}_{MP}$ is the angular velocity vector of the LSC's magnetoprecession. We assume that the precession frequency and the angular speed of the flywheel are nearly time-invariant, $d\boldsymbol{\omega}/dt \approx 0$. Then eq. (4.55) reduces to

$$\boldsymbol{\tau}^{net} = (\omega_{LSC} \hat{e}_x + \boldsymbol{\omega}_{MP}) \times L_{LSC} \hat{e}_x = \boldsymbol{\omega}_{MP} \times L_{LSC} \hat{e}_x, \quad (4.57)$$

Symbols	Description	Value
σ_0	Cu-Ga effective electric conductivity (4.5)	3.63×10^6 S/m
B	magnetic field intensity	120 gauss
\mathcal{L}	Horizontal length scale of TE current loops, $\approx \Gamma H$	197.2 mm
X_0	Cu-Ga Seebeck prefactor (4.46)	-7.89×10^{-9} V/K ²
ρ	Liquid gallium density	6.08×10^3 kg/m ³
R^*	Effective radius of the LSC (4.41)	0.08 m
U_{ff}	Free-fall velocity, eq. (4.10)	0.03 m/sec
\bar{T}	Mean fluid temperature, eq. (4.34)	42.50 °C
ΔT	Vertical temperature difference across the fluid (4.32)	7.03 K
T^{bot}	Bottom interface mean temperature	319.23 K
δT^{bot}	Bottom interface mean temperature difference (4.40)	3.44 K
T^{top}	Top interface mean temperature	312.07 K
δT^{top}	Top interface mean temperature difference (4.40)	2.24 K
\mathcal{T}	$(T^{bot} \delta T^{bot} - \delta T^{top} \delta T^{top})$	399.11 K ²

Table 4.2: Experimental parameter values from the *Conducting MC⁻* subcase. These values are characteristic of those used in calculating ω_{MP} in figure 4.14.

where $\boldsymbol{\omega}_{LSC} \times \mathbf{L}_{LSC} = 0$ since these vectors are parallel. Expression eq. (4.57) requires that $\boldsymbol{\omega}_{MP}$ remain orthogonal to both \mathbf{L}_{LSC} and $\boldsymbol{\tau}_{net}$ such that

$$\boldsymbol{\tau}_{net}(\hat{\mathbf{e}}_{\mathbf{x}} \times \hat{\mathbf{e}}_{\mathbf{b}}) = \boldsymbol{\omega}_{MP} \times L_{LSC} \hat{\mathbf{e}}_{\mathbf{x}} = \omega_{MP} L_{LSC} (\hat{\boldsymbol{\omega}}_{MP} \times \hat{\mathbf{e}}_{\mathbf{x}}). \quad (4.58)$$

Therefore, $\hat{\boldsymbol{\omega}}_{MP} = -\hat{\mathbf{e}}_{\mathbf{b}}$ and the precessional angular velocity vector is

$$\boldsymbol{\omega}_{MP} = \frac{\tau_{net}}{L_{LSC}} (-\hat{\mathbf{e}}_{\mathbf{b}}). \quad (4.59)$$

Substituting eqs. (4.44) and (4.53) into eq. (4.59) yields our analytical estimate for the thermoelectrically-driven angular velocity of LSC precession in the $N_c \lesssim 1$ TEMC experiments:

$$\boldsymbol{\omega}_{MP} = \frac{\sigma_0 X_0 B}{2\rho U_{ff} \Gamma R^*} (T^{bot} \delta T^{bot} - T^{top} \delta T^{top}) (-\hat{\mathbf{e}}_{\mathbf{b}}) \quad (4.60a)$$

$$= \frac{\sigma_0 X_0 B \mathcal{T}}{2\rho U_{ff} \Gamma R^*} (-\hat{\mathbf{e}}_{\mathbf{b}}) \quad (4.60b)$$

$$= \frac{\pi^{1/2} \sigma_0 X_0 B \mathcal{T}}{\Gamma^{3/2} 2\rho U_{ff} H} (-\hat{\mathbf{e}}_{\mathbf{b}}). \quad (4.60c)$$

Expressions (4.59) and eq. (4.60) predict that the LSC's magnetoprecessional angular velocity vector, $\boldsymbol{\omega}_{MP}$, will always be antiparallel to the imposed magnetic field vector in our Cu-Ga TEMC experiments in which $\mathcal{T} > 0$. Further, the magnetoprecession should flip direction such that $\boldsymbol{\omega}_{MP}$ would be parallel to \mathbf{B} in a comparable Cu-Ga TEMC system with $\mathcal{T} < 0$. These predictions agree with the precession directions found in our MP regime experiments, as shown in figure 4.7(a).

4.7.5 Experimental Verification

The direction of magnetoprecession is sensitive to the sign of \mathcal{T} . The value and sign of \mathcal{T} are, however, both likely related to the details of the experimental set up. For instance, we have a thermostated bath controlling the top thermal block temperature, whereas a fixed thermal flux is input below the bottom thermal block. Further, the top and bottom thermal

blocks have different thicknesses. It is possible that \mathcal{T} could behave differently with much thinner or thicker end-blocks, and for differing thermal boundary conditions. Thus, further modeling efforts are required before \mathcal{T} can be predicted *a priori*.

Figure 4.14(a) provides a test of our magnetoprecession model using data from the *Conducting MC⁻* case. The blue line shows the experimentally determined LSC angular velocity via measurements of the azimuthal drift velocity of the LSC plane, $d\xi_j^{mid}/dt$, made with the best fits to eq. (4.37). The magenta line shows the instantaneous angular velocity of LSC precession, $(\omega_{MP})_j$, calculated by feeding instantaneous thermal data from the *Conducting MC⁻* case into eq. (4.60). The green line is a modified theoretical estimate, in which the U_{MC} velocity prediction (4.29) is used in eq. (4.60) instead of the upper bounding U_{ff} estimate.

The three time series in figure 4.14(a) show that the predicted magnetoprecessional angular speeds compare well with the LSC azimuthal drift speed, especially when accounting for the simplifications that are underlying eq. (4.60). The time series all have similar gross shapes, but with the peaks in $d\xi_j^{mid}/dt$ slightly delayed in time relative to those in the ω_{MP} curves. The dashed lines in figure 4.14 show the time-mean angular velocity values. The time mean LSC plane velocity is $d\xi_j^{mid}/dt = 5.27 \times 10^{-3}$ rad/s. The mean value of the magnetoprecessional flywheel (magenta) is $\omega_{MP} = 2.48 \times 10^{-3}$ rad/s = $0.47 d\xi_j^{mid}/dt$. The mean value of the modified estimate (green) is $\omega_{MP} U_{ff}/U_{MC} = 3.10 \times 10^{-3}$ rad/s = $0.59 d\xi_j^{mid}/dt$. Moreover, there is a good agreement between the converted angular speed from the peak frequency $2\pi f_{peak}$ of the FFTs (black dashed lines) and the mean LSC azimuthal drift speed by direct thermal measurement $d\xi_j^{mid}/dt$ (blue dashed lines). The direct measurement is about 2.5% higher than $2\pi f_{peak}$.

Figure 4.14(b) shows the correlation between the measured angular velocity $d\xi_j^{mid}/dt$ and \mathcal{T} . The angular velocity values correspond to the blue curve in panel (a). The dashed red line is the best linear fit to the data, and shows that there is a net positive correlation between $d\xi_j^{mid}/dt$ and the asymmetry of the thermal condition in end-blocks, represented

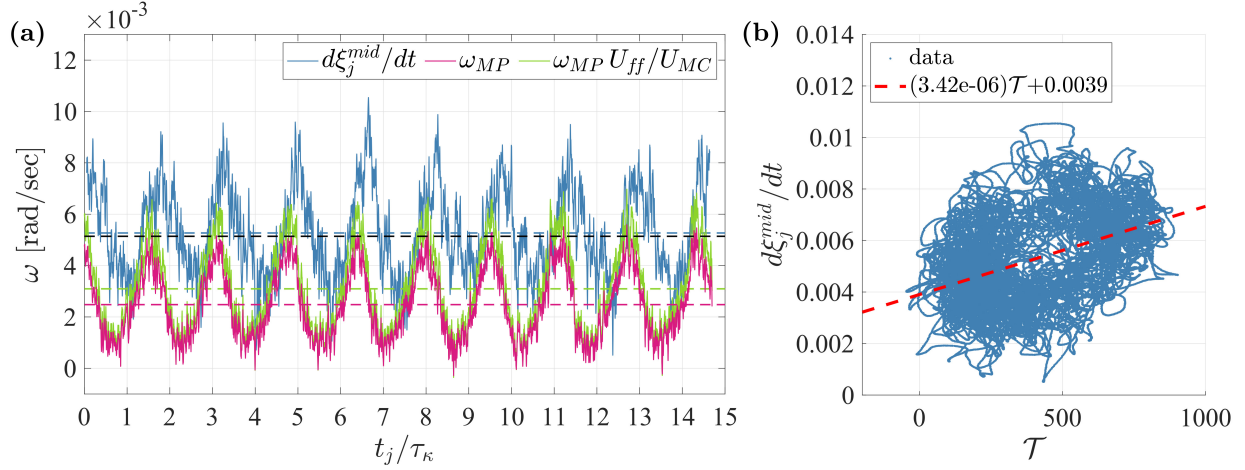


Figure 4.14: (a) Time series of LSC precessional rate for the *Conducting MC⁻* case at $Ra = 1.83 \times 10^6$, $Ch = 2.59 \times 10^3$, and $N_C = 0.31$. The horizontal axis shows time t normalized by the diffusion timescale τ_κ . The vertical axis is the LSC's instantaneous angular precession speed ω . The blue line shows angular velocity of the LSC plane, $d\xi_j^{mid}/dt$, measured via eq. (4.37) using temperature data on the midplane sidewall. The magenta line marks ω_{MP} model predictions made using eq. (4.60) and instantaneous temperature data. The green line shows the alternative MP prediction made using eq. (4.60) with Zürner *et al.* (2020)'s U_{MC} velocity scaling eq. (4.29). The horizontal dashed lines are mean values for their corresponding angular speeds. The black horizontal dashed line represents the peak frequency from the FFT converted into the angular speed. (b) Scatter plot of $d\xi_j^{mid}/dt$ versus \mathcal{T} . The red dashed line is a linear fit for this particular case. The best fit slope, $3.42 \times 10^{-6} \text{ K}^2/\text{s}$, is 55.3% of the theoretical prediction from (4.60), where the prefactor $\sigma_0 X_0 B / (4\rho U_{ff} R^*) \approx 6.18 \times 10^{-6} \text{ K}^2/\text{s}$.

by \mathcal{T} . The best fit slope is $(d\xi_j^{mid}/dt)/\mathcal{T} = 3.42 \times 10^{-6} \text{ K}^2/\text{s}$. Theoretical prediction (4.60) gives $\omega_{MP}/\mathcal{T} = \sigma_0 X_0 B / (4\rho U_{ff} R^*) = 6.18 \times 10^{-6} \text{ K}^2/\text{s}$. Thus, the best-fit slope agrees with theory to within approximately a factor of two.

The thermoelectric LSC precession model is tested further in figure 4.9(a) and figure 4.15 using the fixed $Ra \approx 2 \times 10^6$ case results. In figure 4.9(a), the peak of each experiment's thermal FFT spectrum is marked by an open black circle. The circles in the MP regime are connected by a best fit parabola (black dashed curve). The white stars show the predicted magnetoprecessional frequency, $f_{MP} = \omega_{MP}/2\pi$, calculated using eq. (4.60). The white dotted line is the best parabolic fit to the f_{MP} values. Adequate agreement is found between the spectral peaks and the f_{MP} values. The low frequency tail of the best fits appears to correlate with secondary peaks in the thermal spectra. This suggests that MP modes exist down to $Ch \simeq 10^3$ in the JRV regime, but with weaker spectral signatures that do not dominate those of the jump rope LSC flow.

Figure 4.15(a) shows a linear plot of FFT spectral peaks (black circles), f_{MP} predictions (magenta stars), and the modified predictions $f_{MP}(U_{ff}/U_{MC})$ (green stars) plotted versus N_C for the fixed $Ra \approx 2 \times 10^6$ MC experiments with $N_C < 1$. The dashed lines show best parabolic fits. The vertical dot-dashed lines are the regime boundaries that separate the JRV, MP and MCMC regimes in figure 4.9(a). The f_{MP} estimates differs by $\lesssim 37\%$ from the experimental spectral data, while the improved model that makes use of U_{MC} differs from the spectral peak frequencies by $\lesssim 16\%$. Further, the intersections of the best fit parabolas with $f/f_\kappa = 0$, near $N_C \approx 0.1$ and $N_C \approx 1$, agree well with the empirically located regime boundaries.

Figure 4.15(b) shows $\mathcal{T} = (T^{bot}\delta T^{bot} - T^{top}\delta T^{top})$ versus N_C for the experimental cases shown in panel (a). Although it resembles the curves in panel (a), the shape of the \mathcal{T} curve is steeper on its $N_C < 0.4$ branch and its peak is shifted to slightly lower N_C . Figure 4.15(c) shows the product $B\mathcal{T}$ plotted in orange as a function of N_C . The magenta dashed curve in Figure 4.15(c) is the best fit parabolic curve from panel (a) normalized by $8\rho U_{ff} R^*/(\sigma_0 X_0)$,

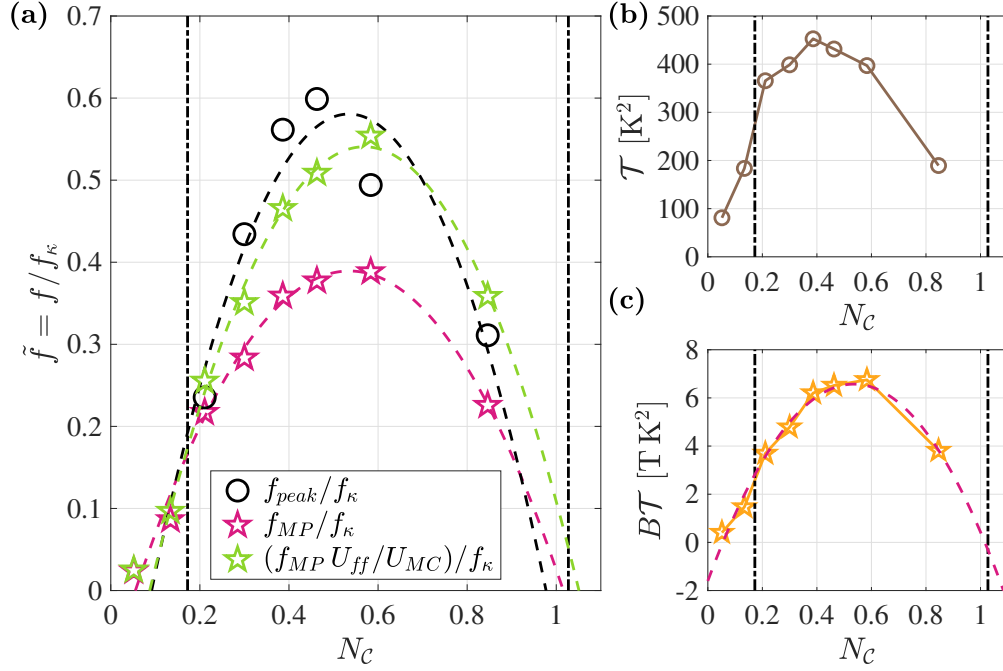


Figure 4.15: (a) Normalized precessional frequency, $\tilde{f} = f/f_\kappa$, versus convective interaction parameter, N_C , where the thermal diffusion frequency is $f_\kappa \equiv 1/\tau_\kappa \approx 1.34 \times 10^{-3}$ Hz. Black circles denote the peak frequencies of FFT spectra for the fixed $Ra \approx 2 \times 10^6$ experimental survey. Magenta stars are frequencies predicted by the TEMC precession model, $f_{MP}/f_\kappa = \omega_{MP}/(2\pi f_\kappa)$. Green stars correspond to $\omega_{MP}U_{ff}/(2\pi U_{MC}f_\kappa)$, the frequency of the precession model using the U_{MC} scaling velocity. Dashed curves represent the second-order best fit curves. (b) \mathcal{T} versus N_C . (c) The product $B\mathcal{T}$ versus N_C . The magenta dashed curve is the second degree best fit curve from panel (a) normalized by the factor $\sigma_0 X_0 / (8\pi f_\kappa \rho U_{ff} R^*) \approx 0.0612 [\text{T}^{-1}\text{K}^{-2}\text{s}^{-1}]$.

which, according to eq. (4.60), separates these values. By comparing figures 4.15(b) and 4.15(c), we argue that the quasi-parabolic structure of the MP frequency data in the MP regime is controlled by trade-offs between the B and \mathcal{T} trends.

4.8 Discussion

We have conducted a series of magnetoconvection (MC) laboratory measurements in turbulent liquid gallium convection with a vertical magnetic field and thermoelectric (TE) currents in cases with electrically-conducting boundaries. Three regimes of TEMC flow are found: i) the LSC sustains its flow structure in the $0 < N_C \lesssim 0.1$ jump rope vortex (JRV) regime; ii) long-period magnetoprecession (MP) of the LSC dominates the $0.1 \lesssim N_C \lesssim 1$ MP regime; and iii) the LSC is replaced by a multi-cellular magnetoconvective flow pattern in the $N_C \gtrsim 1$ MCMC regime.

Figure 4.16(a) shows the convective and thermoelectric interaction parameters, N_C and N_{TE} respectively, as a functions of Ch . The vertical dashed lines separate the parameter space into the three characteristic regimes in figure 4.9, with JRV on the left hand side, MP in the middle and MCMC on the right hand side. Both N_C and N_{TE} are approximately of the same order in the MP regime. The blue open triangles correspond to the experimentally derived thermoelectric interaction parameters at the bottom boundary for the fixed- Ra survey, $N_{TE}^{bot} = \sigma B |\tilde{S}| \delta T^{bot} / (\rho U_{ff}^2)$. The bottom boundary temperature data, δT^{bot} , are used here because it has the larger N_{TE} than the top layer, and dominates the dynamics of the magnetoprecession.

Figure 4.16(b) uses U_{MC} as the characteristic flow speed instead of U_{ff} . Similar to (a), both N_C and N_{TE} are of the same order and roughly aligned with each other in the MP regime, which means the quasistatic Lorentz forces from the fluid motions are comparable to the thermoelectric Lorentz forces. Panels (c) and (d) show Se and Se_{MC} , which are the ratios of the blue and black lines in panels (a) and (b), respectively. Since the convective

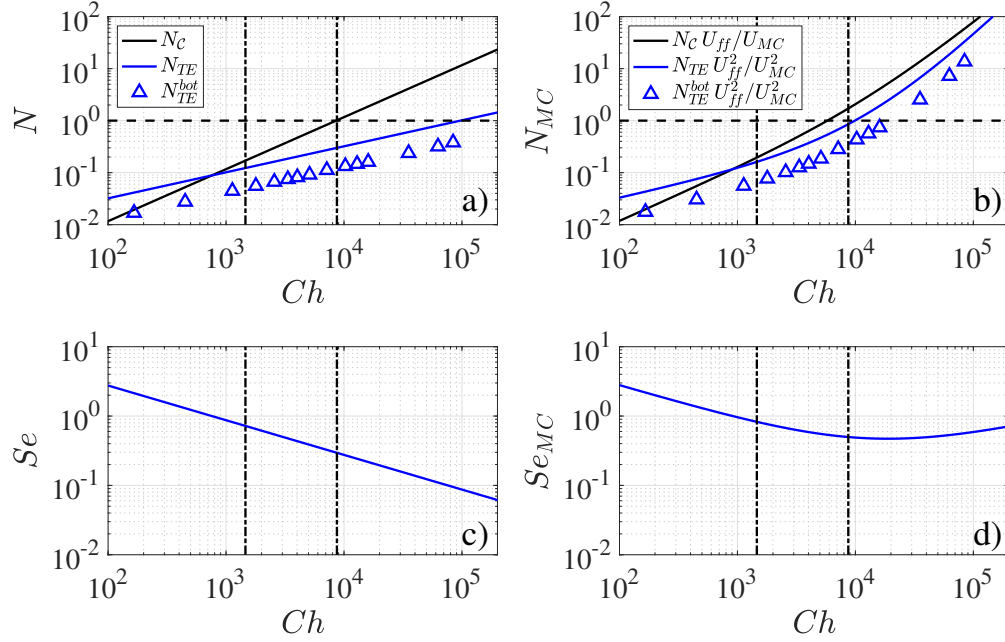


Figure 4.16: a) Convective and thermoelectric interaction parameters, N_C and N_{TE} , plotted versus Chandrasekhar number Ch over the parameter space of the fixed- Ra survey. The black line shows $N_C = \sigma B^2 H / (\rho U_{ff})$, and the blue line shows $N_{TE} = \sigma B |\tilde{S}| \Delta T / (\rho U_{ff}^2)$, following the definitions in eq. (4.23) and eq. (4.24). The net Seebeck coefficient $\tilde{S} = X_0 \bar{T}$ is defined using the mean temperature of the system. The blue triangles denote $N_{TE}^{bot} = \sigma B |\tilde{S}| \delta T^{bot} / (\rho U_{ff}^2)$ calculated for the experimental data of the fixed- Ra cases. The two vertical black dot-dashed lines separate the parameter space into the JRV, MP and MCMC regimes from left to right in each panel. Panel (b) is comparable to (a), but employs the characteristic MC flow speed U_{MC} in place of U_{ff} . Panels (c) and (d) show the corresponding Seebeck numbers, $Se = N_{TE}/N_C$ and $Se_{MC} = (N_{TE}/N_C) (U_{ff}/U_{MC})$, respectively.

and TE interaction parameters are order unity in the MP regime in figure 4.16, this shows that both the Lorentz forces are approximately comparable to the buoyant inertia. Thus, a triple balance is possible between the motionally-induced Lorentz forces, the thermoelectric Lorentz forces and the buoyancy forces in the MP regime.

Our thermoelectrically-driven precessional flywheel model provides an adequate characterization of the MP mode that is observed in turbulent MC experiments with electrically conducting boundaries. The model predicts the zeroth-order precessional frequencies of the MP mode. Further, it explains the changing direction of precession when the imposed magnetic field direction is reversed (figure 4.7).

There are, however, a number of limitations to our flywheel model. First, we have allowed Ga to corrode the Cu end-blocks in order to ensure good material contact across the interfaces. The reaction between Cu and Ga forms a gallium alloy layer on the copper boundary. This ongoing reaction should decrease the interfacial electrical conductivity over time, resulting in a smaller net torque on the LSC and a slower rate of magnetoprecession. This may explain a subtle feature in figure 4.9: the peak frequency from the MC^- case is higher than the comparable fixed- Ra survey case that was carried out months later but with similar control parameters. Thus, Ga-Cu chemistry at the interface appears to matter in the TE dynamics, yet we are currently unable to control or to parameterize these interfacial reaction processes. Second, our model requires measurements of the horizontal temperature gradients in the conducting end-blocks. A fully self-consistent model would use the input parameters to predict these gradients *a priori*, independent of the experimental data.

A long-period precessional drift of the LSC has also been observed in water-based laboratory experiments influenced by the Earth's rotation (Brown & Ahlers, 2006). In their experiments, the LSC rotates azimuthally with a period of days. This period is over two orders of magnitude greater than our MP period. Since MP modes are found only to develop in the presence of imposed vertical magnetic fields and electrically-conducting boundaries, it is not possible to explain the MP mode solely due to Coriolis effects from Earth's rotation.

Alternatively, the rotation of the Earth could couple with the magnetic field to induce magneto-Coriolis (MC) waves in the convecting gallium (Finlay, 2008; Hori *et al.*, 2015; Schmitt *et al.*, 2013). In the limit of strong rotation, MC waves have a slow branch that might appear to be relevant to our experimental MP data. However, our current TEMC experiments are stationary in the lab frame and, thus, are only spun by Earth’s rotation, similar to Brown & Ahlers (2006) and unlike King & Aurnou (2015). They therefore exist in the weakly rotating MC wave limit. As shown in subsection 4.10, the weakly rotating MC wave dispersion relation can be reduced to

$$\omega_{MC} = \pm \left(\frac{\mathbf{B} \cdot \mathbf{k}_0}{\sqrt{\rho\mu}} (1 \pm \epsilon) \right) \approx \omega_A, \quad \text{where} \quad \epsilon = \frac{\sqrt{\rho\mu}}{k_0} \frac{\boldsymbol{\Omega} \cdot \mathbf{k}_0}{\mathbf{B}_0 \cdot \mathbf{k}_0} \ll 1, \quad (4.61)$$

\mathbf{k}_0 is the wavevector, $\boldsymbol{\Omega}$ is the angular velocity vector, \mathbf{B} is the applied magnetic flux density, μ is the magnetic permeability and $\omega_A = \pm(\mathbf{B} \cdot \mathbf{k}_0)/\sqrt{\rho\mu}$ is the Alfvén wave dispersion relation. With $\epsilon \simeq 4 \times 10^{-6} \text{ s}^{-1}$ in our experiments, the MC wave period is well approximated by an Alfvén wave timescale $\tau_A = H/(B/\sqrt{\rho\mu})$ that is typically less than 1 s in our system. For instance, $\tau_A \simeq 0.74 \text{ s}$ for the *Conducting MC⁻* case, a value three orders of magnitude shorter than the observed MP periods. Thus, we conclude that the MP mode is best explained via TEMC dynamics.

4.9 TEMC at Earth’s core-mantle boundary

Turbulent magnetoconvection is relevant for understanding many geophysical and astrophysical phenomena (e.g., Proctor & Weiss, 1982; King & Aurnou, 2015; Vogt *et al.*, 2021). If $\tilde{S} \approx 0$ under planetary interior conditions (Chen *et al.*, 2019), then thermoelectric currents can exist in the vicinity of the core-mantle boundary (CMB) and inner core boundary of Earth’s liquid metal outer core and those of other planets. Assuming Se is not trivially small across these planetary interfaces, then TEMC-like dynamics could influence planetary core processes and could prove important for our understanding of planetary magnetic field observations (Merrill & McElhinny, 1977; Stevenson, 1987; Schneider & Kent, 1988; Giampieri &

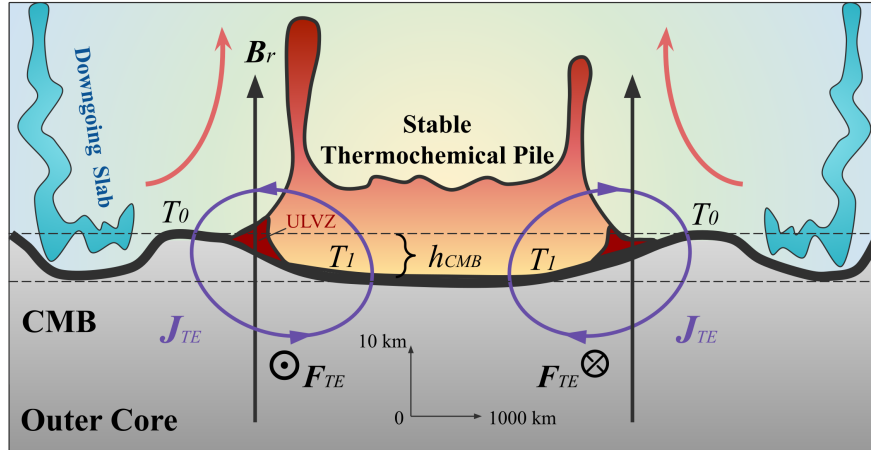


Figure 4.17: Schematic adapted from [Garnero *et al.* \(2016\)](#) and [Deschamps *et al.* \(2018\)](#) showing thermoelectric currents J_{TE} and forces F_{TE} in the vicinity of the core-mantle boundary (CMB). The vertical scale is considerably exaggerated. The black arrows are radial magnetic field, $B_r \sim 19$ gauss. The temperature contrast between the thermochemical pile or the ULVZs and the surrounding mantle is denoted by $T_1 - T_0 = \Delta T_p \sim 10^2$ K. The dynamic depression of the CMB, $h_{CMB} \sim 5$ km, can generate smaller adiabatic temperature differences of order 5 K.

Balogh, 2002; Meduri *et al.*, 2020). Previous models of planetary core thermoelectricity have focused predominantly on magnetic fields produced as a byproduct of CMB thermoelectric current loops (Stevenson, 1987; Giampieri & Balogh, 2002). In contrast, our experimental results suggest that TE processes can generate ‘slow modes,’ which could change a body’s observed magnetic field by altering the local CMB magnetohydrodynamics. Further, thermoelectric effects provide a \mathbf{B} -dependent symmetry-breaker that does not exist in current models of planetary core magnetohydrodynamics.

Two dominant structures are known to exist at the base of Earth’s mantle: thermochemical piles (Trampert *et al.*, 2004; Mosca *et al.*, 2012; Garnero *et al.*, 2016; Deschamps *et al.*, 2018) and ultra low velocity zones (ULVZs) (Garnero *et al.*, 1998), both shown schematically in figure 4.17. Seismic tomographic inversions reveal that the continental-sized thermochemical piles have characteristic length scales of approximately 5000 km along the CMB (Cottaar & Lekic, 2016; Garnero *et al.*, 2016). The ULVZs are patches a few tens of kilometers thick

just above the CMB where the seismic shear wave speed is about 30% lower than the surrounding material (Garnero *et al.*, 1998). The lateral length scale of ULVZs ranges from 10 km (Garnero *et al.*, 2016) to over 1000 km based on recent studies of so-called mega-ULVZs (Thorne *et al.*, 2020, 2021). Lateral thermal gradients can exist along the CMB between the piles or ULVZs and surrounding regions. By estimating the excess temperature of mantle plumes (Bunge, 2005) or by taking the temperature difference between the ULVZ melt (Liu *et al.*, 2016; Li *et al.*, 2017) and cold slabs (Tan *et al.*, 2002) near the CMB, we argue that the lateral temperature difference on the CMB to be $\lesssim 3 \times 10^2$ K. Therefore, the lateral thermal gradient across the edge of ULVZs is possibly on the order of magnitude of 1 K/km.

On the fluid core side of the CMB, Mound *et al.* (2019) have argued that the outer core fluid situated just below the thermochemical piles will tend to form regional stably-stratified lenses. If such lenses exist, thermal gradients will also exist in the outer core across the boundaries between the stable lenses, where the heat flux is subadiabatic, and the surrounding convective regions. ULVZs may have high electrical conductivity due to iron enrichment and silicate melt (Holmström *et al.*, 2018), such that the electrical conductivity is $\sigma \simeq 3.6 \times 10^4$ S/m at CMB-like condition (136 GPa and 4000 K). Therefore, these structures may prove well-suited to host TE current loops.

In Earth’s core, we take the radial magnetic field strength B_r to be of order 1 mT on the CMB and estimate the flow speed to be $U_C \sim 0.1$ mm/s, based on inversions of geomagnetic field data (Holme, 2015; Finlay *et al.*, 2016). Note that the outer core flow velocity might be lower if there are convectively stable layers (Buffett & Seagle, 2010) or stable fluid lenses (Mound *et al.*, 2019) situated below the CMB. Seebeck numbers across Earth’s core-mantle boundary may then be estimated as

$$Se = \frac{|\tilde{S}|\Delta T_p}{U_C B_r L_p} \text{ for the thermochemical piles,} \quad (4.62a)$$

$$Se = \frac{|\tilde{S}|\Delta T_p}{U_C B_r L_{ulvz}} \text{ for the ULVZs,} \quad (4.62b)$$

where $\Delta T_p \sim 300$ K is the lateral temperature difference between the thermochemical piles

Parameters	Description	Estimates
ΔT_p	Lateral temperature difference between the thermochemical pile and its surrounding mantle in the CMB	~ 300 K
U_C	Outer core flow speed near CMB	~ 0.1 mm/s
B_r	Radial geomagnetic field at the CMB	~ 1 mT
L_p	Characteristic length of a thermochemical pile	~ 5000 km
L_{ulvz}	Characteristic length of the ULVZs	~ 500 km

Table 4.3: Parameters used to estimate Seebeck numbers (4.62) across Earth’s core-mantle boundary (CMB).

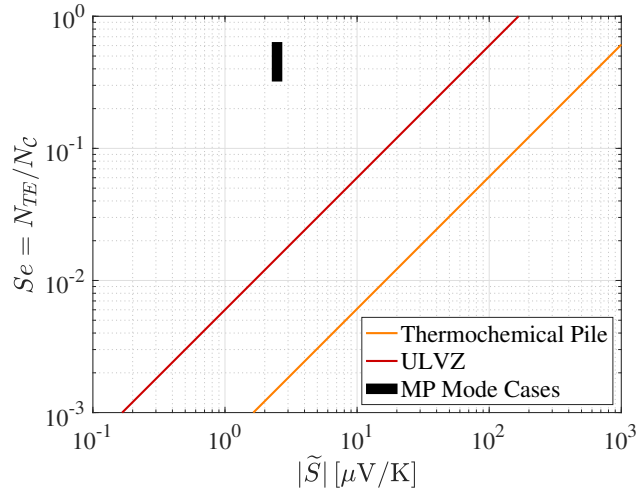


Figure 4.18: The Seebeck number Se as a function of the net Seebeck coefficient \tilde{S} . The red (orange) line represents estimated values for ULVZs (thermochemical piles) via eqs. (4.62). The thick black line marks the range of cases that have magnetoprecessional modes in this study. Here, \tilde{S} is defined with the mean temperature of the fluid, \bar{T} , so that $\tilde{S} = X_0 \bar{T}$. Our experiments show that TEMC dynamics can emerge at Se below unity.

and the surrounding mantle.

Figure 4.18 shows estimated CMB Seebeck numbers as a function of the net Seebeck coefficient \tilde{S} . The orange line represents the thermochemical pile with a characteristic length $L_p \sim 5 \times 10^3$ km. The red line represents the ULVZ with a characteristic length $L_{ulvz} \sim 500$ km. The cases from this study that have MP modes are denoted by a thick black line. The Seebeck number is defined as $Se = |\tilde{S}|\Delta T/(U_{ff}BH)$, with \tilde{S} defined with the mean temperature of the fluid, \bar{T} , so that $\tilde{S} = X_0\bar{T}$. Our experimental results show TEMC dynamics emerge at Se below 1. This plot suggests then that net Seebeck coefficients at the CMB must exceed values of order $10 \mu\text{V/K}$ in order for TEMC dynamics to affect Earth's local CMB dynamics and possibly alter the observed magnetic field.

We do not know at present if \tilde{S} can actually attain the values necessary to drive significant thermoelectric currents across planetary core interfaces. It should be noted that many thermoelectric materials, especially semiconductors, are known to have large Seebeck coefficients that can exceed $100 \mu\text{V/K}$. Silicon, for instance, has a Seebeck coefficient of $\sim 800 \mu\text{V/K}$ at 500 K (Fulkerson *et al.*, 1968). Moreover, recent studies in thermoelectric materials show that Seebeck coefficients can increase with increasing pressures and temperatures (Chen *et al.*, 2019; Morozova *et al.*, 2019; Yoshino *et al.*, 2020). How the TE coefficients of deep Earth materials extrapolate to core-mantle boundary conditions has, however, yet to be determined.

4.10 Weakly rotating Magneto-Coriolis Waves

One of the possible origin of precessional behavior of the LSC in liquid metal magnetoconvection is the excitation of the Magnetic-Coriolis (M-C) wave. Here we will calculate the characteristic frequency of the weakly rotating M-C wave that is likely to reside in our

system. The dispersion relation for the Magnetic-Coriolis wave is (Finlay, 2008)

$$\omega_{M-C} = \pm \frac{\boldsymbol{\Omega} \cdot \mathbf{k}_0}{k_0} \pm \left(\frac{(\boldsymbol{\Omega} \cdot \mathbf{k}_0)^2}{k_0^2} + \frac{(\mathbf{B} \cdot \mathbf{k}_0)^2}{\rho\mu} \right)^{1/2}, \quad (4.63)$$

where \mathbf{k}_0 is the wavenumber, $\boldsymbol{\Omega}$ is the angular rotation vector, and \mathbf{B} is the magnetic flux density. In the weakly rotating limit, the Alfvén wave frequency, ω_A , is much larger than the inertial wave frequency: $|\mathbf{B} \cdot \mathbf{k}/\sqrt{\rho\mu}| \gg |2\boldsymbol{\Omega} \cdot \mathbf{k}_0/k_0|$. The dispersion relation can then be rewritten as

$$\omega_{M-C} = \pm \frac{\boldsymbol{\Omega} \cdot \mathbf{k}_0}{k_0} \pm \frac{\mathbf{B} \cdot \mathbf{k}_0}{\sqrt{\rho\mu}} \left(1 + \frac{(\boldsymbol{\Omega} \cdot \mathbf{k}_0)^2 \rho\mu}{(\mathbf{B} \cdot \mathbf{k}_0)^2 k_0^2} \right)^{1/2}. \quad (4.64)$$

The last term of eq. (4.64) is small, allowing us to carry out a Taylor expansion,

$$\omega_{M-C} = \pm \frac{\boldsymbol{\Omega} \cdot \mathbf{k}_0}{k_0} \pm \frac{\mathbf{B} \cdot \mathbf{k}_0}{\sqrt{\rho\mu}} \left(1 + \frac{(\boldsymbol{\Omega} \cdot \mathbf{k}_0)^2 \rho\mu}{2(\mathbf{B} \cdot \mathbf{k}_0)^2 k_0^2} \right). \quad (4.65)$$

A small quantity ϵ can be defined as:

$$\epsilon = \frac{\sqrt{\rho\mu}}{k_0} \frac{\boldsymbol{\Omega} \cdot \mathbf{k}_0}{\mathbf{B} \cdot \mathbf{k}_0} \ll 1. \quad (4.66)$$

Eq. (4.65) can then be recast with ϵ ,

$$\omega_{M-C} = \pm \frac{\mathbf{B} \cdot \mathbf{k}_0}{\sqrt{\rho\mu}} \left(\epsilon \pm \left(1 + \frac{1}{2}\epsilon^2 \right) \right). \quad (4.67)$$

Two branches of solution emerge: the fast branch, ω_{M-C}^f , is acquired when the first two signs in eq. (4.67) are the same. In contrast, the slow branch, ω_{M-C}^s , is acquired when the first two signs in eq. (4.67) are the opposite. Therefore, the slow branch solution will have a smaller absolute values than the fast branch. The solution becomes

$$\left. \begin{aligned} \omega_{M-C}^f &= \pm \frac{\mathbf{B} \cdot \mathbf{k}_0}{\sqrt{\rho\mu}} \left(\frac{1}{2}(1 + \epsilon)^2 + \frac{1}{2} \right); \\ \omega_{M-C}^s &= \pm \frac{\mathbf{B} \cdot \mathbf{k}_0}{\sqrt{\rho\mu}} \left(\frac{1}{2}(1 - \epsilon)^2 + \frac{1}{2} \right). \end{aligned} \right\} \quad (4.68)$$

We can further simplify this dispersion relation by applying another Taylor expansion, $(1 \pm \epsilon)^2 \approx 1 \pm 2\epsilon$, such that:

$$\left. \begin{aligned} \omega_{M-C}^f &= \pm \frac{\mathbf{B} \cdot \mathbf{k}_0}{\sqrt{\rho\mu}} (1 + \epsilon) \approx \omega_A; \\ \omega_{M-C}^s &= \pm \frac{\mathbf{B} \cdot \mathbf{k}_0}{\sqrt{\rho\mu}} (1 - \epsilon) \approx \omega_A. \end{aligned} \right\} \quad (4.69)$$

Thus, both fast and slow Magnetic-Coriolis waves behave as Alfvén waves in the weakly rotating limit. This frequency is simply too fast in our experiment to be related to magneto-precession.

4.11 LSC torsional/sloshing modes in liquid gallium

Characteristic internal oscillations, including torsional and sloshing modes, have been a major topic in the RBC community. To broaden our understanding of TEMC dynamics, we have added a set of experimental results of liquid gallium turbulent magnetoconvection (MC) in an aspect ratio $\Gamma = 1$ cell. We have compared the fundamental internal oscillations in $\Gamma = 1$ and $\Gamma = 2$ experiments and have understood better how the thermoelectric precession is affecting these internal oscillations. Specifically, we do not observe the base modes of $\Gamma = 1$ Rayleigh Bénard convection, sloshing and torsional oscillations, in the $\Gamma = 2$ experiments of this study. Instead, we find a much weakened ‘jump rope vortex’ (JRV) mode in the $\Gamma = 2$ precessional cases. This observation addresses the important questions from the referees of this publication and provides experimental constraints for future MC studies.

4.11.1 Torsional and sloshing modes in liquid metal convection

In Rayleigh-Bénard convection, the most characteristic and fundamental turbulent coherent structure is the large-scale circulation (LSC). In $\Gamma = 1$ cylindrical containers, it is known to have horizontal sloshing and torsional oscillatory mode coupled with the recurring turbulent LSC (Funfschilling *et al.*, 2008; Zhou *et al.*, 2009; Horn *et al.*, 2022). However, the three-dimensional ‘jump rope vortex (JRV)’ is the dominant mode of the turbulent RBC in $\Gamma = 2$ cylinders (Vogt *et al.*, 2018a). The recent work of dynamic mode decomposition (DMD) analysis on direct numerical simulation of liquid metal (Horn *et al.*, 2022) shows that both types of modes co-exist in $\Gamma = 1$ & 2 cylinders but are much weaker in $\Gamma = 2$ geometries. Therefore, we do not expect to observe significant sloshing or torsional modes in our $\Gamma = 2$

RBC cases. However, since the extra thermoelectric torque has been exerted on the LSC in our *Conducting MC*[±] cases, it could become a symmetry breaker and cause deformation and oscillation of the LSC plane in the same frequency as the magnetoprecession (MP) mode.

To broaden our understanding of TEMC dynamics, here we compare and contrast a set of $\Gamma = 1$ experiments with comparable $\Gamma = 2$ cases. Using the same setup described in the main text, the $H \simeq 10$ cm sidewall ($\Gamma = 2$) is exchanged with an $H \simeq 20$ cm sidewall to create an experimental device with a $\Gamma = 1$ tank geometry.

Figure 4.19 shows Hovmöller plots of the sidewall temperature field in four separate experimental cases, one RBC case and one *Conducting MC*⁻ case in each geometry. Figure 4.19(b) shows that the thermal field precesses in the $\Gamma = 1$ *Conducting MC*⁻ case, similarly to the MP behavior found in $\Gamma = 2$ experiments. The $\Gamma = 1$ magnetoprecession rate is $d\xi_j^{mid}/dt = 8.40 \times 10^{-3}$ rad/s. Our model predicts the angular frequency of magnetoprecession to be $\omega_{MP}(U_{MC}/U_{ff}) = 6.22 \times 10^{-3}$ rad/s, which is in good zeroth order agreement with the data.

The biggest difference then between the $\Gamma = 1$ and 2 cases is found to be the internal oscillation mode of the LSC. We have previously demonstrated in convection cells with $\Gamma = 2$ that the dominant LSC mode is a jump rope vortex (JRV), whereas in $\Gamma = 1$, the dominant mode is the coupled sloshing-torsional mode (Vogt *et al.*, 2018a). Brown & Ahlers (2009) and Zhou *et al.* (2009) have shown that the sloshing and torsional mode are contained in the very same advected oscillation. Therefore, both modes have the same frequency but a phase difference of π , and the torsional mode cannot exist without a sloshing mode.

We have verified this behaviour in our current set-up. The Conducting RBC case in $\Gamma = 1$ (figure 4.19(a)) shows a zigzag pattern, which is characteristic of sloshing. The Conducting RBC case in $\Gamma = 2$ (figure 4.19(c)) shows an accordion pattern, which is characteristic of the jump rope vortex (JRV). In Vogt *et al.* (2018a), we have demonstrated that this is the most straightforward method to identify either mode. In the magnetoconvection cases (figure 4.19(b,d)), both the sloshing and the JRV modes are suppressed by the magneto-

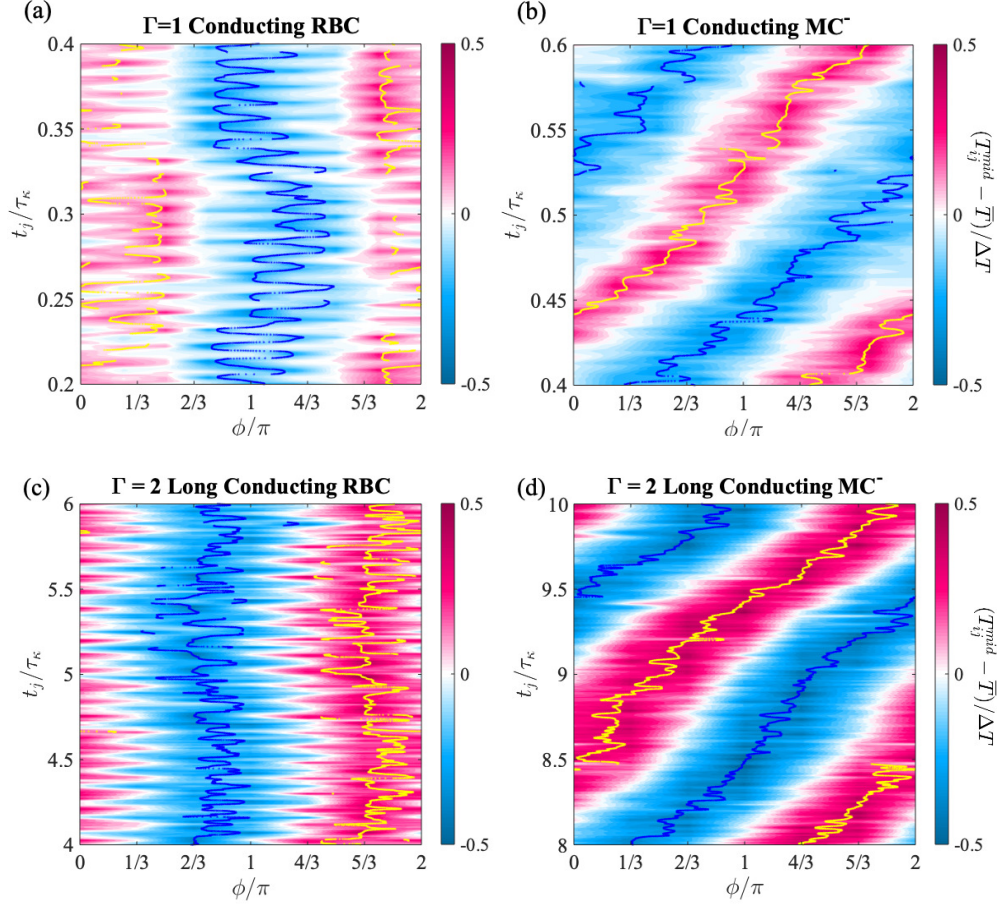


Figure 4.19: Hovmöller diagrams of the sidewall midplane temperature fluctuation. (a) *Conducting RBC* case in the $\Gamma = 1$ tank at $Ra = 2 \times 10^7$, showing the zig-zag pattern characteristic for sloshing. (b) Corresponding *Conducting MC⁻* case at ($Ra = 2.8 \times 10^7$, $Ch = 4.1 \times 10^4$; $N_C = 1.27$, $N_{TE} = 0.16$) showing a drifting magnetoprecession mode. (c) *Long Conducting RBC* case in $\Gamma = 2$ tank at $Ra = 1.79 \times 10^6$ (same as in the main manuscript), showing the accordion pattern characteristic for a jump rope vortex (JRV). (d) Corresponding *Long Conducting MC⁻* at ($Ra = 1.82 \times 10^6$, $Ch = 2.6 \times 10^3$; $N_C = 0.31$, $N_{TE} = 0.16$), showing a drifting magnetoprecession mode similar to (b). The yellow (blue) lines indicate the position of the maximum (minimum) temperature obtained with the TEE method. The time windows are selected to show approximately one full precession, corresponding, respectively, to $0.2\tau_\kappa$ for $\Gamma = 1$ and to $2\tau_\kappa$ for $\Gamma = 2$.

precession mode, which manifests itself through a strong azimuthal drift of the temperature pattern. But there are faint indications in the MC cases that a much weakened sloshing mode still exists in $\Gamma = 1$ cases, and similarly, a much weakened JRV mode still exists in $\Gamma = 2$ cases. The spectral data shown in figure 4.9(a) further supports the latter.

We have analysed our data more quantitatively by applying the TEE method of Zhou *et al.* (2009) to the sidewall midplane, top, and bottom temperature measurements, as also indicated by the yellow and blue lines in figure 4.19. These TEE measurements confirm the existence of the torsional mode in our $\Gamma = 1$ tank by measuring the difference in the azimuthal angles of the best-fit extrema between the top and bottom (not shown). We did not find clear evidence of torsional oscillations in the $\Gamma = 2$ cases, neither in the *Insulating* and *Conducting RBC* cases nor in the *Insulating MC[±]*, in agreement with the previous $\Gamma = 2$ results of Vogt *et al.* (2018a). This decoupling between the torsional and sloshing motion in the turbulent MC is novel and interesting, thus, it should be investigated further in future studies. The detailed methods and analysis are shown as follows.

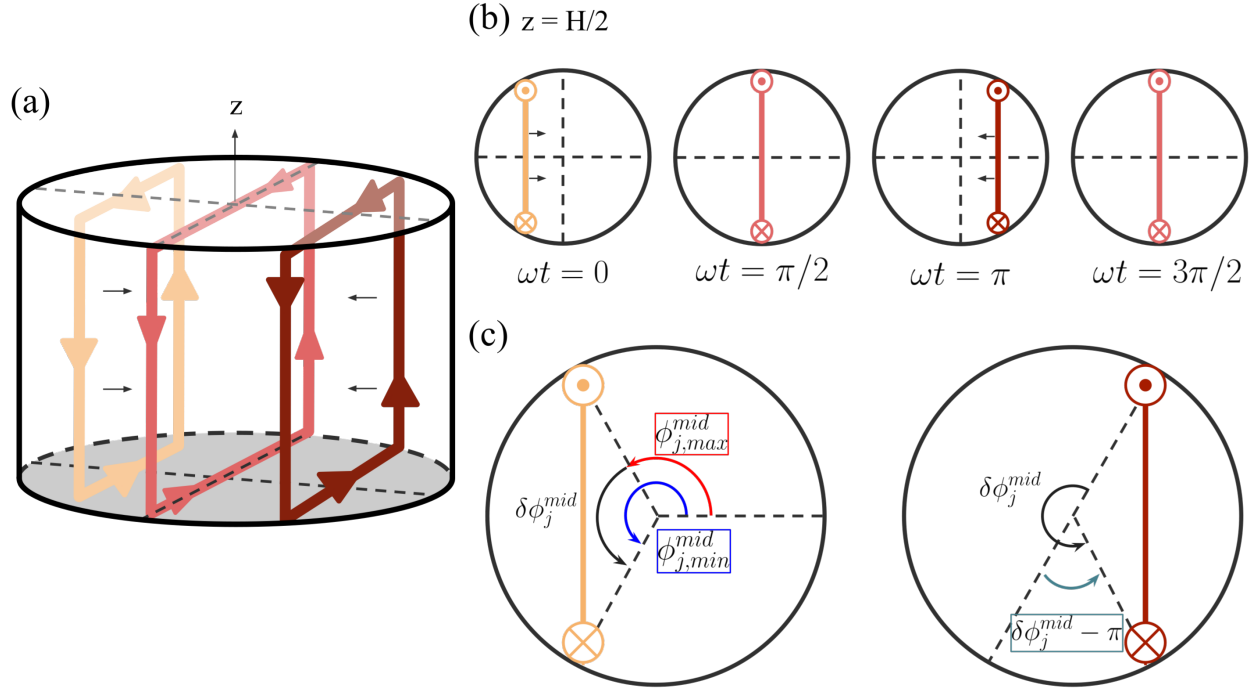


Figure 4.20: (a) A three-dimensional diagram showing the LSC that undergoes sloshing oscillation. (b) Diagrams of horizontal cross-sections showing periodic horizontal oscillation of the LSC at different phases in the mean LSC frame. (c) Schematic diagram showing the definitions of the orientation $\phi_{j,max}^{mid}$, $\phi_{j,min}^{mid}$, and $\delta\phi_j^{mid}$. The angle displacement in sloshing oscillation $\delta\phi_j^{mid} - \pi$. All the angles are measured in the right-hand direction, $\hat{\phi}$.

The thermometry data is discretized in both space and time. The discrete temperature time series data is expressed in 4.31. Using the TEE method (Zhou *et al.*, 2009), the temperature extrema are found at every time step by two quadratic fits from two sets of three data points adjacent to the maximum and minimum. Around the extrema,

$$T_{fit}^k(t_j) = a_j^k \phi^2 + b_j^k \phi + c_j^k, \quad (4.70)$$

where a_j^k , b_j^k , and c_j^k are instantaneous best-fitted parameters. The extrema at each time step are located at azimuthal angles

$$\max(\phi_j^k) = -\frac{b_j^k}{2a_j^k}, \quad \text{if } a_j^k < 0; \quad \min(\phi_j^k) = -\frac{b_j^k}{2a_j^k}, \quad \text{if } a_j^k > 0. \quad (4.71)$$

Figure 4.20 shows schematics of the sloshing motion of the LSC. The colored lines and arrows represent LSCs at a different time of the period. Figure 4.20(b) shows how the position of the LSC plane oscillates horizontally with time at the midplane with a frequency of $\omega = 2\pi/t$. The midplane azimuthal location of the extrema on the LSC are defined as

$$\phi_{j,max}^{mid} = \max(\phi_j^{mid}); \quad \phi_{j,min}^{mid} = \min(\phi_j^{mid}), \quad (4.72)$$

and their difference is

$$\delta\phi_j^{mid} \hat{\phi} = \phi_{j,max}^{mid} \hat{\phi} - \phi_{j,min}^{mid} \hat{\phi}. \quad (4.73)$$

The LSC undergoes a horizontal period oscillation with respect to the centering position. This change in horizontal location can be measured by the $\delta\phi_j^{mid}$ as shown in panel (c) from the sidewall midplane thermistors, in a similar way to figure 3 of [Brown & Ahlers \(2009\)](#). By analyzing the dominant frequency of the $\delta\phi_j^{mid}$ in FFT spectra, we can measure the sloshing frequency accordingly.

Figure 4.21 shows the behavior of torsional oscillation at different heights and phases. The diagram only shows the orientation and location of the LSC at top/midplane/bottom that undergoes torsional oscillation over a complete period. The torsional oscillation has the largest amplitude at $\omega t = \pi/2$ and $3\pi/2$, presumably different from the sloshing by $\pi/2$.

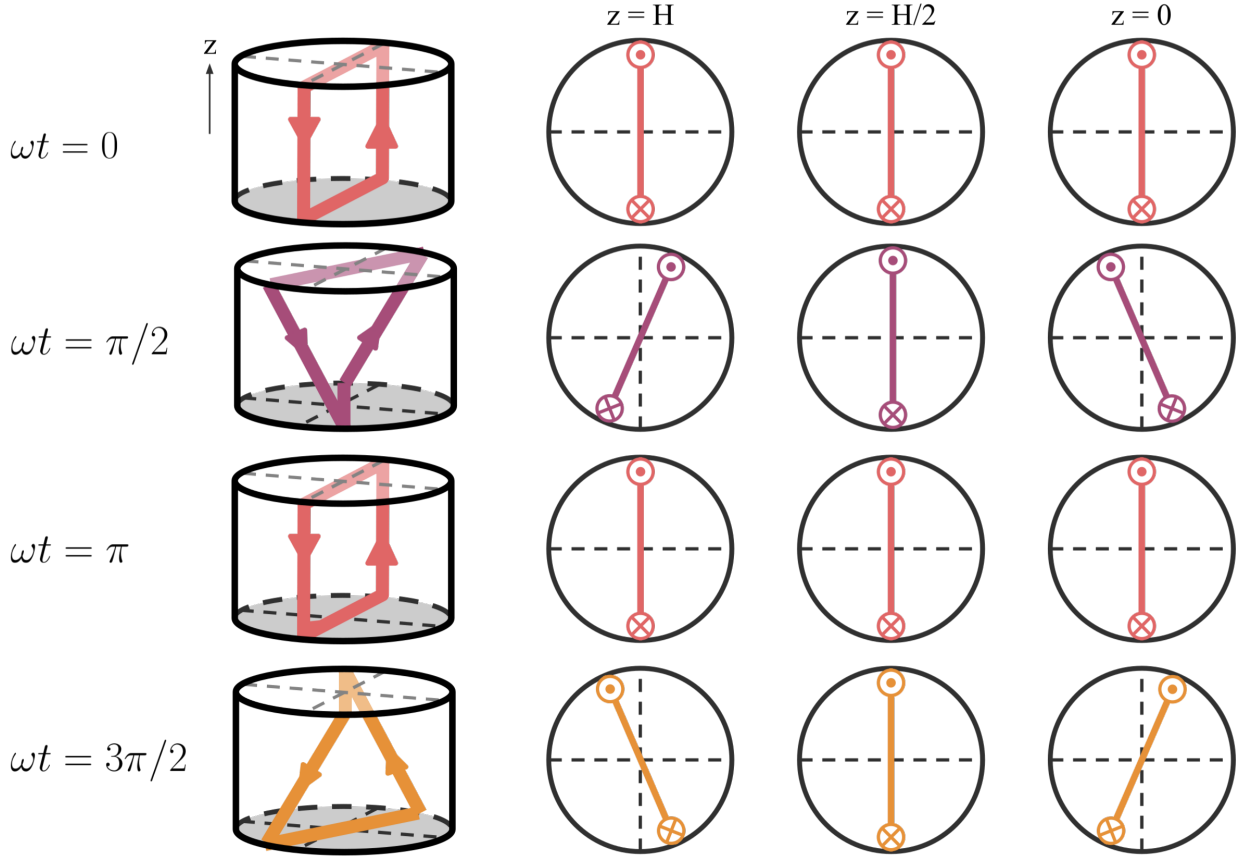


Figure 4.21: The torsional oscillations at different heights and phases in the mean LSC frame. The torsional motion should have a $\pi/2$ phase difference from the sloshing mode. The torsional oscillation reaches its maximum amplitude at $\omega t = \pi/2$ and $3\pi/2$, while the sloshing oscillation reaches its maximum $\omega t = 0$ and π , as shown in figure 4.20(b). Schematics adapted from (Brown & Ahlers, 2009).

We compare the difference in the azimuthal angles of the best-fit extrema between top and bottom, namely $\Delta\phi_{max}$ and $\Delta\phi_{min}$, to detect torsional oscillations in our data. They are defined as

$$\Delta\phi_{max}\hat{\phi} = \max(\phi_j^{top})\hat{\phi} - \max(\phi_j^{bot})\hat{\phi}; \quad \Delta\phi_{min}\hat{\phi} = \min(\phi_j^{top})\hat{\phi} - \min(\phi_j^{bot})\hat{\phi}. \quad (4.74)$$

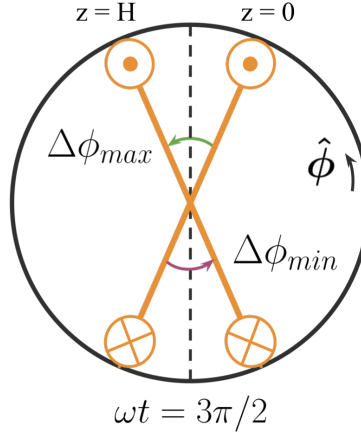


Figure 4.22: A top-view schematic diagram of the LSC at time $\omega t = 3\pi/2$ showing the definition of $\Delta\phi_{max}$ and $\Delta\phi_{min}$, which are displacement angles of hot and cold flows of the LSC, respectively. The LSC's top and bottom components overlays each other. We expect that $\Delta\phi_{max} \simeq \Delta\phi_{min}$.

The timeseries of $\Delta\phi_{max}$ and $\Delta\phi_{min}$ indicate the orientation difference in the LSC between the top and bottom as they describe the twisting angles of the LSC plane at different heights. Figure 4.22 shows a snapshot of the LSC at the top and bottom boundary overlaying each other in the mean LSC frame. The angle between the upwelling LSC flows is $\Delta\phi_{max}$, whereas the downwelling LSC flows have a $\Delta\phi_{min}$ difference in between.

Moreover, we apply the following criteria for identifying our system's sloshing and torsional modes.

- I The torsional mode has a $\pi/2$ phase difference from the sloshing mode (Brown & Ahlers, 2009; Zhou *et al.*, 2009).
- II The torsional oscillation should have a same amplitude for $\Delta\phi_{max}$ and $\Delta\phi_{min}$. This means $|\Delta\phi_{max}| \simeq |\Delta\phi_{min}|$.
- III The amplitude of the azimuthal angle displacement in sloshing oscillation $\delta_j^{mid} - \pi$, should be the same as the torsional oscillation. Equation (4.3) and (4.4) in Brown & Ahlers (2009) states that the amplitude of the torsional oscillation is $A \sin(\pi z/L)$ and

$A \cos(\pi z/L)$ for sloshing. Their z is defined to be 0 at the midplane. When substituting in the top and bottom boundary as $\pm L/2$ as the height for the torsional mode and $z = 0$ for the sloshing mode, we get the amplitude of both oscillations should be the same. This means $\delta_j^{mid} - \pi \simeq \Delta\phi_{min} \simeq \Delta\phi_{max}$. This can be examined by comparing the standard deviations of the data over time.

4.11.2 No Sloshing or Torsional Modes in *Long Conducting RBC*

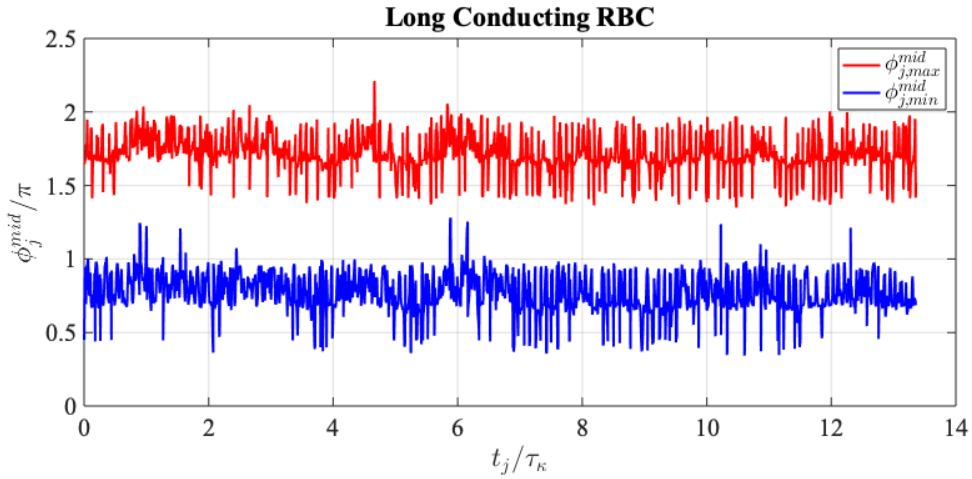


Figure 4.23: Timeseries of the azimuthal angles of the temperature extrema ($\phi_{j,max}^{mid}$ and $\phi_{j,min}^{mid}$) in the midplane using the TEE method (Zhou *et al.*, 2009) for the *Long Conducting RBC* case. The displacement between these two angles infers the locations of the hot and cold LSC flows and, therefore can be used to interpret the LSC’s dynamic positions at the midplane.

The *Long Conducting RBC* case has an LSC that is roughly fixed location. The cold and hot flows are approximately separated by π in azimuth, as shown in the timeseries of best-fit angles of the temperature extrema at the midplane in figure 4.23. The azimuthal angle data of the temperature extrema can be used to interpret the position of the LSC. And we can use the lab frame to approximate the mean LSC frame.

Figure 4.24 shows the timeseries of $\delta\phi_j^{mid}$ does not resemble the periodic sloshing motion as shown in Brown & Ahlers (2009) and Zhou *et al.* (2009). Further analysis on the frequency

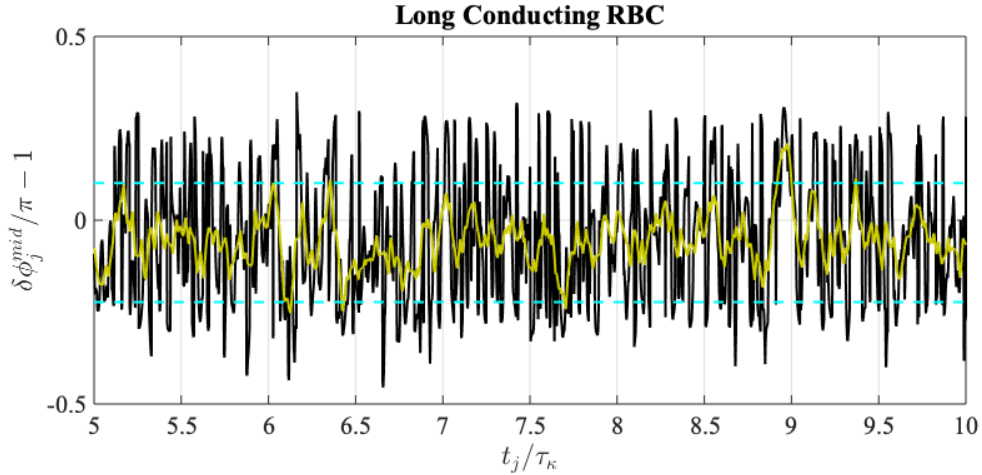


Figure 4.24: Timeseries of the $\delta\phi_j^{mid}/\pi - 1$ for the *Long Conducting RBC* case for 5 thermal diffusion time. We define $\delta\phi_j^{mid}/\pi - 1$ as the azimuthal angle difference between the temperature extrema in the midplane using the TEE method as shown in figure 4.20(c). The oscillation does not resemble the periodic sloshing motion shown in Brown & Ahlers (2009) and Zhou *et al.* (2009). The line has been smoothed using a local span of 0.5% of the total data and plotted in the yellow line. The standard deviation of $\delta\phi_j^{mid}/\pi - 1$ is $\sigma_0 = 0.16$, marked by the cyan dashed lines.

spectrum of $\delta\phi_j^{mid}$ (figure 4.25) reveals that there is a weak peak frequency which coincides with the ‘jump rope vortex’ frequency (Vogt *et al.*, 2018a). The peak is most likely picking up the background JRV mode since it is the dominant mode of the turbulent RBC in an aspect-ratio-2 tank. One reason is that the appendix of Vogt *et al.* (2018a) has shown that the turbulent RBC in an aspect-ratio-2 cell has lateral temperature oscillations at the midplane. Another reason is that the $\delta\phi_j^{mid}$ is measured in the lab frame as an approximation to the mean LSC frame. As the LSC naturally drifts around, it could pick up the dominant JRV mode.

We find $\Delta\phi_{max}$ are not correlated to $\Delta\phi_{min}$ when comparing the top and bottom temperature extrema over time (upper panel of figure 4.26). Moreover, there is no clear phase difference between $\Delta\phi_{max}$ and $\delta\phi_j^{mid} - \pi$. The amplitude of the oscillation of these two quantities which are measured by standard deviations also differs by a factor of 2 (lower panel of

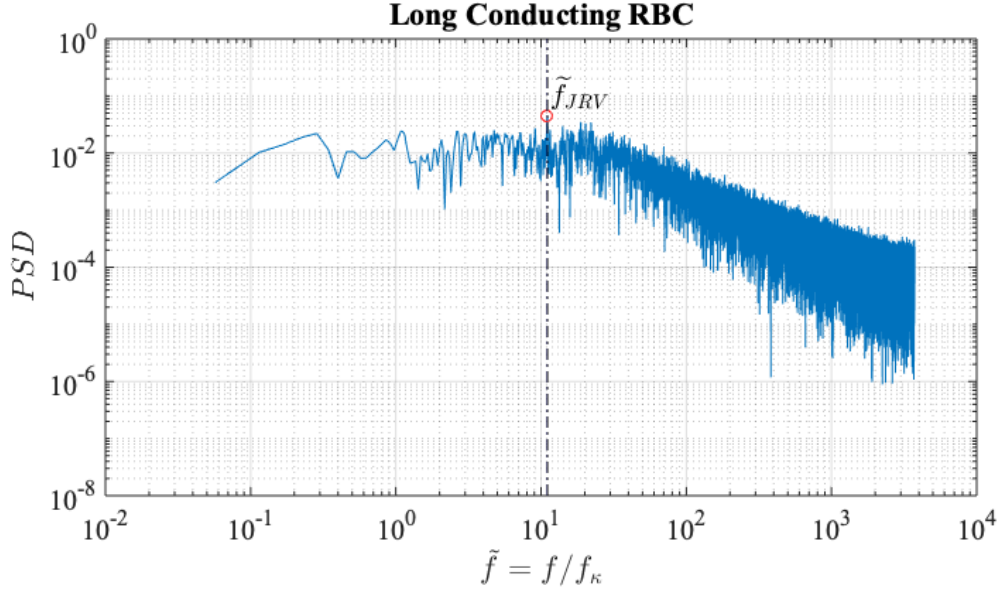


Figure 4.25: FFT of $\delta\phi_j^{mid}$ with Hanning window for the *Long Conducting RBC* case. The frequency is normalized by thermal diffusion frequency, $\tilde{f} = f/f_\kappa$. The FFT gives a weak peak at $\tilde{f} = 11.02$, marked by a red circle. This result corresponds to the background ‘jump rope vortex’ frequency (Vogt *et al.*, 2018a), where the appendix shows that the turbulent RBC in an aspect-ratio-2 cell has lateral temperature oscillations at the midplane. Moreover, the $\delta\phi_j^{mid}$ is measured in the lab frame to approximate the mean LSC frame. As the LSC naturally drifts around, it could pick up the dominant JRV mode in the background, which has a characteristic frequency of $\tilde{f}_{JRV} = 11.07$ in this case, denoted by the black vertical dash-dotted line.

figure 4.26).

Figure 4.27 shows the frequency peaks of $\Delta\phi_{max}$ and $\Delta\phi_{min}$ also coincide with the JRV peak frequency, suggesting the background origin of the oscillations that we observe.

Thus, in violating all three criteria, we conclude that there is unlikely a sloshing or torsional mode in this *Long Conducting RBC* case.

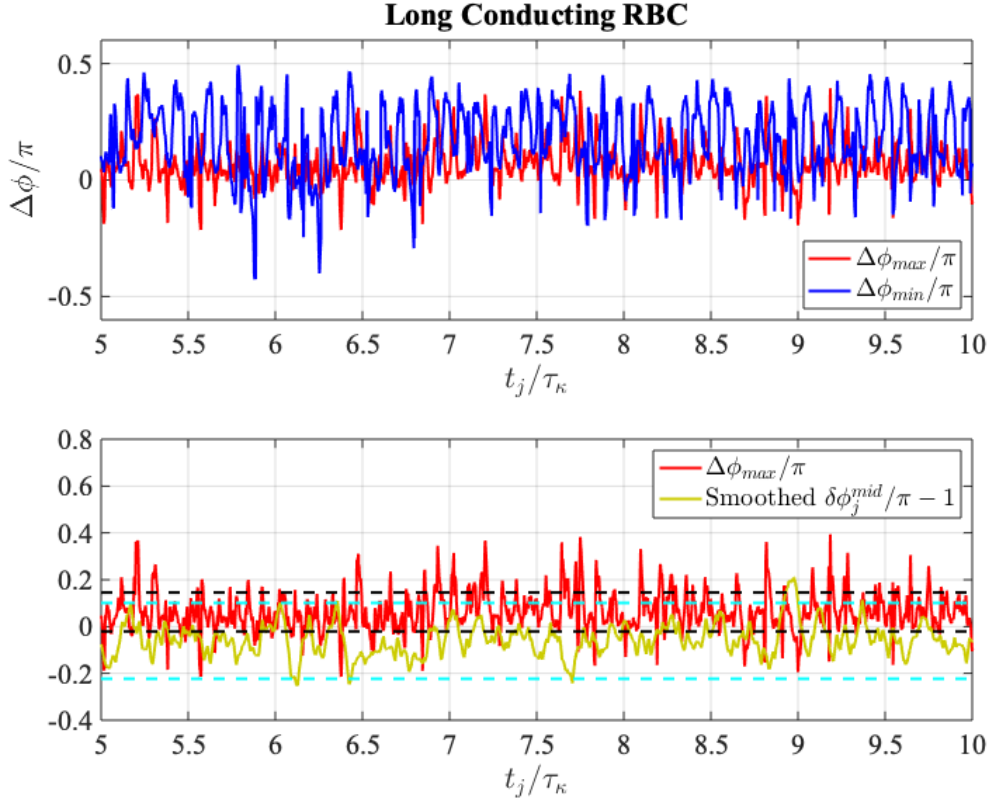


Figure 4.26: (Upper) Timeseries of $\Delta\phi_{max}/\pi$ and $\Delta\phi_{min}/\pi$ for the *Long Conducting RBC* case. It clearly shows that $\Delta\phi_{max} \neq \Delta\phi_{min}$. (Lower) Timeseries of $\Delta\phi_{max}/\pi$ and the smoothed $\delta\phi_j^{mid}/\pi - 1$. There is no clear phase difference between these two largely uncorrelated quantities. The standard deviation for $\Delta\phi_{max}/\pi$ is marked by the black horizontal dashed line and denoted as $\sigma_1 = 0.08$, which is 50% of the standard deviation of $\delta\phi_j^{mid}/\pi - 1$. Effectively, $|\Delta\phi_{max}| \neq |\delta\phi_j^{mid} - \pi|$. Thus, in violating all three criteria, there is unlikely a sloshing or torsional mode in our system for the *Long Conducting RBC* case.

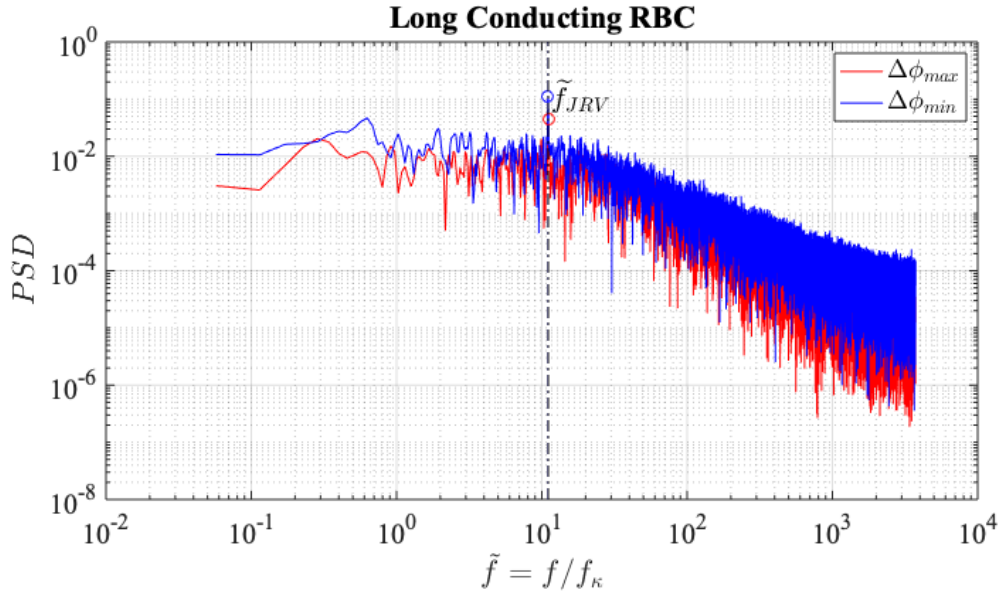


Figure 4.27: Hanning window FFT of $\Delta\phi_{max}$ and $\Delta\phi_{min}$. The spectrum for $\Delta\phi_{max}$ is shown in red. The frequency peaks at $\tilde{f} = 11.08$ and is marked by a red circle, whereas the spectrum for $\Delta\phi_{min}$ is shown in blue, which peaks at a similar $\tilde{f} = 11.02$, marked by a blue circle. This result peak frequency does not correspond to the torsional modes but to the dominant background JRV frequency where $\tilde{f}_{JRV} = 11.07$ in this case, denoted by the black vertical dash-dotted line.

4.11.3 No Sloshing or Torsional Modes in *Insulating MC-*

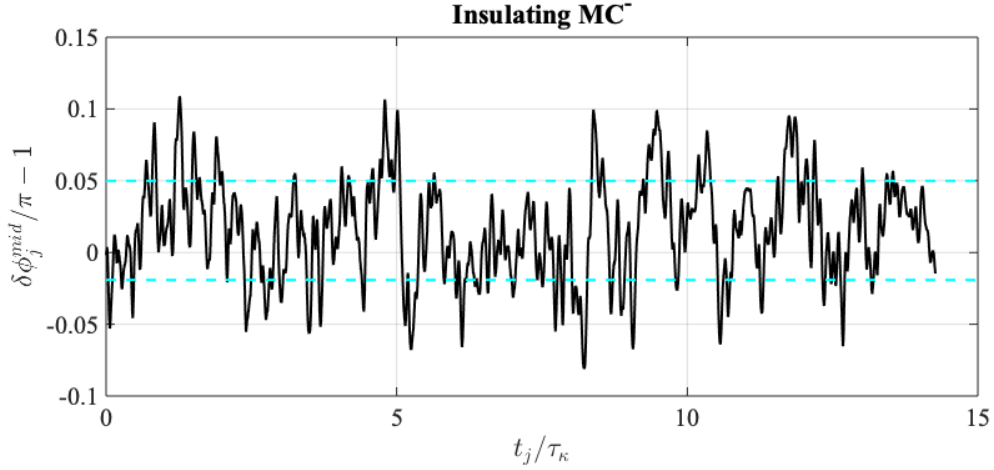


Figure 4.28: Timeseries of the $\delta\phi_j^{mid}/\pi - 1$ for the *Insulating MC-* case. We define $\delta\phi_j^{mid}/\pi - 1$ as the azimuthal angle difference between the temperature extrema in the midplane using the TEE method as shown in figure 4.20(c). The oscillation does not resemble the periodic sloshing motion. The standard deviation of $\delta\phi_j^{mid}/\pi - 1$ is $\sigma_2 = 0.03$, marked by the cyan dashed lines. The standard deviation is an order of magnitude smaller than the *Long Conducting RBC* case, possibly due to a different sidewall and the magnetic damping from the external field.

Figure 4.28 shows the timeseries of $\delta\phi_j^{mid}$ does not resemble the periodic sloshing motion as shown in Brown & Ahlers (2009) and Zhou *et al.* (2009). The standard deviation is an order of magnitude smaller than the *Long Conducting RBC* case. This is likely caused by the acrylic sidewall having thicker thermal skin depths. The thermistor has a lower temporal resolution than the conducting cases. In addition, the vertical magnetic field generates Lorentz forces on the horizontal motions of the fluid and consequently suppresses the oscillation.

The frequency FFT spectrum of $\delta\phi_j^{mid}$ in figure 4.29 shows no meaningful peak. A small peak near the JRV peak frequency could be interpreted as the background remnant from the JRV mode.

We find $\Delta\phi_{max}$ are not correlated to $\Delta\phi_{min}$ (upper panel of figure 4.30). Moreover, there

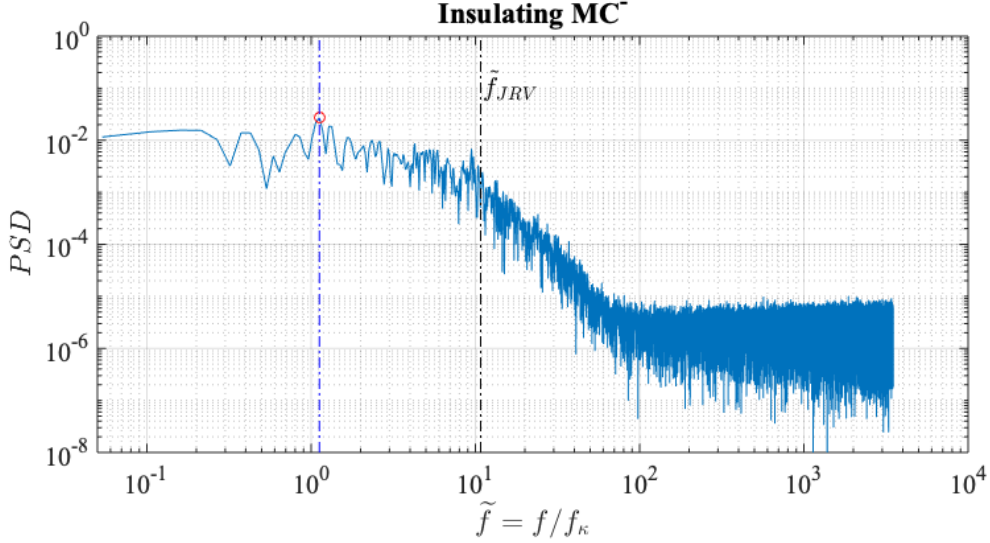


Figure 4.29: FFT of $\delta\phi_j^{mid}$ with Hanning window for the *Insulating MC⁻* case. The frequency is normalized by thermal diffusion frequency, $\tilde{f} = f/f_\kappa$. The FFT gives a weak peak at $\tilde{f} = 1.12$, marked by a red circle and a vertical blue dash-dotted line. We think this peak does not have a meaningful interpretation. No other predominant peaks are found. However, there is a small peak near the JRV frequency (Vogt et al. 2018), which has a characteristic frequency of $\tilde{f}_{JRV} \approx 10.77$ in this case, denoted by the black vertical dash-dotted line on the right. This result infers that the magnetic forces have suppressed the oscillations of the LSC.

is no clear phase difference between $\Delta\phi_{max}$ and $\delta\phi_j^{mid} - \pi$. The amplitude of the oscillation of these two quantities, measured by standard deviations, also differs by a factor of 3 (lower panel of figure 4.30). Figure 4.31 is an FFT spectrum showing both frequency peaks of $\Delta\phi_{max}$ and $\Delta\phi_{min}$ are close to the JRV peak frequency, suggesting the background origin of the oscillations that we observe. Thus, in violating all three criteria, we conclude that there is unlikely a sloshing or torsional mode in this *Insulating MC⁻* case.

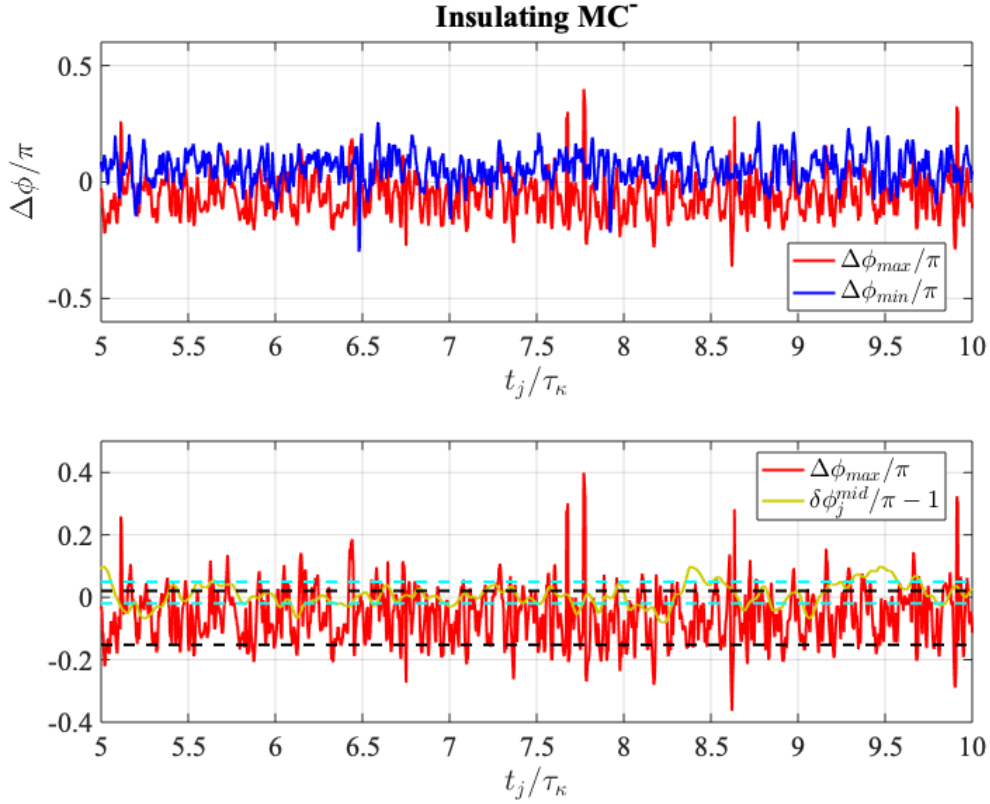


Figure 4.30: (Upper) Timeseries of $\Delta\phi_{max}/\pi$ and $\Delta\phi_{min}/\pi$ for the *Insulating MC⁻* case. It clearly shows that $\Delta\phi_{max} \neq \Delta\phi_{min}$. (Lower) Timeseries of $\Delta\phi_{max}/\pi$ and $\delta\phi_j^{mid}/\pi - 1$. There is no clear phase difference between these two largely uncorrelated quantities. The standard deviation for $\Delta\phi_{max}/\pi$ is marked by the black horizontal dashed line and denoted as $\sigma_3 = 0.09$, which is 300% of the standard deviation of $\delta\phi_j^{mid}/\pi - 1$. Effectively, $|\Delta\phi_{max}| \neq |\delta\phi_j^{mid} - \pi|$. Thus, in violating all three criteria, there is unlikely a sloshing or torsional mode in our system for the *Insulating MC⁻* case.

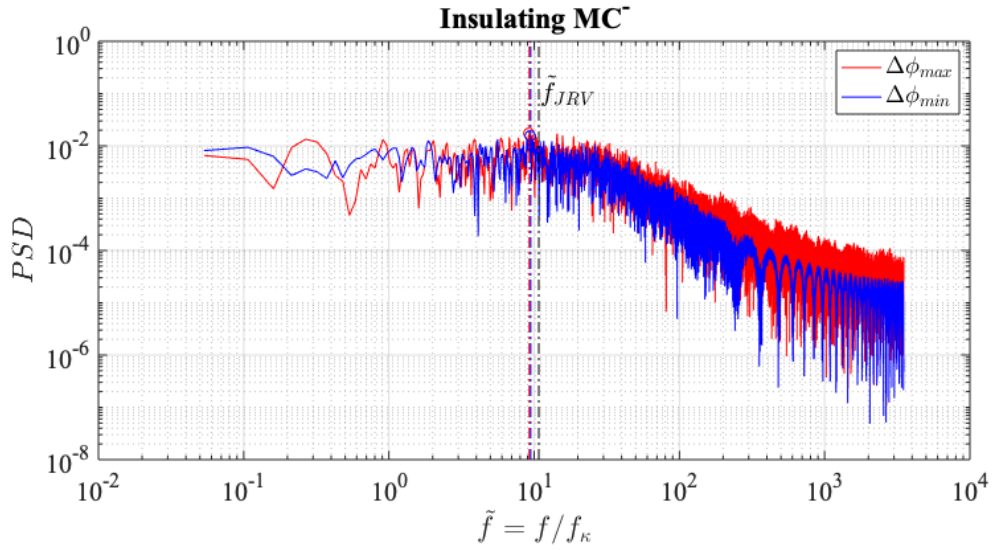


Figure 4.31: Hanning window FFT of $\Delta\phi_{max}$ and $\Delta\phi_{min}$. The FFT shows a peak at $\tilde{f} = 9.25$ for $\Delta\phi_{max}$ and $\tilde{f} = 9.46$ for $\Delta\phi_{min}$. Circles and vertical dash-dotted lines mark the peaks in their respective color. They are about 13% smaller than the predicted JRV frequency $\tilde{f}_{jrv} = 10.77$, denoted by the black vertical dash-dotted line on the right. This result peak frequency does not correspond to the torsional modes but to the dominant background JRV frequency.

4.11.4 Weak Sloshing and Strong Torsional Modes in *Long Conducting MC*

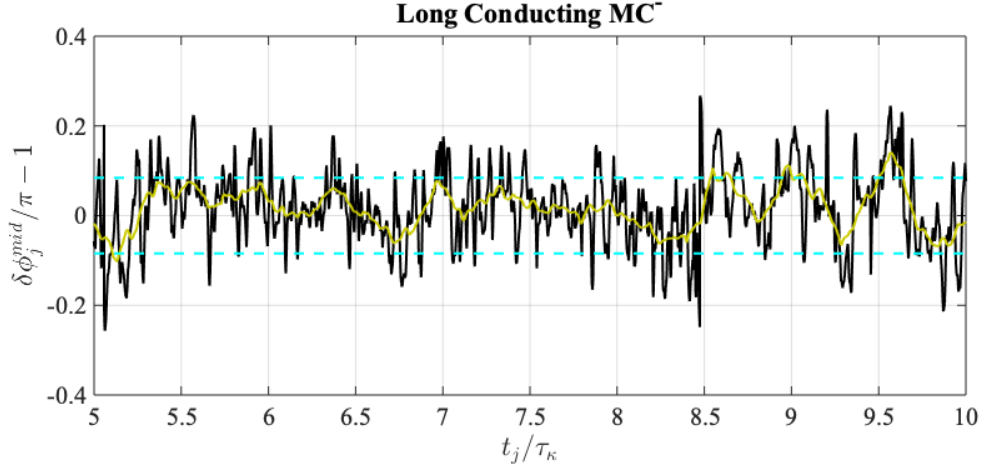


Figure 4.32: Timeseries of the $\delta\phi_j^{mid}/\pi - 1$ for the *Long Conducting MC*⁻ case for 5 thermal diffusion time. The oscillation has a weak periodicity that could associate with sloshing motion. The line has been smoothed using a local span of 0.5% of the total data and plotted in the yellow line. The standard deviation of $\delta\phi_j^{mid}/\pi - 1$ is $\sigma_4 = 0.08$, marked by the cyan dashed lines.

Figure 4.32 shows a weak periodicity in the smoothed timeseries of $\delta\phi_j^{mid}$, which could associate with the sloshing oscillation of the LSC.

The frequency FFT spectrum of $\delta\phi_j^{mid}$ in figure 4.33 shows a peak frequency that coincides with the MP mode. As the LSC precesses along the MP mode, a torque is exerted perpendicular to the LSC plane. Therefore, it is possible to excite a weak sloshing oscillation at the same frequency as the precession.

We find strong correlation between $\Delta\phi_{max}$ and $\Delta\phi_{min}$ (upper panel of figure 4.34). This satisfies criterion II that $\Delta\phi_{max} \simeq \Delta\phi_{min}$, and indicates a clear torsional mode in this case. Criterion I is only weakly satisfied, as there is no clear phase difference between $\Delta\phi_{max}$ and $\delta\phi_j^{mid} - \pi$ (see lower panel of figure 4.34). However, they have opposite signs for most of the time, i.e., $\delta\phi_j^{mid}/\pi - 1 \gtrsim 0$ when $\Delta\phi_{max}/\pi \lesssim 0$. This could interpret as a weakly constrained $\pi/2$ phase difference. The standard deviation for $\Delta\phi_{max}/\pi$ is $\sigma_5 = 0.13$, which is 162.5% of

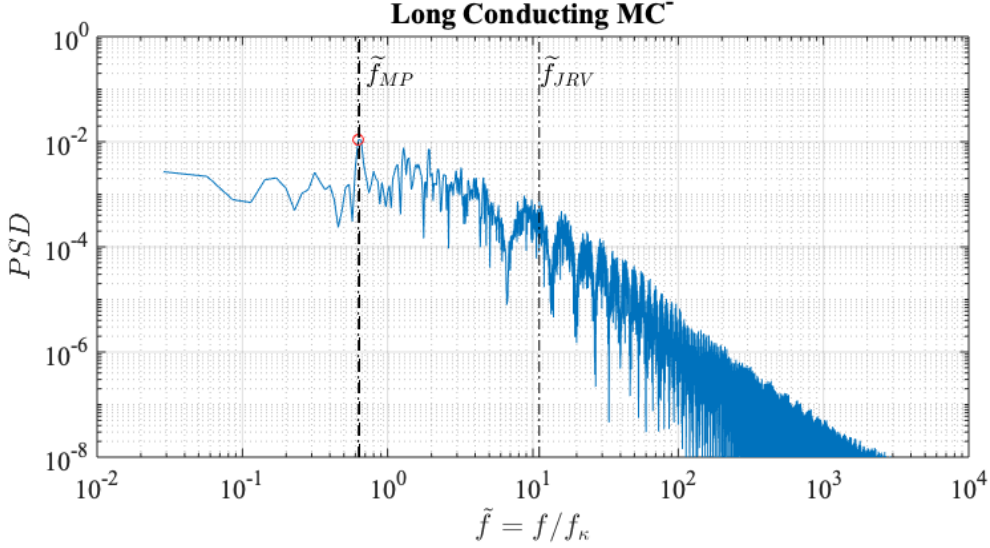


Figure 4.33: FFT of $\delta\phi_j^{mid}$ with Hanning window for the *Long Conducting MC⁻* case. The frequency is normalized by thermal diffusion frequency, $\tilde{f} = f/f_\kappa$. The FFT gives a peak at $\tilde{f} = 0.63$, marked by a red circle and a vertical dash-dotted line. This peak is almost the same as the dominant MP mode $\tilde{f}_{MP} = 0.64$, marked by a black vertical dashed line. In this case, no peak is found near the JRV frequency $\tilde{f}_{JRV} \approx 11.07$, denoted by the black vertical dash-dotted line on the right. As the LSC precesses along the MP mode, a torque is exerted perpendicular to the LSC plane. Therefore, it is possible to excite a weak sloshing oscillation.

the standard deviation of $\delta\phi_j^{mid}/\pi - 1$. Effectively, $|\Delta\phi_{max}| \neq |\delta\phi_j^{mid} - \pi|$. Thus, the sloshing motion is too weak and violates criterion III.

Figure 4.35 is an FFT spectrum showing both frequency peaks of $\Delta\phi_{max}$ and $\Delta\phi_{min}$ coincide with the MP mode peak frequency, suggesting this torsional oscillation originates from the MP mode. This is expected as the LSC is not exactly a solid-body rotation. It would twist and deform as the LSC precesses in the same frequency.

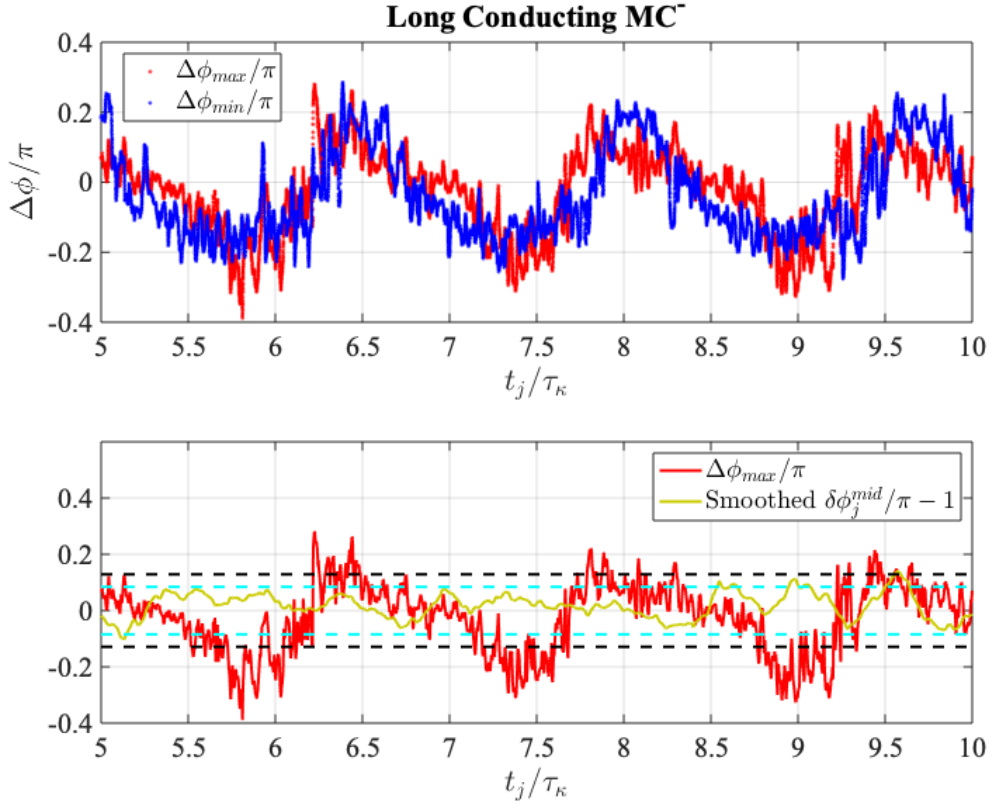


Figure 4.34: (Upper) Timeseries of $\Delta\phi_{max}/\pi$ and $\Delta\phi_{min}/\pi$ for the *Long Conducting MC⁻* case. It clearly shows that $\Delta\phi_{max}$ is in phase with $\Delta\phi_{min}$, and they both have periodic oscillations with similar amplitude and frequency. This satisfies criterion II that $\Delta\phi_{max} \simeq \Delta\phi_{min}$. This indicates a strong signal for torsional mode in the *Long Conducting MC⁻* case. (Lower) Timeseries of $\Delta\phi_{max}/\pi$ and $\delta\phi_j^{mid}/\pi - 1$. There is no clear phase difference between these two quantities. However, they have opposite signs for most of the time, i.e., $\delta\phi_j^{mid}/\pi - 1 \gtrsim 0$ when $\Delta\phi_{max}/\pi \lesssim 0$. This could interpret as a weak $\pi/2$ phase difference and thus weakly satisfies criterion I. The standard deviation for $\Delta\phi_{max}/\pi$ is marked by the black horizontal dashed line and denoted as $\sigma_5 = 0.13$, which is 162.5% of the standard deviation of $\delta\phi_j^{mid}/\pi - 1$. Effectively, $|\Delta\phi_{max}| \neq |\delta\phi_j^{mid} - \pi|$. Thus, the sloshing motion is too weak and violates criterion III.

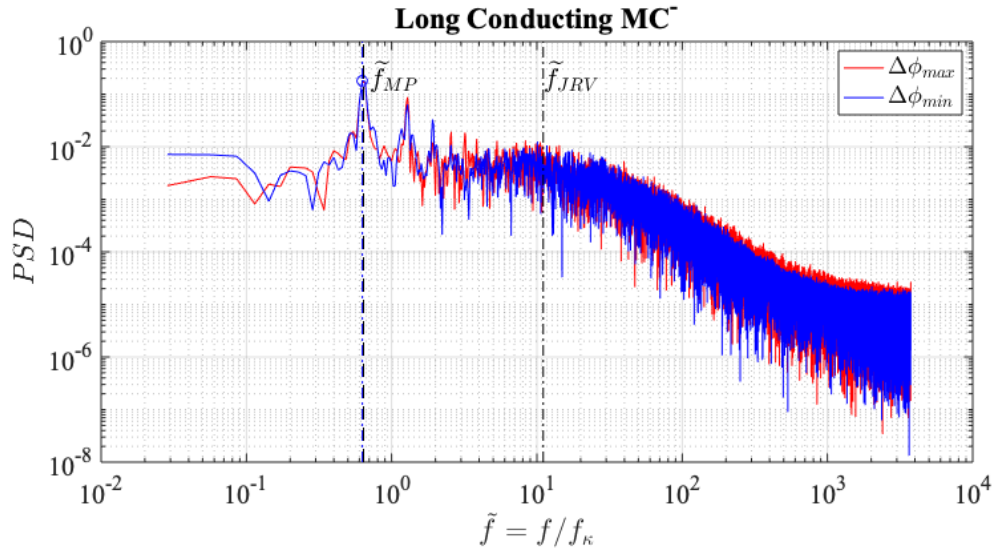


Figure 4.35: Hanning window FFT of $\Delta\phi_{max}$ and $\Delta\phi_{min}$. The FFT shows a strong peak at $\tilde{f} = 0.63$ for both $\Delta\phi_{max}$ and $\Delta\phi_{min}$. This coincides with $\tilde{f}_{MP} = 0.64$, marked by a black vertical dashed line. There is a clear signal of torsional oscillation, which has the same frequency as the MP mode. This makes sense since the LSC is not exactly solid-body rotation. It would twist and deform as the LSC precesses.

In conclusion, there is likely a strong torsional mode but a weak sloshing mode in the *Long Conducting MC⁻* case. The uncoupling between the torsional and the sloshing mode is interesting and is likely due to the pre-existing asymmetry that mainly contributes to the twisting of the LSC. I propose that the asymmetry is caused by the top lid temperature anomalies since the location of the inlet/outlet has been shown to generate periodic fluctuation in the horizontal temperature at different heights. Very similar results have been shown in the *Long Conducting MC⁺* case. Therefore, the direction of the magnetic field does not affect the oscillation nature of the LSC as expected.

CHAPTER 5

Large Scale Structures in Turbulent RC and RMC

“Out of chaos comes a dancing star.”

— Friedrich Nietzsche

Adding rotation is a leap toward the core-style convection from the reduced model of magnetoconvection discussed in prior chapters. To answer the third question in 1.4, “do large-scale structures such as LSVs exist in turbulent liquid metal rotating convection? Is the magnetostrophic mode dominant in a low-Rm liquid metal rotating magnetoconvection system?” I have conducted rotating convection (RC) and rotating magnetoconvection (RMC) experiments in liquid gallium using the ROMAG device. Thermal-velocimetry data have been obtained to analyze the spatial-temporal structures of both RC and RMC systems. Preliminary results suggest that our liquid metal RC may be manifested in large-scale vortices. These preliminary results address a possible pathway from small-scale turbulence to large-scale dynamics in the planetary cores.

Section 5.1 introduces the motivation of this study. Section 5.2 describes the experimental setup for this study. Section 5.3 shows preliminary results on large-scale vortices (LSVs) in rotating convection (RC) experiments. Section 5.4.1 shows the disappearance of the LSVs with increasing Ro_C . Section 5.4.2 shows preliminary results on characteristics of the rotating magnetoconvection (RMC) flows in our experiments. Section 5.5 discuss future works and implications of this study.

5.1 Large-scale flows in core convection

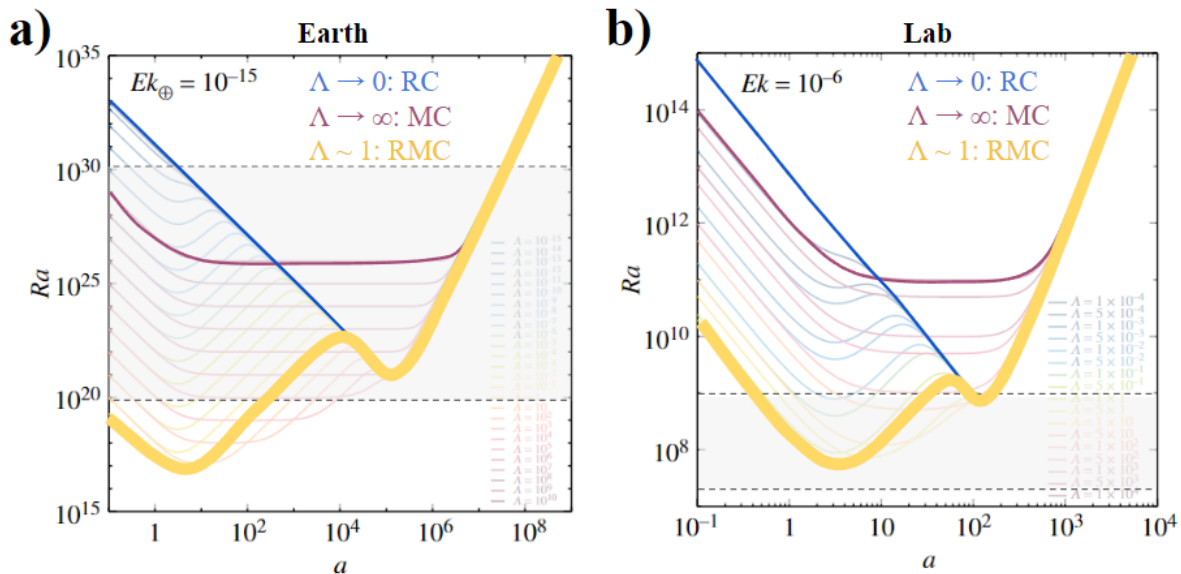


Figure 5.1: Linear stability curves of Ra as a function wave number $a \equiv \pi d/L$ in RC, MC, and RMC, at a) the Earth’s condition where $Ek = 10^{-15}$, in which d is the height of the infinite plane fluid layer, and L is the half-wavelength of the convection cell, assuming in the form of two-dimension rolls; b) a typical lab parameter where $Ek = 10^{-6}$. The shaded grey box indicates the range of Ra in each system. Figures modified from [Horn & Aurnou \(2022\)](#).

The rotating magnetoconvection system contains essential dynamic elements of turbulent convection, rotation, and magnetism that governs the dynamics of the electrically conducting fluid layers in planets (e.g., [King & Aurnou, 2015](#); [Aurnou & King, 2017](#)). A long-held view of dynamo theory is that the Lorentz forces relax the rotation constraint of the planet from the generated magnetic field and form a steady large-scale bulk mode (e.g. [Roberts & King, 2013](#)). This “magnetostrophic mode,” in which Coriolis and Lorentz forces are approximately in balance, is derived from the classical linear stability analysis ([Chandrasekhar, 1961](#); [Eltayeb & Roberts, 1970](#); [Eltayeb, 1972](#)).

Linear theory predicts a separation of scales in the leading steady modes. ([Horn & Aurnou, 2022](#)). Figure 5.1 shows stationary marginal stability curves of Ra as a function of

the nondimensional wave number $a \equiv \pi d/L$ at $Ek = 10^{-15}$ representing the Earth core, and $Ek = 10^{-6}$ representing current lab experiments and numerical simulations. Here d is the height of an infinite plane layer, and L is the half-wavelength of the convection cell. Both in the Earth and in the lab, the magnetostrophic balance has two minimums in its stability curve. The lowest one is the steady onset of the magnetostrophic mode, which has a small wave number and a large scale. The second minimum is the geostrophic onset.

Although the mono-modal magnetostrophic mode is appealing, it is not geophysically realistic (Calkins, 2018; Horn & Aurnou, 2022). As discussed in the first chapter, the large-scale bulk dynamics of the planetary core are likely to be governed by rotating convection (e.g., Gillet *et al.*, 2012). The dynamic Elsasser number (Soderlund *et al.*, 2015) at the Earth's core is likely $\Lambda_d \sim \Lambda Rm^{-1/2} \sim 10^{-2}$, which means the Lorentz forces is only a fraction of the Coriolis force on a planetary scale. However, fig. 5.1 a) shows that as the Coriolis force becomes more dominant, $\Lambda \rightarrow 0$, the geostrophic mode replaces the magnetostrophic one as the most accessible mode with the lowest critical Ra . However, it is not a large-scale mode as the wave number for the geostrophic mode is $a \gtrsim 10^5$. Therefore, the linear geostrophic mode cannot represent the large-scale magnetic structures observed in the geomagnetic data.

As discussed in section 1.3.5, the inverse cascade of kinetic energy from the small-scale into large-scale flows in three-dimensional turbulence has been studied extensively (e.g., Julien *et al.*, 2012; Favier *et al.*, 2014; Guervilly *et al.*, 2014; Rubio *et al.*, 2014; Stellmach *et al.*, 2014). The resulting turbulent barotropic large-scale vortices (LSVs) provide a promising pathway to explain the large-scale structures observed in geomagnetic data.

However, turbulent RC with core-like material properties is often too expensive for the current numerical models to resolve. The effect of changing from $Pr \sim 1$ which has been used in most of the numerical simulations, to $Pr \ll 1$ in the core, remains poorly understood. In lieu of the difficulties in numerical simulations, laboratory experiments in liquid metal have much more realistic material properties. In particular, $Pr \approx 0.025$ and $Pm \approx 10^{-6}$ in liquid gallium, in perfect agreement with the core flow, where $Pr \sim 10^{-2}$, and $Pm \sim 10^{-6}$. Our

system also has a relatively high $Re \gtrsim 10^4$, which is considered turbulent.

To look for the possible existence of LSVs in the liquid metal, I conduct a fixed- Ek four-case study of RC and RMC on ROMAG. Figure 5.2 shows these four cases with linear onset prediction of an infinite plane layer for different convective modes at $Ek = 8 \times 10^{-7}$. The RC cases, namely “RC 60W” and “RC 2kW”, are actually located at $\Lambda = 0$ which is not shown in the figure because there is no magnetic field. The RC 60W case has a raw input power of around 60W for the heat pad and $Ra = 1.521 \times 10^8$, about an order of magnitude supercritical of the oscillatory bulk onset, and at least three times of the wall mode onset. Therefore, we expect to see wall modes and oscillatory modes in this case. RC 2kW has an input power of 2kW, and a $Ra = 1.014^9$, large enough to potentially see geostrophic mode. However, it might be too supercritical and turbulent to see the onset modes of oscillatory and wall modes. The detailed parameters are listed in table 5.1.

Furthermore, I conduct two RMC experiments at $\Lambda \approx 1.90$ using the same output power of 60W and 2kW. Due to the difference in heat transfer efficiency between RC and RMC at these two heat fluxes, these two cases have slightly different Ra than the RC cases. Specifically, the RMC 60W case has $Ra = 9.703 \times 10^7$, while the RMC 2kW case has $Ra = 1.007 \times 10^9$.

Case Name	Ra	Nu	Pr	Ek	Ch	Λ	Ro_C
RC 60W	1.521E+8	2.75	0.027	8.617E-7	0	0	0.065
RC 2kW	1.014E+9	15.83	0.024	7.771E-7	0	0	0.160
RMC 60W	9.703E+7	4.33	0.027	8.679E-7	2.188E+6	1.899	0.052
RMC 2kW	1.007E+9	15.93	0.024	7.783E-7	2.494E+6	1.941	0.159

Table 5.1: Experimental data for liquid gallium RC and RMC cases in the 40-cm tank.

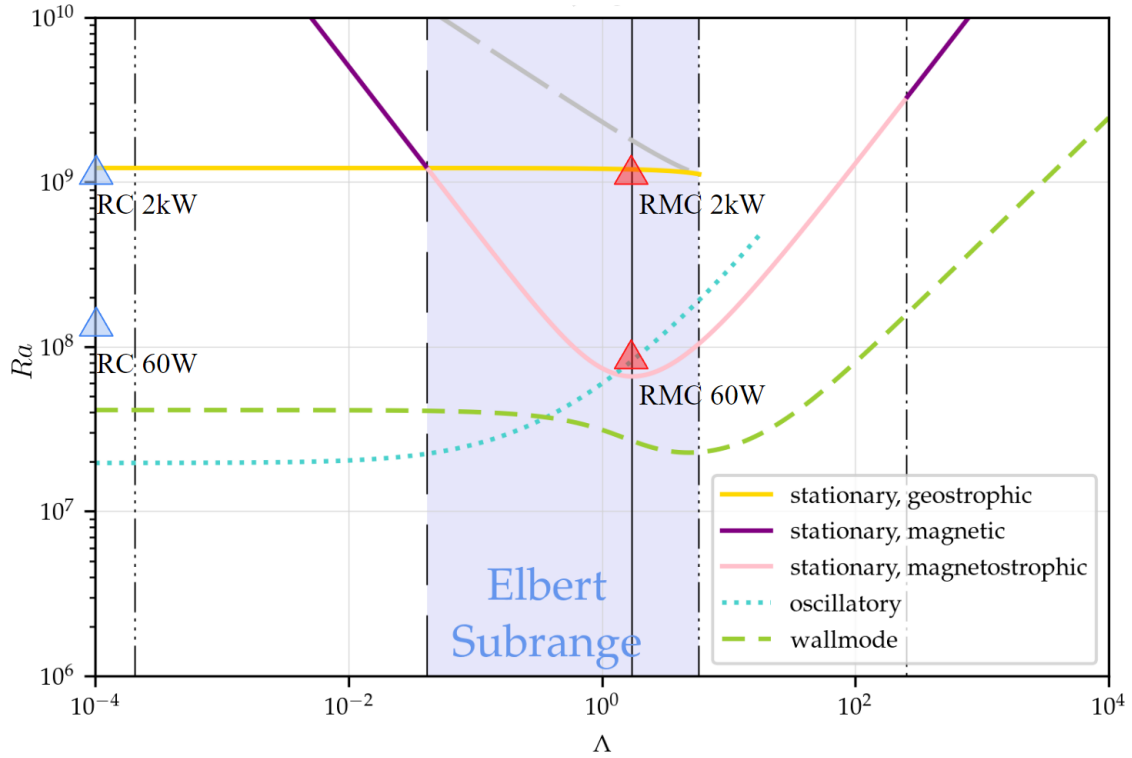


Figure 5.2: Experimental cases of RC and RMC and critical Ra curves for different onset modes at $Ek = 8 \times 10^{-7}$, modified from the Python notebook by (Horn & Aurnou, 2022). The horizontal axis is the linear Elsasser number, and the vertical axis is Ra . The different curves represent the marginal Ra required for onset modes of convection to occur. The shaded area marks the Elbert subrange where stationary geostrophic and magnetostrophic modes coexist.

5.2 Experimental methods

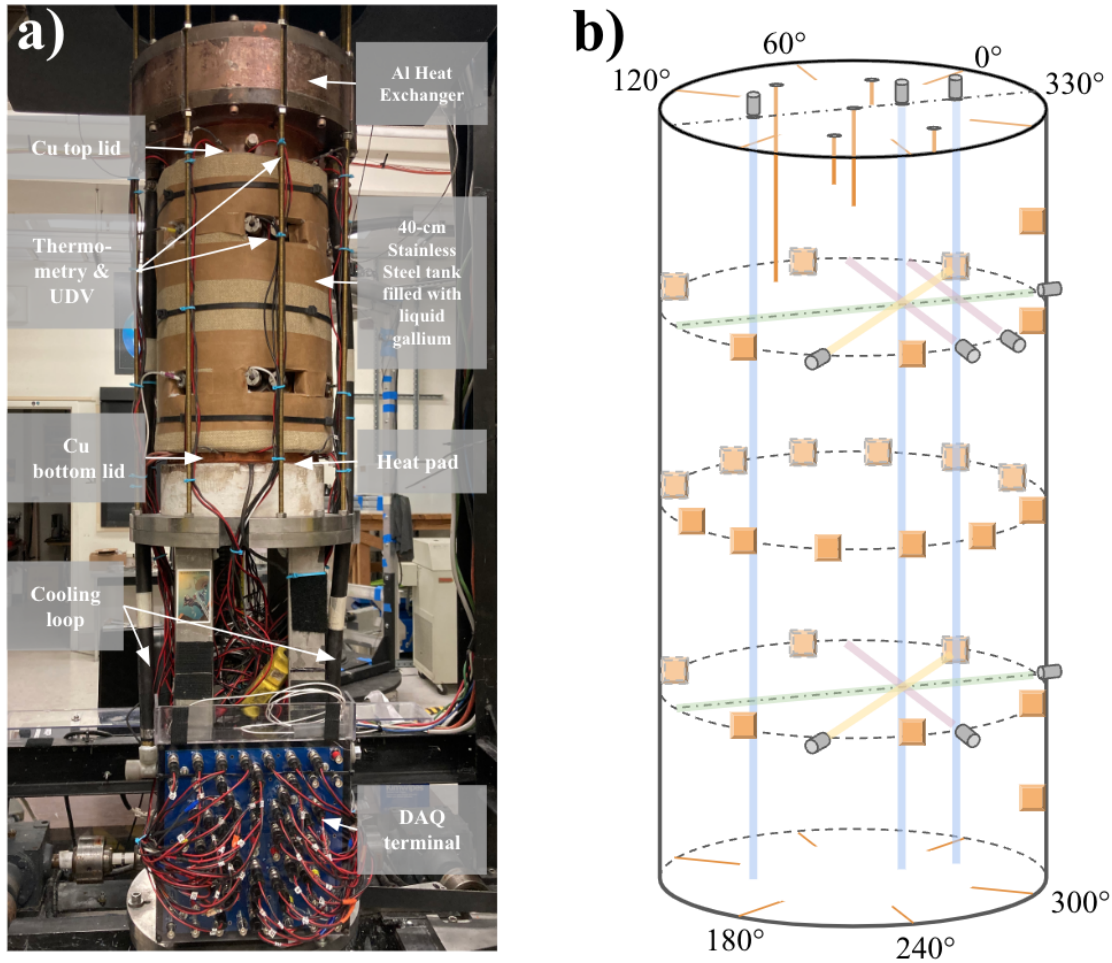


Figure 5.3: Experimental setup on ROMAG with 40-cm tank. a) A photo of the apparatus. b) DAQ transducers on the cylinder tank.

These four experiments were conducted in a 40-cm tank filled with liquid gallium on ROMAG. Figure 5.3 a) shows the apparatus with descriptions of its components visible in the photo. With the upgrade diagnostics and instrumentation shown in fig. 5.3 b), ROMAG has a total of 43 thermistors for measuring spatial-thermal information of the liquid gallium. Moreover, 10 Doppler probes – three on top, three at $1/4H$, and four at $3/4H$ – were also implemented.

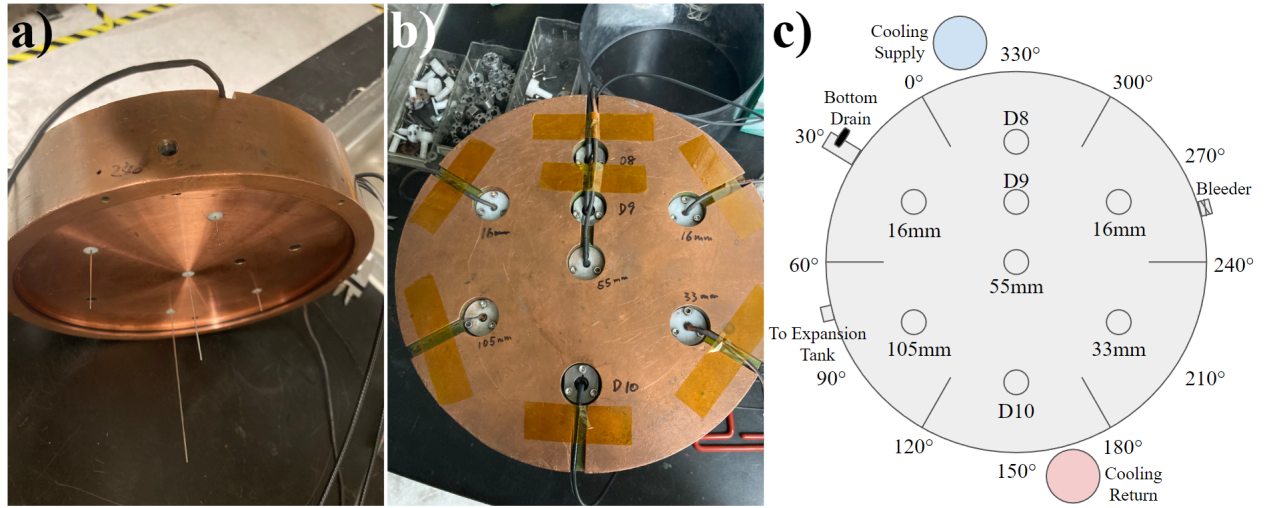


Figure 5.4: Top-lid internal thermometry. a) The various length of metal stems are internal thermistors. The dark spots flush against the top boundary are Doppler probes. b) Photo of the top-down view of the top lid. c) Schematics of the top lid sensors with azimuthal references.

Figure 5.4 a) shows five internal thermistors are also installed from the top lid to extend into the fluid bulk. The longest thermistor is 105 mm in length from the top. Three Doppler probes (D8, D9, and D10) are aligned on the 150° to 330° diameter. The detailed setup is shown in fig. 5.4 b) and c).

5.3 Large-scale vortices in liquid metal rotating convection turbulence?

5.3.1 The bulk mode onset

Here I briefly discuss the base flow of our system at the onset of convection. Convective instabilities in RC require thermal buoyancy to overcome the stabilizing influence of the Coriolis force. The rotating convection of liquid metal in a cylindrical geometry has asymptotic onset solutions for both wall modes and bulk modes (Zhang & Liao, 2009, 2017) with no-slip boundary. The wall mode and bulk modes have also been shown in many numerical

simulations (e.g., Horn & Schmid, 2017) and laboratory experiments (e.g., Ecke *et al.*, 1992; Aurnou *et al.*, 2018; Vogt *et al.*, 2021). The wall modes are upwelling/downwelling patches near the sidewall and travel retrograde with respect to the rotation. The bulk modes are oscillatory inertial structures in the fluid bulk due to overstability (Chandrasekhar, 1961).

Implementing the asymptotic results of Zhang & Liao (2009), we are able to find the asymptotic minimum Ra for both wall modes and bulk oscillatory modes of our experiment system: RC at $Ek = 8 \times 10^{-7}$, $Pr = 0.027$, and $\Gamma = 0.5$. Assuming a simplest vertical wavenumber $n = 1$, the wall modes onsets at $Ra = 3.228 \times 10^7$ with an azimuthal wavenumber $m = 1.43$; the bulk oscillatory mode onsets at $Ra = 4.248 \times 10^7$ with an azimuthal wavenumber $m = 1$, and a radial wavenumber $k = 4$. Figure 5.5 shows a horizontal plane of this RC onset oscillatory bulk mode at $Ek = 8 \times 10^{-7}$, $Pr = 0.027$, and $\Gamma = 0.5$. The rotation is set to be left-handed. The color is the dimensionless azimuthal velocity with respect to the system rotation. The onset radial scale of the bulk mode is thus $\ell_r = R/4 \approx 24.6$ mm.

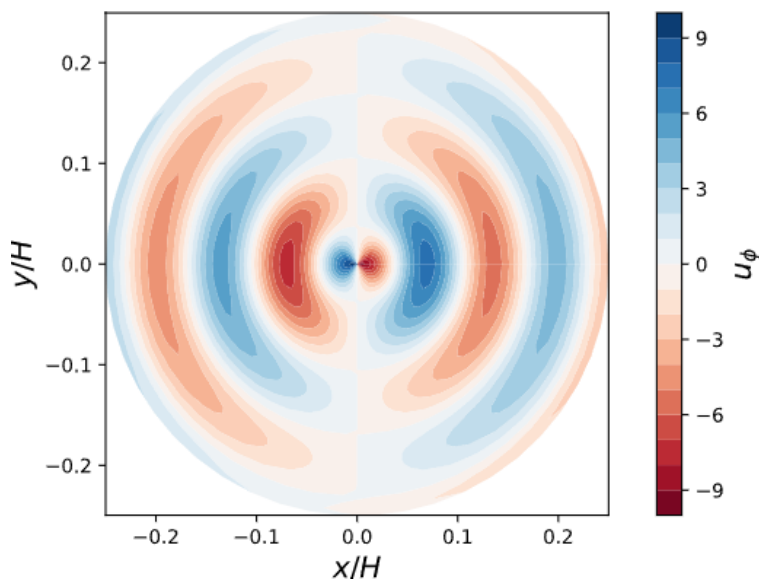


Figure 5.5: Azimuthal velocity on a horizontal plane of RC onset oscillatory bulk mode at $Ek = 8 \times 10^{-7}$, $Pr = 0.027$, and $\Gamma = 0.5$. The color represents dimensionless positive or negative azimuthal velocity with respect to rotation. Solution is based on Zhang & Liao (2017).

5.3.2 Experimental results

Our preliminary results show the first experimental evidence of liquid metal large-scale vortices (LSVs) using ROMAG’s upgraded Doppler velocimetry. Figure 5.6 are velocity Hovmöller diagrams of the RC 60W case ($Ro_C = 0.065$) at four locations (shown on the left) on the ROMAG’s convection tank. The detailed parameters are shown in table 5.1. The horizontal axes are time intervals of $0.1\tau_\kappa$. The vertical axes are distances normalized by the path length of the Ultrasonic beam. The red color in vertical probe D10 represents positive velocity flowing upwards, whereas in chord probe D6 and radial probes D7 and D3, the red means fluid moving away from the probe.

An important observation here is that the flow is nearly barotropic. Chord probes D7 and D3 are located at different heights of $3/4H$ and $1/4H$, yet their velocity measurements are almost identical to each other, indicating a large-scale structure consistent in \hat{z} , $\partial_z \mathbf{u} \approx 0$. The structure approximately follows the Taylor-Proudman theorem that the fluid motion is invariant along the direction of rotation.

Another interesting observation is that the time scales of upwelling and downwelling plumes in D10 are much smaller than the other velocity maps. Further analysis is required to decipher the spatial-temporal structure in the vertical direction.

Further analysis of velocity profiles in D6 and D7 using a synthetic vorticity model leads to a hint in the spatial-temporal structure of the flow. Figure 5.7 shows a Doppler velocity Hovmöller diagram of chord probe D6 in RC 60W case, in comparison to a synthetic Hovmöller diagram of the one-dimensional velocity at the exact location as the D6. This synthetic velocity field comprises a $m = 2$, $k = 1$ structure with four neighboring opposing vortices circumscribed by a circle with an imposed net rotation. The tilted and alternating velocity patches along the chord are similar to the ones shown in the synthetic Hovmöller.

Moreover, Figure 5.8 shows a Doppler velocity Hovmöller diagram of the radial probe D7 in RC 60W case, in comparison to a synthetic Hovmöller diagram of the velocity profile

at the exact location as the D7. The alternating triangular patterns in the real data set are captured by the alternating patterns of synthetic data vortices as they pass through the radial beam. The dark spots in the synthetic Hovmöller are attributed to artificial errors from the singularity of the synthetic vortex model.

I propose that only $m = 2$ vortices with a background zonal flow can explain the velocity data in chord and radial measurements, as shown in fig. 5.7 and fig. 5.8. The tilted stripes in fig. 5.7 b) have the same velocity spanning the entire chord. This can only be explained by a large-scale flow that spans at least half a radius. Any $m > 2$ vortices patterns will result in more tilted stripes, and more than two color stripes will be seen in fig. 5.7 b) at a fixed time. Moreover, the alternating triangular shape in radial velocity indicates two alternating structures along the diameter, and the wavenumber m has to be even. Moreover, compared with fig. 5.5, this $m = 2$, $k = 1$ structure cannot be explained by the onset bulk oscillatory modes. Future analysis of the fastest-growing bulk mode might be helpful to compare against the LSVs.

In conclusion, retrograde rotating $m = 2$ vortices can explain the spatial-temporal data from the Doppler measurements. Further analysis of the net zonal velocity of the data captured in chord probes can help compare the temporal frequency of the periodic appearance of these patterns. I am currently conducting a detailed analysis of the RC 60W case and, therefore, only presenting some of the preliminary results here. These findings of the RC 60W, along with my coauthors, will be included in a forthcoming paper. Additionally, I plan to further analyze the RC 2kW and RMC cases in the following papers.

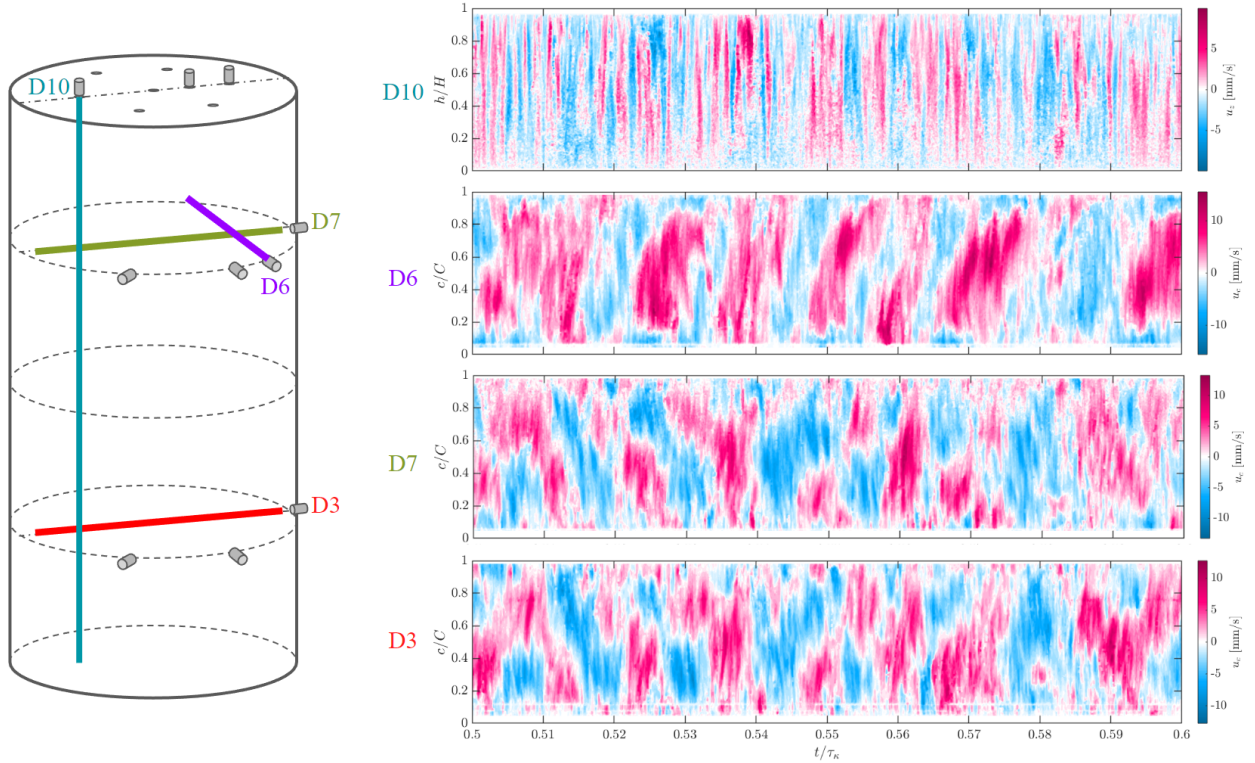


Figure 5.6: Hovmöller diagrams of UDVs for the RC 60W case. Four Doppler probes are set up as the schematics on the left. Probe D7 and D3 are the radial probes, D10 is the vertical probe, and D6 is the chord probe. The diagrams show the velocity in color along the beam direction. The vertical axes are the distance normalized by the path length. The horizontal axes are time normalized by thermal diffusion time τ_K . All the diagrams show $t = 0.1\tau_K$ intervals. For vertical probes, red represents positive velocity in the up direction. For chord and radial probes, red represents velocity moving away.

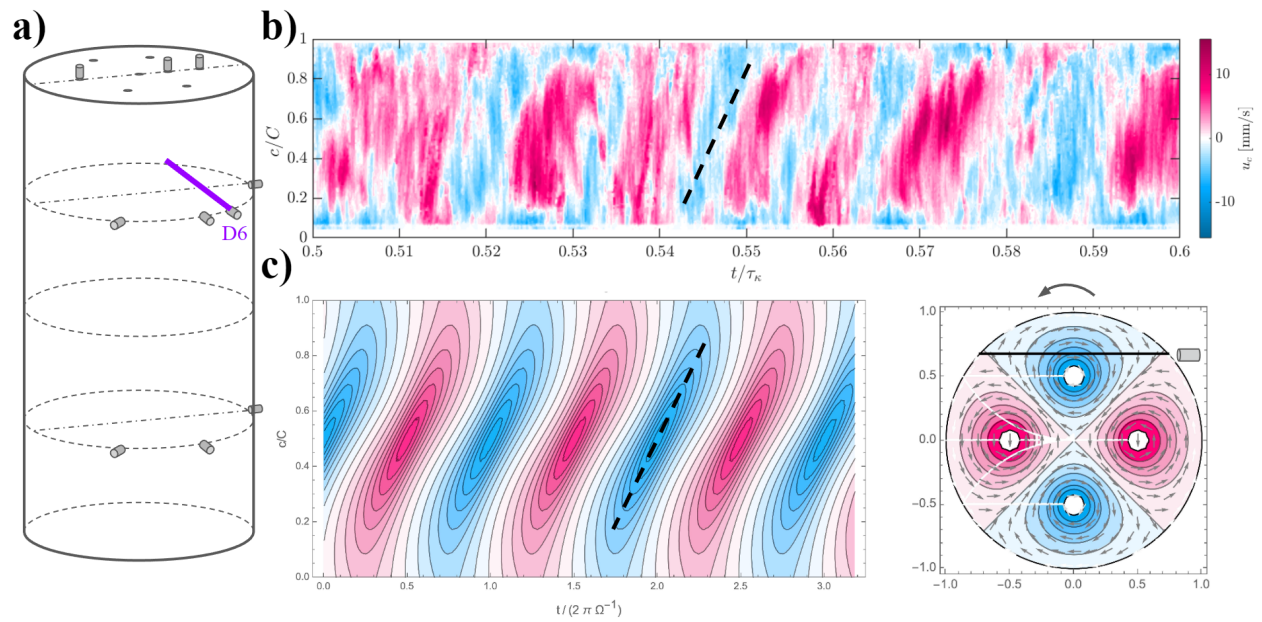


Figure 5.7: a) Location of the chord probe D6. b) Doppler velocity Hovmöller diagram of D6 in RC 60W case. c) Hovmöller diagram of the synthetic Doppler D6's data and a horizontal velocity contour of the $m = 2$ synthetic vortices. An arbitrary constant background retrograde rotation has been applied to the vortices. The color represents the velocity. The synthetic data figure was made in collaboration with Cy David.

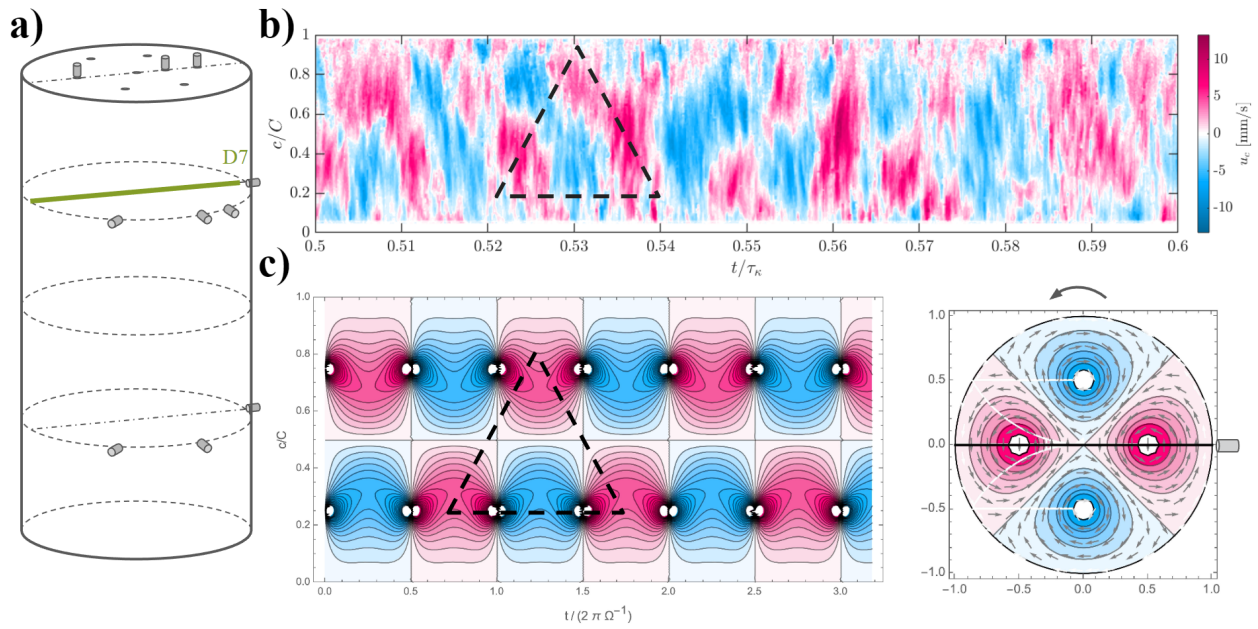


Figure 5.8: a) Location of the radial probe D7. b) Doppler velocity Hovmöller diagram of D7 in RC 60W case. c) Hovmöller diagrams of the synthetic Doppler D7's data. The contour map on the right shows the same $m = 2$ LSV with an arbitrary background retrograde rotation as fig. 5.7. The color represents the velocity. The synthetic data figure was made in collaboration with Cy David.

5.4 Comparison with other cases

5.4.1 RC 2kW

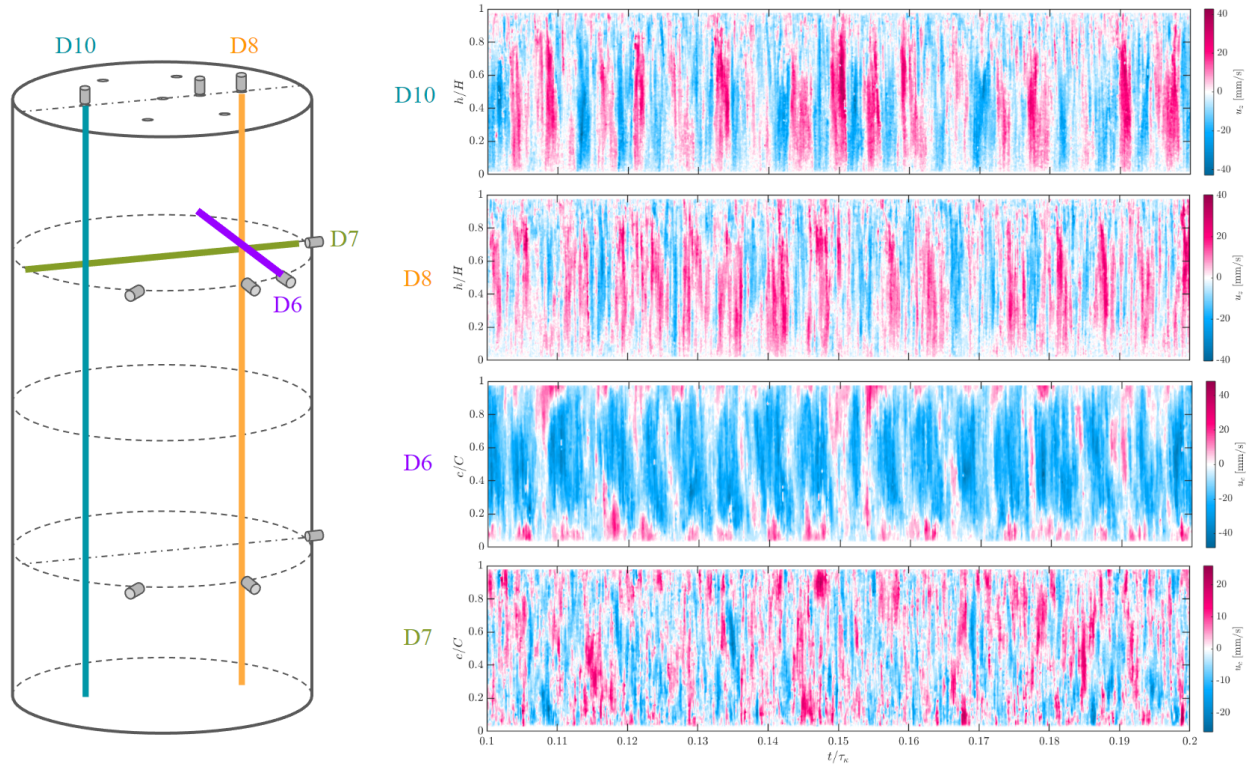


Figure 5.9: Hovmöller diagrams of UDVs for the RC 2kW case. Four Doppler probes are set up as the schematics on the left. Probe D7 is the radial probes, D10 and D8 are the vertical probe, and D6 is the chord probe. The diagrams show the velocity in color along the beam direction. The vertical axes are the distance normalized by the path length. The horizontal axes are time normalized by thermal diffusion time τ_κ . All the diagrams show $t = 0.1\tau_\kappa$ intervals. For vertical probes, red represents positive velocity in the up direction. For chord and radial probes, red represents velocity moving away.

Figure 5.9 shows the velocity Hovmöller diagrams for four velocity transducers: chord D6, radial D7, vertical D8 and D10 for the RC 2kW case. Detailed parameters are displayed in table 5.1. In sharp contrast to RC 60 W case, the structures in D6 and radial D7 are completely different. Strong negative flows in D6 indicate the zonal jet still exists, happening

at a much faster speed. No coherent structures can be observed in D7. This is likely because the strong thermal forcing relaxes the Taylor-Proudman constraint.

The convective Rossby number, Ro_c , is defined in eq. (3.20).

$$Ro_c = \frac{\text{Inertia}}{\text{Coriolis}} = Re_{ff} Ek = \sqrt{\frac{RaEk^2}{Pr}}, \quad (5.1)$$

where $Re_{ff} = U_{ff}H/\nu$. The convective Rossby number for this case $Ro_c \approx 0.160$ is more than twice the RC 60W case. This convective Ro_c cannot be considered rapidly rotating, thus not representative of the core dynamics where $Ro_c \sim 10^{-6}$. The buoyancy inertia of the flow is no longer insignificant compared with the Coriolis forces. The disappearance of LSVs at $Ro_c \approx 0.160$ qualitatively agrees with Cai (2021) that smaller aspect ratio geometry requires a smaller Rossby number threshold for LSVs to form, comparing with $Ro \leq 0.4$ in $\Gamma = 1$ (Cai, 2021).

The strong upwelling and downwelling flow reaches a maximum speed of around 40 mm/s. The periodic alternating patterns of upwelling and downwelling in D10 versus D8 are absent in the RC 60W case. Further correlation analysis between D8 and D10 could give insights into the lateral structure of the convective flow in the same vertical plane as D8 and D10.

5.4.2 RMC cases

Figure 5.10 shows the velocity Hovmöller diagrams of vertical D8 and D10 velocity measurement for the RMC 60W and 2kW cases at $\Lambda \approx 1.9$. Detailed parameters are displayed in table 5.1. In contrast to the RC 60W case, the RMC 60W exhibits an organized, anti-phased, and periodic upwelling/downwelling pattern in the vertical direction. This implies that there might be a coherent large-scale circulation (LSC) in the vertical plane in the RMC 60W case. Furthermore, there is also a net zonal velocity from the chord velocity measurement. I postulate that a tank-scale magnetostrophic mode has been developed in the RMC 60W case, at $Ra/Ra_{MS} \approx 1.2$, where Ra_{MS} is the magnetostrophic mode onset in a plane layer, as shown as the green dashed curve in fig. 5.2. The magnetostrophic balance relaxes

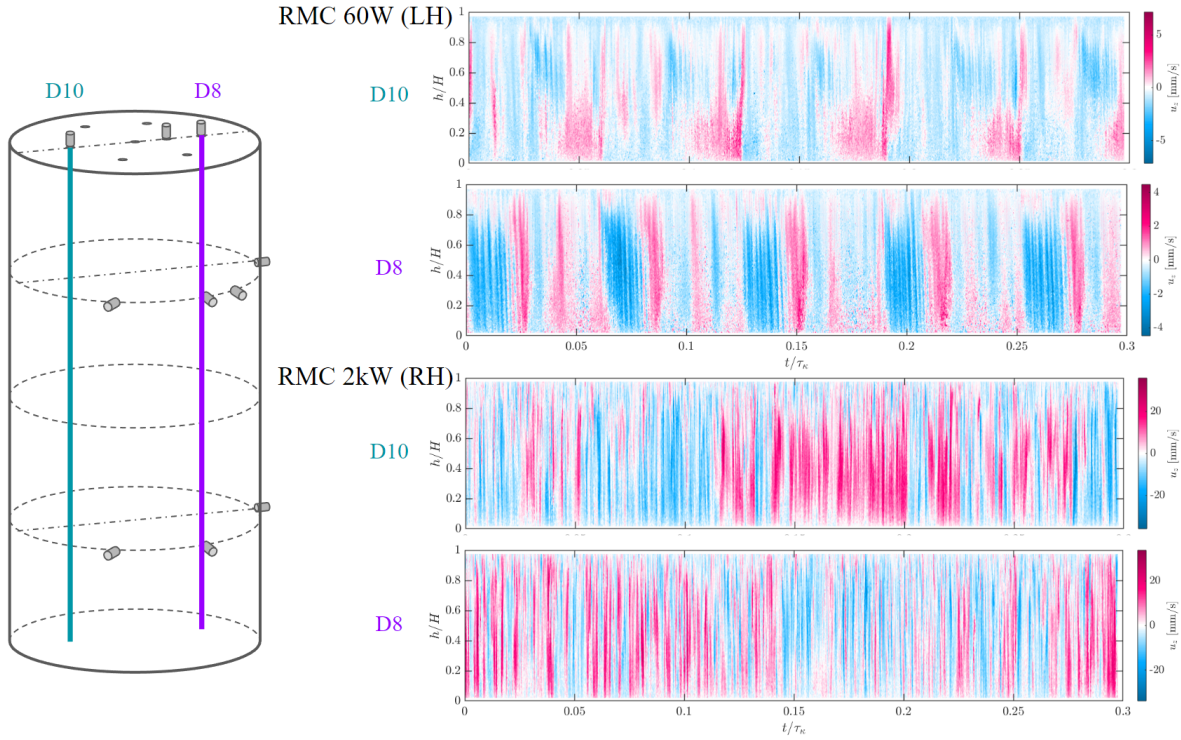


Figure 5.10: Hovmöller diagrams of UDVs for the RMC 60W and 2kW cases. Two vertically oriented Doppler probes D8 and D10 are set up as the schematics on the left. These two probes have the same radial distance to the center of the top lid, and therefore, they measure vertical velocity in opposite halves of the radius. The four diagrams on the right show the velocity in color along the beam direction as a function of space and time. The vertical axes are the distance normalized by the path length. The horizontal axes are time normalized by thermal diffusion time τ_κ . All the diagrams show $t = 0.3\tau_\kappa$ intervals. Red represents positive velocity in the up direction.

the Taylor-Proudman constraint, allowing this large-scale structure to appear (e.g., Cardin & Olson, 1995; Roberts & King, 2013; Soderlund *et al.*, 2015).

Furthermore, this large-scale processing LSC mode seems to contribute to more efficient heat transfer. RMC 60W has a $Nu = 4.33$, in contrast to RC 60W's $Nu = 2.75$. For future work, we need to calculate the phase anticorrelation to quantify the connection between the upwelling and downwelling flows.

Figure 5.10 also shows D8 and D10 measurements in the RMC 2kW case. Although there

is a certain level of anti-correlation in the upwelling and downwelling motions, similar to the RMC 60W case. However, the structure is more complex and less regular. More details of the observations on RMC 2kW will be studied in the future.

5.5 Discussion and future works

5.5.1 Wave propagations in RMC

The dispersion relation of the Magneto-Coriolis (M-C) wave, as shown in eq. (4.63), is (Finlay, 2008)

$$\omega_{M-C} = \pm \frac{(\boldsymbol{\Omega} \cdot \mathbf{k}_0)}{k_0} \pm \left(\frac{(\boldsymbol{\Omega} \cdot \mathbf{k}_0)^2}{k_0^2} + \frac{(\mathbf{B} \cdot \mathbf{k}_0)^2}{\rho\mu} \right)^{1/2}, \quad (5.2)$$

where \mathbf{k}_0 is the wavenumber, $\boldsymbol{\Omega}$ is the angular rotation vector, and \mathbf{B} is the magnetic flux density. A fast branch and a slow branch solutions emerge depending on the signs of the two terms. I then convert these two frequencies and wavenumbers into a phase diagram using 2D FFT, also called a “frequency-wavenumber spectrum”. Note that the M-C wave is dispersive, which means the frequency changes with the wavenumber so that the phase speed is not constant. This method is commonly used in seismology and other areas to investigate wave properties.

Figure 5.11 shows two frequency-wavenumber (f-k) spectra of the 2D vertical velocity data (time+1D space) from two vertical probes D10 and D8 at the top lid. Figure 5.11 a) gives the location of two vertical transducers. They have the same distance to the center of the lid. Panel b) and c) shows the f-k diagrams for D8 and D10 data, respectively. A clear wave can be seen in D8, which approximately follows the M-C wave prediction in eq. (5.2). For D10, however, it is unclear whether the prediction works for our data except for some faint tails. The power of the spectra has been amplified by taking the logarithm. Further investigation is needed to conclude the wave properties of the magnetostrophic mode.

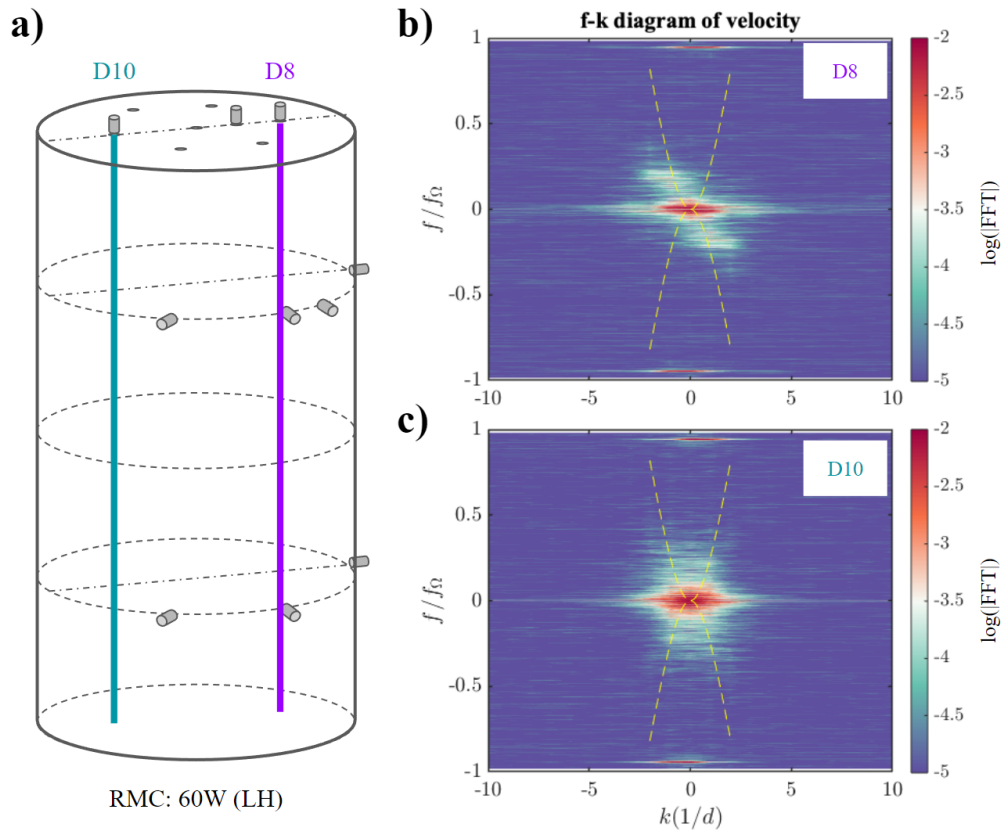


Figure 5.11: Frequency-wavenumber (f - k) spectra of the vertical velocity data from the RMC 60W case. a) The schematics of the vertical UDVs. b) Frequency-wavenumber spectrum from probe “D8”. c) Frequency-wavenumber spectrum from probe “D10”. The wavenumber in the horizontal axis is normalized by the inverse of the path length, so it is the total wavenumber of structures along the beam. The vertical axis is frequency normalized by the rotational frequency f_Ω . The color represents the logarithm of the FFT power. The yellow dashed line shows the theoretical predicted frequency-wavenumber curves of the slow Magnetic-Coriolis wave (Finlay, 2008).

5.5.2 Characterizing the turbulence

A substantial amount of novel observations have emerged from our experimental results. However, exploring the rotating magnetoconvection turbulence in liquid metal has barely begun. Since the core-style convection is mostly likely turbulent ($Re \sim 10^8$), an important goal in our experiments is to determine the characteristics of the turbulent flow. Several methods can be implemented to acquire information on the state of turbulence. But first, wavelength information is required from the experiments.

The flow's spatial structure and characteristic length scale can be evaluated using the spatial-temporal auto-correlation method (Proakis, 2007) on the velocity data acquired by the UDV. Spatial-temporal auto-correlation has been proven successful in numerical simulation and particle image velocimetry (PIV) (Nieves *et al.*, 2014; Rajaei *et al.*, 2017; Madonia *et al.*, 2021). For instance, the 1-D spatial auto-correlation between a scalar variable f at position x and f at $(x + r)$ gives, modified from Madonia *et al.* (2021):

$$R_f(r) = \frac{\langle f(x)f(x+r) \rangle}{\langle f^2(x) \rangle}, \quad (5.3)$$

where x is the 1-D position vector of the measurements along the ultrasound beam, r is the separation connecting any two points along the measurements. The brackets denote spatial averaging of all the variables. The spatial autocorrelation $R_f(r)$ can be calculated by the Fourier convolution theorem (Nieves *et al.*, 2014). And R_f satisfies $R_f(0) = 1$. The same technique can be implemented in time to find the temporal auto-correlation (Nieves *et al.*, 2014). The integral length scale can then be used to determine the wavelength of the variable f in both space and time, respectively:

$$L_f = \int_0^\infty R_f(r) dr, \quad (5.4)$$

$$T_f = \int_0^\infty R_f(\tau) d\tau, \quad (5.5)$$

where τ is the separation in time.

Applying spatial auto-correlation in liquid metal UDV data will provide access to energy spectral analysis. Specifically, we could compare the power exponent of the kinetic energy-wavenumber spectrum against the classical turbulent energy cascade scaling, $Ek \sim k^{-5/3}$ (Kolmogorov *et al.*, 1942), and proposed MHD turbulence scaling, $Ek \sim k^{-3/2}$ (Perez *et al.*, 2012).

The probability density function (PDF) of the spatial-temporal data can also be used to determine the status of the turbulence (e.g. Castaing *et al.*, 1990; Frisch, 1995). The PDF of our velocity and temperature data can be compared against the characteristic non-Gaussian shapes with exponential tails of the turbulence disturbance.

5.5.3 The wall modes

The existence of wall modes in the interior of a planet is unlikely. However, retrograde wall modes with respect to the rotation of the apparatus appeared to have a dominant presence in both thermal and velocity signals of the RC and RMC experiments. Figure 5.12 shows a side-by-side comparison between RC 60W and RMC 60W cases Hovmöller diagrams, which describe the sidewall midplane temperature evolution in time. Both figures have the same time intervals of $0.3 \tau_\kappa$. The RMC case has a much slower wall mode signal at a frequency $f/f_\kappa \approx 16.81$, while the RC case has a much faster frequency, $f/f_\kappa \approx 47.40$. Moreover, another important observation is both cases have a dominant $m = 1$ wall mode. At any time, there is only one hot and one cold patch along the azimuth, and each occupies about 180° .

Madonia *et al.* (2021) has pointed out in their water experiments there is a dominant $m = 2$ wall mode which is drifting in the azimuthal retrograde direction. The wall mode may have induced an $m = 2$ quadrupolar vortices in their system. In contrast, our wall mode is retrograde $m = 1$, inconsistent with the wavenumber of the $m = 2$ LSVs found in the liquid metal RC 60W case. Thus, the LSVs found in our study are fundamentally different from Madonia *et al.* (2021) that they are not likely to be driven by the wall modes. Regardless,

the wall mode's dynamic interaction with the bulk mode remains unclear, which should be addressed in the future and investigate whether large-scale structures can arise from the wall modes in liquid metal.

Following Terrien *et al.* (2023), the wall modes can probably be removed by adding a rim of fins at the inner cylinder wall. Thus, future upgrades on ROMAG's convection tanks would help better compare the lab experiments with the plane layer studies (e.g., Rubio *et al.*, 2014; Stellmach *et al.*, 2014; Julien *et al.*, 2016; Yan & Calkins, 2022; Horn & Aurnou, 2022), and with the planetary core flows where the existence of any wall mode is highly questionable.

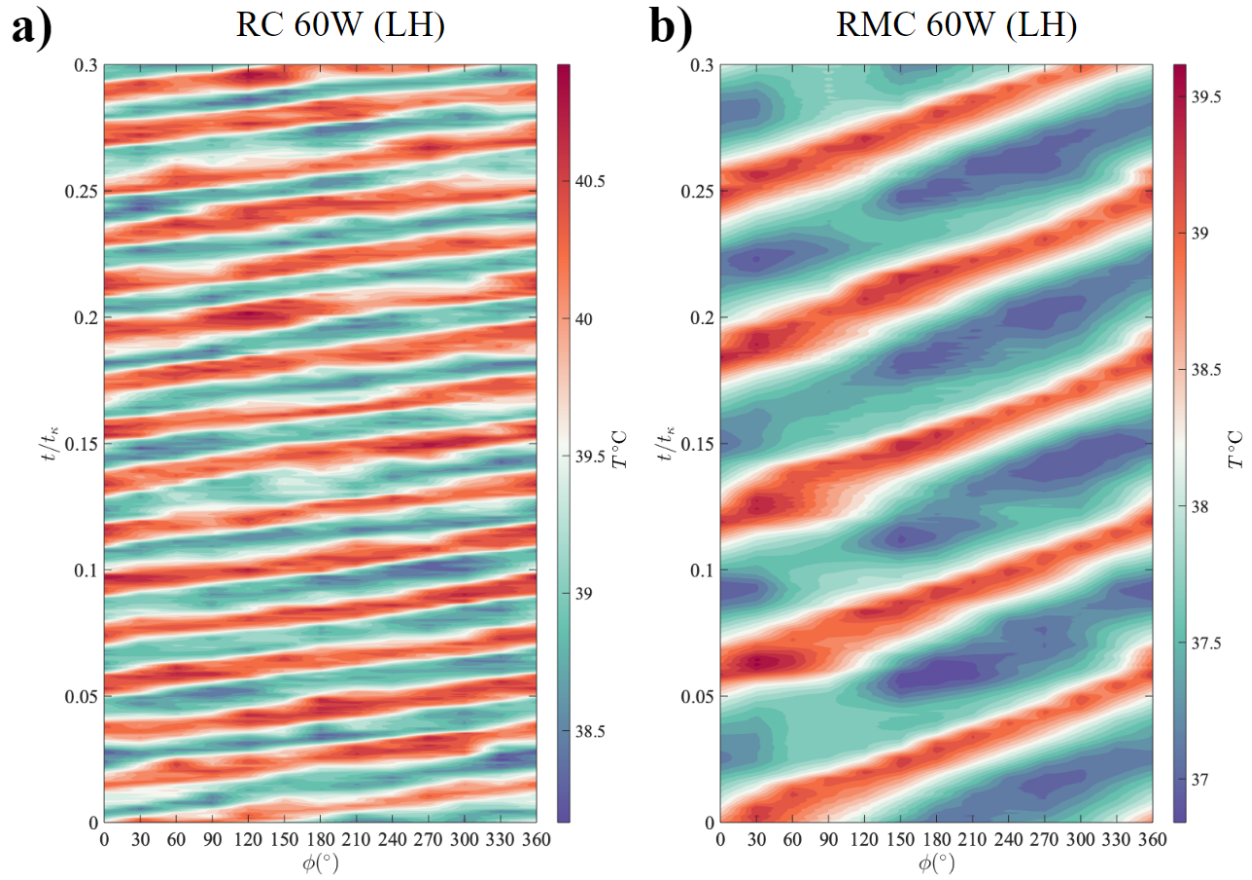


Figure 5.12: Sidewall midplane thermometry Hovmöller diagram shows an $m = 1$ azimuthal retrograde wall mode in both a) RC and b) RMC 60W cases. The color represents the raw temperature. The horizontal axis is the azimuthal angle, increasing in the right-handed direction. The vertical axis is the time normalized by τ_κ . The time interval shown here is $t = 0.3\tau_\kappa$ for both cases.

5.5.4 Transport efficiency and scaling law

Another perspective of understanding the dynamo processes is through transport properties and energy (e.g. Nimmo, 2009; Roberts & King, 2013; Landeau *et al.*, 2022). In addition to comparing the heat transfer efficiency in Nu , I am also interested in comparing the momentum transfer efficiencies (Re) and the kinetic energies between the RMC and RC cases. And investigate whether there is flow anisotropy that could contribute to the differences in transport efficiencies.

Scaling laws can help to extrapolate laboratory nondimensional parameters to a planetary scale. These power tools have been used in almost every dynamo study. In the future, with the upgraded diagnostics, the ROMAG system is now set up to conduct an extensive survey for scaling behaviors in liquid metal RMC, potentially updating our current dynamo scalings laws used in the literature. For instance, most planetary dynamo models rely on the energy flux – magnetic field strength scaling law (Christensen & Aubert, 2006) to estimate a theoretical criterion for a dynamo to exist. However, the assumptions in length scales and energy in this scaling law have yet to be tested experimentally.

Future experiments on ROMAG will hopefully verify and expand many aspects of our current views on planetary dynamos.

CHAPTER 6

Conclusion

6.1 Thesis work

I have attempted in this thesis to provide insights into the fundamental questions listed in section 1.4, focusing on investigating the near-boundary and interior core flow dynamics using laboratory magnetoconvection and rotating magnetoconvection experiments in liquid gallium.

Thermal measurements of liquid gallium magnetoconvection (MC) experiments on ROMAG have been used to characterize the behavior of liquid metal magnetoconvection from the onset of wall modes to multimodality. I highlighted the need for improved predictions of the onset of magnetoconvection in liquid metals within cylindrical cells. Combining numerical simulation results, I have characterized the MC's flow morphology near magneto-wall mode onset, which exhibits nose-like protuberances extending into the fluid bulk as the supercriticality increases. I have shown that the change in wall mode wavenumber results in fluctuation of the total heat transfer in the system.

The overall heat transfer behaviors in magnetoconvection and rotating convection systems are similar but differ at Rossby number less than unity (when the system is weakly influenced by rotation or magnetic field). Further investigation is needed to explain the discrepancy in full. ***This work paved the way to understanding higher complexity systems such as thermoelectric magnetoconvection and rotating magnetoconvection.***

To understand the flow induced by planetary boundary heterogeneity, I have conducted

laboratory experiments of liquid metal turbulent convection and advanced a novel theory to examine the thermoelectric effects on MC systems that may shed light on the planetary boundary interface dynamics. I have characterized a self-sustaining thermoelectric effect in different liquid metal turbulent convection flows. The thermoelectric currents at the electrically conducting boundaries generate a large-scale precession of the bulk fluid. To explain this phenomenon, I developed a solid-liquid analytical model that accurately predicted precession frequencies similar to the lab data. This model also produces a set of new dimensionless parameters capable of describing under what conditions the thermoelectric effect could become prominent near the interior layer boundaries of the planetary bodies.

My work shows that thermoelectric effects could be prominent at planetary layer boundaries such as the ULVZ regions of the CMB on Earth, and are ideal symmetry-breaking mechanisms in dynamo processes. A detailed thermoelectric model, however, has yet to be developed. The thermoelectric properties of planetary interior materials and the effects of rotation and stratification remain largely unknown. Nevertheless, the preliminary results of my collaborated research indicate that the thermoelectric properties at CMB heterogeneity could support the presence of the thermoelectric effect near the planetary interior boundaries.

Moreover, I have conducted experiments using the ROMAG device to investigate rotating convection (RC) and rotating magnetoconvection (RMC) in liquid gallium. Using thermal-velocimetry data, I have analyzed the spatial-temporal structures of both RC and RMC systems. My preliminary findings indicate that our $Ro \sim 0.065$ liquid metal RC experiments exhibit prominent self-excited large-scale barotropic vortices. This hints, for the first time, the rapidly rotating liquid metal RC could generate large-scale vortices (LSV) through the inverse cascade of kinetic energy. This experiment connects the existing numerical studies with liquid metal flows in the planetary cores. ***This implies that since turbulent RC represents the Earth's core's large-scale dynamics, the large-scale magnetic lobes from the observation could come from hydrodynamically formed large-***

scale vortices through the inverse cascade. These initial results highlight a potential pathway from local-scale turbulence to large-scale dynamics within planetary cores. Further analyses are required to confirm this hypothesis.

6.2 Collaborations

Here I list my contribution to other collaborative works during my Ph.D. I am a co-author on [Grannan *et al.* \(2022\)](#). I interpreted the thermoelectric precession mode that appeared in the MC cases of this study using the results derived from [Xu *et al.* \(2022\)](#).

As an extension of the thermoelectric magnetoconvection project, I am currently collaborating on a project led by Ph.D. student Francis Dragulet on exploring the thermoelectricity effect at the CMB and other planetary interfaces with ab-initio simulated material properties at realistic high-temperature high-pressure planetary interior conditions. I plan to estimate the temperature distribution of the CMB using the state-of-art seismic tomographic model ([French & Romanowicz, 2015](#)) with velocity-temperature conversion (e.g. [Stixrude & Lithgow-Bertelloni, 2007](#)). The thermal gradients on the map can then be converted into thermoelectric torques. The correlation between the torques and acceleration of the observed magnetic flux patches can be used to verify my hypothesis.

I am also collaborating on an MHD project led by Ph.D. student Cy David. In this study, we study Magneto-Stokes flow in a shallow free-surface annulus. Applying a radial current to an electrically conducting fluid surrounded by a circular metal annulus and a vertical magnetic field on ROMAG, the flow rotates due to the Lorentz force. I helped design and conduct the experiments. This work will be submitted to *JFM*.

Lastly, I am collaborating on a liquid gallium RC study led by Ph.D. student Jewel Abbate. We conducted RC experiments on ROMAG to characterize diffusivity-free heat and momentum transfer behavior. This work is currently in preparation and is planned to be submitted to *Nature Astronomy*.



Figure 6.1: On Oct 28th, 2017, a dinosaur with a Ukulele left the Halloween party early and broke into the lab. Rumor has it that the dinosaur insisted on helping clean up the ROMAG device.

Bibliography

- ABDOU, M. A., YING, A., MORLEY, N., GULEC, K., SMOLENTSEV, S., KOTSCHENREUTHER, M., MALANG, S., ZINKLE, S., ROGNLIEN, T., FOGARTY, P. & NELSON, B. 2001 On the exploration of innovative concepts for fusion chamber technology. *Fusion Eng. Des.* **54** (2), 181–247.
- AHLERS, G., GROSSMANN, S. & LOHSE, D. 2009 Heat transfer and large scale dynamics in turbulent Rayleigh-Bénard convection. *Rev. Mod. Phys.* **81** (2), 503.
- AKHMEDAGAEV, R., ZIKANOV, O., KRASNOV, D. & SCHUMACHER, J. 2020 Turbulent Rayleigh-Bénard convection in a strong vertical magnetic field. *J. Fluid Mech* **895**.
- AUBERT, J. 2019 Approaching earth’s core conditions in high-resolution geodynamo simulations. *Geophysical Journal International* **219** (Supplement_1), S137–S151.
- AUBERT, J., FINLAY, C. C. & FOURNIER, A. 2013 Bottom-up control of geomagnetic secular variation by the earth’s inner core. *Nature* **502** (7470), 219–223.
- AUJOGUE, K., POTHÉRAT, A., BATES, I., DEBRAY, F. & SREENIVASAN, B. 2016 Little earth experiment: An instrument to model planetary cores. *Review of Scientific Instruments* **87** (8), 084502.
- AUJOGUE, K., POTHÉRAT, A., SREENIVASAN, B. & DEBRAY, F. 2018 Experimental study of the convection in a rotating tangent cylinder. *J. Fluid Mech* **843**, 355–381.
- AURNOU, J. M., BERTIN, V., GRANNAN, A. M., HORN, S. & VOGT, T. 2018 Rotating thermal convection in liquid gallium: Multi-modal flow, absent steady columns. *J. Fluid Mech.* **846**, 846–876.
- AURNOU, J. M., CALKINS, M. A., CHENG, J. S., JULIEN, K., KING, E. M., NIEVES, D., SODERLUND, K. M. & STELLMACH, S. 2015a Rotating convective turbulence in earth and planetary cores. *Phys. Earth Planet. Inter.* **246**, 52–71.

- AURNOU, J. M., CALKINS, M. A., CHENG, J. S., JULIEN, K., KING, E. M., NIEVES, D., SODERLUND, K. M. & STELLMACH, S. 2015*b* Rotating convective turbulence in earth and planetary cores. *Phys. Earth Planet. Inter.* **246**, 52–71.
- AURNOU, J. M., HORN, S. & JULIEN, K. 2020 Connections between nonrotating, slowly rotating, and rapidly rotating turbulent convection transport scalings. *Phys. Rev. Research* **2** (4), 043115.
- AURNOU, J. M. & KING, E. M. 2017 The cross-over to magnetostrophic convection in planetary dynamo systems. *Proc. Math. Phys. Eng. Sci.* **473** (2199), 20160731.
- AURNOU, J. M. & OLSON, P. L. 2001 Experiments on Rayleigh-Bénard convection, magnetoconvection and rotating magnetoconvection in liquid gallium. *J. Fluid Mech.* **430**, 283–307.
- BARLEON, L., CASAL, V. & LENHART, L. 1991 MHD flow in liquid-metal-cooled blankets. *Fusion Eng. Des.* **14** (3-4), 401–412.
- BERHANU, M., VERHILLE, G., BOISSON, J., GALLET, B., GISSINGER, C., FAUVE, S., MORDANT, N., PÉTRÉLIS, F., BOURGOIN, M., ODIER, P. *et al.* 2010 Dynamo regimes and transitions in the vks experiment. *The European Physical Journal B* **77**, 459–468.
- BLOXHAM, J. & GUBBINS, D. 1987 Thermal core–mantle interactions. *Nature* **325** (6104), 511–513.
- BLOXHAM, J., GUBBINS, D. & JACKSON, A. 1989 Geomagnetic secular variation. *Philosophical Transactions of the Royal Society of London. Series A, Mathematical and Physical Sciences* **329** (1606), 415–502.
- BOETTINGER, W. J., CORIELL, S. R., GREER, A. L., KARMA, A., KURZ, W., RAPPAZ, M. & TRIVEDI, R. 2000 Solidification microstructures: recent developments, future directions. *Acta Mater.* **48** (1), 43–70.

- BOUSSINESQ, J. 1903 *Theorie Analytique de la Chaleur vol 2*. (Paris: Gauthier-Villars).
- BRANDENBURG, A. & SUBRAMANIAN, K. 2005 Astrophysical magnetic fields and nonlinear dynamo theory. *Physics Reports* **417** (1-4), 1–209.
- BROWN, E. & AHLERS, G. 2006 Effect of the Earth’s Coriolis force on the large-scale circulation of turbulent Rayleigh–Bénard convection. *Phys. Fluids* **18** (12), 125108.
- BROWN, E. & AHLERS, G. 2007 Large-scale circulation model for turbulent Rayleigh–Bénard convection. *Phys. Rev. Lett.* **98** (13), 134501.
- BROWN, E. & AHLERS, G. 2009 The origin of oscillations of the large-scale circulation of turbulent Rayleigh–Bénard convection. *J. Fluid Mech.* **638**, 383–400.
- BUFFETT, B. A. & SEAGLE, C. T. 2010 Stratification of the top of the core due to chemical interactions with the mantle. *J. Geophys. Res. Solid Earth* **115** (B4).
- BULLARD, E. C. 1949 The magnetic field within the earth. *Proceedings of the Royal Society of London. Series A. Mathematical and Physical Sciences* **197** (1051), 433–453.
- BUNGE, H. 2005 Low plume excess temperature and high core heat flux inferred from non-adiabatic geotherms in internally heated mantle circulation models. *Phys. Earth Planet. Inter.* **153** (1-3), 3–10.
- BURKE, B. F. & FRANKLIN, K. L. 1955 Observations of a variable radio source associated with the planet jupiter. *Journal of Geophysical Research* **60** (2), 213–217.
- BURR, U. & MÜLLER, U. 2001 Rayleigh–bénard convection in liquid metal layers under the influence of a vertical magnetic field. *Physics of Fluids* **13** (11), 3247–3257.
- BUSSE, F. H. 2008 Asymptotic theory of wall-attached convection in a horizontal fluid layer with a vertical magnetic field. *Phys. Fluids* **20** (2), 024102.

- CAI, T. 2021 Large-scale vortices in rapidly rotating rayleigh–bénard convection at small prandtl number. *The Astrophysical Journal* **923** (2), 138.
- CALKINS, M. A. 2018 Quasi-geostrophic dynamo theory. *Physics of the Earth and Planetary Interiors* **276**, 182–189.
- CALKINS, M. A., JULIEN, K., TOBIAS, S. M. & AURNOU, J. M. 2015 A multiscale dynamo model driven by quasi-geostrophic convection. *Journal of Fluid Mechanics* **780**, 143–166.
- CALKINS, M. A., NOIR, J., ELDREDGE, J. D. & AURNOU, J. M. 2012 The effects of boundary topography on convection in earth’s core. *Geophysical Journal International* **189** (2), 799–814.
- CAMPUZANO, S. A., GÓMEZ-PACCARD, M., PAVÓN-CARRASCO, F. J. & OSETE, M. L. 2019 Emergence and evolution of the south atlantic anomaly revealed by the new paleomagnetic reconstruction shawq2k. *Earth and Planetary Science Letters* **512**, 17–26.
- CAO, H., DOUGHERTY, M. K., HUNT, G. J., PROVAN, G., COWLEY, S. W., BUNCE, E. J., KELLOCK, S. & STEVENSON, D. J. 2020 The landscape of saturn’s internal magnetic field from the cassini grand finale. *Icarus* **344**, 113541.
- CARDIN, P., BRITO, D., JAULT, D., NATAF, H.-C. & MASSON, J.-P. 2002 Towards a rapidly rotating liquid sodium dynamo experiment. *Magnetohydrodynamics c/c of Magnitnaia Hidrodinamika* **38**, 177–189.
- CARDIN, P. & OLSON, P. 1995 The influence of toroidal magnetic field on thermal convection in the core. *Earth and Planetary Science Letters* **132** (1-4), 167–181.
- CASTAING, B., GAGNE, Y. & HOPFINGER, E. 1990 Velocity probability density functions of high reynolds number turbulence. *Physica D: Nonlinear Phenomena* **46** (2), 177–200.

- CASTRO-TIRADO, A. J., DE UGARTE POSTIGO, A., GOROSABEL, J., JELÍNEK, M., FATKHULLIN, T. A., SOKOLOV, V. V., FERRERO, P., KANN, D. A., KLOSE, S., SLUSE, D. *et al.* 2008 Flares from a candidate galactic magnetar suggest a missing link to dim isolated neutron stars. *Nature* **455** (7212), 506.
- CHAN, K. L. & MAYR, H. G. 2013 Numerical simulation of convectively generated vortices: Application to the jovian planets. *Earth and Planetary Science Letters* **371**, 212–219.
- CHANDRASEKHAR, S. 1952 Xlvi. on the inhibition of convection by a magnetic field. *The London, Edinburgh, and Dublin Philosophical Magazine and Journal of Science* **43** (340), 501–532.
- CHANDRASEKHAR, S. 1961 *Hydrodynamic and hydromagnetic stability*. Courier Corporation.
- CHEN, L., CHEN, P., LI, W., ZHANG, Q., STRUZHKIN, V. V., GONCHAROV, A. F., REN, Z. & CHEN, X. 2019 Enhancement of thermoelectric performance across the topological phase transition in dense lead selenide. *Nat. Mater.* **18** (12), 1321–1326.
- CHEN, L., HERREMAN, W., LI, K., LIVERMORE, P. W., LUO, J. & JACKSON, A. 2018 The optimal kinematic dynamo driven by steady flows in a sphere. *Journal of Fluid Mechanics* **839**, 1–32.
- CHENG, J. S. & AURNOU, J. M. 2016 Tests of diffusion-free scaling behaviors in numerical dynamo datasets. *Earth Planet. Sci. Lett.* **436**, 121–129.
- CHENG, J. S., AURNOU, J. M., JULIEN, K. & KUNNEN, R. P. 2018 A heuristic framework for next-generation models of geostrophic convective turbulence. *Geophysical & Astrophysical Fluid Dynamics* **112** (4), 277–300.
- CHENG, J. S., MOHAMMAD, I., WANG, B., FORER, J. M. & KELLEY, D. H. 2022a Laboratory model of electrovortex flow with thermal gradients for liquid metal batteries. *Experiments in Fluids* **63** (11), 178.

- CHENG, J. S., MOHAMMAD, I., WANG, B., KEOGH, D. F., FORER, J. M. & KELLEY, D. H. 2022*b* Oscillations of the large-scale circulation in experimental liquid metal convection at aspect ratios 1.4–3. *Journal of Fluid Mechanics* **949**, A42.
- CHENG, J. S., STELLMACH, S., RIBEIRO, A., GRANNAN, A., KING, E. M. & AURNOU, J. M. 2015 Laboratory-numerical models of rapidly rotating convection in planetary cores. *Geophysical Journal International* **201** (1), 1–17.
- CHILLÀ, F. & SCHUMACHER, J. 2012 New perspectives in turbulent Rayleigh-Bénard convection. *Eur. Phys. J. E* **35** (7), 58.
- CHONG, K. L., YANG, Y., HUANG, S.-D., ZHONG, J.-Q., STEVENS, R. J., VERZICCO, R., LOHSE, D. & XIA, K.-Q. 2017 Confined rayleigh-bénard, rotating rayleigh-bénard, and double diffusive convection: A unifying view on turbulent transport enhancement through coherent structure manipulation. *Physical review letters* **119** (6), 064501.
- CHRISTENSEN, U. 2010 Dynamo scaling laws and applications to the planets. *Space science reviews* **152**, 565–590.
- CHRISTENSEN, U. R. & AUBERT, J. 2006 Scaling properties of convection-driven dynamos in rotating spherical shells and application to planetary magnetic fields. *Geophysical Journal International* **166** (1), 97–114.
- CIONI, S., CHAUMAT, S. & SOMMERIA, J. 2000*a* Effect of a vertical magnetic field on turbulent rayleigh-bénard convection. *Physical Review E* **62** (4), R4520.
- CIONI, S., CHAUMAT, S. & SOMMERIA, J. 2000*b* Effect of a vertical magnetic field on turbulent Rayleigh-Bénard convection. *Phys. Rev. E* **62** (4), R4520.
- CIONI, S., CILIBERTO, S. & SOMMERIA, J. 1997 Strongly turbulent Rayleigh-Bénard convection in mercury: comparison with results at moderate prandtl number. *J. Fluid Mech.* **335**, 111–140.

- CLEVER, R. M. & BUSSE, F. H. 1981 Low-Prandtl-number convection in a layer heated from below. *J. Fluid Mech.* **102**, 61–74.
- CONNERNEY, J., KOTSIAROS, S., OLIVERSEN, R., ESLEY, J., JOERGENSEN, J. L., JOERGENSEN, P., MERAYO, J. M., HERCEG, M., BLOXHAM, J., MOORE, K. *et al.* 2018 A new model of jupiter’s magnetic field from juno’s first nine orbits. *Geophysical Research Letters* **45** (6), 2590–2596.
- COTTAAR, S. & LEKIC, V. 2016 Morphology of seismically slow lower-mantle structures. *Geophys. suppl. mon. not. R. Astron. Soc.* **207** (2), 1122–1136.
- COWLING, T. G. 1933 The magnetic field of sunspots. *Monthly Notices of the Royal Astronomical Society* **94**, 39–48.
- CUSACK, N. E. 1963 The electronic properties of liquid metals. *Rep. Prog. Phys.* **26** (1), 361.
- DAVIDSON, P. 2016 *Introduction to Magnetohydrodynamics*, 2nd edn. *Cambridge Texts in Applied Mathematics* 1. Cambridge University Press.
- DAVIDSON, P. A. 1999 Magnetohydrodynamics in materials processing. *Annu. Rev. Fluid Mech.* **31** (1), 273–300.
- DERBY, N. & OLBERT, S. 2010 Cylindrical magnets and ideal solenoids. *American Journal of Physics* **78** (3), 229–235.
- DESCHAMPS, F., ROGISTER, Y. & TACKLEY, P. J. 2018 Constraints on core–mantle boundary topography from models of thermal and thermochemical convection. *Geophys. J. Int.* **212** (1), 164–188.
- DOUGHERTY, M. K., CAO, H., KHURANA, K. K., HUNT, G. J., PROVAN, G., KELLOCK, S., BURTON, M. E., BURK, T. A., BUNCE, E. J., COWLEY, S. W. *et al.* 2018 Saturn’s magnetic field revealed by the cassini grand finale. *Science* **362** (6410), eaat5434.

- ECKE, R. E., ZHONG, F. & KNOBLOCH, E. 1992 Hopf bifurcation with broken reflection symmetry in rotating Rayleigh-Bénard convection. *EPL* **19** (3), 177.
- ELSASSER, W. M. 1939 On the origin of the earth's magnetic field. *Physical Review* **55** (5), 489.
- ELTAYEB, I. 1972 Hydromagnetic convection in a rapidly rotating fluid layer. *Proceedings of the Royal Society of London. A. Mathematical and Physical Sciences* **326** (1565), 229–254.
- ELTAYEB, I. A. & ROBERTS, P. H. 1970 Note: on the hydromagnetics of rotating fluids. *The Astrophysical Journal* **162**, 699.
- ENGBERS, Y. A., GRAPPONE, J. M., MARK, D. F. & BIGGIN, A. J. 2022 Low paleointensities and ar/ar ages from saint helena provide evidence for recurring magnetic field weaknesses in the south atlantic. *Journal of Geophysical Research: Solid Earth* **127** (3), e2021JB023358.
- FAVIER, B., SILVERS, L. J. & PROCTOR, M. R. 2014 Inverse cascade and symmetry breaking in rapidly rotating boussinesq convection. *Physics of Fluids* **26** (9), 096605.
- FINLAY, C. C. 2008 Course 8: Waves in the presence of magnetic fields, rotation and convection. In *Les Houches*, , vol. 88, pp. 403–450. Elsevier.
- FINLAY, C. C., GILLET, N., AUBERT, J., LIVERMORE, P. W. & JAULT, D. 2023 Gyres, jets and waves in the earth's core. *Nature Reviews Earth & Environment* pp. 1–16.
- FINLAY, C. C., JACKSON, A., GILLET, N. & OLSEN, N. 2012 Core surface magnetic field evolution 2000–2010. *Geophys. J. Int.* **189** (2), 761–781.
- FINLAY, C. C., KLOSS, C., OLSEN, N., HAMMER, M. D., TØFFNER-CLAUSEN, L., GRAYVER, A. & KUVSHINOV, A. 2020 The chaos-7 geomagnetic field model and observed changes in the south atlantic anomaly. *Earth, Planets and Space* **72** (1), 1–31.

- FINLAY, C. C., OLSEN, N., KOTSIAROS, S., GILLET, N. & TØFFNER-CLAUSEN, L. 2016 Recent geomagnetic secular variation from swarm and ground observatories as estimated in the chaos-6 geomagnetic field model. *Earth Planets Space* **68** (1), 1–18.
- FRENCH, S. W. & ROMANOWICZ, B. 2015 Broad plumes rooted at the base of the earth’s mantle beneath major hotspots. *Nature* **525** (7567), 95–99.
- FRISCH, U. 1995 *Turbulence: the legacy of AN Kolmogorov*. Cambridge university press.
- FROST, B. R. & SHIVE, P. N. 1986 Magnetic mineralogy of the lower continental crust. *Journal of Geophysical Research: Solid Earth* **91** (B6), 6513–6521.
- FU, R. R., WEISS, B. P., SHUSTER, D. L., GATTACCECA, J., GROVE, T. L., SUAVET, C., LIMA, E. A., LI, L. & KUAN, A. T. 2012 An ancient core dynamo in asteroid vesta. *Science* **338** (6104), 238–241.
- FULKERSON, W., MOORE, J. P., WILLIAMS, R. K., GRAVES, R. S. & MCELROY, D. L. 1968 Thermal conductivity, electrical resistivity, and Seebeck coefficient of silicon from 100 to 1300 k. *Phys. Rev* **167** (3), 765.
- FUNFSCHILLING, D. & AHLERS, G. 2004 Plume motion and large-scale circulation in a cylindrical Rayleigh-Bénard cell. *Phys. Rev. Lett.* **92** (19), 194502.
- FUNFSCHILLING, D., BROWN, E. & AHLERS, G. 2008 Torsional oscillations of the large-scale circulation in turbulent Rayleigh-Bénard convection. *J. Fluid Mech.* **607**, 119.
- GARNERO, E. J., MCNAMARA, A. K. & SHIM, S. 2016 Continent-sized anomalous zones with low seismic velocity at the base of earth’s mantle. *Nat. Geosci.* **9** (7), 481–489.
- GARNERO, E. J., REVENAUGH, J., WILLIAMS, Q., LAY, T. & KELLOGG, L. H. 1998 Ultralow velocity zone at the core-mantle boundary. *The core-mantle boundary region* **28**, 319–334.

- GASTINE, T., HEIMPEL, M. & WICHT, J. 2014 Zonal flow scaling in rapidly-rotating compressible convection. *Physics of the Earth and Planetary Interiors* **232**, 36–50.
- GASTINE, T., WICHT, J. & AUBERT, J. 2016 Scaling regimes in spherical shell rotating convection. *Journal of Fluid Mechanics* **808**, 690–732.
- GAUSS, C. F. 1877 *Allgemeine theorie des erdmagnetismus*. Springer.
- GIAMPIERI, G. & BALOGH, A. 2002 Mercury’s thermoelectric dynamo model revisited. *Planet. Space Sci.* **50** (7-8), 757–762.
- GILLET, N., SCHAEFFER, N. & JAULT, D. 2012 Rationale and geophysical evidence for quasi-geostrophic rapid dynamics within the earth’s outer core. *Physics of the Earth and Planetary Interiors* **202**, 78–88.
- GLATZMAIERS, G. A. & ROBERTS, P. H. 1995 A three-dimensional self-consistent computer simulation of a geomagnetic field reversal. *Nature* **377** (6546), 203–209.
- GLAZIER, J. A., SEGAWA, T., NAERT, A. & SANO, M. 1999 Evidence against ‘ultrahard’ thermal turbulence at very high Rayleigh numbers. *Nature* **398** (6725), 307–310.
- GOLUSKIN, D., JOHNSTON, H., FLIERL, G. R. & SPIEGEL, E. A. 2014 Convectively driven shear and decreased heat flux. *J. Fluid Mech.* **759**, 360–385.
- GRANNAN, A. M. 2017 *Experimental and numerical studies of mechanically-and convectively-driven turbulence in planetary interiors*. University of California, Los Angeles.
- GRANNAN, A. M., CHENG, J. S., AGGARWAL, A., HAWKINS, E. K., XU, Y., HORN, S., SÁNCHEZ-ÁLVAREZ, J. & AURNOU, J. M. 2022 Experimental pub crawl from rayleigh–bénard to magnetostrophic convection. *Journal of Fluid Mechanics* **939**.
- GRANNAN, A. M., VOGT, T., HORN, S., HAWKINS, E. K., AGGARWAL, A. & AURNOU, J. M. 2017 Behaviors and transitions along the path to magnetostrophic convection. In *AGU Fall Meeting Abstracts*.

- GRAY, D. D. & GIORGINI, A. 1976 The validity of the boussinesq approximation for liquids and gases. *Int. J. Heat Mass Transf.* **19** (5), 545–551.
- GRIESSMEIER, J.-M., STADELMANN, A., GRENFELL, J. L., LAMMER, H. & MOTSCHMANN, U. 2009 On the protection of extrasolar earth-like planets around k/m stars against galactic cosmic rays. *Icarus* **199** (2), 526–535.
- GROSSMANN, S. & LOHSE, D. 2004 Fluctuations in turbulent Rayleigh–Bénard convection: the role of plumes. *Phys. Fluids* **16** (12), 4462–4472.
- GUBBINS, D. 1987 Mechanism for geomagnetic polarity reversals. *Nature* **326** (6109), 167–169.
- GUBBINS, D. & BLOXHAM, J. 1987 Morphology of the geomagnetic field and implications for the geodynamo. *Nature* **325** (6104), 509–511.
- GUBBINS, D. & RICHARDS, M. 1986 Coupling of the core dynamo and mantle: thermal or topographic? *Geophysical Research Letters* **13** (13), 1521–1524.
- GUERVILLY, C., CARDIN, P. & SCHAEFFER, N. 2019 Turbulent convective length scale in planetary cores. *Nature* **570** (7761), 368–371.
- GUERVILLY, C., HUGHES, D. W. & JONES, C. A. 2014 Large-scale vortices in rapidly rotating rayleigh–bénard convection. *Journal of Fluid Mechanics* **758**, 407–435.
- HALE, C. & DUNLOP, D. 1984 Evidence for an early archean geomagnetic field: A paleomagnetic study of the komati formation, barberton greenstone belt, south africa. *Geophysical Research Letters* **11** (2), 97–100.
- HARTMANN, G. A. & PACCA, I. G. 2009 Time evolution of the south atlantic magnetic anomaly. *Anais da Academia Brasileira de Ciências* **81**, 243–255.
- HARTMANN, J. & LAZARUS, F. 1937 *Hg-dynamics*. Levin & Munksgaard Copenhagen.

- HAWKINS, E. K. 2020 *Experimental Investigations of Convective Turbulence in Planetary Cores*. University of California, Los Angeles.
- HAWKINS, E. K., CHENG, J. S., ABBATE, J. A., PILEGARD, T., STELLMACH, S., JULIEN, K. & AURNOU, J. M. 2023 Laboratory models of planetary core-style convective turbulence. *Fluids* **8** (4), 106.
- HERRMANN, J. & BUSSE, F. H. 1993 Asymptotic theory of wall-attached convection in a rotating fluid layer. *Journal of Fluid Mechanics* **255**, 183–194.
- HOLME, R. 2015 Large-scale flow in the core. *Treatise on Geophysics* **8**, 107–130.
- HOLMSTRÖM, E., STIXRUDE, L., SCIPIONI, R. & FOSTER, A. S. 2018 Electronic conductivity of solid and liquid (Mg, Fe)O computed from first principles. *Earth Planet. Sci. Lett.* **490**, 11–19.
- HORANYI, S., KREBS, L. & MÜLLER, U. 1999 Turbulent rayleigh–bénard convection in low prandtl–number fluids. *International journal of heat and mass transfer* **42** (21), 3983–4003.
- HORI, K., JONES, C. A. & TEED, R. J. 2015 Slow magnetic Rossby waves in the Earth’s core. *Geophys. Res. Lett.* **42** (16), 6622–6629.
- HORN, S. & AURNOU, J. M. 2018 Regimes of coriolis-centrifugal convection. *Physical review letters* **120** (20), 204502.
- HORN, S. & AURNOU, J. M. 2019 Rotating convection with centrifugal buoyancy: Numerical predictions for laboratory experiments. *Physical Review Fluids* **4** (7), 073501.
- HORN, S. & AURNOU, J. M. 2021 Tornado-like vortices in the quasi-cyclostrophic regime of coriolis-centrifugal convection. *Journal of Turbulence* **22** (4-5), 297–324.
- HORN, S. & AURNOU, J. M. 2022 The elbert range of magnetostrophic convection. i. linear theory. *Proceedings of the Royal Society A* **478** (2264), 20220313.

- HORN, S. & SCHMID, P. 2017 Prograde, retrograde, and oscillatory modes in rotating rayleigh–bénard convection. *Journal of Fluid Mechanics* **831**, 182–211.
- HORN, S., SCHMID, P. J. & AURNOU, J. M. 2022 Unravelling the large-scale circulation modes in turbulent rayleigh–bénard convection (a). *Europhysics Letters* **136** (1), 14003.
- HORN, S. & SHISHKINA, O. 2015 Toroidal and poloidal energy in rotating Rayleigh–Bénard convection. *J. Fluid Mech.* **762**, 232–255.
- HOUCHENS, B. C., WITKOWSKI, L. M. & WALKER, J. S. 2002 Rayleigh–Bénard instability in a vertical cylinder with a vertical magnetic field. *J. Fluid Mech.* **469**, 189–207.
- HUGHES, D. & TOBIAS, S. 2010 An introduction to mean field dynamo theory. *Relaxation Dynamics in Laboratory and Astrophysical Plasmas* **1**, 15.
- HULOT, G., EYMIN, C., LANGLAIS, B., MANDEA, M. & OLSEN, N. 2002 Small-scale structure of the geodynamo inferred from oersted and magsat satellite data. *Nature* **416** (6881), 620–623.
- JAUPART, C., LABROSSE, S., LUCAZEAU, F. & MARESCHAL, J. 2007 7.06-temperatures, heat and energy in the mantle of the earth. *Treatise on geophysics* **7**, 223–270.
- JAWORSKI, M. A., GRAY, T. K., ANTONELLI, M., KIM, J. J., LAU, C. Y., LEE, M. B., NEUMANN, M. J., XU, W. & RUZIC, D. N. 2010 Thermoelectric magnetohydrodynamic stirring of liquid metals. *Phys. Rev. Lett.* **104** (9), 094503.
- JOHNSON, C. L. & CONSTABLE, C. G. 1998 Persistently anomalous pacific geomagnetic fields. *Geophysical research letters* **25** (7), 1011–1014.
- JOHNSON-GROH, M. & MERZDORF, J. 2020 Nasa researchers track “dent” in earth’s magnetic field.
- JONES, C. A. 2011 Planetary magnetic fields and fluid dynamos. *Annu. Rev. Fluid Mech.* **43**, 583–614.

- JONES, C. A. 2015 Thermal and compositional convection in the outer core. *Treatise in Geophysics, Core Dynamics* **8**, 131–185.
- JULIEN, K., AURNOU, J. M., CALKINS, M. A., KNOBLOCH, E., MARTI, P., STELLMACH, S. & VASIL, G. M. 2016 A nonlinear model for rotationally constrained convection with ekman pumping. *Journal of Fluid Mechanics* **798**, 50–87.
- JULIEN, K. & KNOBLOCH, E. 2007 Reduced models for fluid flows with strong constraints. *Journal of Mathematical physics* **48** (6), 065405.
- JULIEN, K., LEGG, S., MCWILLIAMS, J. & WERNE, J. 1996 Rapidly rotating turbulent Rayleigh–Bénard convection. *J. Fluid Mech.* **322**, 243–273.
- JULIEN, K., RUBIO, A. M., GROOMS, I. & KNOBLOCH, E. 2012 Statistical and physical balances in low rossby number rayleigh–bénard convection. *Geophysical & Astrophysical Fluid Dynamics* **106** (4-5), 392–428.
- KAO, A., PERICLEOUS, K., PATEL, M. K. & VOLLER, V. 2009 Effects of magnetic fields on crystal growth. *Int. J. Cast Met. Res.* **22** (1-4), 147–150.
- KÄPYLÄ, P. J., MANTERE, M. J. & HACKMAN, T. 2011 Starspots due to large-scale vortices in rotating turbulent convection. *The Astrophysical Journal* **742** (1), 34.
- KASAP, S. 2001 Thermoelectric effects in metals: thermocouples. *Canada: Department of Electrical Engineering University of Saskatchewan* .
- KELLEY, D. H. & WEIER, T. 2018 Fluid mechanics of liquid metal batteries. *Appl. Mech. Rev.* **70** (2).
- KING, E. M. 2009 *An investigation of planetary convection: The role of boundary layers*. University of California, Los Angeles.
- KING, E. M. & AURNOU, J. M. 2013 Turbulent convection in liquid metal with and without rotation. *Proceedings of the National Academy of Sciences* **110** (17), 6688–6693.

- KING, E. M. & AURNOU, J. M. 2015 Magnetostrophic balance as the optimal state for turbulent magnetoconvection. *Proc. Natl. Acad. Sci. U.S.A.* **112** (4), 990–994.
- KING, E. M. & BUFFETT, B. A. 2013 Flow speeds and length scales in geodynamo models: the role of viscosity. *Earth and Planetary Science Letters* **371**, 156–162.
- KING, E. M., STELLMACH, S. & AURNOU, J. M. 2012*a* Heat transfer by rapidly rotating rayleigh–bénard convection. *Journal of Fluid Mechanics* **691**, 568–582.
- KING, E. M., STELLMACH, S. & AURNOU, J. M. 2012*b* Heat transfer by rapidly rotating Rayleigh–Bénard convection. *J. Fluid Mech.* **691**, 568–582.
- KIVELSON, M. G. 1995 *Introduction to space physics*. Cambridge university press.
- KNAEPEN, B. & MOREAU, R. 2008 Magnetohydrodynamic turbulence at low magnetic reynolds number. *Annu. Rev. Fluid Mech.* **40**, 25–45.
- KOCHUKHOV, O. 2021 Magnetic fields of m dwarfs. *The Astronomy and Astrophysics Review* **29** (1), 1.
- KOLMOGOROV, A. *et al.* 1942 Equations of motion of an incompressible turbulent fluid. *Izv Akad Nauk SSSR Ser Phys* **6** (6), 56–58.
- KONO, M. 2015 *Geomagnetism: An Introduction and Overview*, pp. 1–31. Elsevier.
- KUNNEN, R. P. J., CLERCX, H. J. H. & GEURTS, B. J. 2008 Breakdown of large-scale circulation in turbulent rotating convection. *Euro. Phys. Lett.* **84** (2), 24001.
- LABROSSE, S. 2015 Thermal evolution of the core with a high thermal conductivity. *Physics of the Earth and Planetary Interiors* **247**, 36–55.
- LAJ, C. & KISSEL, C. 2015 An impending geomagnetic transition? hints from the past. *Frontiers in Earth Science* **3**, 61.

- LANDAU, L. D. & LIFSHITZ, E. M. 1976 Theoretical physics. vol. 1. *Mechanics*. Moscow, Nauka .
- LANDEAU, M., FOURNIER, A., NATAF, H.-C., CÉBRON, D. & SCHAEFFER, N. 2022 Sustaining earth’s magnetic dynamo. *Nature Reviews Earth & Environment* **3** (4), 255–269.
- LANDIN, N. R., MENDES, L. T. S., VAZ, L. P. R. & ALENCAR, S. H. P. 2023 Rossby numbers of fully and partially convective stars. *Monthly Notices of the Royal Astronomical Society* **519** (4), 5304–5314.
- LANGEL, R. & ESTES, R. 1982 A geomagnetic field spectrum. *Geophysical Research Letters* **9** (4), 250–253.
- LARMOR, J. 1919 How could a rotating body such as the sun become a magnet? In *A Source Book in Astronomy and Astrophysics, 1900–1975*, pp. 106–107. Harvard University Press.
- LAY, T., WILLIAMS, Q. & GARNERO, E. J. 1998 The core–mantle boundary layer and deep earth dynamics. *Nature* **392** (6675), 461–468.
- LAZIO, J., HALLINAN, G., AIRAPETIAN, V., BRAIN, D., DONG, C., DRISCOLL, P., GRIESSMEIER, J.-M., FARRELL, W., KASPER, J., MURPHY, T. *et al.* 2018 Magnetic fields of extrasolar planets: planetary interiors and habitability. *arXiv preprint arXiv:1803.06487* .
- LI, M., MCNAMARA, A. K., GARNERO, E. J. & YU, S. 2017 Compositionally-distinct ultra-low velocity zones on earth’s core-mantle boundary. *Nat. Commun* **8** (1), 1–9.
- LIM, Z. L., CHONG, K. L., DING, G. Y. & XIA, K. Q. 2019 Quasistatic magnetoconvection: heat transport enhancement and boundary layer crossing. *Journal of Fluid Mechanics* **870**, 519–542.

- LIU, J., LI, J., HRUBIAK, R. & SMITH, J. S. 2016 Origins of ultralow velocity zones through slab-derived metallic melt. *Proc. Natl. Acad. Sci. U.S.A.* **113** (20), 5547–5551.
- LIU, W., KRASNOV, D. & SCHUMACHER, J. 2018 Wall modes in magnetoconvection at high Hartmann numbers. *J. Fluid Mech.* **849**.
- LOWES, F. 1974 Spatial power spectrum of the main geomagnetic field, and extrapolation to the core. *Geophysical Journal International* **36** (3), 717–730.
- LU, H. Y., DING, G. Y., SHI, J. Q., XIA, K. Q. & ZHONG, J. Q. 2021 Heat-transport scaling and transition in geostrophic rotating convection with varying aspect ratio. *Physical Review Fluids* **6** (7), L071501.
- MADONIA, M., GUZMÁN, A. J. A., CLERCX, H. J. & KUNNEN, R. P. 2021 Velocimetry in rapidly rotating convection: spatial correlations, flow structures and length scales (a). *Europhysics Letters* **135** (5), 54002.
- MAFFEI, S., KROUSS, M. J., JULIEN, K. & CALKINS, M. A. 2021 On the inverse cascade and flow speed scaling behaviour in rapidly rotating rayleigh–bénard convection. *Journal of Fluid Mechanics* **913**, A18.
- MANDEA, M., KORTE, M., MOZZONI, D. & KOTZÉ, P. 2007 The magnetic field changing over the southern african continent: a unique behaviour. *South African Journal of Geology* **110** (2-3), 193–202.
- MAO, H., HU, Q., YANG, L., LIU, J., KIM, D. Y., MENG, Y., ZHANG, L., PRAKAPENKA, V. B., YANG, W. & MAO, W. L. 2017 When water meets iron at Earth’s core–mantle boundary. *Natl. Sci. Rev.* **4** (6), 870–878.
- MAUERSBERGER, P. 1956 Das mittel der energiedichte des geomagnetischen hauptfeldes an der erdoberfläche und seine saulare anderung. *Gerlands Beitr. Geophys.* **65**, 207–215.

- MCDONOUGH, W. F. & SUN, S.-S. 1995 The composition of the earth. *Chemical geology* **120** (3-4), 223–253.
- MCWILLIAMS, J. C. 1984 The emergence of isolated coherent vortices in turbulent flow. *Journal of Fluid Mechanics* **146**, 21–43.
- MCWILLIAMS, J. C. 2006 *Fundamentals of geophysical fluid dynamics*. Cambridge University Press.
- MEDURI, D. G., BIGGIN, A. J., DAVIES, C. J., BONO, R. K., SPRAIN, C. J. & WICHT, J. 2020 Numerical dynamo simulations reproduce palaeomagnetic field behaviour. *Geophys. Res. Lett.* p. e2020GL090544.
- MERRILL, R. T. & MCELHINNY, M. W. 1977 Anomalies in the time-averaged paleomagnetic field and their implications for the lower mantle. *Rev. Geophys.* **15** (3), 309–323.
- MININNI, P. D. & POUQUET, A. 2010 Rotating helical turbulence. i. global evolution and spectral behavior. *Physics of Fluids* **22** (3), 035105.
- MOFFATT, H. K. 1978 Magnetic field generation in electrically conducting fluids. *Cambridge Monographs on Mechanics and Applied Mathematics* .
- MOFFATT, K. & DORMY, E. 2019a *Self-exciting fluid dynamos*, , vol. 59. Cambridge University Press.
- MOFFATT, K. & DORMY, E. 2019b *Self-Exciting Fluid Dynamos*, , vol. 59. Cambridge University Press.
- MOORE, K. M., YADAV, R. K., KULOWSKI, L., CAO, H., BLOXHAM, J., CONNERNEY, J. E. P., KOTSIAROS, S., JØRGENSEN, J. L., MERAYO, J. M. G. & STEVENSON, D. J. 2018 A complex dynamo inferred from the hemispheric dichotomy of jupiter’s magnetic field. *Nature* **561** (7721), 76.

- MOORE, T. & KHAZANOV, G. 2010 Mechanisms of ionospheric mass escape. *Journal of Geophysical Research: Space Physics* **115** (A12).
- MOREAU, R. 1999 The fundamentals of MHD related to crystal growth. *Prog. Cryst. Growth Charact. Mater.* **38** (1-4), 161–194.
- MOROZOVA, N. V., KOROBENIKOV, I. V. & OVSYANNIKOV, S. V. 2019 Strategies and challenges of high-pressure methods applied to thermoelectric materials. *J. Appl. Phys.* **125** (22), 220901.
- MOSCA, I., COBDEN, L., DEUSS, A., RITSEMA, J. & TRAMPERT, J. 2012 Seismic and mineralogical structures of the lower mantle from probabilistic tomography. *J. Geophys. Res. Solid Earth* **117** (B6).
- MOTT, N. F. & JONES, H. 1958 *The theory of the properties of metals and alloys*. Dover.
- MOUND, J., DAVIES, C., ROST, S. & AURNOU, J. 2019 Regional stratification at the top of earth’s core due to core–mantle boundary heat flux variations. *Nat. Geosci.* **12** (7), 575–580.
- NAKAGAWA, Y. 1955 An experiment on the inhibition of thermal convection by a magnetic field. *Nature* **175** (4453), 417.
- NIEVES, D., RUBIO, A. M. & JULIEN, K. 2014 Statistical classification of flow morphology in rapidly rotating rayleigh–bénard convection. *Physics of Fluids* **26** (8), 086602.
- NIMMO, F. 2009 Energetics of asteroid dynamos and the role of compositional convection. *Geophysical Research Letters* **36** (10).
- OBERBECK, A. 1879 Ueber die Wärmeleitung der Flüssigkeiten bei Berücksichtigung der Strömungen infolge von Temperaturdifferenzen. *Ann. Phys* **243** (6), 271–292.

- OLIVER, T. G., JACOBI, A. S., JULIEN, K. & CALKINS, M. A. 2023 Small scale quasi-geostrophic convective turbulence at large rayleigh number. *arXiv preprint arXiv:2303.03467* .
- OLSEN, N. & MANDEA, M. 2008 Rapidly changing flows in the earth’s core. *Nature geoscience* **1** (6), 390–394.
- OLSEN, N., MANDEA, M., SABAKA, T. J. & TØFFNER-CLAUSEN, L. 2009 Chaos-2—a geomagnetic field model derived from one decade of continuous satellite data. *Geophysical Journal International* **179** (3), 1477–1487.
- OLSON, P. & AMIT, H. 2006 Changes in earth’s dipole. *Naturwissenschaften* **93**, 519–542.
- PANDEY, A., SCHEEL, J. D. & SCHUMACHER, J. 2018 Turbulent superstructures in Rayleigh-Bénard convection. *Nat. Commun.* **9** (1), 1–11.
- PAVÓN-CARRASCO, F. J. & DE SANTIS, A. 2016 The south atlantic anomaly: The key for a possible geomagnetic reversal. *Frontiers in Earth Science* **4**, 40.
- PEREZ, A. & KELLEY, D. H. 2015 Ultrasound velocity measurement in a liquid metal electrode. *JoVE (Journal of Visualized Experiments)* **1** (102), e52622.
- PEREZ, J. C., MASON, J., BOLDYREV, S. & CATTANEO, F. 2012 On the energy spectrum of strong magnetohydrodynamic turbulence. *Physical Review X* **2** (4), 041005.
- PLUMLEY, M. & JULIEN, K. 2019 Scaling laws in rayleigh-benard convection. *Earth and Space Science* **6** (9), 1580–1592.
- POZZO, M., DAVIES, C., GUBBINS, D. & ALFE, D. 2012 Thermal and electrical conductivity of iron at earth’s core conditions. *Nature* **485** (7398), 355–358.
- PROAKIS, J. G. 2007 *Digital signal processing: principles, algorithms, and applications, 4/E*. Pearson Education India.

- PROCTOR, M. R. E. & WEISS, N. O. 1982 Magnetoconvection. *Rep. Prog. Phys.* **45** (11), 1317.
- RÄDLER, K.-H. 1980 Mean-field approach to spherical dynamo models. *Astronomische Nachrichten* **301** (3), 101–129.
- RAJAEI, H., KUNNEN, R. P. & CLERCX, H. J. 2017 Exploring the geostrophic regime of rapidly rotating convection with experiments. *Physics of Fluids* **29** (4), 045105.
- RAMSTAD, R. & BARABASH, S. 2021 Do intrinsic magnetic fields protect planetary atmospheres from stellar winds? lessons from ion measurements at mars, venus, and earth. *Space Science Reviews* **217**, 1–39.
- REMPEL, M., SCHÜSSLER, M. & KNÖLKER, M. 2009 Radiative magnetohydrodynamic simulation of sunspot structure. *Astrophys. J.* **691** (1), 640.
- ROBERTS, P. & SCOTT, S. 1965 On analysis of the secular variation 1. a hydromagnetic constraint: theory. *Journal of geomagnetism and geoelectricity* **17** (2), 137–151.
- ROBERTS, P. H. 1967 *An introduction to magnetohydrodynamics*, , vol. 6. Longmans London.
- ROBERTS, P. H. & KING, E. M. 2013 On the genesis of the Earth’s magnetism. *Rep. Prog. Phys.* **76** (9), 096801.
- ROJAS, R. E., PEREVALOV, A., ZÜRNER, T. & LATHROP, D. P. 2021 Experimental study of rough spherical couette flows: Increasing helicity toward a dynamo state. *Physical Review Fluids* **6** (3), 033801.
- RUBIO, A. M., JULIEN, K., KNOBLOCH, E. & WEISS, J. B. 2014 Upscale energy transfer in three-dimensional rapidly rotating turbulent convection. *Physical review letters* **112** (14), 144501.

- RUDOLPH, P. 2008 Travelling magnetic fields applied to bulk crystal growth from the melt: The step from basic research to industrial scale. *J. Cryst. Growth* **310** (7-9), 1298–1306.
- RUSSELL, C. & DOUGHERTY, M. 2010 Magnetic fields of the outer planets. *Space science reviews* **152**, 251–269.
- SALAVY, J. F., BOCCACCINI, L. V., LÄSSER, R., MEYDER, R., NEUBERGER, H., POITEVIN, Y., RAMPAL, G., RIGAL, E., ZMITKO, M. & AIELLO, A. 2007 Overview of the last progresses for the european test blanket modules projects. *Fusion Eng. Des.* **82** (15-24), 2105–2112.
- SARRIS, I. E., ZIKOS, G. K., GRECOS, A. P. & VLACHOS, N. S. 2006 On the limits of validity of the low magnetic Reynolds number approximation in MHD natural-convection heat transfer. *Numer. Heat Tr. B-Fund.* **50** (2), 157–180.
- SCHAEFFER, N., JAULT, D., NATAF, H. & FOURNIER, A. 2017 Turbulent geodynamo simulations: a leap towards earth’s core. *Geophysical Journal International* **211** (1), 1–29.
- SCHLINGER, C. M. 1985 Magnetization of lower crust and interpretation of regional magnetic anomalies: Example from lofoten and vesterålen, norway. *Journal of Geophysical Research: Solid Earth* **90** (B13), 11484–11504.
- SCHMIDT, A. F. K. 1917 Erdmagnetismus. (*No Title*) .
- SCHMITT, D., CARDIN, P., LA RIZZA, P. & NATAF, H. C. 2013 Magneto–Coriolis waves in a spherical Couette flow experiment. *Eur. J. Mech. B. Fluids* **37**, 10–22.
- SCHNEIDER, D. A. & KENT, D. V. 1988 Inclination anomalies from indian ocean sediments and the possibility of a standing nondipole field. *J. Geophys. Res. Solid Earth* **93** (B10), 11621–11630.
- SCHÜSSLER, M. & VÖGLER, A. 2006 Magnetoconvection in a sunspot umbra. *Astrophys. J. Lett.* **641** (1), L73.

- SESHASAYANAN, K. & ALEXAKIS, A. 2018 Condensates in rotating turbulent flows. *Journal of Fluid Mechanics* **841**, 434–462.
- SHERCLIFF, J. A. 1953 Steady motion of conducting fluids in pipes under transverse magnetic fields. *Mathematical Proceedings of the Cambridge Philosophical Society* **49** (1), 136–144.
- SHERCLIFF, J. A. 1979 Thermoelectric magnetohydrodynamics. *J. Fluid Mech.* **91** (2), 231–251.
- SHISHKINA, O. & HORN, S. 2016 Thermal convection in inclined cylindrical containers. *Journal of Fluid Mechanics* **790**.
- SHISHKINA, O., HORN, S., WAGNER, S. & CHING, E. S. 2015 Thermal boundary layer equation for turbulent rayleigh–bénard convection. *Physical Review Letters* **114** (11), 114302.
- SMITH, L. M. & WALEFFE, F. 1999 Transfer of energy to two-dimensional large scales in forced, rotating three-dimensional turbulence. *Physics of fluids* **11** (6), 1608–1622.
- SODERLUND, K. M., KING, E. M. & AURNOU, J. M. 2012 The influence of magnetic fields in planetary dynamo models. *Earth and Planetary Science Letters* **333**, 9–20.
- SODERLUND, K. M., SHEYKO, A., KING, E. M. & AURNOU, J. M. 2015 The competition between lorentz and coriolis forces in planetary dynamos. *Progress in Earth and Planetary Science* **2** (1), 1–10.
- STACEY, F. D. & DAVIS, P. M. 2008 *Physics of the Earth*. Cambridge University Press.
- STEENBECK, M., KRAUSE, F. & RÄDLER, K.-H. 1966 Berechnung der mittleren lorentzfeldstärke für ein elektrisch leitendes medium in turbulenter, durch coriolis-kräfte beeinflusster bewegung. *Zeitschrift für Naturforschung A* **21** (4), 369–376.

- STELLMACH, S., LISCHPER, M., JULIEN, K., VASIL, G., CHENG, J. S., RIBEIRO, A., KING, E. M. & AURNOU, J. M. 2014 Approaching the asymptotic regime of rapidly rotating convection: boundary layers versus interior dynamics. *Physical review letters* **113** (25), 254501.
- STEVENS, R. J. A. M., BLASS, A., ZHU, X., VERZICCO, R. & LOHSE, D. 2018 Turbulent thermal superstructures in Rayleigh-Bénard convection. *Phys. Rev. Fluid* **3** (4), 041501.
- STEVENSON, D. J. 1987 Mercury's magnetic field: a thermoelectric dynamo? *Earth Planet. Sci. Lett.* **82** (1-2), 114–120.
- STEVENSON, D. J. 2003 Planetary magnetic fields. *Earth and planetary science letters* **208** (1-2), 1–11.
- STIXRUDE, L. & LITHGOW-BERTELLONI, C. 2007 Influence of phase transformations on lateral heterogeneity and dynamics in earth's mantle. *Earth and Planetary Science Letters* **263** (1-2), 45–55.
- SUN, C., XIA, K. & TONG, P. 2005 Three-dimensional flow structures and dynamics of turbulent thermal convection in a cylindrical cell. *Phys. Rev.* **72** (2), 026302.
- TABERLET, E. & FAUTRELLE, Y. 1985 Turbulent stirring in an experimental induction furnace. *J. Fluid Mech.* **159**, 409–431.
- TAN, E., GURNIS, M. & HAN, L. 2002 Slabs in the lower mantle and their modulation of plume formation. *Geochem. Geophys. Geosystems* **3** (11), 1–24.
- TARDUNO, J. A., COTTRELL, R. D., WATKEYS, M. K., HOFMANN, A., DOUBROVINE, P. V., MAMAJEK, E. E., LIU, D., SIBECK, D. G., NEUKIRCH, L. P. & USUI, Y. 2010 Geodynamo, solar wind, and magnetopause 3.4 to 3.45 billion years ago. *science* **327** (5970), 1238–1240.

- TARDUNO, J. A., WATKEYS, M. K., HUFFMAN, T. N., COTTRELL, R. D., BLACKMAN, E. G., WENDT, A., SCRIBNER, C. A. & WAGNER, C. L. 2015 Antiquity of the south atlantic anomaly and evidence for top-down control on the geodynamo. *Nature Communications* **6** (1), 7865.
- TASAKA, Y., IGAKE, K., YANAGISAWA, T., VOGT, T., ZUERNER, T. & ECKERT, S. 2016 Regular flow reversals in Rayleigh-Bénard convection in a horizontal magnetic field. *Phys. Rev. E* **93** (4), 043109.
- TERASAKI, I. 2011 1.09 thermal conductivity and thermoelectric power of semiconductors. *Semicond. Sci. Technol.* p. 326.
- TERRA-NOVA, F., AMIT, H., HARTMANN, G. A., TRINDADE, R. I. & PINHEIRO, K. J. 2017 Relating the south atlantic anomaly and geomagnetic flux patches. *Physics of the Earth and Planetary Interiors* **266**, 39–53.
- TERRIEN, L., FAVIER, B. & KNOBLOCH, E. 2023 Suppression of wall modes in rapidly rotating rayleigh-bénard convection by narrow horizontal fins. *Physical Review Letters* **130** (17), 174002.
- THORNE, M. S., LENG, K., PACHHAI, S., ROST, S., WICKS, J. & NISSEN-MEYER, T. 2021 The most parsimonious ultralow-velocity zone distribution from highly anomalous spdks waveforms. *Geochem. Geophys. Geosystems* **22** (1), e2020GC009467.
- THORNE, M. S., PACHHAI, S., LENG, K., WICKS, J. K. & NISSEN-MEYER, T. 2020 New candidate ultralow-velocity zone locations from highly anomalous spdks waveforms. *Minerals* **10** (3), 211.
- THUAL, O. 1992 Zero-Prandtl-number convection. *J. Fluid Mech.* **240**, 229–258.
- TIKOO, S. M. & EVANS, A. J. 2022 Dynamos in the inner solar system. *Annual Review of Earth and Planetary Sciences* **50**, 99–122.

- TRAMPERT, J., DESCHAMPS, F., RESOVSKY, J. & YUEN, D. 2004 Probabilistic tomography maps chemical heterogeneities throughout the lower mantle. *Science* **306** (5697), 853–856.
- TRINDADE, R. I., JAQUETO, P., TERRA-NOVA, F., BRANDT, D., HARTMANN, G. A., FEINBERG, J. M., STRAUSS, B. E., NOVELLO, V. F., CRUZ, F. W., KARMANN, I. *et al.* 2018 Speleothem record of geomagnetic south atlantic anomaly recurrence. *Proceedings of the National Academy of Sciences* **115** (52), 13198–13203.
- TRITTON, D. J. 1977 *Physical Fluid Dynamics*. Springer Science & Business Media.
- TURCOTTE, D. L. & SCHUBERT, G. 2002 *Geodynamics*. Cambridge university press.
- VERZICCO, R. 2004 Effects of nonperfect thermal sources in turbulent thermal convection. *Phys. Fluids* **16** (6), 1965–1979.
- VOGT, T., HORN, S. & AURNOU, J. M. 2021 Oscillatory thermal–inertial flows in liquid metal rotating convection. *J. Fluid Mech.* **911**.
- VOGT, T., HORN, S., GRANNAN, A. M. & AURNOU, J. M. 2018*a* Jump rope vortex in liquid metal convection. *Proc. Natl. Acad. Sci. U.S.A.* **115** (50), 12674–12679.
- VOGT, T., ISHIMI, W., YANAGISAWA, T., TASAKA, Y., SAKURABA, A. & ECKERT, S. 2018*b* Transition between quasi-two-dimensional and three-dimensional Rayleigh–Bénard convection in a horizontal magnetic field. *Phys. Rev. Fluid* **3** (1), 013503.
- VON HARDENBERG, J., PARODI, A., PASSONI, G., PROVENZALE, A. & SPIEGEL, E. A. 2008 Large-scale patterns in Rayleigh–Bénard convection. *Phys. Lett.* **372** (13), 2223–2229.
- WEISS, N. O. & PROCTOR, M. R. E. 2014 *Magnetoconvection*. Cambridge University Press.

- DE WIJS, G. A., KRESSE, G., VOČADLO, L., DOBSON, D., ALFE, D., GILLAN, M. J. & PRICE, G. D. 1998 The viscosity of liquid iron at the physical conditions of the earth's core. *Nature* **392** (6678), 805–807.
- XI, H., LAM, S. & XIA, K. 2004 From laminar plumes to organized flows: the onset of large-scale circulation in turbulent thermal convection. *J. Fluid Mech.* **503**, 47.
- XI, H., ZHOU, S., ZHOU, Q., CHAN, T. & XIA, K. 2009 Origin of the temperature oscillation in turbulent thermal convection. *Phys. Rev. Lett.* **102** (4), 044503.
- XIA, K., SUN, C. & ZHOU, S. 2003 Particle image velocimetry measurement of the velocity field in turbulent thermal convection. *Phys. Rev.* **68** (6), 066303.
- XU, Y., HORN, S. & AURNOU, J. M. 2022 Thermoelectric precession in turbulent magnetoconvection. *Journal of Fluid Mechanics* **930**.
- YADAV, R. K., GASTINE, T., CHRISTENSEN, U. R., DUARTE, L. D. V. & REINERS, A. 2016 Effect of shear and magnetic field on the heat-transfer efficiency of convection in rotating spherical shells. *Geophysical Journal International* **204** (2), 1120–1133.
- YAN, M. & CALKINS, M. A. 2022 Asymptotic behaviour of rotating convection-driven dynamos in the plane layer geometry. *Journal of Fluid Mechanics* **951**, A24.
- YAN, M., CALKINS, M. A., MAFFEI, S., JULIEN, K., TOBIAS, S. M. & MARTI, P. 2019 Heat transfer and flow regimes in quasi-static magnetoconvection with a vertical magnetic field. *J. Fluid Mech.* **877**, 1186–1206.
- YOSHINO, T., WANG, R., GOMI, H. & MORI, Y. 2020 Measurement of the seebeck coefficient under high pressure by dual heating. *Rev. Sci. Instrum.* **91** (3), 035115.
- ZELDOVICH, Y. B. 1957 The magnetic field in the two-dimensional motion of a conducting turbulent fluid. *Sov. Phys. JETP* **4**, 460–462.

- ZHANG, K. & LIAO, X. 2009 The onset of convection in rotating circular cylinders with experimental boundary conditions. *Journal of Fluid Mechanics* .
- ZHANG, K. & LIAO, X. 2017 *Theory and modeling of rotating fluids: convection, inertial waves and precession*. Cambridge University Press.
- ZHANG, X., CRAMER, A., LANGE, A. & GERBETH, G. 2009 Model experiments on macroscopic thermoelectromagnetic convection. *Magnetohydrodynamics* **45** (1), 25–42.
- ZHONG, F., ECKE, R. E. & STEINBERG, V. 1993 Rotating rayleigh–bénard convection: asymmetric modes and vortex states. *Journal of Fluid Mechanics* **249**, 135–159.
- ZHOU, Q., XI, H., ZHOU, S., SUN, C. & XIA, K. 2009 Oscillations of the large-scale circulation in turbulent Rayleigh–Bénard convection: the sloshing mode and its relationship with the torsional mode. *J. Fluid Mech.* **630**, 367.
- ZIMMERMAN, D. S., TRIANA, S. A., NATAF, H.-C. & LATHROP, D. P. 2014 A turbulent, high magnetic reynolds number experimental model of earth’s core. *Journal of Geophysical Research: Solid Earth* **119** (6), 4538–4557.
- ZÜRNER, T., LIU, W., KRASNOV, D. & SCHUMACHER, J. 2016 Heat and momentum transfer for magnetoconvection in a vertical external magnetic field. *Phys. Rev. E* **94** (4), 043108.
- ZÜRNER, T., SCHINDLER, F., VOGT, T., ECKERT, S. & SCHUMACHER, J. 2019 Combined measurement of velocity and temperature in liquid metal convection. *J. Fluid Mech.* **876**, 1108–1128.
- ZÜRNER, T., SCHINDLER, F., VOGT, T., ECKERT, S. & SCHUMACHER, J. 2020 Flow regimes of Rayleigh–Bénard convection in a vertical magnetic field. *J. Fluid Mech.* **894**.